ISSN
2712-8172

Magazine of Civil Engineering

110(2), 2022



Федеральное государственное автономное образовательное учреждение высшего образования
Санкт-Петербургский политехнический университет Петра Великого

ПОЛИТЕХ
Санкт-Петербургский политехнический университет Петра Великого

Инженерно-строительный институт
Центр дополнительных профессиональных программ

195251, г. Санкт-Петербург, Политехническая ул., 29,
тел/факс: 552-94-60, www.stroikursi.spbstu.ru,
stroikursi@mail.ru

Приглашает специалистов организаций, вступающих в СРО, на курсы повышения квалификации (72 часа)

Код	Наименование программы	Виды работ*
	Курсы по строительству	
БС-01-04	«Безопасность и качество выполнения общестроительных работ»	п.1,2, 3, 5, 6, 7, 9, 10, 11, 12, 13, 14
БС-01	«Безопасность и качество выполнения геодезических, подготовительных и земляных работ, устройства оснований и фундаментов»	1,2,3,5
БС-02	«Безопасность и качество возведения бетонных и железобетонных конструкций»	6,7
БС-03	«Безопасность и качество возведения металлических, каменных и деревянных конструкций»	9,10,11
БС-04	«Безопасность и качество выполнения фасадных работ, устройства кровель, защиты строительных конструкций, трубопроводов и оборудования»	12,13,14
БС-05	«Безопасность и качество устройства инженерных сетей и систем»	15,16,17,18,19
БС-06	«Безопасность и качество устройства электрических сетей и линий связи»	20,21
БС-08	«Безопасность и качество выполнения монтажных и пусконаладочных работ»	23,24
БС-12	«Безопасность и качество устройства мостов, эстакад и путепроводов»	29
БС-13	«Безопасность и качество выполнения гидротехнических, водолазных работ»	30
БС-14	«Безопасность и качество устройства промышленных печей и дымовых труб»	31
БС-15	«Осуществление строительного контроля»	32
БС-16	«Организация строительства, реконструкции и капитального ремонта. Выполнение функций технического заказчика и генерального подрядчика»	33
	Курсы по проектированию	
БП-01	«Разработка схемы планировочной организации земельного участка, архитектурных решений, мероприятий по обеспечению доступа маломобильных групп населения»	1,2,11
БП-02	«Разработка конструктивных и объемно-планировочных решений зданий и сооружений»	3
БП-03	«Проектирование внутренних сетей инженерно-технического обеспечения»	4
БП-04	«Проектирование наружных сетей инженерно-технического обеспечения»	5
БП-05	«Разработка технологических решений при проектировании зданий и сооружений»	6
БП-06	«Разработка специальных разделов проектной документации»	7
БП-07	«Разработка проектов организации строительства»	8
БП-08	«Проектные решения по охране окружающей среды»	9
БП-09	«Проектные решения по обеспечению пожарной безопасности»	10
БП-10	«Обследование строительных конструкций и грунтов основания зданий и сооружений»	12
БП-11	«Организация проектных работ. Выполнение функций генерального проектировщика»	13
Э-01	«Проведение энергетических обследований с целью повышения энергетической эффективности и энергосбережения»	
	Курсы по инженерным изысканиям	
И-01	«Инженерно-геодезические изыскания в строительстве»	1
И-02	«Инженерно-геологические изыскания в строительстве»	2,5
И-03	«Инженерно-гидрометеорологические изыскания в строительстве»	3
И-04	«Инженерно-экологические изыскания в строительстве»	4
И-05	«Организация работ по инженерным изысканиям»	7

***(согласно приказам Минрегионразвития РФ N 624 от 30 декабря 2009 г.)**

По окончании курса слушателю выдается удостоверение о краткосрочном повышении квалификации установленного образца (72 ак. часа)

Для регистрации на курс необходимо выслать заявку на участие, и копию диплома об образовании по телефону/факсу: 8(812) 552-94-60, 535-79-92, , e-mail: stroikursi@mail.ru.

Magazine of Civil Engineering
SCHOLAR JOURNAL

ISSN 2712-8172

Свидетельство о государственной регистрации:
Эл № ФС77-77906 от 19.02.2020,
выдано Роскомнадзором

Специализированный научный журнал.

Выходит с 09.2008.

Включен в Перечень ВАК РФ

Индексируется в БД Scopus

Периодичность: 8 раз в год

Учредитель и издатель:

Санкт-Петербургский политехнический университет Петра Великого

Адрес редакции:

195251, СПб, ул. Политехническая, д. 29

Главный редактор:
Виталий Владимирович Сергеев

Заместитель главного редактора:
Галина Леонидовна Козинец

Ответственный секретарь:
Екатерина Александровна Линник

Редакционная коллегия:
PhD, проф. Т. Аввад;
д.т.н., проф. М.И. Бальзанников
д.т.н., проф. А.И. Белостоцкий;
к.т.н., проф. А.И. Боровков;
д.т.н., проф. А. Бородинец;
PhD, проф. М. Велькович;
PhD, проф. Р.Д. Гарг;
PhD, М.Р. Гарифуллин;
Dr.-Ing, проф. Т. Грис;
д.т.н., проф. Т.А. Дацюк;
д.т.н., проф. В.В. Елистратов;
Dr.-Ing., проф. Т. Кэрки;
д.т.н., проф. Д.В. Козлов;
д.т.н., доцент С.В. Корниенко;
д.т.н., проф. Ю.Г. Лазарев;
д.т.н., проф. М.М. Мухаммадиев;
Dr.-Ing. Habil., проф. Х. Пастернак;
Dr.-Ing., проф. Ф. Рёгинер;
д.т.н., проф. Т.З. Султанов;
д.т.н., проф. М.Г. Тягунов;
акад. РАН, д.т.н., проф. М.П. Федоров;
Dr.-Ing., проф. Д. Хецк;
д.г.-м.н. А.Г. Шашкин;
д.т.н. В.Б. Штильман

Дата выхода: 04.04.2022

© ФГАОУ ВО СПбПУ, 2022
© Иллюстрация на обложке: Илья Смагин

Magazine of Civil Engineering
SCHOLAR JOURNAL

ISSN 2712-8172

Peer-reviewed scientific journal

Start date: 2008/09

8 issues per year

Publisher:

Peter the Great St. Petersburg Polytechnic University

Indexing:

Scopus, Web of Sceince (ESCI, RSCI), Compendex, EBSCO, Google Academia, Index Copernicus, ProQuest, Ulrich's Serials Analysis System, CNKI

Corresponding address:

29 Polytechnicheskaya st., Saint-Petersburg, 195251, Russia

Science editor:
Vitaly V. Sergeev

Deputy chief science editor:
Galina L. Kozinetc

Executive editor:
Ekaterina A. Linnik

Editorial board:
T. Awwad, PhD, professor
M.I. Balzannikov, D.Sc., professor
A.I. Belostotsky, D.Sc., professor
A.I. Borovkov, PhD, professor
A. Borodinecs, Dr.Sc.Ing., professor
M. Veljkovic, PhD, professor
R.D. Garg, PhD, professor
M. Garifullin, PhD, postdoctorant
T. Gries, Dr.-Ing., professor
T.A. Datsyuk, D.Sc., professor
V.V. Elistratov, D.Sc., professor
T. Kärki, Dr.-Ing., professor
D.V. Kozlov, D.Sc., professor
S.V. Korniyenko, D.Sc., professor
Yu.G. Lazarev, D.Sc., professor
M.M. Muhammadiev, D.Sc., professor
H. Pasternak, Dr.-Ing.habil., professor
F. Rögener, Dr.-Ing., professor
T.Z. Sultanov, D.Sc., professor
M.G. Tyagunov, D.Sc., professor
M.P. Fedorov, D.Sc., professor
D. Heck, Dr.-Ing., professor
A.G. Shashkin, D.Sc.
V.B. Shtilman, D.Sc.

Date of issue: 04.04.2022

© Peter the Great St. Petersburg Polytechnic University. All rights reserved.
© Coverpicture – Ilya Smagin

Contacts:
E-mail: mce@spbstu.ru
Web: http://www.engstroy.spbstu.ru

Contents

Nizhegorodtcev, E.I., Gerasimov, V.M., Svalova, K.V. Layer drainage of fibrous materials in the composition of the ground dams 11001

Al-Rousan, R. Impact of elevated temperature on the shear behavior of strengthened RC beams 11002

Semenov, V.S., Bessonov, I.V., Zhukov, Zh.A., Mednikova, E.A., Govryakov, I.S. Thermal insulation systems for road bases with foam glass gravel 11003

Lukashevich, A.A. Finite element models based on the approximation of discontinuous stress fields 11004

Cheng, Y., Dong, Y.R., Wang, Y.Y., Qin, L., Li, Y.X., Bai, G.L. Quantitative bounded method of special long-period ground motions 11005

Khatib, M., Abou Saleh, Z., Baalbaki, O., Hamdan, Z. Numerical shear of post-tensioned beams with inverted-U shaped reinforcements 11006

Abdulla, N.A. Application of artificial neural networks for prediction of concrete properties 11007

Rezaei, S., Hasanzadeh, A. The site effect investigation using nonlinear and Iranian seismic code methods in Babol city 11008

Galishnikova, V.V., Gebre, T.H. The behaviour of thin-walled beam with restrained torsion 11009

Shaikezhan, A., Anuarova, A.D. Belite-containing clinkers from phosphoric slags for refractory materials 11010

Ofrikhter, I.V., Ponomaryov, A.B., Zakharov, A.V., Shenkman, R.I. Estimation of soil properties by an artificial neural network 11011

Shukla, R.P. Bearing capacity of skirted footing subjected to inclined loading 11012

Kolesnikov, A.O., Popov, V.N., Kostiuk, T.N. Pile group effect at vertical vibrations 11013

Abrar, O., Tuhta, S. Performance of elastomeric seismic isolators under long-period earthquakes 11014

Rassokhin, A.S., Ponomarev, A.N., Karlina, A.I. Nanostructured high-performance concretes based on low-strength aggregates 11015



Magazine of Civil Engineering

ISSN 2712-8172

journal homepage: http://engstroy.spbstu.ru/

DOI: 10.34910/MCE.110.1

Layer drainage of fibrous materials in the composition of the ground dams

E.I. Nizhegorodtcev* , ***V.M. Gerasimov*** , ***K.V. Svalova***

Transbaikal State University, Chita, Russia

**E-mail: dj_world@mail.ru*

Keywords: groundwater dams, dikes, drainage, filtration, fibrous materials

Abstract. The article is devoted to the design substantiation of a new type of drainage structures based on fibrous materials for ground dams. To assess the effectiveness of the application, two-dimensional modeling of hydraulic processes using the software environment Plaxis 2D AE 2013 finite-element method of a ground dam was carried out. Experimental research has become the basis study the effect of the rock mass on the filtration flow of water passing through the drainage from fibrous polymeric materials. Method of valuation suggested in article of the height of the layer and the slope of drainage from fibrous materials take into account the experimental data obtained for ground dams.

1. Introduction

Embankments and dams from local natural materials made from local natural materials serve as water reserve generators, settling basins for gravitational clarification of process water and liquid waste storage. Most often, such structures (up to 10 m in height) are arranged at mining enterprises that carry out gold surface mining from placer deposits. [1]. The construction of embankments and dams in taiga conditions is made from local natural materials: rocks and semi-rocks, sedimentary materials, and loose rocks(gravel, sand, clay) [2]. As a rule, embankment and dam arrays have a mixed composition of these materials with the highest percentage of loose rocks that differ in compressibility. Sandy rocks are characterized by low compressibility and high-speed settlement, while clay rocks have high compressibility and slow settlement.

Embankments and dams are constantly in contact with water, which affects their stability; there are examples of emergency cases at rock embankments [3, 4]. The main reasons of these accidents and damage to structures are the following: water overflow through the crest of soil dams; concentrated filtration through the dam body or foundation; deformation and embankment of slopes; seismic and wave effects [5–10]. To reduce the deformation of the structure rock mass, filtration control devices in the body of the structure made of natural and artificial materials are used to minimize emergency cases due to violations of the filtration regime of the body and the foundation of the soil dam. Modern domestic industry offers a number of new polymeric materials with unique properties, the use of which allows you to create reliable and filtering efficient control-based devices [11, 12].

There are quite extensive scientific studies in the field of reinforcing various soil structures with fibrous polymer materials, a detailed description, and the scope of their application is presented in the works E.V. Sherbinoj, V.G. Ofrihtera, A.B. Ponomareva [13–16]. However, very few publications have been devoted to the issues of the arrangement of drainage structures based on fibrous polymeric materials in ground hydraulic structures.

Nizhegorodtcev, E.I., Gerasimov, V.M., Svalova, K.V. Layer drainage of fibrous materials in the composition of the ground dams. Magazine of Civil Engineering. 2022. 110(2). Article No. 11001. DOI: 10.34910/MCE.110.1

© Nizhegorodtcev, E.I., Gerasimov, V.M., Svalova, K.V., 2022. Published by Peter the Great St. Petersburg Polytechnic University.

This work is licensed under a CC BY-NC 4.0

Using fiber polymeric materials in order to control the filtration of water in a rock mass is a rather strategic pathway, which allows achieving significant results at minimum cost. Nevertheless, we haven't done yet any industrial tests of reservoir drains based on fiber materials in soil dams [17].

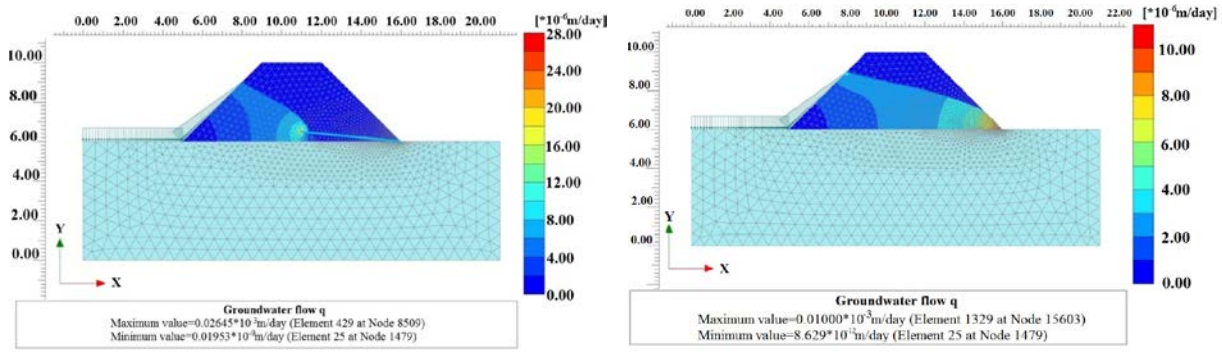
In order to assess the effectiveness of using fiber polymeric materials in controlling the water filtration in the body of the soil embankment, the filtration processes (finite element technique) that took place in the body of the structure were simulated using the Plaxis 2D AE 2013 program. The result of modeling the structure filtration fields with fiber polymer drain materials and without it, graphically presented in Fig. 1. It was found that the point of the maximum value of the field of water filtration in the absence of fiber material is located on the downstream surface, with the risk of erosion and suffusion slope. On the other hand, the maximum value of the filtration field for the case with a device made of fiber materials is in the body of the dam (the point of water entry into the material); water is filtered through the material, which excludes risk of erosion.

This survey was to investigate the effect of layer drainage from fibrous materials on the filtration process of ground dams, to analyze the effect of changes in the pressure of rocks of the structure on the filtration flow rate of water passing through the drainage.

The following tasks were set and then solved in order to achieve this goal:

1. To elaborate a numerical model of an embankment dam with layer drainage from fibrous materials based on the Plaxis 2D AE 2013 finite-element software package.
2. To elaborate experimental unit to investigate the effect of changes in the pressure of rocks of the structure on the filtration flow rate of water passing through the drainage
3. To elaborate methods for calculating the layer height and slope of the drain from fiber materials.

2. Methods



a **b**

Figure 1. Water filtration field in the rock mass of the structure: a – fiber material devices, b – without using fiber material devices.

Based on the modeling results, it was found that filtration control devices based on fiber polymeric materials can reduce the possibility of emergency situations due to erosion and suffusion of the lower slope; it was also established that the main parameters of these filtration control devices are: bias towards the downstream and the layer height of fiber materials [18–20].

Horizontal drains based on fiber materials are characterized by the main parameters that determine their effectiveness: filtration water flow, position of the drawdown curve, layer height and bias of the fiber material towards the downstream.

The drain should be located in the lower part of the soil embankment with a slope towards the downstream, which ensures water removal (Fig. 2). Drain undergoes pressure from an overlying rock mass. The fiber polymer material is a porous medium, depending on the density of 70...130 kg/m^3, the average pore diameter is 13...82.4 microns. Previous research has established that the fiber material has a decrease in pore diameters of 3.67–4.57 times when compressed to 80 %. A drop in pore diameter leads to a decrease in the filtration water flow rate passing through the material; therefore, it affects the efficiency of the formation device made of fiber polymeric materials [21–23].

Changing the filtration water flow rate by drain (Kf) affects the main parameters: layer height (h_D) and slope towards the drain system (i_D) [20].

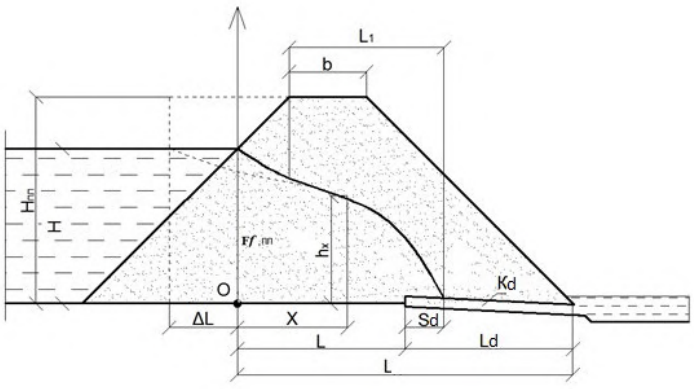


Figure 2. Location of the filtering control device in the body of the embankment.

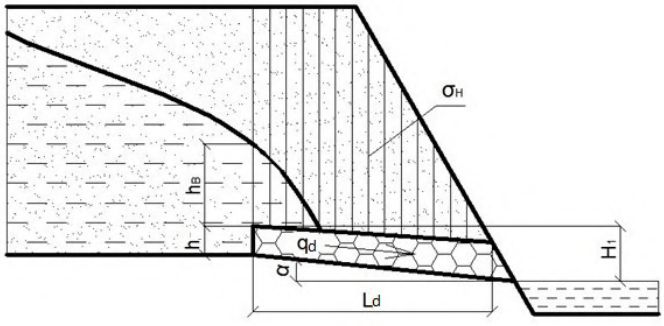


Figure 3. Calculation of the layer height of the reservoir device.

The filtration process follows the law of A. Darcy for liquids and gases in a porous medium. Previously, there was a formula proposed for determining the layer height of the reservoir device (Fig. 3) made of fiber materials [25, 26]:

$$h_D = \frac{q_D \cdot L_D}{Ff\left(h_B + H_1\right)}. \tag{1}$$

A filtering control device for fiber material is located at a certain angle in the body of the soil embankment. To calculate the slope angle, a formula was proposed based on the use of V.S. Kozlov [21], in relation to devices made of fiber polymeric materials:

$$i_D = \frac{2 \cdot q_D - \dfrac{F_f \cdot H_1^2}{L_D}}{F_f \cdot H_1}, \tag{2}$$

where q_D is filtration flow rate of the device, m²/s; L_D is width of the reservoir device, m; F_f is material filtration coefficient, m/s; h_B is pressure at front of the device, determined by the lines of equal pressure, m; H_1 is height of the drain towards the water level in the downstream, m

Formulas 1 and 2 include the width of the device and the filtration coefficient of the fiber material, but do not consider the change in the filtration water flow rate under the influence of external rock pressure.

An experiment was conducted in order to assess the change in the filtration water flow rate with a change in the pressure of the rock mass [23–26]. During the experimental studies, we selected Russian-made Dornite fiber type of the following grades by surface density: M250, M300, and M400. This type of fiber polymeric material is widely used in the road and railway construction, strengthening of coastal slopes, land-improvement works, etc. It is made of needle-punched material; surface density is 250–400 g/cm²; filtration coefficient is 70–150 m/day. These characteristics allow the use of this type of fiber polymeric material to design reservoir drain. The experimental unit is shown in Fig. 4.

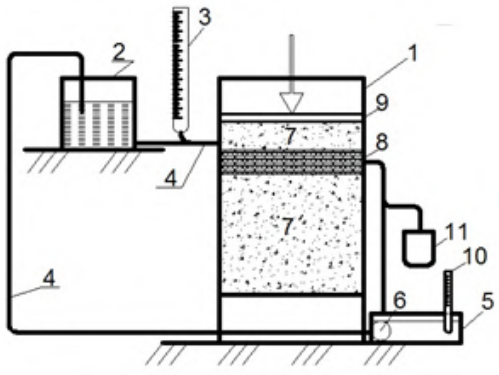


Figure 4. Scheme of the experimental unit for laboratory research:
1 – Prismatic body; 2 – water container; 3 – piezometer; 4 – flexible supply line;
5 – drain tank; 6 – pump; 7 – rock; 8 – drain design; 9 – stamp for load transfer;
10 – thermometer; 11 – dimensional cylinder.

In the unit body 1, the solid 7 is loaded to the level of the slot in the body of the unit. Then the drain design is made of fiber material 8, under a certain slope, which is set by changing the angle of inclination of the underlying soil surface. The upper layer of the rock is laid, and on top of which the plate 9 is laid, which later serves to transfer the load. A water tank maintains a constant amount of water. By changing the height of the location of the tank 2 we achieve the necessary water pressure according to the piezometer 3. The water from the tank 2 through a flexible connection 4 enters the unit body 1, passes through the rock 7, reaches the drain 8, discharged through a slot in the body, and enters the drain tank 5, from which it is pumped 6 to the tank 2. This cycle ensures the stability of the water temperature measured in the drain tank 5 using a thermometer 10. The measurement of the volume of water is carried out by a measuring graduate 11 on the way to the drain tank for a certain time.

3. Results and Discussion

During the experiments, it was found that the dependence of the filtration water flow rate passing through the drain on external pressure has two characteristic sections: 0...8 kPa (the dependence is non-linear) and 8...200 kPa (the dependence is linear), Fig. 5 and 6.

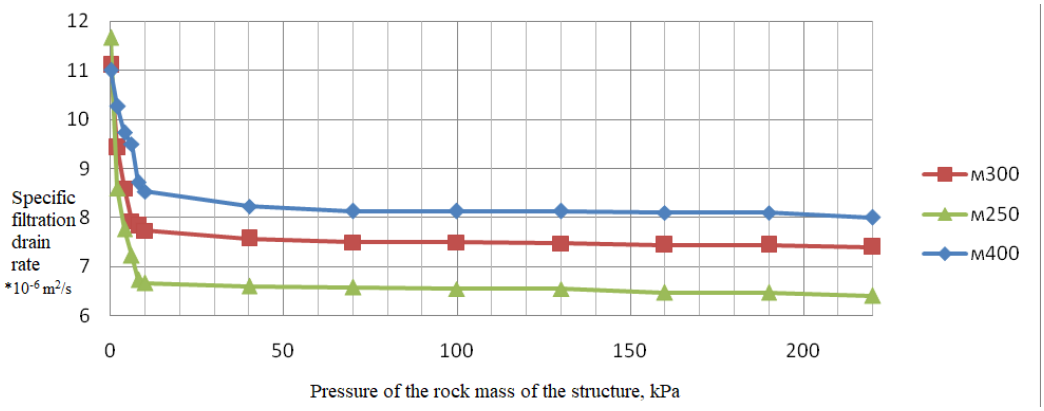


Figure 5. The dependence of the specific filtration water flow rate passing through the reservoir drain pressured by the rock mass.

Because the graphs are variable in the load range 0...200 kPa it is necessary to approximate the experimental results separately for two sections: 0...8 kPa and 8...200 kPa.

Let us consider the change in filtration flow in the load range 0...8 kPa (Fig. 6).

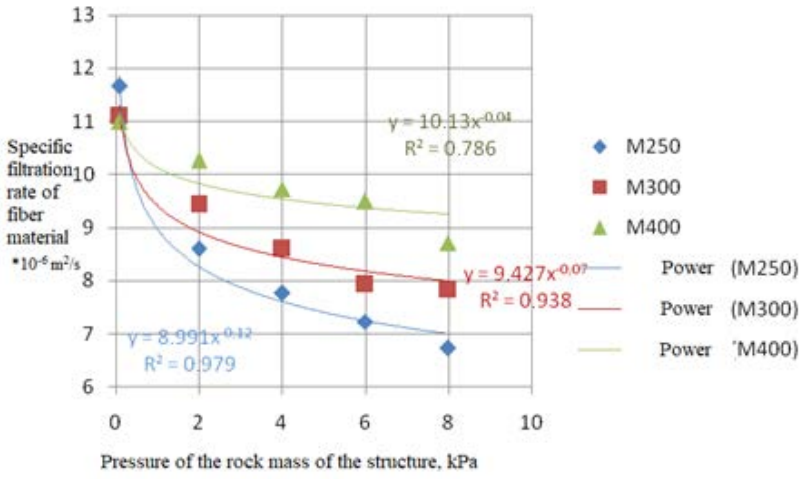


Figure 6. Approximation of the dependence of the specific filtration flow rate of reservoir drain pressured by the rock mass in the load range 0...8 kPa.

The math dependencies obtained in the course of approximation by means of Microsoft Excel have the nature of a power function of the form:

$$y = a_1 \cdot x^{-b_1}, \quad (3)$$

where a_1, b_1 are empirical coefficients of change in filtration flow obtained during approximation in the load range 0...8 kPa (Fig. 6).

Confidence level of the power approximation of experimental data, depending on the grade of material has the following meanings:

- for the fiber material M400, the accuracy of the approximation is $R^2 = 0.79$;
- for the fiber material M300, the accuracy of the approximation is $R^2 = 0.94$;
- for the fiber material M250, the accuracy of the approximation is $R^2 = 0.98$.

The change in filtration water flow in the load range of 0...8 kPa is:

- for the fiber material M400 – 42.3 %;
- for the fiber material M300 – 29.5 %;
- for the fiber material M250 – 20.8 %.

Let's consider the change in filtration water flow in the load range of 10...200 kPa (Fig. 7).

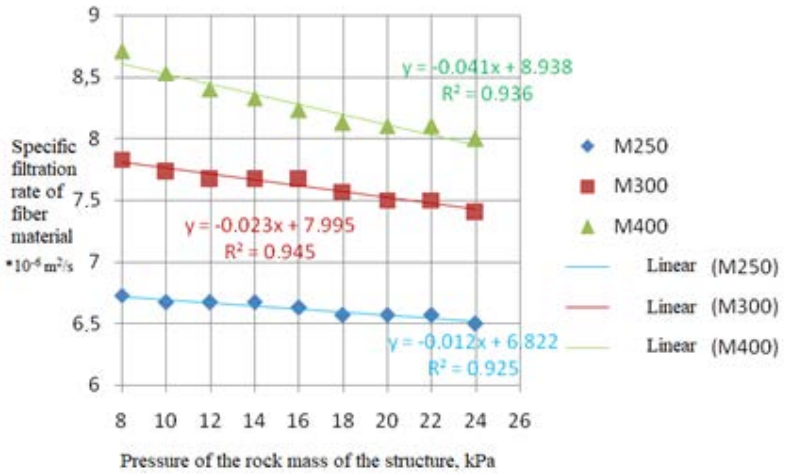


Figure 7. Approximation of the dependence of the specific filtration flow rate of reservoir drain pressured by the rock mass in the load range of 10...200 kPa.

The dependence obtained during the approximation is expressed in general terms by the formula (linear dependence):

$$y = a_2 \cdot x + b_2, \tag{4}$$

where a_2, b_2 are empirical coefficients of change in the filtration flow obtained during the approximation in the load range of 10...200 kPa (Fig. 7).

The confidence level of the power approximation of experimental data, depending on the grade of material has the following meanings:

- for the fiber material M400, the accuracy of the approximation is $R^2 = 0.67$;
- for the fiber material M300, the accuracy of the approximation is $R^2 = 0.76$;
- for the fiber material M250, the accuracy of the approximation is $R^2 = 0.93$.

The change in filtration water flow in the load range of 10…200 kPa is:

- for the fiber material M400 – 8.2 %;
- for the fiber material M300 – 5.5 %;
- for the fiber material M250 – 4.8 %.

A decrease in the filtration water flow rate of a fiber device under pressure is determined by the gradient of the filtration flow rate according to Formula 5, depending on the surface density of the material.

$$\Delta q_D = \left(q_{D,0} - q_{D,P} \right) = \frac{\partial q_D}{\partial \sigma_n} \cdot \sigma_n, \tag{5}$$

where $q_{D,0}$ is filtration flow rate without load, m²/s; $q_{D,P}$ is filtration flow rate at a given load, m²/s; σ_n is pressure of the rock mass of the structure on the polymeric material, kPa.

The height value of the gradient of the filtration water flow rate is obtained by the experiment and is presented in Table 1.

Table 1. The gradient of the filtration water flow rate passing through the drain.

Material grade	Gradient of filtration water flow $\frac{\partial q_D}{\partial \sigma_n}$ for pressure range:	
	0…8 kPa	8…200 kPa
M250	0.618	$0.146*10^{-2}$
M300	0.409	$0.208*10^{-2}$
M400	0.286	$0.333*10^{-2}$

Therefore, to determine the parameters of the filtration control device (layer height and slope), taking into account the change in the gradient of the filtration flow rate of the fiber polymer material is carried out according to Formulas 6 and 7 (A. Darcy's formula for calculating the layer height, V.S. Kozlov's formula for determining the slope of the unit [21, 24, 25]).

$$h_D = \frac{\left(q_D + \frac{\partial q_D}{\partial \sigma_n} \cdot \sigma \right) \cdot L_D}{F_f \left(h_B + H_1 \right)}, \tag{6}$$

$$i_D = \frac{2 \cdot \left(q_D + \frac{\partial q_D}{\partial \sigma_n} \cdot \sigma \right) - \frac{K_f \cdot H_1^2}{L_D}}{F_f \cdot H_1}. \tag{7}$$

Formulas 6 and 7 allow to determine the main parameters of filtration control devices based on fiber polymeric materials of artificial hydraulic rock structures, taking into account the decrease in longitudinal

filtration flow caused by the presence of external pressure created by the overlying rock mass of embankments and dams [27].

Calculation of and embankments made from rocks is performed by the equivalent profile method [17]. It determines the filtration coefficient of the rocks composing the body of the structure and the base (in this case there is a permeable base under the structure), and generates the drawdown curve. Next, it determines the filtration water flow rate passing through the fiber material, the drain width L_D, and material load. The layer height and slope is determined according to Formulas 6 and 7.

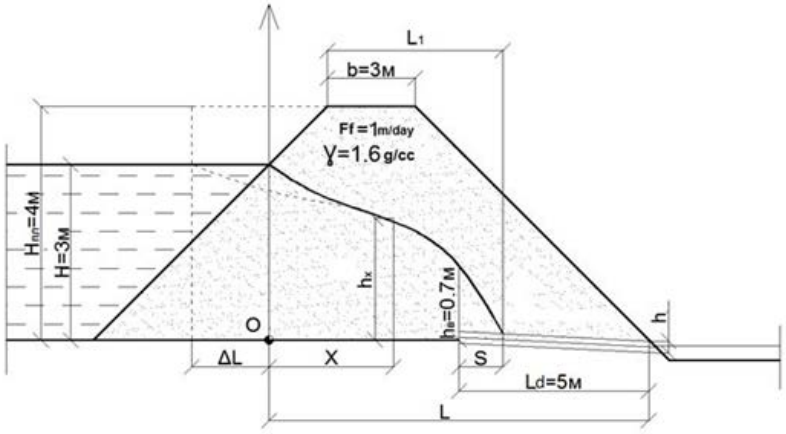


Figure 8. Water filtration through the body of the dam with drain of fiber materials on a waterproof base.

It is done with the following parameters of the structure: the height of the structure is 4m, the filtration coefficient of rocks is 1 m/day, the slope is 1:2, and the fiber material is M300 with a filtration coefficient of 100 m/day. The calculation showed: the pressure at the front of the device is 0.7 m, the drain width is 5 m, the drain load is 0.04 MPa, the filtration water flow rate passing through the structure is 0.6 m²/day, and the filtration water flow rate through the drain is 0.69 m²/day.

$$h_D = \frac{\left(q_D + \frac{\partial q_D}{\partial \sigma_n}\cdot\sigma\right)\cdot L_D}{K_D\left(h_B + H_1\right)} = \frac{\left(0.69 + 0.208\cdot 10^{-2}\cdot 0.04\right)\cdot 5}{100\left(0.7 + 0.1\right)} = \frac{3.45}{80} = 0.04\ \text{m},$$

$$i_D = \frac{2\cdot\left(q_D + \frac{\partial q_D}{\partial \sigma_n}\cdot\sigma\right) - \frac{K_D\cdot H_1^2}{L_D}}{K_D\cdot H_1} = \frac{2\cdot\left(0.69 + 0.208\cdot 10^{-2}\cdot 0.04\right) - \frac{100\cdot 0.1^2}{5}}{100\cdot 0.1} = 0.118\left(6.7^{\circ}\right).$$

4. Conclusions

1. There has been established the possibility of using reservoir drain structures based on fiber polymeric materials, including the weight of the rock mass of the structure.

2. Experimental research were conducted to investigate the effect of changes in the pressure of rocks of the structure on the filtration flow rate of water passing through the drainage.

3. Methods for calculating the layer height and slope of the drain from fiber materials was developed.

Professor Gerasimov V.M. a methodology for calculating reservoir drainages was proposed [21], but it does not take into account the influence of the pressure of the rock mass on specific filtration water flow rate passing through the reservoir drain. The proposed formulas for calculating the layer height and slope allow taking into account pressure of the rock mass.

The question of clogging of fibrous materials with fine particles remains open; in future works, this issue will be elucidated.

References

1. Kossoff, D. et al. Mine tailings dams: characteristics, failure, environmental impacts, and remediation. Applied Geochemistry, 2014. 51. Pp. 229–245.
2. Tanchev, L. Dams and appurtenant hydraulic structures. CRC Press, London, 2014.
3. Environmental and Safety Incidents concerning Tailings Dams at Mines: Results of a Survey for the years 1980–1996. United Nations, Paris, 1996.
4. Petticrew, E. et al. The impact of a catastrophic mine tailings impoundment spill into one of North America's largest fjord lakes: Quesnel Lake, British Columbia, Canada. Geophys. Res. Lett., 2015. 42. Pp. 3347–3355. DOI: 10.1002/2015GL-063345
5. Richmond, B. Omai Tailings Dam Failure - Final Report on Technical Causation. BiTech Publishers Ltd, Canada, 1996.
6. Bulatov, G. Reliability of earth dams on compound base. Mafazine Civil engeneering, 2012. 30(4). Pp. 2–9. DOI: 10.5862/MCE.30.1
7. Jha, A. Hungary toxic sludge spill an 'ecological catastrophe' says government. Guard., 2010. Pp. 3–4.
8. Li, W. et al. Real-Time Warning and Risk Assessment of Tailings Dam Disaster Status Based on Dynamic Hierarchy-Grey Relation Analysis. Complexity, 2019. DOI: 10.1155/2019/5873420
9. Lyu, Z. et al. A Comprehensive Review on Reasons for Tailings Dam Failures Based on Case History. Adv. Civ. Eng. 2019. Vol. 2019. DOI: 10.1155/2019/4159306
10. Azam, S. et al. Tailings dam failures: a review of the last one hundred years. Geotechnical news, 2010. 28(4). Pp. 50–54.
11. Ding, Z. et al. Spunbonded needle-punched nonwoven geotextiles for filtration and drainage applications: Manufacturing and structural design. Composites Communications, 2020. 21(5). 100481. DOI: 10.1016/j.coco.2020.100481
12. Sabiri, N.E. et al. Performance of nonwoven geotextiles on soil drainage and filtration. European Journal of Environmental and Civil Engineering, 2020. 24(5). Pp. 670–688. DOI: 10.1080/19648189.2017.1415982
13. Sherbina, E.V. Geosinteticheskie materialy v stroitel'stve [Geosynthetics in construction]. ASV, Moscow, 2004. (rus)
14. Ponomarev, A.B. et al. Analiz i problemy issledovanij geosinteticheskih materialov v Rossii [Analysis and problems of research of geosynthetic materials in Russia]. Vestnik Permskogo gosudarstvennogo tekhnicheskogo universiteta. Stroitel'stvo i arhitektura. 2013. 2. Pp. 68–73. (rus)
15. Ofrihter, V.G. et al. Metody stroitel'stva armogruntovyh konstrukcij [Methods for the construction of reinforced soil structures]. ASV, Moscow, 2013. (rus)
16. Kosichenko, Y.M. Protivofil'tracionnye pokrytiya iz geosinteticheskih materialov [Anti-seepage coatings made of geosynthetics]. RosNIIPM, Novocherkassk, 2014. (rus)
17. Palmeira, E.M. et al. Drainage and filtration properties of non-woven geotextiles under confinement using different experimental techniques. Geotextiles and Geomembranes, 2002. 20(2). Pp. 97–115. DOI: 10.1016/S0266-1144(02)00004-3
18. Shao, W. et al. Quantification of the influence of preferential flow on slope stability using a numerical modelling approach. Hydrology and Earth System Sciences. 2015. 19(5). Pp. 2197–2212. DOI: 10.5194/hess-19-2197-2015
19. Sharafi, A. Static analysis of soral embankment dam during operation using precise dam tool data and finite element method. Journal of Critical Reviews. 2020. 19(7). Pp. 9089–9101. DOI: 10.31838/jcr.07.19.1015
20. Ormann, L. et al. Numerical analysis of curved embankment of an upstream tailings dam. The Electronic journal of geotechnical engineering. 2011. 16(1). Pp. 931–944.
21. Gerasimov, V. Voloknistye polimernye materialy v geotekhnologii [Fibrous polimeric material in geotechnology]. ChitGU. Chita, 2010. (rus)
22. Gerasimov, V. et al. Plotina [Dam], Patent Russia № 2126868, 1999. (rus)
23. Palmeira, E.M., et al. A study on the behaviour of soil geotextile systems in filtration tests. Canadian Geotechnical Journal, 1997. 33(6). Pp. 899–912. DOI: 10.1139/t96-120
24. Xu, Y.Q. et al Optimal hydraulic design of earth dam cross section using saturated – unsaturated seepage flow model. Advances in Water Resources, 2003. 26(1). Pp.1–7. DOI: 10.1016/S0309-1708(02)00124-0
25. Rushton, A. et al. Solid-liquid filtration and separation technology. VCH, Weinhein, 1996.
26. Damak, K. et al. A new Navier-Stokes and Darcy's law combined model for fluid flow in crossflow filtration tubular membranes. Desalination, 2004. 161(1). Pp. 67–77. DOI: 10.1016/S0011-9164(04)90041-0
27. Svalova, K. et al. Geosinteticheskie materialy v processah fil'trovaniya i drenirovaniya [geosynthetic materials in filtration and drainage processes]. ZabGU, Chita, 2016. (rus)
28. Palmeira, E.M. et al. Drainage and filtration properties of non-woven geotextiles under confinement using different experimental techniques. Geotextiles and Geomembranes. 2002. 20(2). Pp. 97–115. DOI: 10.1016/S0266-1144(02)00004-3
29. Liu, L.F. et al. Modeling the slurry filtration performance of nonwoven geotextiles. Geotextiles and geomembranes. 2006. 24(5). Pp. 325–330. DOI: 10.1016/j.geotexmem.2006.03.005
30. Ingold, T.S. ed. Geotextiles and geomembranes handbook. Elsevier, 2013.

Contacts:

Evgenii Nizhegorodtcev, dj_world@mail.ru

Viktor Gerasimov, kafsmim@zabgu.ru

Kristina Svalova, kristi24091990s@yandex.ru

Received 28.10.2019. Approved after reviewing 25.05.2021. Accepted 07.07.2021.



Magazine of Civil Engineering

ISSN 2712-8172

journal homepage: http://engstroy.spbstu.ru/

DOI: 10.34910/MCE.110.2

Impact of elevated temperature on the shear behavior of strengthened RC beams

R. Al-Rousan

Jordan University of Science and Technology, Irbid, Jordan

E-mail: rzalrousan@just.edu.jo

Keywords: reinforced concrete, elevated temperature, shear strength, fiber reinforced polymer, experimental

Abstract. When the concrete structures are exposed to escalated temperatures (500°C and higher), concrete fails because of the decay of cement hydration products, development of vapor pressure, and undesired variations in the volume of ingredients. Heat-damaged concrete structures can restore their strength when strengthened with carbon fiber-reinforced polymer (CFRP). Therefore, an experimental study investigated the influence of elevated temperatures on the shear behavior of reinforced concrete (RC) beams strengthened externally with CFRP. For this purpose, forty reinforced concrete beams were cast. Thirty-two of them were externally strengthened with CFRP and eight beams were unanchored and left as a control. The beams then were tested under four-point bending to assess their structural performance in terms of failure modes, and load-displacement relations. Results have shown, explicitly, that the control specimens encountered a brittle failure, unlike the ones strengthened with CFRP, as those had a ductile mode. The strengthened beams showed an increase in the ultimate load-carrying capacity accompanied by an enhancement in mid-span deflection in different percentages with respect to the control beam. This technique also improved the shear capacity of the anchorage area, reflecting an improvement in the effectiveness of the anchored CFRP laminates. Finally, the influence of the exposed temperature on the ductility, energy absorption, and ultimate load reduction percentage is significant and increased with the increase of temperature.

1. Introduction

Concrete is the most extensively used material for structures since numerous decades. Nevertheless, concrete material is classified as a brittle material with a low strain limits and tensile strength capacity. There have been ongoing efforts to help overcome these deficiencies using several strategies. The utilization of fibers in structural concrete elements began in 1970s because of their ability in the upgrading the mechanical properties of concrete. These days, broad examinations were completed on the utilization of various types of fibers for enhancing the concrete mechanical properties of structures. Nowadays, carbon fiber-reinforced polymer materials (CFRP) are considered as main strengthening and rehabilitation composite materials of shear or in flexure deficient reinforced concrete structures.

CFRP materials are frequently used in structural engineering applications for repair and strengthening of existing concrete structures. Externally bonded FRP composite is used to strengthen concrete beams in flexure and shear. Many experimental observations indicated that the debonding that occurs at the interface between concrete and FRP is a typical failure mode of reinforced concrete beams strengthened with externally bonded CFRP [1, 2]. CFRP composite materials have come to the forefront as promising materials and systems for structural retrofit. Glass fiber reinforced polymer (GFRP) and carbon fiber reinforced polymer (CFRP) have higher tensile strength but its strength is not fully utilized due to de-bonding problem and brittle tensile behavior. The general influence is clearly an increase in the peak loads of the specimens [3, 4].

Al-Rousan, R. Impact of elevated temperature on the shear behavior of strengthened RC beams. Magazine of Civil Engineering. 2022. 110(2). Article No. 11002. DOI: 10.34910/MCE.110.2

© Al-Rousan, R., 2022. Published by Peter the Great St. Petersburg Polytechnic University.

This work is licensed under a CC BY-NC 4.0

Extreme temperatures harm severely RC structures, including beams, because these structures experience significant degradation in stiffness and strength, in addition to big, consistent deformations [5]. The reason behind this is that high temperatures cause decay in the mechanical properties of concrete and steel rebar, in addition to the stresses' redistribution in the beam [5, 6]. The CFRP sheets are distinguished because they are easy to install, corrosion-resistant, flexible, and ductile. The flexural behavior of RC beams, strengthened with external wraps of CFRP sheets, has been evaluated by several researchers, who found that this technique of strengthening improved the beams' flexural behavior. They, also found that this method helped the heat-damaged elements to restore their flexural strength to an extent. The quality of the heat-damaged beams' recovery or strengthening is governed by a number of factors, such as the material's resistance to fire [5, 7], elevated temperature [8, 9], fiber type [10–13], analysis type [14–18], energy integrity resistance [19], anchored system [20], heating condition [21, 22], the sheets' shape and dimensions, the severity of damage [23], and safety factors for CFRP strengthening of bridges [24].

The concrete's stability in some RC structures (such as chimneys, the area around furnaces, rocket launcher platforms, nuclear power stations, the rabidly extinguished ones) is threatened due to frequent heat cycles heating-cooling cycles resulting from the big gradient in temperatures. Therefore, the design process must consider the heat cycles [5, 25, 26]. In fact, concrete can maintain its mechanical characteristics in temperatures up to 300°C. However, when the concrete is exposed to a temperature exceeding 500 °C, its properties degrade considerably, causing concrete's cracking due to high superficial tensile stresses. In sum, exposing concrete to very high temperatures or big difference in temperatures due to frequent heat cycles or rabid extinguishing of fire lead to a degradation in concrete's integrity because of irregular expansions and contractions of concrete contents, i.e., aggregate and paste of cement. Several factors govern the amount of damage in RC structures, such as the structure's dimensions, type of cement and aggregate, the moisture content in concrete, the duration and how frequent structure is subjected to high temperatures, the cooling method, and the highest obtained temperature [5, 27]. Various methods and materials have been adopted to strengthen and repair concrete structures, such as steel plate bolting, RC jacketing, pre-stressed external tendons, and CFRP laminates. Recently, the CFRP laminates have been used in many applications all over the world because they have many remarkable features, such as: simple to shape and install, high ratio of strength-to-weight, highly strong mechanically, and non-corrosive; as it is worth mentioning that structures are, mostly, endure damages because of: steel's corrosion, heat cycles, and dynamic loads [28-30].

This research is expected to be useful for retrofitting the existing buildings, mainly for buildings located in areas prone to medium earthquake. Therefore, critical concerns to produce a practical and cost-effective material used to retrofit standing concrete buildings [5]. Also, the impact of CFRP external strengthening on the behavior of deficient reinforced concrete beams exposed to elevated temperature must receive miniature consideration. The issue discussed in this study is actually a matter of concern to the practitioners in the field of strengthening and repairing heat-damaged RC beams, particularly that there is very little available literature related to this subject [5]. In this study, experimental program was carried out to find the improvements in the strength and ductility behavior of RC beams confined internally with CFRP. The main parameters studied were number of CFRP strips (1, 2, 3, and 4 strips) and elevated temperature (23 °C, 150 °C, 250 °C, and 500 °C).

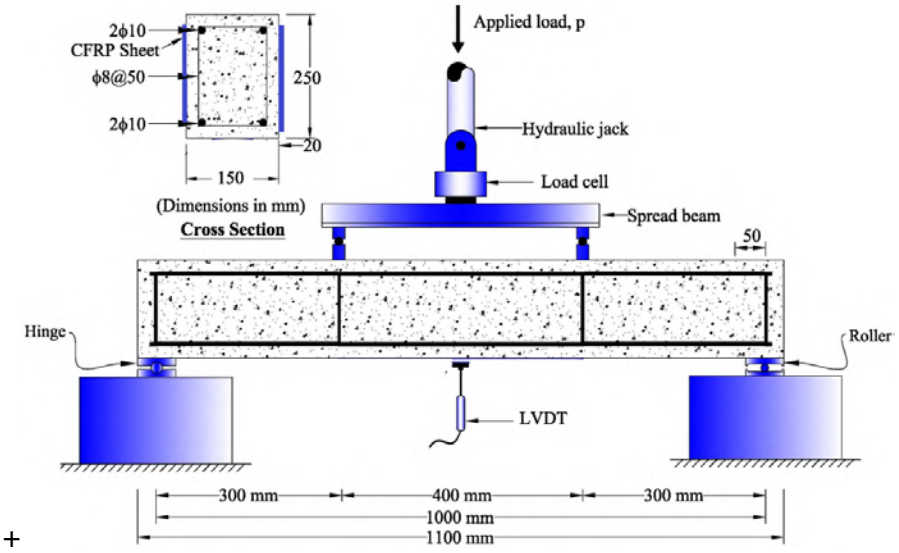


Figure 1. Setup and reinforcement details of the beams.

2. Methods

2.1. Experimental Work

Forty (two beams were made from each type) beams had been constructed and experimented, as simply supported, by subjecting them to four-points loading as shown in Fig. 1. The tested beams were 1100 mm long with cross-sectional dimensions of 150×200 mm. The investigated parameters in this study are the number of CFRP strips (1, 2, 3, and 4 strips) and elevated temperature (23 °C, 150 °C, 250 °C, and 500 °C) as shown in Table 1. The designation and steel reinforcement (yielding stress of 420 MPa) of the tested beams are summarized in Table 1 and Fig. 1, respectively.

Table 1. The details of failure of tested shear beams.

Group	Beam	Temperature, °C	CFRP Configuration	P_u, kN	Δ_u, mm	Steel strain, με	CFRP strain
1	SBT23-0S	23	None	55.7	4.73	0	---
	SBT23-1S		1 Strip of CFRP	59.4	5.27	5040	$0.307\varepsilon_{fu}$
	SBT23-2S		2 Strips of CFRP	63.6	5.55	5318	$0.324\varepsilon_{fu}$
	SBT23-3S		3 Strips of CFRP	68.0	5.99	5624	$0.343\varepsilon_{fu}$
	SBT23-4S		4 Strips of CFRP	72.9	6.16	5878	$0.368\varepsilon_{fu}$
2	SBT150-0S	150	None	52.3	4.49	0	---
	SBT150-1S		1 Strip of CFRP	55.0	4.80	4244	$0.259\varepsilon_{fu}$
	SBT150-2S		2 Strips of CFRP	59.4	5.11	4578	$0.279\varepsilon_{fu}$
	SBT150-3S		3 Strips of CFRP	63.5	5.37	4704	$0.287\varepsilon_{fu}$
	SBT150-4S		4 Strips of CFRP	68.7	5.64	5076	$0.309\varepsilon_{fu}$
3	SBT250-0S	250	None	45.0	4.36	0	---
	SBT250-1S		1 Strip of CFRP	47.4	4.64	4199	$0.256\varepsilon_{fu}$
	SBT250-2S		2 Strips of CFRP	51.7	4.75	4295	$0.262\varepsilon_{fu}$
	SBT250-3S		3 Strips of CFRP	55.1	4.94	4489	$0.274\varepsilon_{fu}$
	SBT250-4S		4 Strips of CFRP	59.3	5.11	4599	$0.280\varepsilon_{fu}$
4	SBT500-0S	500	None	32.9	4.26	0	---
	SBT500-1S		1 Strip of CFRP	34.9	4.39	3513	$0.214\varepsilon_{fu}$
	SBT500-2S		2 Strips of CFRP	38.0	4.53	3732	$0.228\varepsilon_{fu}$
	SBT500-3S		3 Strips of CFRP	40.9	4.79	4044	$0.247\varepsilon_{fu}$
	SBT500-4S		4 Strips of CFRP	43.5	4.99	4204	$0.256\varepsilon_{fu}$

Note: The values between parentheses are normalized with respect to the control, P_u: Ultimate Load, Δ_u: Ultimate deflection, ε_f = CFRP strain, ε_{fu}: CFRP ultimate strain of 16400 με.

2.2. Design of concrete mixture

The mixture of concrete (Table 2) with the proportions by weight of 0.61(water):1.00(cement (Ordinary Type I Portland cement)):2.98(Crushed limestone coarse aggregates with absorption of 2.3 %, a maximum aggregate size of 12.5 mm, and a specific gravity of 2.62)):2.62 (fine aggregates with absorption of 1.9 %, fineness modulus of 2.69, and specific gravity of 2.65). The superplasticizer as a percent of the cement weight was used to improve the workability of the concrete mixture and result a slump of about 50 mm.

Table 2. Mix design proportions.

Ingredient	Quantity (kg/m³)
Cement	269
Water	158
w/c	0.40
Super- plasticizer	8
Coarse aggregate	891
Fine aggregate	834

The beams are casted by using a tilting drum mixer with a capacity of 0.15 m³ (Fig. 2). Firstly, the tilting drum mixer inner surface was wetted. During the tilting drum mixer running, all the crushed limestone coarse aggregates with portion of the used water were added (Fig. 2). After that, the fine aggregates, cement, and water were added gradually. Finally, the super-plasticizer with the last amount of used water was added to the concrete mixture. Lastly, all the concrete mixture ingredients were mixed for five minutes before pouring into wooden molds with inner dimensions of (100×150×1100 mm) and compacted with an electrical vibrator (Fig. 2). After twenty-four hours from the beams casting, all beams were de-molded and then cured in lime-saturated water tank for 28 days (Fig. 2).



Preparing the ingredients of mixture | **Mixing concrete by tilting drum mixer** | **Wooden mold for casting beams**

Casting concrete into molds | **Casting concrete into cylinders** | **Water-cured tank for 28 days**

Figure 2. The mixing, casting, and curing of reinforced concrete beams.

2.3. Heat treatment Method

The average 28-day splitting compressive and tensile strengths of the tested cylinders were 25.0 MPa and 3.0 MPa, respectively. Cylindrical specimens and block were subjected to heat treatment for two hours at temperatures from 150–500 °C before allowed to cool inside the special electrical furnace. The furnace is equipped with an electronic panel to control automatically the time of exposure and the temperature (maximum of 1200 °C). Fig. 3 shows the time-temperature schedule for the furnace.

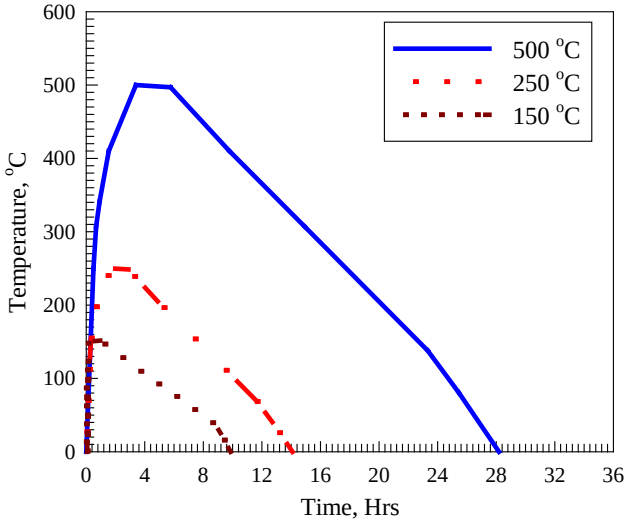


Figure 3. The time-temperature schedule.

The effect of exposing specimens to elevated temperatures is demonstrated in Fig. 4 which depicts the residuals for compressive and slitting strength versus temperature. The curves followed almost similar trend behavior represented in a slight decrease at a temperature of 150 °C followed by a significant decrease at higher temperatures. The detrimental effect of high temperatures greater than 250 °C on both strengths can be referred to thermally induced cracks and/or decomposition of cement binding materials (beyond 250 °C). The damage by heating caused map type cracking which increased with elevated temperature without being accompanied with an apparent surface alteration. The reduction in residual strengths (compressive, splitting) which is (98 %, 97 %) at 150 °C to (61 %, 60 %) at 500 °C, as can be deduced from Fig. 4.

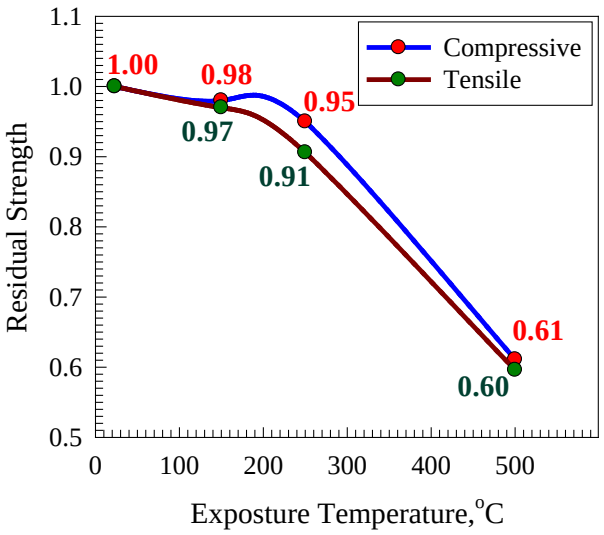


Figure 4. Residuals for compressive and splitting strengths versus exposure temperature.

2.4. Bonding of CFRP sheets to the concrete beams

The concrete beams were demolded after 24 hours of casting and cured in a lime-saturated water tank for 28 days. Firstly, the concrete bonded area were roughened and brushed with steel wire cup brush in order to provide leveled contact between CFRP sheets and concrete (Fig. 5). Secondly, any dust and lose particles was removed from the bonded area by using air vacuum cleaner and then the bonded area was marked while the un-bonded area was covered with plastering tape to be free of epoxy (Fig. 5). Based on investigated parameters, the CFRP composite sheets cut into sheets with a width of 50 mm and different lengths. Thirdly, the epoxy compounds (part A and B) were prepared by using low-speed electric drill for at least 3 minutes to get a homogenous epoxy mixture. Fourthly, the epoxy first layer was applied uniformly over the bonded area and then the CFRP composite sheet (the tensile strength of 4900 MPa, thickness of 0.166 mm, elongation at break of 2.1 %, elastic modulus of 230 GPa) was placed onto the epoxy. Plastic roller was used along the fiber direction in order to remove any entrapped air bubbles. Finally, the epoxy second layer was applied over the CFRP sheet bonded area to make sure epoxy homogeneous distribution (Fig. 5).



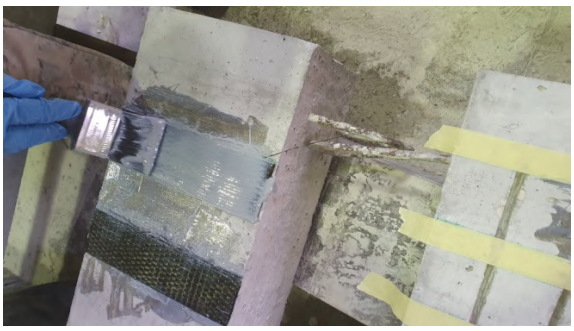
Marking the area of CFRP sheets bonded using plastering tape



Concrete bonded area were roughened and brushed with steel wire cup brush



Applying the first layer of epoxy onto CFRP sheets surface



Applying the two layers of epoxy onto CFRP sheets surface

Figure 5. Bonding of CFRP sheets to reinforced concrete beams.

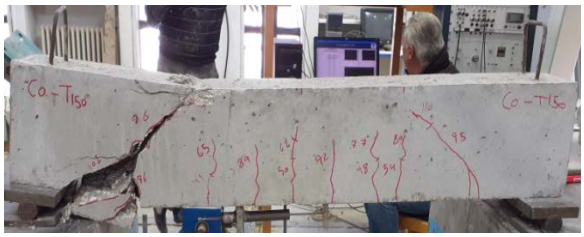
2.5. Testing Setup

All beams were tested under four-point loading with a simply supported span of 1000 mm (Fig. 1). The two supports are one roller and the other one is hinge as well as the loading points were made from steel to make sure zero deformation. A hydraulic testing machine is used to apply the load with a displacement loading rate of 0.1 mm/sec. The vertical linear variable displacement transducer (LVDT) is used to record the mid-span deflection which is placed at the bottom of the beam (Fig. 1). Also, one strain gage was placed in position such that to record the CFRP tensile strain. The tested results (load-deflection curves and the CFRP strain) were collected by using data acquisition system while the failure modes and cracks pattern are obtained visually.

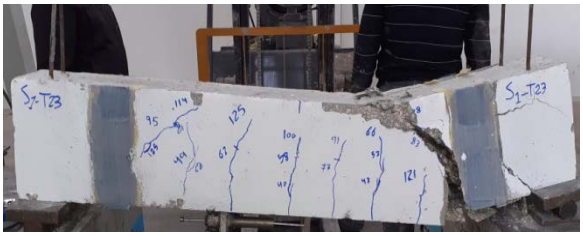
3. Results and Discussion

3.1. Mode of failure

The modes of failure of the control beam as well as the beams with CFRP strips are shown in Fig. 6. All failures were occurred within the shear span as was intentionally designed with inclined failure planes. This allows for a reasonable estimation of the contribution of the CFRP strips to the shear strength of the concrete. Formation of web-shear cracks was observed during loading; the number as well as widths and lengths of the web shear cracks increased as the loading increased. At ultimate, a sudden crushing within the shear span was observed after the development of major multiple web-shear cracks. The loads at which concrete crushing occurred was different reflecting the contribution and effectiveness of the CFRP strips in providing shear resistance. In some occasions, at failure, a significant portion of the concrete shattered from the shear span. Shear failure is sudden in nature and once happens, it causes large inclined cracks accompanied by loud sound. This typically occurs at either one of the beam ends due to very slight variation in the beam or loading after deflection. Compared with the control beam, the shear span of the anchored beams experienced less intense shear cracks with the inner core remained nearly intact. This is attributed to alleviation of the intensity of the web-shear stresses and consequent cracking by the anchored CFRP strips that participated in resisting the induced stresses.



Control



1 CFRP strip



2 CFRP strips



3 CFRP strips **4 CFRP strips**

(a) Effect of number of CFRP strips



23 °C **150 °C**



250 °C **500 °C**

(b) Effect of elevated temperature

Figure 6. Typical mode of failure.

3.2. Strain in CFRP strips

Figure 7 shows the standard curves of load vs. CFRP strain for all the specimens. It could be observed that the emergence of diagonal cracks in concrete produced tensile stresses in CFRP laminates due to the development of shear force. The maximum level of tensile stresses was at the CFRP's middle point, intersecting diagonal cracks, close to the mid-height of the beam's cross-section (Figure 6). Also, the whole specimens' CFRP strain was found to be less than 16400 με, the ultimate value, as illustrated in Table 1. In addition, in Table 1, it was revealed that the number of CFRP strips impacted, to a far extent, the effectiveness of CFRP strips. In strengthened beam specimens at 23 °C, the enhancement percentages, as per the ultimate strain of CFRP strips, were: 30.7 %, 32.4 %, 34.3 %, and 35.8 % for one, two, three, and four strips, respectively, and these percentages are similar to Al-Rousan [5]. At 150 °C, the percentages, as per the ultimate strain of CFRP strips, were: 25.9 %, 27.9 %, 28.7 %, and 30.9 % for one, two, three, and four strips, respectively, achieving 0.85 of the beam's strains at 23ºC, and these percentages are similar to Al-Rousan [5]. At 250 °C, the beams' strain percentages, as per the ultimate strain of CFRP strips, were: 25.6 %, 26.2 %, 27.4 %, and 28.0 % for one, two, three, and four strips, respectively, achieving 0.80 of the beams' strains at 23 °C, and these percentages are similar to Al-Rousan [5]. At 500 °C, the percentages of strains, as per the ultimate strain of CFRP strips, were: 21.4 %, 22.8 %, 24.7 %, and 24.7 % for one, two, three, and four strips respectively, achieving 0.71 of the beams strains at 23 °C.

In the sage of pre-cracking, CFRP strains did not develop. After the emergence of diagonal shear cracks in the shear span, the strains of CFRP became higher, at a fast rate, till failure (Figure 7), and this behavior is similar to Al-Rousan [5]. It was also found that the CFRP's strains CFRP appeared extensively when the bonding area was larger. Results also showed the strain of the CFRP laminates was highly influenced when the specimens were strengthened with four grooved strips of CFRP.

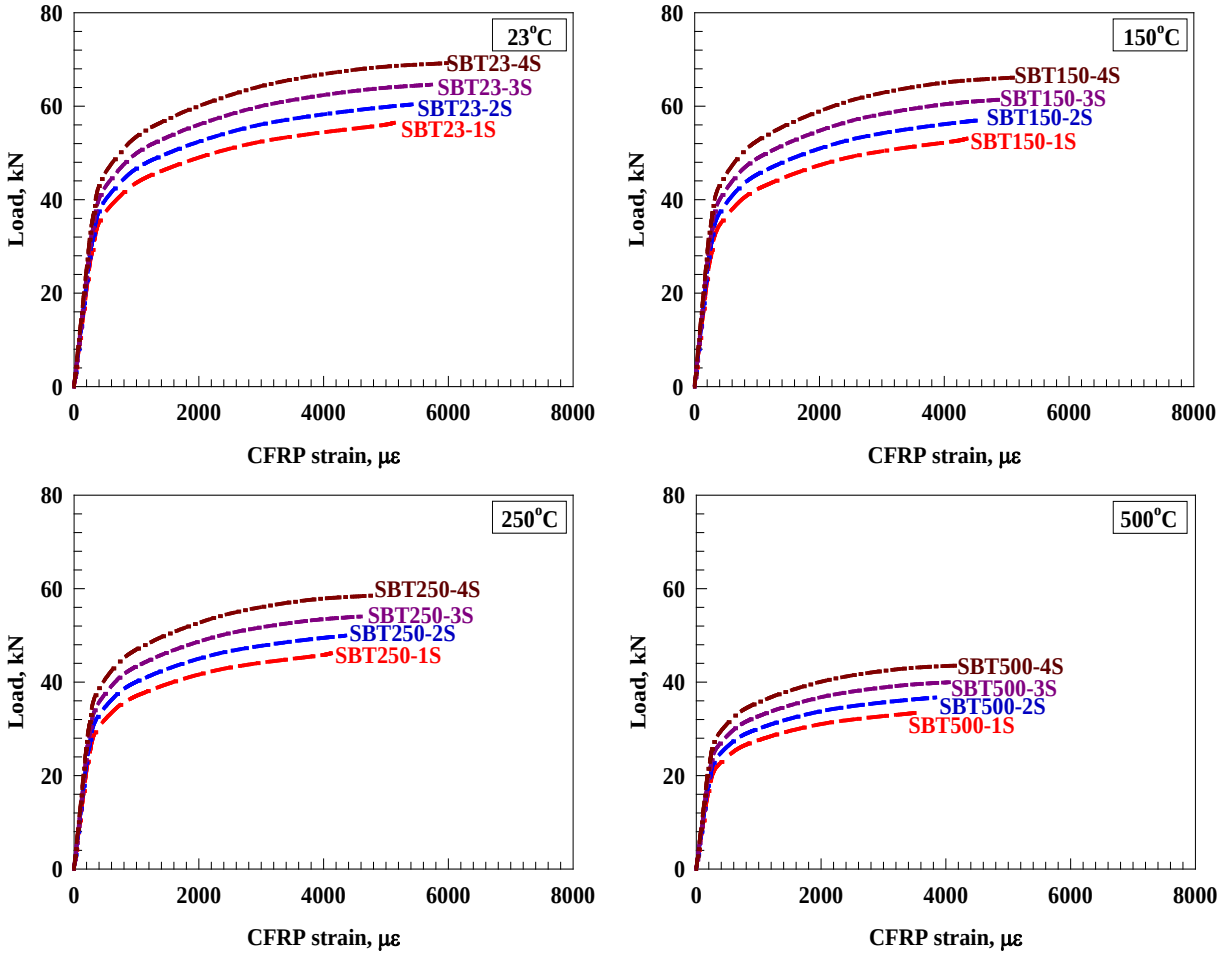


Figure 7. Typical load versus CFRP strain curve

3.3. Load versus deflection behavior

Table 3 shows the load vs. deflection characteristics curves for both anchored and un-anchored strengthened beams and control ones. The characteristics included stiffness and toughness. The initial stiffness can be specified from the slope of the linear elastic stage of the load-deflection curve ($k = P/\delta$) [5]. Also, toughness can be specified by computing the total constrained area underneath the load-deflection curve up to the point of ultimate load capacity [5]. The load vs. deflection, at mid-span, curve (Figure 8) has three distanced parts: the pre-cracking part, it is linearly elastic, and it extends to the first flexural crack; the second part is the transition, extending to the point at which the diagonal shear cracks appear; and the third part is the post-cracking, extending to the beam's ultimate capacity. Inspecting Figure 8, the anchored grooves technique significantly influenced the specimens': toughness, stiffness, ultimate load, and maximum deflection (Table 3). In addition, it has been deduced that the bigger the bonded area of CFRP, the better the beam's behavior. Furthermore, the higher the temperatures, the less the performance (Figure 8).

Table 3. Characteristics of load deflection behavior.

Group	Beam	Temperature, °C	Elastic stiffness (kN/mm)	Toughness (kN.mm^2)	Strength factor	Ductility factor	Performance Factor
1	SBT23-0S	23	13	139	1.00	1.00	1.00
	SBT23-1S		15	186	1.07	1.12	1.19
	SBT23-2S		17	223	1.14	1.17	1.34
	SBT23-3S		19	269	1.22	1.27	1.55
	SBT23-4S		20	301	1.31	1.30	1.71
2	SBT150-0S	150	12	124	0.94	0.95	0.89
	SBT150-1S		14	154	0.99	1.01	1.00
	SBT150-2S		16	190	1.07	1.08	1.15
	SBT150-3S		17	221	1.14	1.14	1.30
	SBT150-4S		19	257	1.23	1.19	1.47

Group	Beam	Temperature, °C	Elastic stiffness (kN/mm)	Toughness (kN.mm^2)	Strength factor	Ductility factor	Performance Factor
3	SBT250-0S	250	11	101	0.81	0.92	0.75
	SBT250-1S		13	126	0.85	0.98	0.83
	SBT250-2S		14	147	0.93	1.00	0.93
	SBT250-3S		16	170	0.99	1.05	1.03
	SBT250-4S		18	194	1.07	1.08	1.15
4	SBT500-0S	500	8	72	0.59	0.90	0.53
	SBT500-1S		9	84	0.63	0.93	0.58
	SBT500-2S		11	101	0.68	0.96	0.65
	SBT500-3S		12	121	0.73	1.01	0.74
	SBT500-4S		13	138	0.78	1.05	0.82

Note: Performance Factor is defined as strength factor multiply by ductility factor

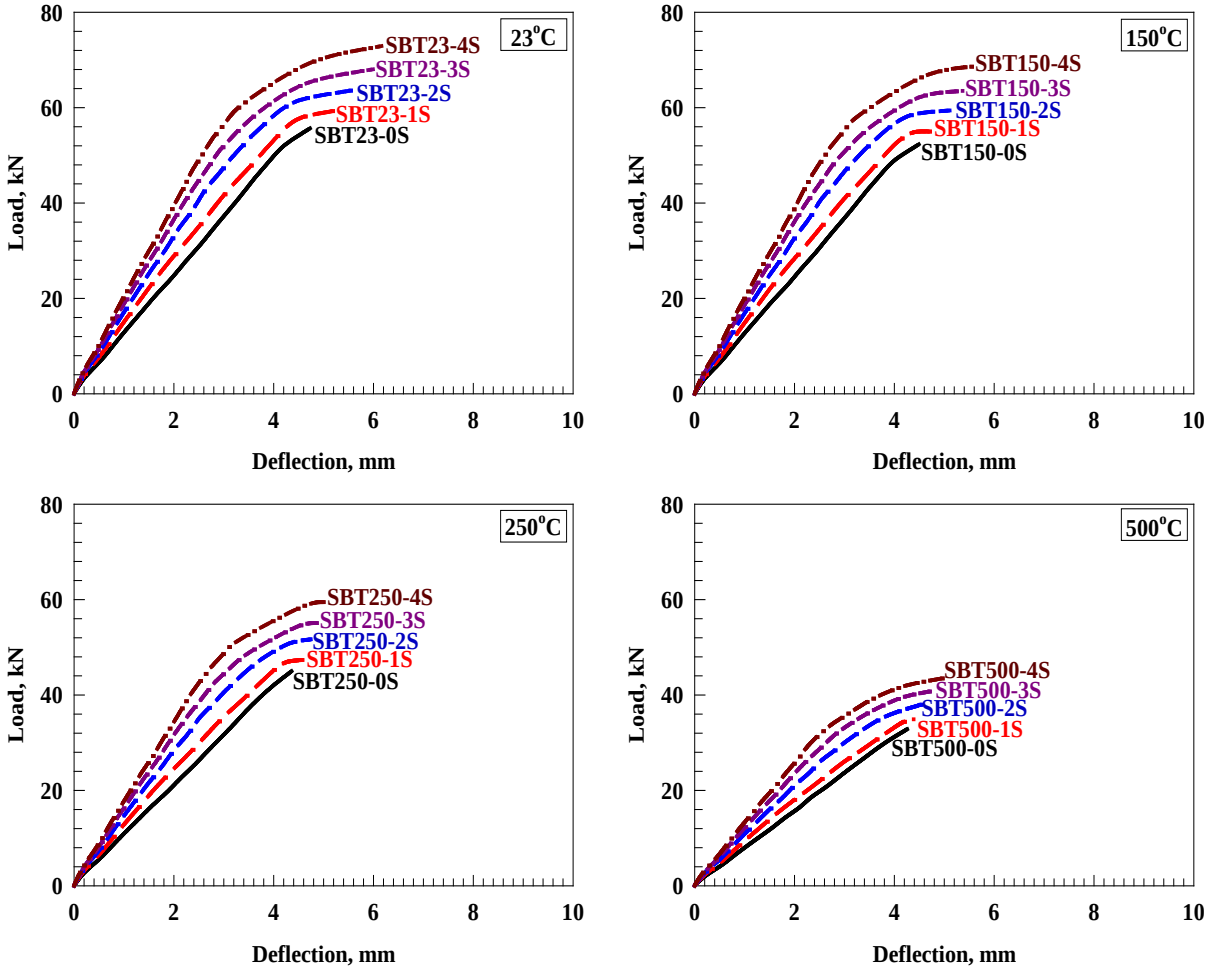


Figure 8. Load-deflection curves for the tested beam.

3.4. Maximum load capacity and corresponding deflection

The evaluation of strengthened RC beams load capacity and resultant deflections has shown tremendous structural performance [5]. The ultimate load capacity is produced by the limit states of the beam's ultimate load, while the deflections are due to the serviceability, as in Table 3. The strengthened beam's load capacity percentage can be found by dividing the ultimate load capacity by the control beam's load capacity [5]. Similarly, the strengthened beam's deflection percentage can be determined by dividing the strengthened beam's ultimate deflection by the control beam's ultimate deflection, as depicted in Figure 9. It is worth mentioning that strength percentage is an indicator of the beam's capability of sustaining load incrementing. Figure 9 showed that rising the number of CFRP strips significantly enhanced the beam's strength percentage. The average ultimate load enhancement percentage (Fig. 9) for tested beams with respect to control beam is 6.7 %, 14.2 %, 22.2 %, and 30.9 % for one, two, three, and four strips, respectively. Whereas, the average ultimate load reduction percentage (Fig. 9) for tested beams with

respect to beams exposed to 23 °C is 6.5 %, 19.1 %, and 40.5 % for 150 °C, 250 °C, and 500 °C strips, respectively.

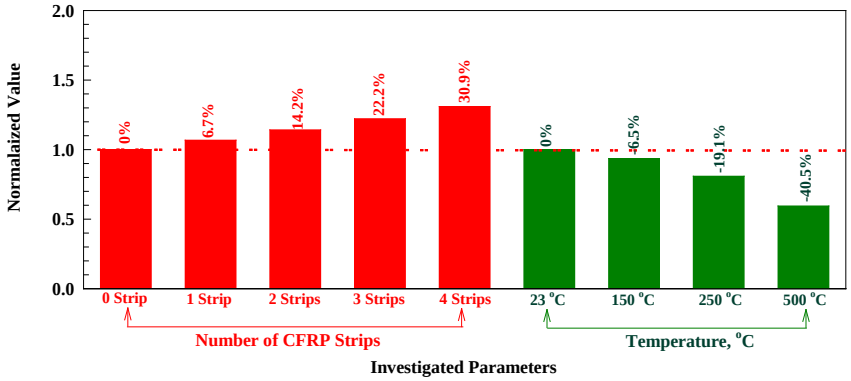


Figure 9. Normalized ultimate load capacity with respect to control beam.

The deflection indicates how much the strengthened RC beams can sustain deformations without failure [5]. The deflection percentage is defined as the ratio of the ultimate deflection of the strengthened beam to the ultimate deflection of the control beam (undamaged beam), as shown in Fig. 10. Fig. 10 shows that the ductility percentage also significantly increased with the increase of the number of CFRP strips and decreased with the increase of exposed temperature. The average ultimate deflection enhancement percentage (Fig. 10) for tested beams with respect to control beam is 6.8 %, 13.7 %, 19.5 %, and 25.6 % for one, two, three, and four strips, respectively, and this equal to 0.83 times the enhancement percentages in ultimate load. Whereas, the average ultimate deflection reduction percentage (Fig. 10) for tested beams with respect to beams exposed to 23 °C is 8.2 %, 13.9 %, and 16.8 % for 150 °C, 250 °C, and 500 °C strips, respectively, and this equal to 0.90 times the reduction percentages in ultimate load.

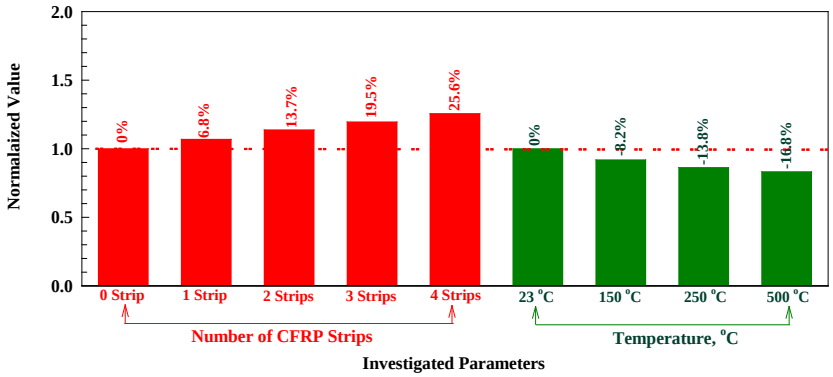


Figure 10. Normalized ultimate deflection with respect to control beam.

3.5. Elastic stiffness

Elastic stiffness indicates the crystal's response to external stresses or strains. Also, stiffness describes the properties of bonding in addition to the stability, mechanically and structurally [5]. The slope of the pre-cracking part of the load-deflection graph represents an elastic stiffness. For the sake of comparison, the values of the CFRP-strengthened specimens' elastic stiffness were modified according to the control beam (Fig. 11).

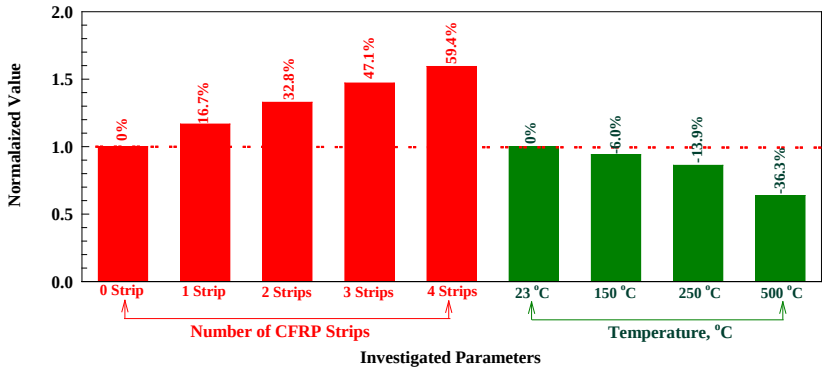


Figure 11. Normalized stiffness with respect to control beam.

In Fig. 11 illustrates the specimens' enhancement percentages of elastic stiffness, as per control beam, averaging 16.7 %, 32.8 %, 47.1 %, and 59.4 % for one, two, three, and four strips, respectively. Whereas, the average elastic stiffness reduction percentage (Figure 11) for tested beams with respect to beams exposed to 23 °C is 6.0 %, 13.9 %, and 36.3 % for 150ºC, 250 °C, and 500 °C strips, respectively.

3.6. Toughness of tested beams

Toughness defines a material's energy absorption capability, per unit volume, before being deformed, plastically, without being ruptured. Toughness can be determined by computing the area beneath the load-deflection curve [5]. The strengthened specimens' toughness values were modified in accordance with the control beams (Fig. 12). Inspection of Fig. 12 reveals that the average toughness enhancement percentage for tested beams with respect to control beam is 33.6 %, 60.7 %, 94.0 %, and 116.9 % for one, two, three, and four strips, respectively. Whereas, the average toughness reduction percentage (Fig. 12) for tested beams with respect to beams exposed to 23 °C is 15 %, 33.3 %, and 53.6 % for 150 °C, 250 °C, and 500 °C strips, respectively.

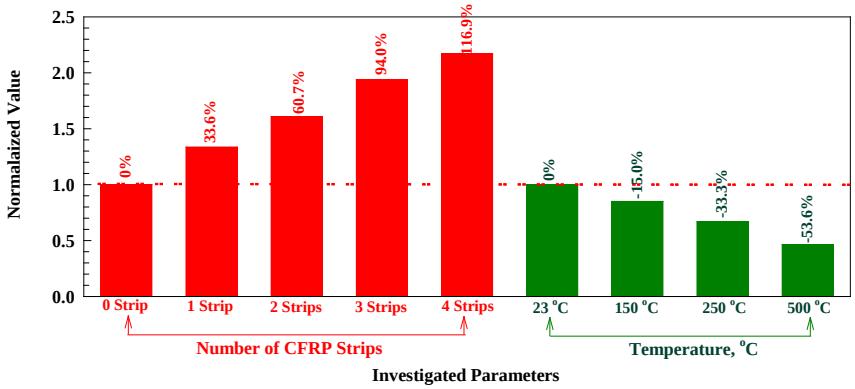


Figure 12. Normalized toughness with respect to control beam.

3.7. Performance evaluation of experimental results

The effectiveness of CFRP laminates was investigated by monitoring three factors: the strength factor (SF), deformability factor (DF), and performance factor (PF), where the PF is SF and DF combined together (Table 3 and Fig. 13) [5]. From Fig. 13, raising the CFRP's bonded area (number of strips) enhanced the PF. On the other side, the PF factor decreased when the temperature was raised. Finally, enlarging the bonded area made the beams highly resistant to the brittle shear failure and enhanced their performance. Inspection of Fig. 13 reveals that the average performance factor enhancement percentage for tested beams with respect to control beam is 55.9 %, 113.4 %, 185.4 %, and 245.7 % for one, two, three, and four strips, respectively. Whereas, the average performance factor reduction percentage (Fig. 13) for tested beams with respect to beams exposed to 23 °C is 20.1 %, 42.6 %, and 70.4 % for 150 °C, 250 °C, and 500 °C strips, respectively.

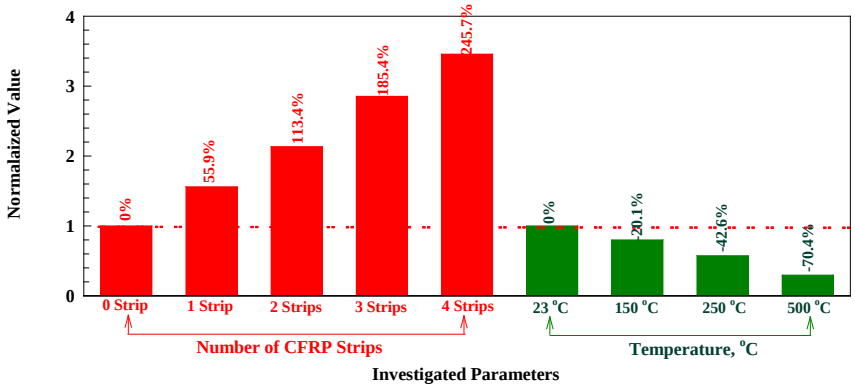


Figure 13. Normalized performance factor with respect to control beam.

Table 4. Index of profitability.

Group Number	Beam	Temperature, °C	Concrete's shear contribution, kN	CFRP shear contribution, kN	Ultimate shear contribution, kN	V_f/A_f, MPa
1	SBT23-0S	23	55.7	0	55.7	0
	SBT23-1S		55.7	3.8	59.4	2.0
	SBT23-2S		55.7	7.9	63.6	1.1
	SBT23-3S		55.7	12.4	68.0	0.8
	SBT23-4S		55.7	17.2	72.9	0.6
2	SBT150-0S	150	52.3	0	52.3	0
	SBT150-1S		52.3	2.7	55.0	1.8
	SBT150-2S		52.3	7.1	59.4	1.0
	SBT150-3S		52.3	11.2	63.5	0.7
	SBT150-4S		52.3	16.4	68.7	0.6
3	SBT250-0S	250	45.0	0	45.0	0
	SBT250-1S		45.0	2.4	47.4	1.6
	SBT250-2S		45.0	6.7	51.7	0.9
	SBT250-3S		45.0	10.1	55.1	0.6
	SBT250-4S		45.0	14.3	59.3	0.5
4	SBT500-0S	500	32.9	0	32.9	0
	SBT500-1S		32.9	2.1	34.9	1.2
	SBT500-2S		32.9	5.1	38.0	0.6
	SBT500-3S		32.9	8.0	40.9	0.5
	SBT500-4S		32.9	10.7	43.5	0.4

Note: V_f: the CFRP shear contribution, A_f : the CFRP bonded area within the shear span

3.8. The index of profitability

For RC beams strengthened with various methods of CFRP, Table 4 illustrates each of the concrete's shear contributions (V_c), the CFRP material's shear contributions (V_f), and the final loads. It was observed that enhancing the bonded area of CFRP (i.e., the number of sheets) increased the contribution of CFRP (V_f) to the shear capacity. A number of strengthening methods, using CFRP laminates, were examined, considering the following aspects: the consumed quantity of CFRP, and the calculated profitability indices. Profitability index is the ratio of CFRP's contribution to shear strength-to-total CFRP bonded area, inside the strengthened beam's shear span with various CFRP methods. Strengthened beams' profitability indices are shown in Table 4, where it is shown that increasing either the number of CFRP sheets (bonded area) or the temperatures has decreased the profitability index.

3.9. Comparison of experimental results with ACI model

For purposes of comparison, the experimental results are compared with ACI model [30], the general design guidance is derived from the experimental data and they are only applicable to external FRP reinforcement. Fig. 14 shows a comparison of the results predicted by the ACI model (V_f, experimental /V_f,ACI [30]). Note that the ACI model was calibrated for CFRP should be used with caution for other types of composites as shown in Fig. 14. The overall predictions by ACI model [30] appear to be overestimated with a mean V_f, experimental /V_f,ACI value of 1.11 and a coefficient of variation (COV) of 26 %. It is also important to take into consideration that all the ACI model are semi empirical in nature, with important governing parameters derived from test data for beams strengthened with FRP laminates, whereas the ACI model cannot be applied in certain cases. In addition, a careful inspection of Fig. 14 will show that the ACI model [30] has a much wider range of experimental/theoretical failure load ratios of 0.80 to 1.46.

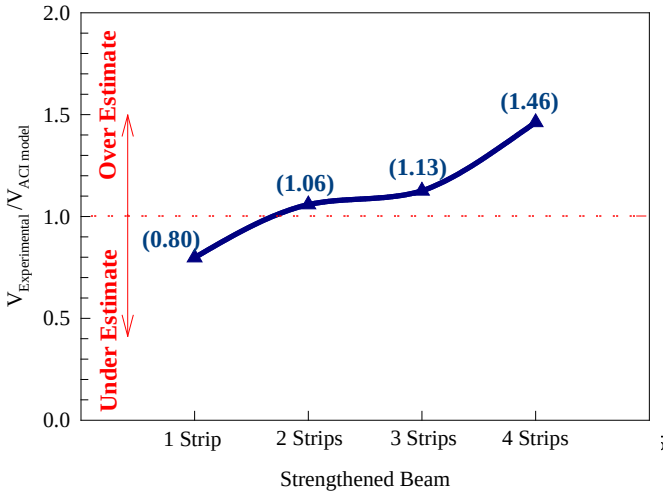


Figure 14. The normalized *e*xperimental FRP shear force with respect to ACI model [41].

4. Conclusions

1. The presence of CFRP strips shifted the forms of end debonding failure modes, i.e. end interfacial debonding and cover separation, to a less critical one, therefore improved the performance of the conventional CFRP-strengthening method.

2. CFRP strips increase the shear capacity of the anchorage zone; therefore result in higher anchorage efficiency of FRP-strengthened concrete beams.

3. The strengthened beams showed an increase in the load-carrying capacity for the strengthened beams accompanied by a reduction in the vertical deflection at the mid-span in different percentages compared with the control beam.

4. The influence of the number of CFRP strips on the ductility, energy absorption, and ultimate load improvement percentage is significant.

5. The influence of the exposed temperature on the ductility, energy absorption, and ultimate load reduction percentage is significant and increased with the increase of temperature.

6. The overall predictions by ACI model [30] appear to be overestimated with a mean value of 1.11 and a coefficient of variation (COV) of 26 %.

5. Acknowledgment

The author gratefully acknowledges the financial support from Deanship of Scientific Research at Jordan University of Science and Technology under Grant number 2021/5.

References

1. Rajai, Z. Al-Rousan. Empirical and NLFEA prediction of bond-slip behavior between DSSF concrete and anchored CFRP composites. Construction and Building Materials. 2018. 169 (1). Pp. 530–542. DOI: 10.1016/j.conbuildmat.2018.03.013
2. Rajai, Z. Al-Rousan. Behavior of macro synthetic fiber concrete beams strengthened with different CFRP composite configurations. Journal of Building Engineering. 2018. 20 (1). Pp. 595–608. DOI: 10.1016/j.jobe.2018.09.009
3. Al-Rousan Rajai, Abo-Msamh Isra'a. Bending and Torsion Behaviour of CFRP Strengthened RC Beams. Magazine of Civil Engineering. 2019. 92 (8). Pp. 62–71. DOI: 10.18720/MCE.92.8
4. Al-Rousan, R. The shear behavior of CFRP Strengthened RC beams. Magazine of Civil Engineering. 2020. No. 6. Pp. 9810–9810. DOI: 10.18720/MCE.98.10
5. Al-Rousan, R. Behavior of strengthened concrete beams damaged by thermal shock. Magazine of Civil Engineering. 2020. No. 2. Pp. 93–107. DOI: 10.18720/MCE.94.8.
6. Al-Rousan, R. Behavior of CFRP strengthened columns damaged by thermal shock. Magazine of Civil Engineering. 2020. No. 5. Pp. 9708–9708. DOI: 10.18720/MCE.97.8
7. Nedviga, E., Beresneva, N., Gravit, M., Blagodatskaya, A. Fire Resistance of Prefabricated Monolithic Reinforced Concrete Slabs of "Marko" Technology. Adv. Intell. Syst. Comput. 2018. 692 (1). Pp. 739–749. DOI: 10.1007/978-3-319-70987-1_78
8. Hezhev, T.A., Zhurtov, A.V., Tsipinov, A.S., Klyuev, S.V. Fire resistant fibre reinforced vermiculite concrete with volcanic application. Magazine of Civil Engineering. 2018. 80 (1). Pp. 181–194. DOI: 10.18720/MCE.80.16
9. Goremikins, V., Blesak, L., Novak, J., Wald, F. Experimental investigation on SFRC behaviour under elevated temperature. Journal of Structural Fire Engineering. 2017. 8 (1). Pp. 287–299. DOI: 10.1108/JSFE-05-2017-0034

10. Goremikins, V., Blesak, L., Novak, J., Wald, F. To testing of steel fibre reinforced concrete at elevated temperature. Applications of Structural Fire Engineering. 2017. 1 (1). Pp. 48–54. DOI: 10.14311/asfe.2015.055
11. Blesak, L., Goremikins, V., Wald, F., Sajdlova, T. Constitutive model of steel fibre reinforced concrete subjected to high temperatures. Acta Polytechnica. 2016. 56 (1). Pp. 417–424. DOI: 10.14311/AP.2016.56.0417
12. Korsun, V., Vatin, N., Franchi, A., Korsun, A., Crespi, P., Mashtaler, S. The strength and strain of high-strength concrete elements with confinement and steel fiber reinforcement including the conditions of the effect of elevated temperatures. Procedia Engineering. 2015. 117 (1). Pp. 970–979. DOI: 10.1016/j.proeng.2015.08.192
13. Goremikins, V., Blesak, L., Novak, J., Wald, F. Experimental method on investigation of fibre reinforced concrete at elevated temperatures. Acta Polytechnica. 2016. 56 (1). Pp. 258–264. DOI: 10.14311/AP.2016.56.0258
14. Selyaev, V.P., Nizina, T.A., Balykov, A.S., Nizin, D.R., Balbalin, A.V. Fractal analysis of deformation curves of fiber-reinforced fine-grained concretes under compression. PNRPU Mechanics Bulletin. 2016. 1 (1). Pp. 129–146. DOI: 10.15593/perm.-mech/2016.1.09
15. Bily, P., Fladr, J., Kohoutkova, A. Finite Element Modelling of a Prestressed Concrete Containment with a Steel Liner. Proceedings of the Fifteenth International Conference on Civil, Structural and Environmental Engineering Computing. Civil-Comp Press. 2015. DOI: 10.4203/ccp.108.1
16. Bílý, P., Kohoutková, A. Sensitivity analysis of numerical model of prestressed concrete containment. Nuclear Engineering and Design. 2015. 295 (1). Pp. 204–214. DOI: 10.1016/j.nucengdes.2015.09.027
17. Al-Rousan, R. Behavior of two-way slabs subjected to drop-weight. Magazine of Civil Engineering. 2019. 90 (6). Pp. 62–71. DOI: 10.18720/MCE.90.6
18. Al-Rousan, R. The impact of cable spacing on the behavior of cable-stayed bridges. Magazine of Civil Engineering. 2019. 91 (7). Pp. 49–59. DOI: 10.18720/MCE.91.5
19. Krishan, A., Rimshin, V., Erofeev, V., Kurbatov, V., Markov, S. The energy integrity resistance to the destruction of the long-term strength concrete. Procedia Engineering. 2015. 117 (1). Pp. 211–217. DOI: 10.1016/j.proeng.2015.08.143
20. Korsun, V., Vatin, N., Korsun, A., Nemova, D. Physical-mechanical properties of the modified fine-grained concrete subjected to thermal effects up to 200°S. Applied Mechanics and Materials. 2014. 633–634. Pp. 1013–1017. DOI: 10.4028/www.scientific.net/AMM.633-634.1013
21. Korsun, V., Korsun, A., Volkov, A. Characteristics of mechanical and rheological properties of concrete under heating conditions up to 200°C. MATEC Web Conference. 2013. 6 (1). Pp. 07002. DOI: 10.1051/matecconf/20130607002
22. Petkova, D., Donchev, T., Wen, J. Experimental study of the performance of CFRP strengthened small scale beams after heating to high temperatures. Construction and Building Materials. 2014. 68 (1). Pp. 55–61. DOI: 10.1016/j.conbuild-mat.2014.06.014
23. Ji, G., Li, G., Alaywan, W. A new fire resistant FRP for externally bonded concrete repair. Construction and Building Materials. 2013. 42 (1). Pp. 87–96. DOI: 10.1016/j.conbuildmat.2013.01.008
24. Trentin, C., Casas, J.R. Safety factors for CFRP strengthening in bending of reinforced concrete bridges. Composite Structures. 2015. 128 (1). Pp. 188–198. DOI: 10.1016/j.compstruct.2015.03.048
25. Ferrari, V.J., de Hanai, J.B., de Souza, R.A. Flexural strengthening of reinforcement concrete beams using high performance fiber reinforcement cement-based composite (HPFRCC) and carbon fiber reinforced polymers (CFRP). Construction and Building Materials. 2013. 48 (1). Pp. 485–498. DOI: 10.1016/j.conbuildmat.2013.07.026
26. Attari, N., Amziane, S., Chemrouk, M. Flexural strengthening of concrete beams using CFRP, GFRP and hybrid FRP sheets. Construction and Building Materials. 2012. 37 (1). Pp. 746– 757. DOI: 10.1016/j.conbuildmat.2012.07.052
27. Kara, I.F., Ashour, A.F., Körog˘lu, M.A. Flexural behavior of hybrid FRP/steel reinforced concrete beams. Composite Structures. 2015. 129 (1). Pp. 111–121. DOI: 10.1016/j.compstruct.2015.03.073
28. Kolchunov, V.I., Dem'yanov, A.I. The modeling method of discrete cracks in reinforced concrete under the torsion with bending. Magazine of Civil Engineering. 2018. 81 (5). Pp. 160–173. DOI: 10.18720/MCE.81.16
29. Travush, V.I., Konin, D.V., Krylov, A.S. Strength of reinforced concrete beams of high-performance concrete and fiber reinforced concrete. Magazine of Civil Engineering. 2018. No. 77 (1). Pp. 90–100. DOI: 10.18720/MCE.77.8
30. ACI Committee 440. Design and Construction of Externally Bonded FRP Systems for strengthening Concrete Structures. *ACI440.2R-02. 2002. American Concrete Institute, Farmington Hills, Mich.: 45 pp. DOI: 10.1061/40753(171)159. ISBN: 9780870312854

Contacts:

Rajai Al-Rousan, rzalrousan@just.edu.jo

Received 12.04.2020. Approved after reviewing 23.12.2020. Accepted 04.03.2021.



Magazine of Civil Engineering

ISSN 2712-8172

journal homepage: http://engstroy.spbstu.ru/

DOI: 10.34910/MCE.110.3

Thermal insulation systems for road bases with foam glass gravel

***V.S. Semenov*[a]* ✉, *I.V. Bessonov*[b], *Zh.A. Zhukov*[a], *E.A. Mednikova*[a], *I.S. Govryakov*[b]**

[a] *National Research Moscow State Civil Engineering University, Moscow, Russia*

[b] *Research Institute of Building Physics (NIISF RAACS), Moscow, Russia*

**E-mail: science-isa@yandex.ru*

Keywords: foam glass gravel; heat-insulating material; permafrost; road system; exploitation stability; soil; freezing level; temperature field

Abstract. The article discusses the systems of roadbed construction on permafrost and heaving soils with foam glass gravel backfill. The aim of the research was to substantiate the expediency of using foam glass gravel in roadway insulation systems on problematic, including heaving and permafrost soils. This goal was achieved by determining the properties of foam glass gravel, as well as calculating the thermal characteristics and temperature fields in the roadbed. The strength of foam glass gravel, depending on its degree of compaction (from 10 to 50 %), is in the range of 0.90...1.58 MPa, and the thermal conductivity coefficient is from 0.087 to 0.099 W/(m°C). It was found that the water absorption of gravel by volume does not exceed 1.8 %, and the sorption humidity does not exceed 4.2 %. The novelty of the work lies in a comprehensive study of insulation systems using domestically produced foam glass gravel using digital imitation of heat transfer and modeling of the formation of temperature fields. It has been established that the use of heat-insulating backfill of foam glass gravel with a thickness of 0.25 m allows to protect the permafrost soil of the road base from thawing, and to limit the freezing depth to 0.2 m, versus 2.6 m without heat-insulating layer – in case of protection of the road base from freezing. The significance of the research is the development of constructive solutions for the use of foam glass gravel in roadway insulation systems, arranged on problem soils in permafrost conditions and on soils with frost heaving.

1. Introduction

The service life of the road pavements is determined by a combination of several factors. Firstly, this is the type of road structure, including the construction of the base and the type of pavement (cover), and the design of the inner layers that take loads and transfer these loads to the ground. Secondly, this is the type of base soil, its condition and stability, including the presence of permafrost, wetlands, water hoses, etc. Thirdly, this is the quality of road work, that is, the fulfillment of all normative requirements to these works.

Insulating materials used in pavement systems should have low heat conductivity and water absorption, have high resistance to aggressive environments and biological corrosion, high frost resistance, good strength properties [1–3]. These requirements are best met by plate products based on extruded foamed polystyrene and foam glass, as well as foam glass gravel, manufactured on specialized lines.

In the harsh permafrost conditions, the construction of thermal insulation layers (from extruded foamed polystyrene: XPS-plates) allows the permafrost soils to be kept in their natural state, which prevents

Semenov, V.S., Bessonov, I.V., Zhukov, Zh.A., Mednikova, E.A., Govryakov, I.S. Thermal insulation systems for road bases with foam glass gravel. Magazine of Civil Engineering. 2022. 110(2). Article No. 11003. DOI: 10.34910/MCE.110.3

© Semenov, V.S., Bessonov, I.V., Zhukov, Zh.A., Mednikova, E.A., Govryakov, I.S., 2022. Published by Peter the Great St. Petersburg Polytechnic University.

This work is licensed under a CC BY-NC 4.0

thawing and excludes subsidence of the subgrade. Also noteworthy is the use of XPS -plates (blocks) in the construction of lightweight embankments on weak foundations.

When using the technology of building light embankments from extruded foamed polystyrene blocks, problems associated with insufficient bearing capacity of the soil, the possibility of large settlements and a long period of foundation stabilization are solved. The term and cost of construction is reduced [4–6].

The disadvantage of such systems is the fact of using plate (piece) products, i.e. the presence of seams and contact areas between the plates. During operation, due to seasonal deformations or changes in the level of groundwater (on soft soils), the base moves and its configuration changes. This can lead to a gradual opening (increase) of the gaps between the plate products, which leads to the creation of areas of intense heat and mass transfer, and therefore to the violation of the thermal integrity of the insulating shell.

Laying boards made of extruded foamed polystyrene requires careful preparation of the base and is highly labor intensive. In addition, during operation, the plates are deformed, crumbled and, over time, lose their heat-insulating properties.

The use of backfill insulation makes it possible to form a uniform insulating shell. Foam glass gravel is a filling thermal insulation. Such material is used as a backfill to thermal insulation the foundations of low-rise buildings, the brick walls of the well masonry or Gerard masonry, as well as to strengthen weak soils and the sub ballast layer of the pavements. Foam glass gravel produced on special lines has a bulk density of 120…200 kg/m^3 and grain size of 40...60 mm.

For the foam glass production recycled glass obtained from bottle fight, defective automotive glass and double-glazed window battle are used as a raw material. An analysis of the glasses recommended by our and foreign researchers to obtain high-quality foam glass showed that the glasses synthesized in the systems SiO_2–Al_2O_3–MgO–CaO–R_2O and SiO_2–B_2O_3–MgO–CaO–R_2O found wide application in the production of foam glass. We can conclude that aluminosilicate and aluminoborosilicate glasses most fully satisfy the requirements for the foam glass quality. In Russia, to obtain heat-insulating foam glass, glass masses are most often used that are close in chemical composition to aluminum-magnesium glass [7–9].

An analysis of the foam glass gravel use shows that about 30 % falls on roofs and about 40 % on stylobates. The remaining volume is used in landscape design, road construction, in the overhaul of blocks of flats and foundations. The forecast shows that, due to its properties, for the period 2020–2022 under favorable conditions, foam glass gravel will occupy more than 2 % of the total market of thermal insulating materials and will amount to at least 1 million m^3. Abroad, foam glass gravel has been used in road systems since the mid-80s of the last century. These technologies are most common in the Scandinavian countries: Finland, Sweden, Norway. At the same time, the duration of the winter period, as well as the presence of heaving soils in the regions of the Russian Federation east of the Urals, impose special requirements on road structures.

As a result of the analysis and experimental studies, it was established that the materials used in road insulation systems should have low thermal conductivity and water absorption, have high resistance to aggressive ambience and biological corrosion, have high frost resistance and high strength characteristics.

The purpose of the research was to substantiate the expediency of using foam glass gravel in roadway insulation systems on problematic, including heaving and permafrost soils, based on studying the patterns of formation of temperature fields in insulation systems.

To achieve the goal of the study, it was envisaged to perform the following particular tasks:

- study of the properties of foam glass gravel at various degrees of its compaction;
- development of soil insulation systems in conditions of its preservation in a frozen state (protection against thawing) and in conditions of maintaining positive temperatures in it (protection against frost heaving);
- calculation of thermal characteristics and temperature fields in roadway insulation systems using the THERM computer program.

2. Materials and Methods

The tests of the properties of crushed glass foam were carried out in accordance with the current standard methods. The calculation of thermal characteristics and temperature fields in roadway insulation systems was evaluated using a special computer program THERM, developed by Lawrence Berkeley Laboratory (LBNL), University of California, USA.

In the experiments, foam glass gravel with a bulk density of 180 kg/m^3 was used (Fig. 1).



Figure 1. Foam glass gravel.

The maximum degree of compaction of foam glass gravel was determined on the installation, equipped with a vibrator and weights with a total weight of 250 kg (Fig. 2). The cylindrical metal-plastic container had a diameter of 500 mm and a height of 380 mm. The dimensions of the container are selected in such a way that they allow placing at least 6 pieces of gravel in height and width. Foam glass gravel was poured into the container, shaking was performed for natural compaction. The amount of crushed stone was selected so that when lowering the loads, the lower edge of the lower disc was flush with the upper level of the container. It was found that the maximum degree of compaction of foam glass gravel with a bulk density of 180 kg/m^3 and a fraction of 30…60 mm is 50 %.



Figure 2. Carrying out experimental determinations of the maximum degree of compaction of foam glass gravel.

The compressive strength in the cylinder was determined on foam glass gravel, filled in a container and compacted with a given coefficient. A container (a metal cylinder with an inner diameter of 308 mm and a height of 210 mm) with a sealed foam glass gravel was installed on the lower platform of the press (Fig. 3). The compressive strength of foam glass gravel was taken as the arithmetic mean value of five tests [10–12].



Figure 3. Experimental determination of the compressive strength of foam glass gravel at different degrees of compaction.

Determination of the thermal conductivity coefficient of foam glass gravel at various degrees of compaction was carried out in a climatic chamber consisting of two chamber (cold and warm) and an aperture in which the studied material was placed (Fig. 4). In the cold zone, a temperature of minus 10 °C was established; in the warm zone, a temperature of + 20 °C was maintained.

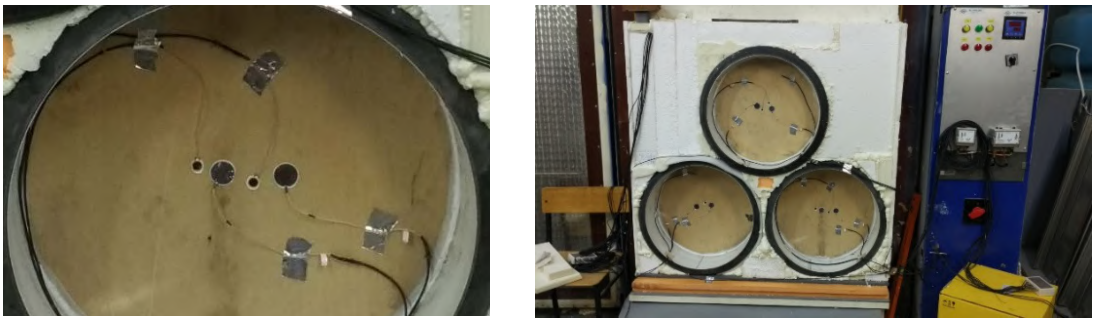


Figure 4. Experimental determination of thermal conductivity of foam glass gravel in a dry state at various degrees of compaction.

The tests were carried out in accordance with the GOST R 54853-2011 methodology with the following changes. Cylindrical containers were used as a test structure, in which foam glass gravel was compacted. The walls of the container on the warm and cold sides consisted of 10 mm thick plywood sheets tightly adjacent to the gravel, the thermal resistance of which was taken into account when calculating the thermal conductivity. The internal dimensions of the container in the plane of movement of the heat flow must exceed the average size of the crushed stone granule (in an unconsolidated state) by at least 5 times. Containers with foam glass gravel were installed in the opening of the climate chamber. Each container was insulated along the side faces, so that the thermal resistance along each of the product faces was at least 5 ($m^2 \cdot °C$)/W. Heat flux density measurements were carried out in accordance with GOST 25380-2014. Temperature sensors were installed on the outer (face of the sample facing the cold zone) and inner (face of the sample facing the warm zone) surfaces of each sample. Converters (sensors) of the heat flux were installed on the inner face. In the experiment performed, the horizontal direction of the temperature gradient was taken. At the same time, taking into account the isotropy of the properties of compacted foam glass gravel and its uniform distribution in the test container, it is permissible to accept the obtained value of the thermal conductivity coefficient in further calculations, with the vertical direction of the heat flow.

The thermal conductivity coefficient of foam glass gravel was determined in dry and wet conditions. A certain amount of foam glass gravel was dried to constant weight at a temperature of (100±5)°C, and then kept in the laboratory for at least 24 hours (conditioning). Further foam glass gravel was tamped layer by layer in the container to the required degree of compaction.

The working density (ρ_w) of foam glass gravel was determined taking into account the degree of compaction (10 %, 20 %, 30 %, 40 % and 50 %). The established value of bulk density (ρ_b) was multiplied, respectively, by compression factors 1.1; 1.2; 1.3; 1.4 or 1.5. For example:

$$\rho_w = 1.3 \times \rho_b, \ \text{kg/m}^3. \quad (1)$$

The mass of gravel, m_g, kg, required for testing, was determined by the formula:

$$m_g = \rho_w \times V, \quad (2)$$

where ρ_w is working density, kg/m^3; V is the volume of the tank for determining the compressive strength in the cylinder, m^3.

The amount of gravel determined by formula (2) was poured in layers into a container, periodically compacting and ramming. Compaction was carried out by manual or mechanical tamping. Gravel compaction was carried out before filling the tank at the level of the upper edges. The coefficient of thermal conductivity was measured at an average temperature of backfill from gravel of 10 °C. Upon reaching the stationary thermal regime, the values of temperatures and heat fluxes were recorded and the equivalent thermal conductivity of foam glass gravel in the dry state was calculated.

Experimental studies were carried out to determine the strength of foam glass gravel by compression in a cylinder with a compaction degree of 10 %, 20 %, 30 %, 40 %, and 50 %. The strength of foam glass gravel was determined on samples compacted to working density. The mass of gravel, m_g (kg), required for testing, was determined by the formula (2). A cylinder with compacted foam glass gravel was installed

on the lower platform of the press. A plunger with a diameter of 300 mm was used to load the surface of the gravel poured into the cylinder from 2 to 25 % relative deformation, that is, before crushing gravel by 2...25 % of the initial height. The arithmetic mean of the results of five tests was taken as the compressive strength in the cylinder of foam glass gravel.

The compressive strength in the cylinder at $N\%$ relative deformation $\left(R_{N\%}\right)$ of the gravel, MPa, was determined by the formula:

$$R_{N\%} = \frac{P}{F}, \tag{3}$$

where P is the load during compression of the aggregate, corresponding to $N\%$ relative deformation, N; F is the cross-sectional area of the plunger, mm^2.

At the same time, the main strength characteristic of foam glass gravel was taken to be the compression strength in a cylinder at 10 % linear deformation, as is customary for thermal insulating materials.

The water absorption of foam glass gravel was determined after being fully immersed in water for 24 hours according to the method of Russian State Standard GOST 17177. The average value of water absorption by volume was 1.8 %. The sorption moisture content of foam glass gravel was investigated according to the method of Russian State Standard GOST 24816-2014.

To study the properties of the pavement and to assess the possibility of its use on problematic soils, it is advisable to study the temperature fields formation in the road base with the help of modern computer analysis systems. These methods and the like ones are widely used in the study of multilayer insulation systems, including bases in contact with the soil [13–15]. Temperature fields were calculated using the THERM computer program based on the finite element method [16–18].

3. Results and Discussion

As the results of the experimental studies, the strength characteristics of bulk thermal insulation and the values of the thermal conductivity at various compaction degrees were determined. Design solutions for the isolation of pavement systems on problematic soils are proposed, and these solutions are evaluated using temperature field modeling in the road massive.

The results of experimental determinations of the compressive strength of foam glass gravel and thermal conductivity at various compaction degrees (squeezing in the cylinder) are given in Table 1. It was found that the compressive strength in the cylinder at 10 % relative deformation increases linearly in the range of compaction degrees from 10 % to 40 %, and practically does not change with further compaction.

Table 1. The results of experimental studies to determine the compressive strength of foam glass gravel in a cylinder and thermal conductivity at various compaction degrees.

The compaction degree of foam glass gravel, %	The average value of the compressive strength in the cylinder at 10 % deformation, MPa	The thermal conductivity coefficient of the foam glass gravel in dry state, W/(m·°C)
50	1.58	0.099
40	1.56	0.086
30	1.26	0.072
20	1.10	0.086
10	0.90	0.087

A decrease of the thermal conductivity coefficient was noted at a compaction degree of 30 %, which is explained by the densest packing of granules in the filling, with a minimum amount of intergranular space. An increase of the thermal conductivity coefficient at a compaction degree of 10 % and 20 % is due to an increase of the convective component of heat transfer (air movement) in an increasing volume of intergranular space. With a compaction degree of 40 % and 50 %, partial destruction of the foam glass granules occurs and the intergranular space is filled with small solid particles, which leads to an increase in thermal conductivity.

Studies of sorption properties showed the difference between the set of mass during adsorption and the drying rate – desorption of the foam glass gravel. The graph (Fig. 5) shows the hysteresis of material sorption. The moisture content of foam glass gravel at 100 % relative humidity was conventionally taken as the moisture content of the material by weight after complete immersion in water for 24 hours, followed by

exposure to air for 24 hours (temperature 23±2 °C and relative humidity 97 %). It should be note that the hysteretic pattern of sorption-desorption is also characteristic of other types of highly porous materials and it can be explained by the conditions for the formation of polymolecular layers on the surfaces of the mineral matrix in open semi-closed and closed pores of the substance [19–21].

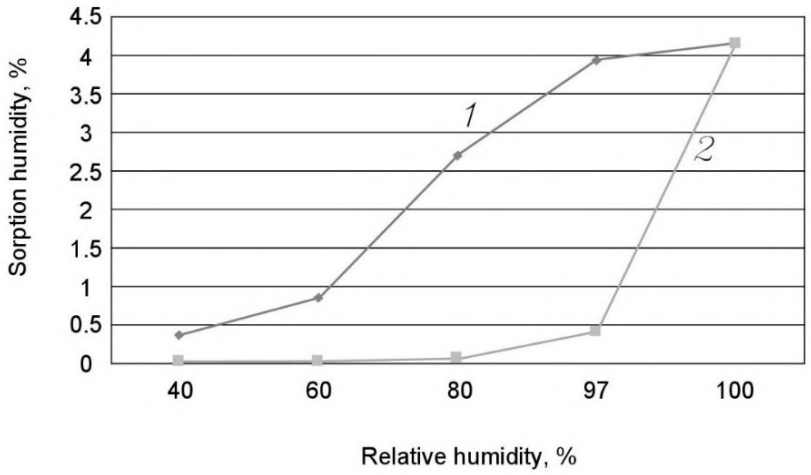


Figure 5. Hysteresis of sorption-desorption of foam glass gravel: 1 – sorption; 2 – desorption.

Based on the obtained values, the dependences of humidity and thermal conductivity, the coefficient of thermal conductivity increment for each percentage of humidity were determined, as well as the calculated values of thermal conductivity of foam glass gravel for operating conditions. The obtained results made it possible to justify the use of foam glass gravel into the insulating layers of the pavements arranged on problematic soils, including permafrost, heaving soils, etc.

The design of road insulation systems was carried out taking into account the principles of laying thermal insulation layers in pavement structures [22–24]. At the same time, two tasks were solved. The first task was to protect the permafrost soil of the base from potential thawing (preservation of permafrost and protection from thawing). The second task was to protect the soil from freezing (protection from soil swelling during freezing). Requirements for foam glass gravel are presented in Table 2.

Table 2. Normative values of the thermal conductivity coefficient of the foam glass gravel for operating conditions.

Indicator	Unit	Value
Coefficient of thermal conductivity in the backfill with compaction (1.3: 1) in a dry state	W/(m·°C)	0.072
Coefficient of thermal conductivity in the backfill with compaction (1.3: 1) in operating conditions	W/(m·°C)	0.085

Calculations of the temperature fields of the road surface using foam glass gravel were carried out using the THERM program developed by Lawrence Berkeley Laboratory (LBNL) of the University of California, USA (THERM Finite Element Simulator version 7.7.10.0, Copyright 1994-2019). This program is at the disposal of NIISF RAASN and is widely used in heat engineering calculations.

Protection against thawing was carried out by laying heat-insulating layers in the body of the embankment in the conditions of the spread of soil permafrost in the first road-climatic zone in order to preserve the soil in a solid-frozen state for the entire service life of the road and to prevent the embankment subsidence on thawing frozen soil.

The following boundary conditions are accepted in the calculations. Soil temperatures are taken from the gas industry worker's handbook table 4.13 [25]. The temperature of the permafrost soil in the climatic conditions of Yakutsk is the average temperature for 12 months at a depth of 0.8 m and is equal to minus 2.6 °C. The air temperature in the calculation is assumed to be 30 °C. The properties of soils and sand embankments were taken in accordance with Russian Construction Norms SP 25.13330.2016 Bases and foundations on permafrost soils (Table B.8).

The thermal conductivity coefficient of soil in a frozen state is taken in accordance with Table B.8. Characteristics of the materials of the layers of the road structure with foam glass gravel backfill: peat soil with a density of 400 kg/m^3; thermal conductivity coefficient in a frozen state of 1.45 W/(m°C); sand embankment with a density of 1400 kg/m^3, thermal conductivity coefficient of 2.48 W/(m°C), layer thickness

of 400 mm; filling with foam glass gravel with a density of 140 kg/m^3, thermal conductivity coefficient of 0.085 W/(m°C), layer thickness of 250 mm (according to research data); asphalt concrete with a density of 2100 kg/m^3, thermal conductivity coefficient of 1.05 W/(m°C), two layers 50 mm thick [26–27].

Characteristics of the materials of the layers of the road structure without foam glass gravel backfill: peat soil with a density of 400 kg/m^3; thermal conductivity coefficient in a frozen state of 1.45 W/(m°C); sand embankment with a density of 1400 kg/m^3, thermal conductivity coefficient of 2.48 W/(m°C), layer thickness of 650 mm; asphalt concrete with a density of 2100 kg/m^3, thermal conductivity coefficient of 1.05 W/(m°C), two layers 50 mm thick.

In the calculations, the width of the roadbed is conventionally taken as 6.0 m.

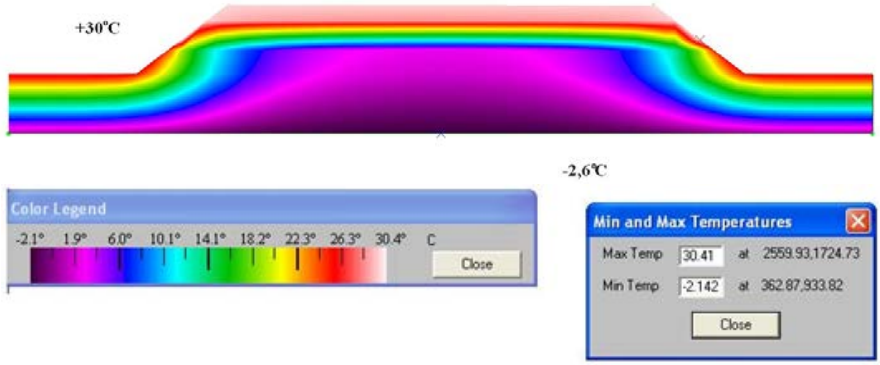


Figure 6. Temperature distribution in a road structure filled with foam glass gravel at an outside air temperature of +30 °C (permafrost, protection against thawing).

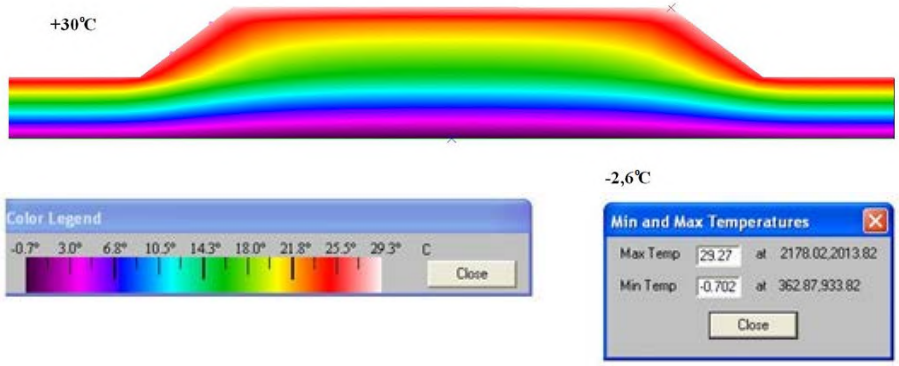


Figure 7. Temperature distribution in a road structure without foam glass gravel filling at an outside air temperature of +30 °C (permafrost, protection against thawing).

When assessing the insulation system using foam glass gravel for frost protection, the following boundary conditions were taken. Soil temperature is 4 °C; the temperature of the outside air in the calculation is taken: minus 30 °C.

Layers of the road structure filled with foam glass gravel: peat soil with a density of 400 kg/m^3; thermal conductivity coefficient of 1.39 W/(m°C); sand embankment with a density of 1400 kg/m^3, thermal conductivity coefficient of 2.48 W/(m°C), layer thickness of 400 mm; filling with foam glass gravel with a density of 140 kg/m^3, thermal conductivity coefficient of 0.085 W/(m°C), layer thickness of 250 mm (according to research data); asphalt concrete with a density of 2100 kg/m^3, thermal conductivity coefficient of 1.05 W/(m°C), two layers 50 mm thick.

Layers of the road structure without foam glass gravel filling: peat soil with a dry density of 400 kg/m^3; thermal conductivity coefficient of 1.39 W/(m°C); sand embankment with a density of 1400 kg/m^3, thermal conductivity coefficient of 2.48 W/(m°C), layer thickness of 650 mm; asphalt concrete with a density of 2100 kg/m^3, thermal conductivity coefficient of 1.05 W/(m°C), two layers 50 mm thick.

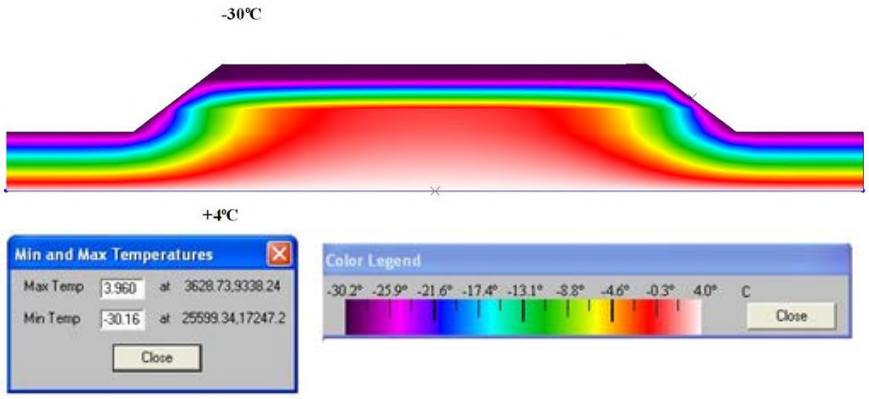


Figure 8. Temperature distribution in a road structure filled with foam glass gravel at an outside air temperature of minus 30 °C (heaving soil, frost protection).

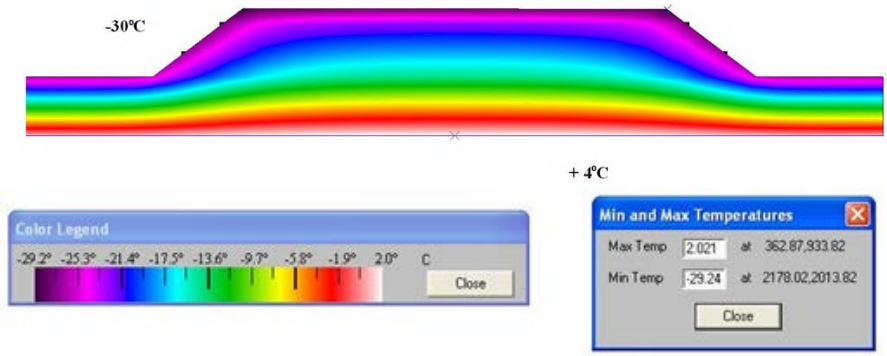


Figure 9. Temperature distribution in a road structure without foam glass gravel filling at an outside air temperature of minus 30 °C (heaving soil, frost protection).

The modeled distribution of temperature fields (Fig. 6, 7) shows that the filling with foam glass gravel allows keeping the permafrost soil from thawing while maintaining positive temperatures in the upper part of the embankment. On problematic bases (heaving sections of highways), in order to reduce the freezing depth to permissible norms and to exclude frost heaving processes in the soil of the embankment and natural base, thermal insulation layers are laid in the bases of pavements and under the ballast (Fig. 8, 9).

Preliminary calculations of the distribution of temperature fields at the base of a conditional road structure on permafrost soils with an insulating layer of foam glass gravel have been carried out. Calculations of real structures must be carried out taking into account the conditions of the construction and climatic zone of construction according to Russian Construction Norms SP131.13330.2012.

Modeling and calculation of temperature fields using the THERM program for structures of various types made it possible to simulate their freezing regime. Freezing simulations on models showed that the freezing depth in a road structure with an insulation layer of coarse sand with thickness of 0.3 m is 2.6 m. The use in a similar road construction with a thermal insulation layer of foam glass gravel with thickness of 0.25 m allows to limit the frost depth to 0.2 m.

Analysis of the use of road structures with thermal insulation from foam glass gravel and the results of modeling thermal fields in insulation systems showed that the construction of road bases with such thermal insulation allows to obtain functionally realizable structures with high durability. This is especially true for the construction of a roadbed on problem soils – permafrost and heaving.

4. Conclusions

Foam glass gravel, which is confirmed by the results of the experiment, in terms of strength and thermophysical characteristics, fully meets the requirements for heat-insulating materials used in road systems when laying a roadway on problem soils. The strength of foam glass gravel, depending on its degree of compaction (from 10 to 50 %), is in the range of 0.90 ... 1.58 MPa, and the thermal conductivity coefficient is from 0.087 to 0.099 W/(m °C), water absorption of gravel by volume does not exceed 1.8 %, and sorption humidity (at a relative air humidity of 98 %) does not exceed 4.2 %.

Calculation of temperature fields using the THERM program in structures of various types made it possible to simulate their freezing regime. The efficiency of using foam glass gravel backfill is shown both for protection against soil freezing and for protection against thawing of permafrost soil. As a result of

calculations, it was found that the use of heat-insulating backfill of foam glass gravel with a thickness of 0.25 m makes it possible to protect the permafrost soil of the road base from thawing for the considered conditions of the first road-climatic zone. At the same time, the imitation of freezing on models (for the considered boundary conditions) showed that the use of a heat-insulating layer of foam glass gravel with a thickness of 0.25 m in the road structure makes it possible to limit the freezing depth to 0.2 m, versus 2.6 m without heat-insulating layer.

The experience of using road structures with thermal insulation from foam glass gravel has shown that the implementation of these systems makes it possible to obtain functionally realizable structures with high durability. This is especially true for the construction of the roadbed on problem soils.

References

1. Gudkov, P., Kagan, P., Pilipenko, A., Zhukova, E.Yu., Zinovieva, E.A., Ushakov, N.A. Usage of thermal isolation systems for low-rise buildings as a component of information models. E3S Web of Conferences. 2019. No. 97. 01039. DOI: 10.1051/e3sconf/20199701039
2. Medvedev, A., Bobrova, E., Poserenin, A., Zarmanyan, E. Evaluation of mineral fiber properties using x-ray fluorescence analysis and measurement of natural radioactivity. MATEC Web of Conferences. 2018. No. 170. 03018. DOI: 10.1051/matecconf/201817003018
3. Efimov, B., Isachenko, S., Kodzoev, M.-B., Dosanova, G., Bobrova, E. Dispersed reinforcement in concrete technology. E3S Web of Conferences. 2019. No. 110. 01032. DOI: 10.1051/e3sconf/201911001032
4. Kozlov, S., Efimov, B., Bobrova, E., Zinovieva, E., Zhukova, E. Optimization of foamed plastic technology. E3S Web of Conferences. 2019. No. 97. 06010. DOI: 10.1051/e3sconf/20199706010
5. Zhukov, A., Semenov, V., Gnip, I., Vaitkus, S. The investigation of expanded polystyrene creep behaviour. MATEC Web of Conferences. 2017. No. 117. 00184. DOI: 10.1051/matecconf/201711700184
6. Myrmin, V., Hackvart, F.M., Alekseev, K., Avanci, M.A., Winter, E., Marinho, G.P., Iarozinski, N.A., Catai, R.E. Construction materials wastes use to neutralize hazardous municipal water treatment sludge. Construction and Building Materials. 2019. No. 204. Pp. 800–808. DOI: 10.1016/j.conbuildmat.2019.01.182
7. Myrmin, V., Presotto, P., Alekseev, K., Avanci, M.F., Rolim, P.H.B., Petukhov, V., Taskin, A., Gidarakos, E., Valouma, A., Yu, G. Application hazardous serpentine rocks extraction wastes in composites with glass waste and clay-sand mix to produce environmentally clean construction materials. Construction and Building Materials. 2020. No. 234. 117319. DOI: 10.1016/j.conbuildmat.2019.117319
8. Shutov, A.I., Mosypanov, V.I., Volya, P.A. Penosteklo kak effektivnyy stroitel'nyy material [Foam glass as an effective building material]. Sovremennyye problemy stroitel'nogo materialovedeniya: Materialy III Mezhdunarodnoy nauchno-prakticheskoy konferentsii-shkoly-seminary molodykh uchenykh, aspirantov i doktorantov [Modern problems of building materials science: Proceedings of the III International Scientific and Practical Conference-School-Seminar for Young Scientists, Postgraduates and Doctoral Students] – Belgorod: Izd-vo BGTU, 2001. Pp. 130–133.
9. Ketov, A.A., Ketov, V.B., Puzanov, A.I., Puzanov, I.S., Rossomagina, A.S., Saulin, D.V. Stekloboy kak syr'ye dlya polucheniya teploizolyatsionnogo materiala [Cullet as a raw material for obtaining a heat-insulating material]. Ecology and industry of Russia. 2002. No. 8. Pp. 17–20.
10. Lotov, V.A., Krivenkova, E.V. Kinetika protsessa formirovaniya poristoy struktury penostekla [Kinetics of the formation of the porous structure of foam glass]. Glass and Ceramics. 2002. No. 3. Pp. 14–28.
11. Chernyak, Y.N. O fizicheskikh osnovakh protsessa vspuchivaniya legkoplavkikh glin i penostekla [On the physical basis of the process of expansion of fusible clays and foam glass]. Glass and Ceramics. 1958. No. 10. Pp. 25–28.
12. Bernardo, E., Albertini, F. Glass foams from dismantled cathode ray tubes. Ceramics International. 2006. 32 (6). Pp. 603–608. DOI: 10.1016/j.ceramint.2005.04.019
13. De Sousa, E., Rambo, C.R., Hotza, D., Oliveira, A.P.N.d., Fey, T., Greil, P. Microstructure and properties of LZSA glass-ceramic foams. Materials Science and Engineering A. 2008. 476(1-2). Pp. 89–97. DOI: 10.1016/j.msea.2007.05.098
14. Rantala, J., Leivo, V. Head, air, and moisture control in slab-on-ground structures. Journal of building physics. 2009. 32(4). Pp. 335–353. DOI: 10.1177/1744259108093919
15. Korotkov, E.A., Chetvertkova, Yu.N. Penostekol'nyy shcheben' – teploizolyatsionnyy material dlya dorozhnogo stroitel'stva v slozhnykh geokriologicheskikh usloviyakh [Foamed glass rubble is a heat-insulating material for road construction in difficult geocryological conditions]. Dorozhniki. 2018. 1(13). Pp. 56–71.
16. Funk, M. Hysteretic moisture properties of porous materials: Part 1: Thermodynamics. Journal of building physics. 2014. 38(1). Pp. 6–49. DOI: 10.1177/1744259113496367
17. Petukhov, R.V., Generalchik, N.I. Penosteklo [Foam glass]. Glass of the world. 2004. No. 6. Pp. 89–92.
18. Ivanov, K.S., Korotkov, E.A. Issledovaniye vozdeystviya sloya granulirovannoy penosteklokera-miki na temperaturnyy rezhim promerzayushchego grunt [Investigation of the effect of a layer of granulated foam glass-ceramic on the temperature regime of freezing soil]. Foundations and soil mechanics. 2017. No. 5. Pp. 32–37.
19. Pyataev, E., Medvedev, A., Poserenin, A., Burtseva, M., Mednikova, E., Mukhametzyanov, V. Theoretical principles of creation of cellular concrete with the use of secondary raw materials and dispersed reinforcement. MATEC Web of Conferences. 2018. No. 251. 01012. DOI: 10.1051/matecconf/201825101012
20. Dos Santos Gerson Henrique, Mendes Nathan. Combined head, air and moisture (HAM) transfer model for porous building materials. Journal of building physics. 2009. 32(3). Pp. 203–220. DOI: 10.1177/1744259108098340
21. Shutov, A.I., Mosypan, V.I., Volya, P.A. Nizkotemperaturnyy sposob proizvodstva penostekla [The low-temperature method for the production of foam glass]. Building materials and products. 2001. No. 4. 29 p.
22. Konig, J., Nemanic, V., Zumer, M., Petersen, R.R., Ostergaard, M.B., Yue, Y., Suvorov, D. Evaluation of the contributions to the effective thermal conductivity of an open-porous-type foamed glass. Construction and Building Materials. 2019. No. 214. Pp. 337–343. DOI: 10.1016/j.conbuildmat.2019.04.109

23. Lesovik, V.S., Bessonov, I.V., Bulgakov, B.I., Larsen, O.A., Puchka, O.V., Vaysera, S.S. Approach on Improving the Performance of Thermal Insulating and Acoustic Glass Composites. IOP Conference Series: Materials Science and Engineering. 2018. 463(4). 042030. DOI: 10.1088/1757-899X/463/4/042030
24. Vaysera, S.S., Puchka, O.V., Lesovik, V.S., Bessonov, I.V., Sergeyev, S.V. Effektivnyye aku-sticheskiye steklo kompozity [Effective acoustic glass composites]. Construction Materials. 2016. No. 6. Pp. 28–32. DOI: 10.31659/0585-430X-2016-738-6
25. Volkov, M.M., Mikheev, A.L., Konev, K.A. Spravochnik rabotnika gazovoj promyshlennosti [Handbook of the gas industry worker]. Moscow: Nedra, 1989. 144 p.
26. Fokin, K.F. Stroitel'naja teplotehnika ograzhdajushhih chastej zdanij [Construction heat engineering of enclosing parts of buildings]. Moscow: AVOK-PRESS, 2006. 256 p.
27. Ji, R., Zheng, Y., Zou, Z., Jin, X., Chen, Z., Wei, S., Zhang, M. Utilization of mineral wool waste and waste glass for synthesis of foam glass at low temperature. Construction and Building Materials. 2019. No. 215. Pp. 623–632. DOI: 10.1016/j.conbuildmat.2019.04.226

Contacts:

Vyacheslav Semenov, science-isa@yandex.ru
Igor Bessonov, ca2so42h2o@rambler.ru
Aleksey Zhukov, lj211@yandex.ru
Elizaveta Mednikova, lisamednikova97@gmail.com
Ilya Govryakov, govr190@mail.ru

Received 03.06.2020. Approved after reviewing 24.08.2021. Accepted 06.09.2021.



Magazine of Civil Engineering

ISSN 2712-8172

journal homepage: http://engstroy.spbstu.ru/

DOI: 10.34910/MCE.110.4

Finite element models based on the approximation of discontinuous stress fields

A.A. Lukashevich

St. Petersburg State University of Architecture and Civil Engineering, St. Petersburg, Russia

E-mail: aaluk@bk.ru

Keywords: finite element method, plane elasticity problem, discontinuous stress approximation, penalty function method, functional of additional energy, Reissner functional

Abstract. The paper develops the finite element method (FEM) in the form of the force method and in the mixed form for the calculation of structures. At present, the displacement-based finite element method is mainly used for engineering calculations. Stress-based and mixed finite element formulations are not so widely spread, but in some cases these formulations can be more effective in particular with respect to calculating stresses and also obtaining a two-sided estimate of the exact solution of the problem. The finite element models based on the approximation of discontinuous stress fields and the use of the penalty function method to satisfy the equilibrium equations are considered. It is shown that the continuity of both normal and tangential stresses only on the adjacent sides of the finite elements contributes to the expansion of the class of statically admissible stress fields. At the same time, the consistent approximation is provided, both of the main part of the functional of additional energy, and its penalty part. The necessary matrix relations for rectangular and triangular finite elements are obtained. The effectiveness of the developed models is illustrated by numerical studies. The calculation results were compared with the solution on the FEM in displacements, as well as with the results obtained using other schemes of approximating the stresses in the finite element. It is shown that the model of discontinuous stress approximations gives the bottom convergence of the solution, both in stresses and in displacements. At the same time, the accuracy on the stresses here is much higher than in the displacement-based FEM or when using conventional stress approximation schemes.

1. Introduction

One of the important steps in the design process of building structures and constructions is to improve the method of their calculation. This problem is very relevant, since it helps to give valid results, which ultimately reduces the efforts and costs in the construction process. Nowadays, the calculation of structures is carried out, as a rule, using the finite element method (FEM). Many fundamental works have been devoted to the development of the theoretical principles of the FEM and questions of its application in structural mechanics [1–3]. They consider the basic variational principles and the corresponding FEM formulations, on the basis of which the finite element models can be constructed to solve different problems.

There are three main forms of FEM, each form is an analogue of one of the three classical methods of structural mechanics of rod systems – the displacement method, the force method, and the mixed method. The most widely used engineering calculations method is the FEM in the displacement method form. The mathematical formulation of the problem here is based on the variational Lagrange principle, i.e., the minimum principle of the total potential energy of the system. The main unknowns in this case are the displacements of the nodal points of the discrete model of the structure. The stresses are secondary and can be calculated by numerically differentiating the displacements. The finite element method in displacements is widely used to solve geometrically and physically nonlinear problems [4–6], constructively

Lukashevich, A.A. Finite element models based on the approximation of discontinuous stress fields. Magazine of Civil Engineering. 2022. 110(2). Article No. 11004. DOI: 10.34910/MCE.110.4

© Lukashevich, A.A., 2022. Published by Peter the Great St. Petersburg Polytechnic University.

This work is licensed under a CC BY-NC 4.0

nonlinear problems with unilateral constraints [7–10], problems of stability and dynamics of structures [11–14].

The advantages and disadvantages of the displacement method are well known. The huge advantage of this FEM form is its complete formalization (and, accordingly, the ease of implementation to software), as well as good stability of the solution with guaranteed convergence to the lower boundary. However, the accuracy of stresses (forces) determination is much lower than the displacements, although it is stress values which are more important in the structural strength analysis. In this connection, special refinement algorithms are often used to calculate stresses, e.g. [15]. In addition, since the approximate solution in displacements corresponds to the lower boundary, the values of both displacements and stresses are underestimated relative to the exact values.

Attempts to overcome these shortcomings, based on the use of FEM schemes directly in stresses (forces) or in a mixed form, have been made repeatedly, but this problem is still far from complete and remains one of the most important problems of the finite element method application in structural mechanics.

Castiliano's minimum principle of additional energy and the related FEM schemes in the form of the force method, as well as the Reissner variational principle (mixed method), have not received such a wide application. This situation is caused by a number of circumstances, in particular, the need to satisfy the equilibrium equations in the force method or an increase in the number of unknowns in the mixed method. However, in some cases, these approaches can be more effective, especially with regard to the accuracy of calculating stresses. In addition, performing dual calculations based on the alternative forms of FEM allows, as a rule, to obtain a two-side estimate of the exact solution of the problem [1, 2].

The FEM schemes, in which the search of the solution is based on the approximation of stresses (forces) in the finite element region, were considered in [1, 2, 16–22]. In [19], the combination of principles of possible displacements and possible changes in the stress state is used to find the solution. The solution to the problems of the elasticity theory in stresses on the basis of the functional of additional energy is considered in [21, 22]. In this case, the principle of possible displacements and Lagrange multipliers are used to satisfy the equilibrium equations.

The main advantage of the FEM in the form of the force method is that the main unknowns here are stresses. And if there were no certain difficulties in implementing the force method [1, 3], the stress values could be obtained with the same degree of accuracy as the displacements in the FEM scheme of the same name. In addition, the use of Castiliano's principle gives the upper boundary of the approximate solution (i.e., the stresses are overestimated), which, in principle, is better for strength calculations than the underestimated estimate. On the other hand, solving the problem in stresses can supplement the usual calculation of FEM in displacements, including from the point of view of the two-sided estimation of the solution of the problem on energy. Nevertheless, there are no algorithms that are equally as simple and stable, with guaranteed convergence in an extensive class of problems, similar to the FEM in the form of the displacement method.

The variational formulation of the mixed method is based on the principle of the *stationarity* of various forms of the Reissner functional. Some variants of the FEM in a mixed formulation were considered in [2, 3, 23–31]. With this approach, displacements and stresses within each finite element are approximated simultaneously, therefore, there is no need to overestimate the requirements for the continuity of the desired functions and their derivatives. On the contrary, it is possible to set the necessary approximations, and since the mixed variational principles lead to a mixed form of relations between stresses and displacements for the finite element, more reliable solution can be obtained.

On the other hand, the Reissner functional is not convex; its surface at the point of stationary has a prominent saddle-like behavior. The system of resolving equations corresponding to the formulation of a mixed type is not a symmetric and positive definite. Therefore, the approximate solution obtained by the FEM in the mixed form is characterized by some imbalance in the fulfillment of the equilibrium conditions and the conditions for the compatibility of deformations and, when crushing the mesh, it can approach the exact solution both from below and above. These circumstances to some extent make the direct use of the Reissner functional in the FEM more difficult [1, 3].

This paper is devoted to the development of alternative forms of the FEM based on the force and mixed methods. It is proposed to use the approximation of discontinuous stress fields in the finite element region to construct a solution to the plane problem of the elasticity theory. Such an approach may have advantages in terms of more accurately fulfilling the equilibrium conditions, as well as in solving contact problems and some problems related to stress concentration.

2. Methods

Let us consider the following version of the FEM in the force method form, which allows us to efficiently solve a wide class of problems directly in stresses. It is based on the approximation of discontinuous stress fields and the use of the penalty method to satisfy equilibrium equations. The corresponding variational formulation for the plane problem of the elasticity theory has the form of a modified functional of additional energy [32, 33]:

$$\Pi(\sigma) = -\frac{1}{2}\int_{\Omega}\{\sigma\}^T[D]^{-1}\{\sigma\}d\Omega + \int_{S_u}\{u_s\}^T[L_s]^T\{\sigma\}dS + \alpha\int_{\Omega}\Big([A]^T\{\sigma\}+\{\rho\}\Big)^T\Big([A]^T\{\sigma\}+\{\rho\}\Big)d\Omega \quad (1)$$

under the additional condition at the region boundary: $[L_s]^T\{\sigma\} = \{g_s\} \in S_g$.

Here $\{\sigma\} = \{\sigma_x\ \sigma_y\ \tau_{xy}\}^T$ is the stress vector; $[D]$ is the stiffness coefficients matrix; $[A]$ is the differentiation operations matrix in the equilibrium equations; $[L_s]$ is the direction cosine matrix of the external normal to the boundary $S = S_g + S_u$ of the plane region Ω; $\{g_s\}$ is the surface force vector at the boundary S_g; $\{u_s\}$ is the vector of given displacements at the boundary S_u; $\{\rho\} = \{\rho_x\ \rho_y\}^T$ is the volumetric force vector.

When solving problems in stresses, the main restrictions on the smoothness of the desired functions are imposed by the equilibrium equations – it is necessary to ensure the existence of piecewise continuous derivatives of the stress components. Therefore, according to them, for the plane problem of the elasticity theory, the differentiability of the normal stresses σ_x is only on *x*, σ_y is only on *y*, and tangential stresses τ_{xy} is both on *x* and on *y* is required. Thus, normal stresses can undergo discontinuities at sites perpendicular to the element boundaries. In comparison with the continuous approximation, the use of such an assumption contributes to the expansion of the class of statically allowable stress fields, among which the solution is sought. This allows to minimize the additional energy functional to a greater extent – as a result, the solution of the problem is, on average, closer to the exact one. The use of discontinuous approximations leads to the need to apply a special class of finite elements. The location of the nodal points here should ensure that the conditions of discontinuity of normal stresses are satisfied.

Figure 1 shows one of the simplest elements of this kind, which is a rectangle, the four nodes at the vertices of which correspond to tangential stresses, two nodes on each of the sides correspond to normal stresses σ_x, two nodes on the upper and lower sides correspond to stresses σ_y.

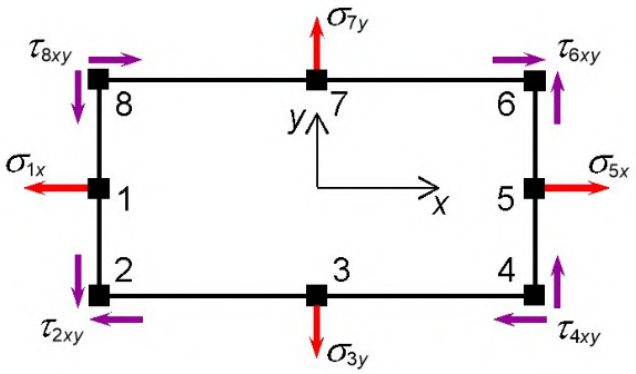


Figure 1. Eight-node finite element with discontinuous stress approximation.

Here the stress distribution is given by the following approximating polynomials:

$$\sigma_x = \alpha_1 + \alpha_2 x;\quad \sigma_y = \alpha_3 + \alpha_4 y;\quad \tau_{xy} = \alpha_5 + \alpha_6 x + \alpha_7 y + \alpha_8 xy. \quad (2)$$

Substituting the approximation data in the equilibrium equations, we obtain:

$$\alpha_2 + \alpha_7 + \alpha_8 x + \rho_x = 0;\quad \alpha_4 + \alpha_6 + \alpha_8 y + \rho_y = 0. \quad (3)$$

Obviously, for the constant volumetric element forces ρ_x, ρ_y the conditions (3) can be satisfied only if the following condition is identically satisfied:

$$\alpha_8 x = \alpha_8 y = 0. \tag{4}$$

Since this is not provided by the exact integration of the penalty term of functional in Eq. (1), a method for artificial lowering the accuracy of calculating the integrals was proposed for the reduced finite element, which facilitates the zeroing of the expression in the integral part of the penalty term [33]. Despite the fact that this finite element gives the acceptable accuracy and convergence of the results of solving problems in stresses, there are certain disadvantages. First, to calculate the coefficients of the deformability matrix related to the penalty term, it is necessary to apply the procedure of numerical integration. Secondly, for the main part of functional (1) and its penalty term, different stress approximations are used – for the penalty term, they are respectively of a lower order than for the main part of the functional. The model proposed here for approximating discontinuous stress fields for a finite element of a plane problem of the elasticity theory is free from these disadvantages.

Consider the above condition (4). For the finite element (Figure 1) and approximation (2) described above, exact execution of (4) is possible only when using the single-point integration scheme of the penalty term, i.e. when the integration order is lowered. However, locating nodes of the finite element on the *x, y* axes (Figure 2(a)), the condition (4) is reduced to the equality $\alpha_8 x = \alpha_8 y$.

Substituting this equality into approximation (2), we obtain the following variants of polynomials for τ_{xy}:

$$\tau_{xy} = \alpha_5 + \alpha_6 x + \alpha_7 y + \alpha_8 x^2; \quad \tau_{xy} = \alpha_5 + \alpha_6 x + \alpha_7 y + \alpha_8 y^2. \tag{5}$$

For each of the polynomials (5), we define the form functions for nodes and average them. Then the nodal stress vector for the finite element

$$\{\sigma\}^e = \{\sigma_{1x} \ \tau_{1xy} \ \sigma_{2y} \ \tau_{2xy} \ \sigma_{3x} \ \tau_{3xy} \ \sigma_{4y} \ \tau_{4xy}\}^T \tag{6}$$

the following form functions will be a respond:

$$N_{1,3x} = \frac{1}{2} \mp \frac{x}{2a}; \quad N_{1,3xy} = \frac{1}{4} \mp \frac{x}{2a} + \frac{x^2}{4a^2} - \frac{y^2}{4b^2}, \quad N_{2,4y} = \frac{1}{2} \mp \frac{y}{2b}; \quad N_{2,4xy} = \frac{1}{4} \mp \frac{y}{2b} - \frac{x^2}{4a^2} + \frac{y^2}{4b^2}. \tag{7}$$

The approximation of the tangential stresses within a given finite element, in particular, for the shape function N_{1xy}, is shown in Figure 2(b).

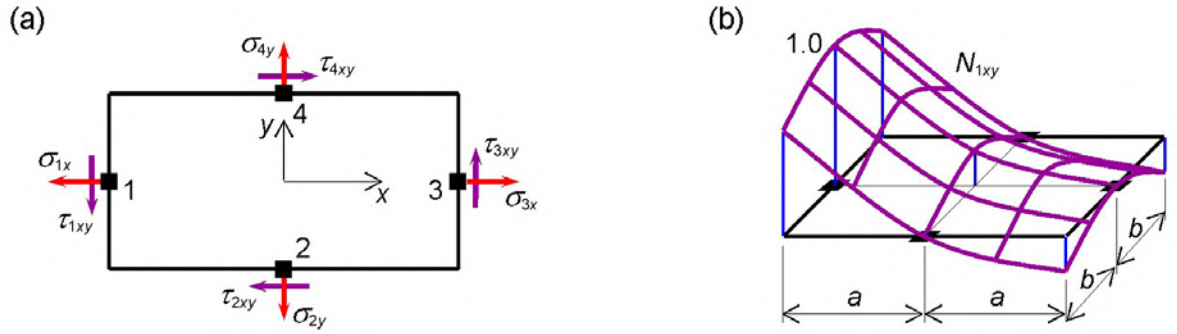


Figure 2. Four-node finite element with discontinuous stress approximation: (a) location of the nodes; (b) approximation of the tangential stresses.

Expressing the stresses using the form functions (7) through the nodal values (6) and substituting them into stationarity condition of the functional (1) for finite element, we obtain the matrix equation for the vector $\{\sigma\}^e$:

$$[K_\sigma]^e \{\sigma\}^e = \{U\}^e. \tag{8}$$

The deformability matrix of the finite element can be represented as the sum of two matrixes $[K_\sigma]^e = [K_0]^e + [K_\alpha]^e$. The first term $[K_0]^e = \int\limits_\Omega [N_\sigma]^T [D]^{-1} [N_\sigma] d\Omega$ corresponds the main part of the functional (1), the second $[K_\alpha]^e = -\alpha \int\limits_\Omega \left([A]^T [N_\sigma] \right)^T [A]^T [N_\sigma] \, d\Omega$ to its penalty part. The right part is the vector of given nodal displacements $\{U\}^e = \int\limits_{S_u} [N_\sigma]^T [L_s]^{-1} \{u_s\} dS + \alpha \int\limits_\Omega \left([A]^T [N_\sigma] \right)^T \{\rho\} \, d\Omega$.

$[N_\sigma] = \begin{bmatrix} N_{1x} & 0 & 0 & 0 & N_{3x} & 0 & 0 & 0 \\ 0 & 0 & N_{2y} & 0 & 0 & 0 & N_{4y} & 0 \\ 0 & N_{1xy} & 0 & N_{2xy} & 0 & N_{3xy} & 0 & N_{4xy} \end{bmatrix}$ is the matrix of form functions for stresses in finite element.

Perfoming the matrix operations and integrating the obtained expressions, we obtain:

$$[K_0]^e = \kappa \begin{bmatrix} 113\mu & 0 & 37\mu & 0 & -7\mu & 0 & 37\mu & 0 \\ 0 & 240 & 0 & -180\nu & 0 & 120 & 0 & -180\nu \\ 37\mu & 0 & 113\mu & 0 & 37\mu & 0 & -7\mu & 0 \\ 0 & -180\nu & 0 & 240 & 0 & -180\nu & 0 & 120 \\ -7\mu & 0 & 37\mu & 0 & 113\mu & 0 & 37\mu & 0 \\ 0 & 120 & 0 & -180\nu & 0 & 240 & 0 & -180\nu \\ 37\mu & 0 & -7\mu & 0 & 37\mu & 0 & 113\mu & 0 \\ 0 & -180\nu & 0 & 120 & 0 & -180\nu & 0 & 240 \end{bmatrix};$$

$$[K_\alpha]^e = \alpha \begin{bmatrix} 4m+n & 0 & -m-n & -1 & n-2m & 0 & -m-n & 1 \\ 0 & 3m & -1 & 0 & 0 & -3m & 1 & 0 \\ -m-n & -1 & m+4n & 0 & -m-n & 1 & m-2n & 0 \\ -1 & 0 & 0 & 3n & 1 & 0 & 0 & -3n \\ n-2m & 0 & -m-n & 1 & 4m+n & 0 & -m-n & -1 \\ 0 & -3m & 1 & 0 & 0 & 3m & -1 & 0 \\ -m-n & 1 & m-2n & 0 & -m-n & -1 & m+4n & 0 \\ 1 & 0 & 0 & -3n & -1 & 0 & 0 & 3n \end{bmatrix}.$$

Here: $\kappa = \frac{ab}{180E}$; $\mu = 2(1-\nu)$; $m = \frac{a}{3b}$; $n = \frac{b}{3a}$, where E, ν are the elastic modulus and Poisson's ratio; a, b are the size of the rectangular finite element.

The penalty parameter α has the physical meaning of the deformability coefficient of the weakest possible elastic base. Its value should be large enough and limited from above only by the accuracy of calculations. The recommendations for choosing the values α for different problems are given in [21, 32, 34]. As applied to the plane problem of the elasticity theory, $\alpha = (10^7 \div 10^9)\kappa$ can be accepted.

Similarly, the approximation of discontinuous stress fields can be applied to construct finite elements in stresses of other geometric shapes, as well as extended to finite elements of the mixed form. In particular, for a finite element in the form of a right triangle (Figure 3(a)), the stress distribution can be represented by the following polynomials:

$$\sigma_x = \alpha_1 + \alpha_2 x; \quad \sigma_y = \alpha_3 + \alpha_4 y; \quad \tau_{xy} = \alpha_5 + \alpha_6 x + \alpha_7 y. \tag{9}$$

It is clear that the fulfillment of the condition similar to (4) is not required here. The following form functions will respond to the vector of nodal stresses of a finite element $\{\sigma\}^e = \{\sigma_{1x}\ \tau_{1xy}\ \sigma_{2y}\ \tau_{2xy}\ \sigma_{3x}\ \sigma_{3y}\ \tau_{3xy}\}^T$:

$$N_{1x} = -\frac{x}{a};\ N_{1xy} = -\frac{x}{a};\ N_{2y} = -\frac{y}{b};\ N_{2xy} = -\frac{y}{b};\ N_{3x} = 1+\frac{x}{a}\ N_{3y} = 1+\frac{y}{b};\ N_{3xy} = 1+\frac{x}{a}+\frac{y}{b}. \quad (10)$$

We replace the nodal stress components $\sigma_{3y}, \sigma_{3x}, \tau_{3xy}$ with the tangent and normal components to the inclined face of the element σ_{3n}, τ_{3n} (Figure 3(b)). The nodal stress vector will then be $\{\sigma\}^e = \{\sigma_{1x}\ \tau_{1xy}\ \sigma_{2y}\ \tau_{2xy}\ \sigma_{3n}\ \tau_{3n}\}^T$.

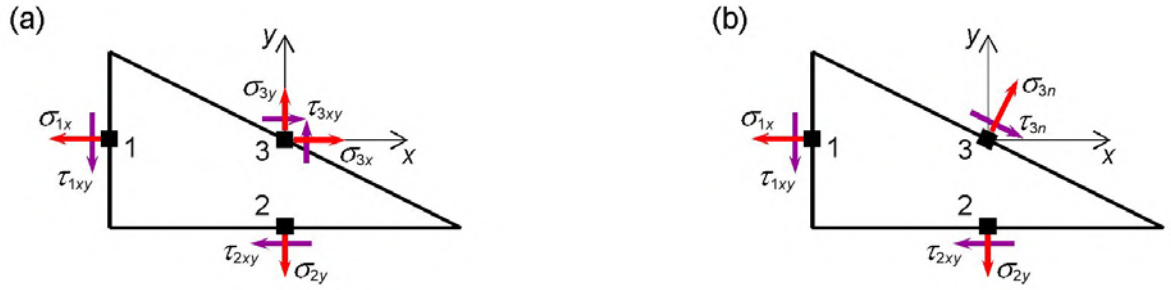


Figure 3. Triangular finite element with discontinuous stress approximation.

After substituting the form functions (10) and converting the stress components during turn of the axes, we obtain the following terms that make up the deformability matrix of a triangular finite element:

$$[K_0]^e = \kappa \begin{bmatrix} \lambda & 0 & 0 & 0 & 0 & 0 \\ 0 & 1 & vlm & -vl^2 & 0 & 0 \\ 0 & vlm & \lambda(l^2-m^2) & lm(2\lambda+2+v) & 0 & -lm(2+v) \\ 0 & -vl^2 & lm(2\lambda+2+v) & 2(m^2-vl^2) & 0 & -vm^2 \\ 0 & 0 & 0 & 0 & \lambda & 0 \\ 0 & 0 & -lm(2+v) & -vm^2 & 0 & 1 \end{bmatrix};$$

$$[K_\alpha]^e = \alpha \begin{bmatrix} \eta & 0 & lm-\eta\chi & -l^2-2\eta\cdot lm & 1 & -1 \\ 0 & \eta & -\eta\cdot lm-\chi & -2lm-\eta\cdot m^2 & 0 & 0 \\ lm-\eta\chi & -\eta\cdot lm-\chi & \chi\cdot\beta & \chi+\eta\cdot lm+\omega+2\beta\cdot lm & -lm-\mu\chi & \mu\cdot lm-\chi \\ -l^2-2\eta\cdot lm & -2lm-\eta\cdot m^2 & \chi+\eta\cdot lm+\omega+2\beta\cdot lm & \eta\cdot m^2+4lm & -m^2-2\mu\cdot lm & -2lm-\mu\cdot l^2 \\ 1 & 0 & -lm-\mu\chi & -m^2-2\mu\cdot lm & \mu & -\mu \\ -1 & 0 & \mu\cdot lm-\chi & -2lm-\mu\cdot l^2 & -\mu & \mu \end{bmatrix}.$$

Here: $\kappa = \frac{2ab}{3E};\ \lambda = 2(1+v);\ \eta = \frac{a}{b};\ \mu = \frac{b}{a};\ \beta = \eta+\mu;\ \chi = (l^2-m^2)$, where E, v are the elastic modulus and Poisson's ratio; a, b are the dimensions of the legs of the triangular finite element; l, m are cosine and sine to the normal of the inclined face.

Let us consider a mixed finite element model that allows to solve effectively the problems of the elasticity theory directly both in displacements and stresses. It is also based on the approximation of discontinuous stress fields and using the penalty method to satisfy equilibrium equations. The variational formulation of the mixed problem corresponds to the principle of stationarity of various forms of the Reissner functional, which directly includes the components of both displacements and stresses as well. As already indicated, this functional is not convex; its surface at the stationary point has a prominent saddle-like shape. This circumstance significantly complicates its use in the finite element method (the matrix of coefficients in this case is not symmetric and positive definite).

A convex mixed functional can be obtained by subtracting the Lagrange functional from the first form of the Reissner functional [33]:

$$\Pi(u,\sigma) = \Pi_{R_1}(u,\sigma) - \Pi_L(u) = \int_\Omega \{\sigma\}^T [A]\{u\}\, d\Omega - \frac{1}{2}\int_\Omega \{\sigma\}^T [D]^{-1}\{\sigma\}\, d\Omega - \\ - \frac{1}{2}\int_\Omega \left([A]\{u\}\right)^T [D][A]\{u\}\, d\Omega - \int_{S_u} \left(\{u\} - \{u_s\}\right)^T [L_s]^T \{\sigma\}\, dS. \tag{11}$$

under the additional conditions: $[A]^T\{\sigma\} + \{\rho\} = 0 \in \Omega$, $[L_s]^T\{\sigma\} = \{g_s\} \in S_g$.

The convexity of the functional (11) is obtained by moving the equilibrium conditions from natural (for the functional $\Pi_{R_1}(u,\sigma)$ to additional ones. We use the penalty method in order to satisfy these conditions:

$$\Pi(u,\sigma) = \int_\Omega \{\sigma\}^T [A]\{u\}\, d\Omega - \frac{1}{2}\int_\Omega \{\sigma\}^T [D]^{-1}\{\sigma\}\, d\Omega - \frac{1}{2}\int_\Omega \left([A]\{u\}\right)^T [D][A]\{u\}\, d\Omega + \\ + \alpha\int_\Omega \left([A]^T\{\sigma\} + \{\rho\}\right)^T \left([A]^T\{\sigma\} + \{\rho\}\right) d\Omega - \int_{S_u} \left(\{u\} - \{u_s\}\right)^T [L_s]^T \{\sigma\}\, dS. \tag{12}$$

with the additional condition $[L_s]^T\{\sigma\} = \{g_s\} \in S_g$.

It is easy to see that the reduced functional is equivalent to the variational statement of the problem in a least squares form. This circumstance provides the convexity condition for the functional (12), which makes it more convenient for applying the finite element method. Thus, setting an approximating expression for displacements $\{u\} = [N_u]\{u\}^e$ and, accordingly, for stresses $\{\sigma\} = [N_\sigma]\{\sigma\}^e$, and varying the functional (12) in a discrete form, we obtain the following matrix equilibrium equation for a finite element with a symmetric, positive definite coefficient matrix:

$$\begin{bmatrix} [K_u]^e & [K_{u\sigma}]^e \\ [K_{\sigma u}]^e & [K_\sigma]^e \end{bmatrix} \times \begin{Bmatrix} \{u\}^e \\ \{\sigma\}^e \end{Bmatrix} = \begin{Bmatrix} \{\overline{R}\}^e \\ \{\overline{U}\}^e \end{Bmatrix}, \tag{13}$$

where $[K_u]^e = \int_\Omega \left([A][N_u]\right)^T [D][A][N_u]\, d\Omega$ and $[K_\sigma]^e = \int_\Omega [N_\sigma]^T [D]^{-1}[N_\sigma]\, d\Omega - \\ - \alpha\int_\Omega \left([A]^T[N_\sigma]\right)^T [A]^T[N_\sigma]\, d\Omega$ are the stiffness and deformability matrixes, respectively; $[K_{u\sigma}]^e = -\int_\Omega \left([A][N_u]\right)^T [N_\sigma]\, d\Omega$ and $[K_{\sigma u}]^e = \left([K_{u\sigma}]^e\right)^T$ are the mixed matrixes; $[N_u]$, $[N_\sigma]$ are the form function matrixes for displacements and stresses, respectively; $\{u\}^e, \{\sigma\}^e$ are the vectors of nodal generalized displacements and stresses, respectively; $\{\overline{R}\}^e, \{\overline{U}\}^e$ are the vectors of generalized reactions and displacements in the nodes of the finite element, respectively.

The approximation of displacements within a finite element (Figure 4) can be similar to that usually used in the FEM in displacement method form. For stresses, however, it is more efficient to use the discontinuous approximations, such, as those discussed above, e.g. (2).

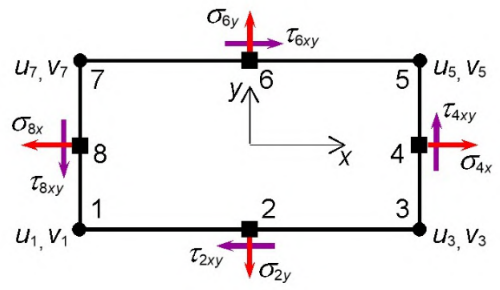


Figure 4. Eight-node finite element with discontinuous stress approximation.

The FEM solutions considered above using discontinuous stress approximations are implemented in a computer program. With its help, numerical studies and a comparative analysis of the finite element solutions based on the formulation of the displacement method, the force method, and the mixed method were performed.

3. Results and Discussion

Let us consider the problem of unilateral contact of a three-layer array with a rigid base (Figure 5). The upper and lower layers are concrete (elasticity modulus E_1 = 1.9·10⁴ MPa, ν = 0.18), the middle layer is brickwork (E_2 = 0.27·10⁴ MPa, ν = 0.16). Under the action of a distributed load applied at the left end of the calculated region, the zone of separation of the lower surface of the array from the rigid base is formed. The dimensions of the contact and separation zones are calculated using the standard iterative algorithm for unilateral constraints.

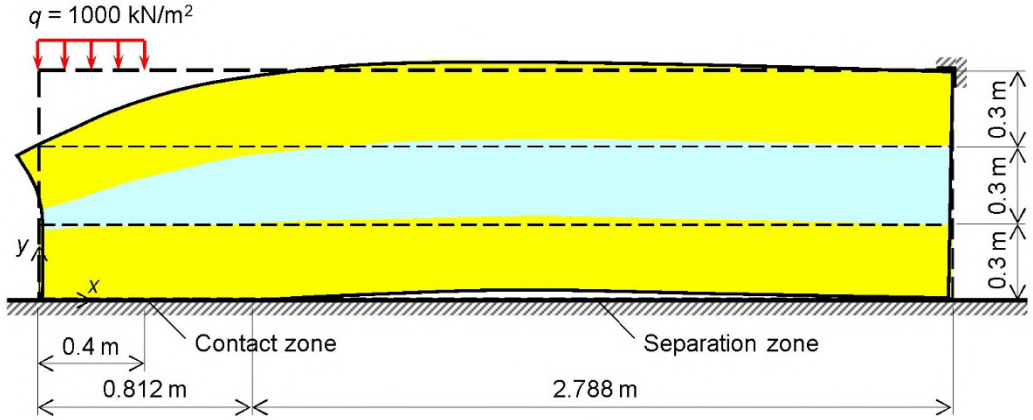


Figure 5. Unilateral contact of the three-layer array with the rigid base.

The solution of the problem based on discontinuous stress approximations was compared with the traditional FEM scheme in the displacement method form, as well as with the relatively accurate solution obtained with a sufficiently dense finite element mesh using the LIRA-SAPR software package [35]. Comparison of the proposed approach with the traditional FEM was carried out under the same discretization of the computational region, i.e. 18 × 6 elements.

The stresses σ_x along the vertical cross-section at a distance of 0.4 m from the left face of the array are compared in Figure 6(a) and the stresses σ_y along the lower face of the contact zone of the array with the rigid base are compared in Figure 6(b). The solid line shows the exact solution, the shaded circles – the FEM solution in the displacement method form, the not shaded circles – in the force method form.

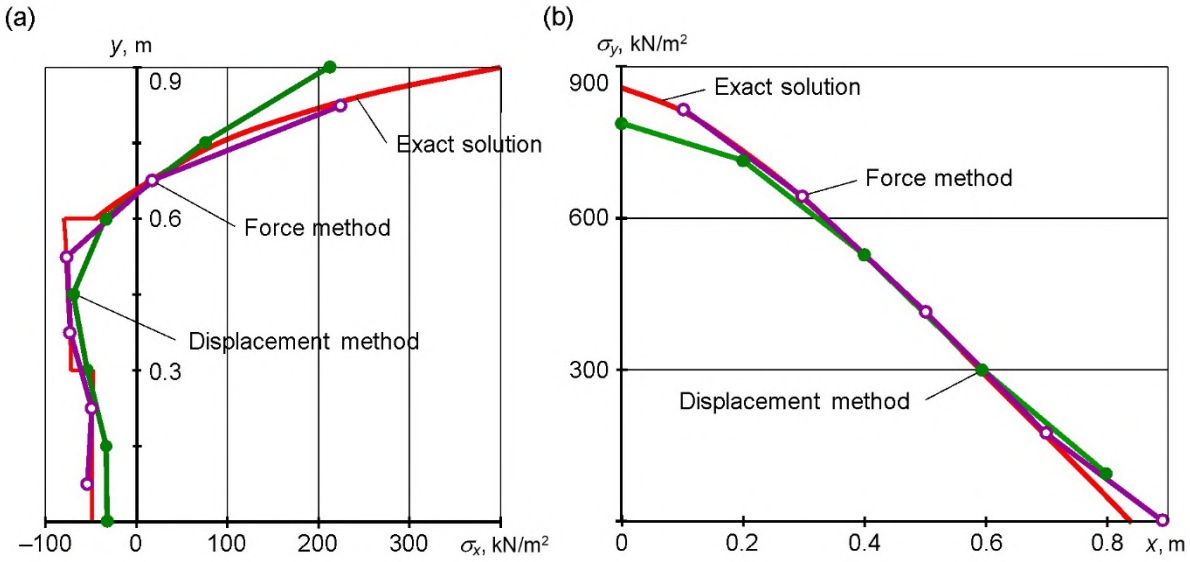


Figure 6. Stress distribution in characteristic sections of the three-layer array.

The graphs show that the stresses obtained by the FEM in the form of the force method are closer to the exact values, than the form of the displacement method gives. This is especially manifested at the region edges under consideration, as well as near the interfaces of different-modular materials.

In order to compare various forms of the finite element method, the problem of determining the stress-strain state of a cantilever plate was solved (Figure 7(a)). The Poisson's ratio was assumed to be 0.3, the remaining values: the elastic modulus E, the plate thickness h, and the load p were expressed in general form (in computer calculations they were set equal to one). Meshes of different densities were used, e.g. Figure 7(b) shows the 2×3 mesh when calculating the plate by the mixed method.

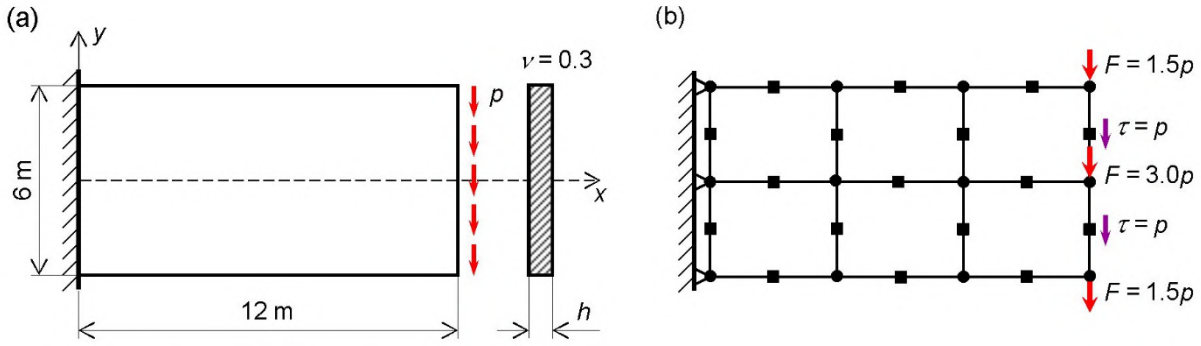


Figure 7. The problem of the cantilever plate.

The stresses and displacements obtained by the considered approaches were compared with the results of the FEM calculation in the displacement method form. Table 1 shows (in the terms of E, h, p) the vertical displacements υ of the middle of the free edge (x = 12 m, y = 0) and the stress σ_x at the upper point of the fixed edge of the plate (x = 0, y = 3 m) for different finite element meshes. The stresses at the extreme points here are obtained using linear interpolation.

Table 1. Comparison of the plate calculation results with different FEM forms.

Mesh	Displacement method			Force method		Mixed method		
	Number of unknowns	$\upsilon\left(\frac{p}{Eh}\right)$	$\sigma_x\left(\frac{p}{h}\right)$	Number of unknowns	$\sigma_x\left(\frac{p}{h}\right)$	Number of unknowns	$\upsilon\left(\frac{p}{Eh}\right)$	$\sigma_x\left(\frac{p}{h}\right)$
2×2	12	152.5	6.67	24	16.63	42	156.2	15.97
3×2	18	156.2	6.83	34	16.20	58	183.8	15.74
3×3	24	184.4	8.94	48	14.27	80	189.4	14.39
4×3	40	200.8	10.34	62	14.42	102	197.6	14.52
5×4	70	213.1	11.70	98	14.56	158	211.7	14.72
6×4	96	216.6	12.19	116	14.90	186	215.9	14.81
Exact solution		225.0	15.10		15.10		225.0	15.10

The calculation results for the given variants of the finite element meshes show the following. The FEM in the force method form provides a monotonic convergence of the solution in stresses to exact values from below. The stresses obtained by the mixed method approach the exact solution at first (for coarse meshes) from above, then (for fine meshes) also from below. Moreover, the use of discontinuous approximations of stress fields allows to achieve better convergence and accuracy of the solution in comparison with the displacement method with approximately the same order of the resolving equations system.

As it can be seen, on coarse meshes, the stresses obtained by the FEM in the force method form are significantly closer to the exact values than those obtained by the FEM in displacements. Under crushing the mesh (with the equivalent dimension of the problem), the accuracy of determining the stress by the force method and the mixed method also remains higher than by the displacement method. So, with the number of unknowns of the order of 100, the values of the stresses obtained by the force method differ from the exact values by 3.6 %, the mixed method by 3.8 %, and the displacement method by 19.3 %. In turn, for the identical meshes, the mixed FEM allows one to obtain stresses with the same accuracy as FEM in stresses, and displacements – as FEM in displacements.

Figure 8 illustrates the convergence of solutions obtained using various forms of the FEM. Obviously, according to the accuracy of calculating the stresses, the approaches considered here are more effective in comparison with the traditional FEM scheme in displacements.

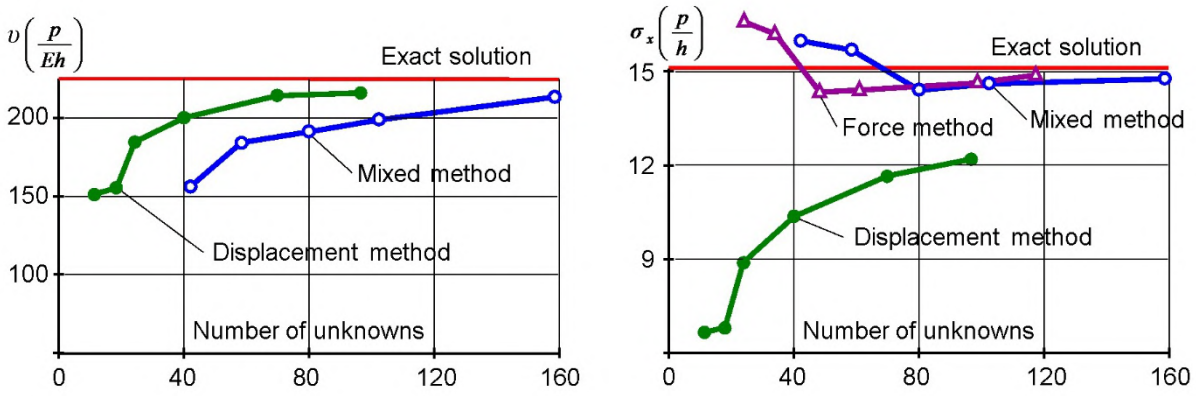


Figure 8. The convergence of solutions obtained by the different FEM forms.

The problem of bending a cantilever plate under the action of a vertical distributed load applied to its free end is presented below in Figure 9(a). The plate thickness is 1 m, the elastic modulus is 10000 kN/m^2, the Poisson's ratio is 0.25. This example was given in [21], where the application of the finite element models in stresses at constant and piecewise-constant approximations of stresses in the finite element region was considered. Below, we compare the solutions constructed on the basis of approximations of discontinuous stress fields with the results obtained in [21] using conventional schemes of stress approximation in the finite element.

Table 2 shows the stress values in the upper fibers of the section at the clamp (x = 0, y = 1 m), obtained using different stress approximation types in the finite element. The calculation results are presented for four variants of the finite element meshes. For comparison, the lower row of the table shows the stress values obtained by FEM in the LIRA-SAPR software package for a relatively dense mesh.

Table 2. Comparison of the plate calculation results for different types of stress approximation.

Mesh	Constant stresses			Piecewise constant stresses			Discontinuous stresses		
	σ_x, kN/m^2	σ_y, kN/m^2	τ_{xy}, kN/m^2	σ_x, kN/m^2	σ_y, kN/m^2	τ_{xy}, kN/m^2	σ_x, kN/m^2	σ_y, kN/m^2	τ_{xy}, kN/m^2
12×4	13.96	0.95	1.11	17.56	3.12	1.75	22.18	3.42	2.75
24×8	16.53	1.43	1.45	19.55	3.52	2.40	23.25	3.67	3.08
48×16	18.91	1.78	1.93	22.06	4.03	3.22	23.62	3.80	3.44
96×32	21.45	2.10	2.49	25.16	4.65	4.06	24.17	3.97	3.69
192×64 (LIRA-SAPR)	24.02	3.46	3.62	24.02	3.46	3.62	24.02	3.46	3.62

The Table shows that even on the coarse meshes, the stress values obtained on the basis of discontinuous approximations are more accurate compared to using the constant and piecewise constant stress approximations. So, for the mesh 12×4, the stress values σ_x differ upward from the constant and piecewise-constant stresses by 37 % and 21 %, respectively. The stresses σ_y and τ_{xy} in our case are also much more accurate than with ordinary schemes of approximations.

When the mesh is crushed, the model of discontinuous approximations gives a monotonous and stable convergence of stresses to the lower boundary. In this case, the numerical stress values are in the gap between the stress values obtained with the constant and piecewise-constant approximations. For example, for mesh 96×32, the stress σ_x is 11% higher than at constant stresses in the element, but 4 % less than for the piecewise-constant stresses variant. Figures 9(b–d) illustrate the convergence of solutions in stresses for different types of stress approximations.

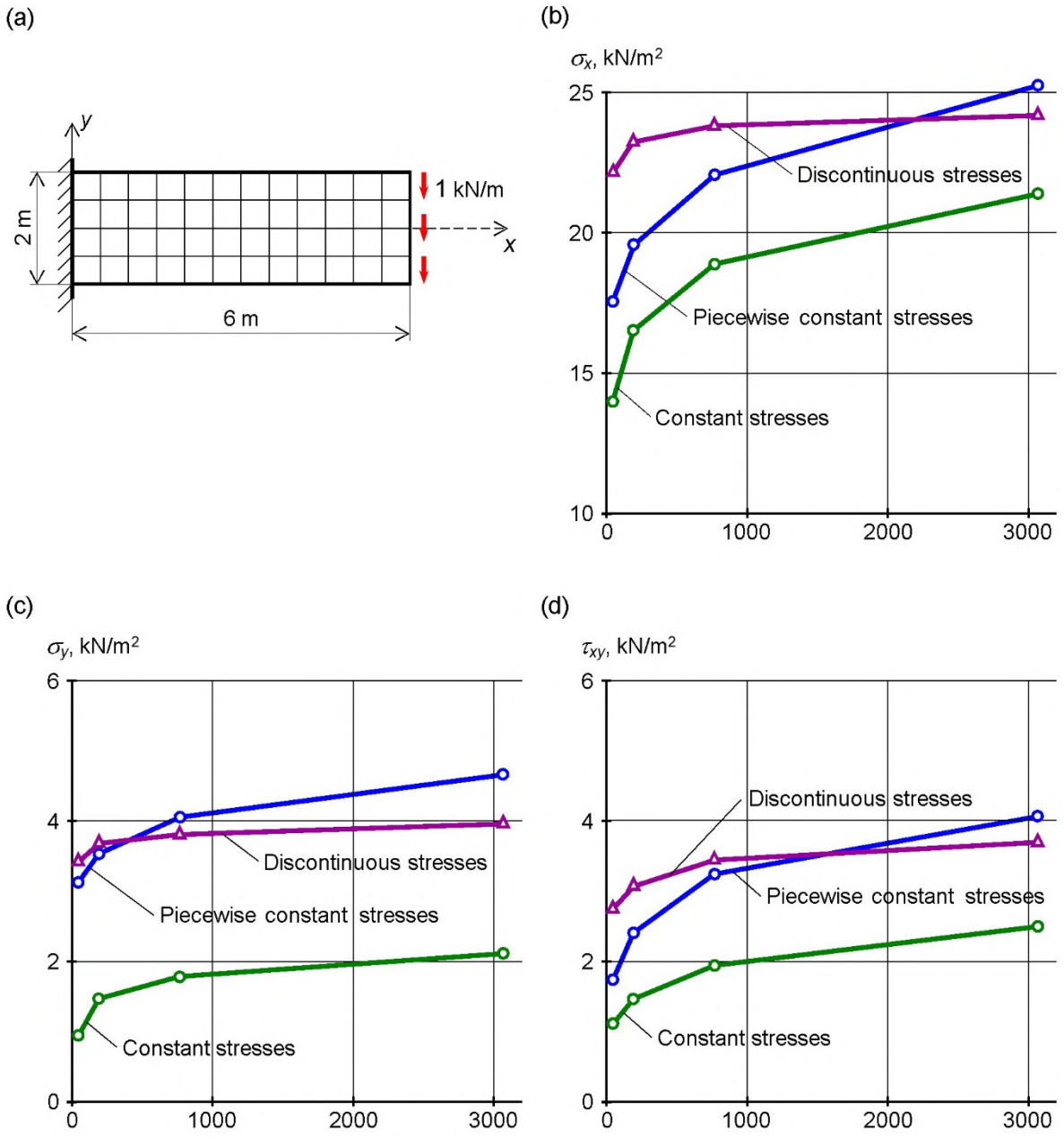


Figure 9. The convergence of solutions in stresses for different types of approximation.

4. Conclusions

Summarizing the results of numerical researches, we can draw the following conclusions:

1. The finite element method in the form of the force method in the general case gives the upper convergence of the solution in stresses. This allows us to obtain a two-sided estimate of the exact solution of the corresponding problem. At the same time, the finite-element solutions built on the stress approximation are much closer to exact values than those obtained in the displacement method formulation.

2. The use of discontinuous stress approximations contributes to the expansion of the class of statically admissible stress fields. In this case, the same approximation is provided for both the main part of the additional energy functional and its penalty part. This allows us to obtain more accurate stress values as compared to the continuous stress approximation.

3. The mixed finite-element models allow to obtain alternative solutions to the considered problems, thereby ensuring their greater validity and reliability. Under identical meshes, the mixed finite element method allows us to obtain stresses with the same accuracy as the FEM in stresses, and displacements – as the FEM in the displacement method form.

4. Discontinuous stress approximations give a fast and stable convergence of the resulting solution to the lower boundary. At the same time, the accuracy of the stress in this case is significantly higher than when using conventional stress approximation schemes, in particular, constant and piecewise constant approximations.

References

1. Gallagher, R.H. Finite element analysis: Fundamentals. Englewood Cliffs: Prentice-Hall, 1975. 416 p.
2. Zienkiewicz, O.C., Taylor, R.L., Zhu, J.Z. The Finite Element Method: Its Basis and Fundamentals. Butterworth-Heinemann, 2013. 756 p.
3. Bathe, K.J. Finite element procedures. Englewood Cliffs: Prentice-Hall, 2016. 1043 p.
4. Lalin, V.V., Rybakov, V.A., Morozov, S.A. The finite elements research for calculation of thin-walled bar systems. Magazine of Civil Engineering. 2012. No. 27(1). Pp. 53–73. (rus). DOI: 10.5862/MCE.27.7.
5. Paola, M., Scimemi, G. Finite element method on fractional visco-elastic frames. Computers & Structures. 2016. Vol. 164. Pp. 15–22. DOI: 10.1016/j.compstruc.2015.10.008.
6. Lukashevich, A.A., Lukashevich, N.K., Timohina, E.I. Modelling of contact interaction with allowance for nonlinear compliance in unilateral constraints. IOP Conference Series: Materials Science and Engineering. 2018. Vol. 463. 042054. DOI: 10.1088/1757-899X/463/4/042054.
7. Wriggers, P., Schroder, J., Schwarz, A. A finite element method for contact using a third medium. Computational Mechanics. 2013. 52(4). Pp. 837–847. DOI: 10.1007/s00466-013-0848-5.
8. Lukashevich, A.A. Computational solution of contact problems with unilateral constraints and friction by step-by-step analysis. Advanced Materials Research. 2014. Vol. 941–944. Pp. 2264–2267. DOI: 10.4028/www.scientific.net/AMR.941-944.2264.
9. Wriggers, P., Rust, W.T., Reddy, B.D. A virtual element method for contact. Computational Mechanics. 2016. 58(6). Pp. 1039–1050. DOI: 10.1007/s00466-016-1331-x.
10. Lukashevich, A.A. Computational modelling of stiffness and strength properties of the contact seam. Magazine of Civil Engineering. 2018. 81(5). Pp. 149–159. DOI: 10.18720/MCE.81.15.
11. Rybakov, V.A., Lalin, V.V., Ivanov, S.S., Azarov, A.A. Coordinate functions quadratic approximation in Slivker's semi-shear stability theory. Magazine of Civil Engineering. 2019. 89(5). Pp. 115–128. DOI: 10.18720/MCE.89.10.
12. Lukashevich, A.A. Modelling of contact interaction of structures with the base under dynamic loading. Magazine of Civil Engineering. 2019. 89(5). Pp. 167–178. DOI: 10.18720/MCE.89.14.
13. Alshurafa, S., Hanan, H., Polyzois, D. Finite element method for the static and dynamic analysis of FRP guyed tower. Journal of Computational Design and Engineering. 2019. Vol. 6. No. 3. Pp. 436–446. DOI: 10.1016/j.jcde.2018.08.004.
14. Lukashevich, A.A., Lukashevich, N.K. Numerical solution of contact problems with friction under dynamic loads. IOP Conference Series: Materials Science and Engineering. 2020. Vol. 753. 022058. DOI: 10.1088/1757-899X/753/2/022058.
15. Stein, E., Ahmad, R. An equilibrium method for stress calculation using finite element displacement models. Comput. Meth. Appl. Mech. And Eng. 1977. Vol. 10. 2. Pp. 175–198. DOI: 10.1016/0045-7825(77)90005-6.
16. Muller, B., Starke, G. Stress-based finite element methods in linear and nonlinear solid mechanics. Advanced Finite Element Technologies. 2016. Pp. 69–104. DOI: 10.1007/978-3-319-31925-4_4.
17. Kuss, F., Lebon, F. Stress based finite element methods for solving contact problems: comparisons between various solution methods. Advances in Engineering Software. 2009. Vol. 40. 8. Pp. 697–706. DOI: 10.1016/j.advengsoft.2008.11.013.
18. Kuo, Y.-L. Stress-based finite element analysis of sliding beams. Appl. Math. Inf. Sci. 2015. Vol. 9. 2. Pp. 609–616. DOI: 10.12785/amis/092L36.
19. Negrozov, O.A., Akimov, P.A. Combined application of finite element method and discrete-continual finite element method. AIP Conference Proceedings 1800. 2017. Vol. 1800. 040014. DOI: 10.1063/1.4973055.
20. Peng, Y., Bai, Y., Guo, Q. Analysis of plane frame structure using base force element method. Structural Engineering and Mechanics. 2017. 62(1). Pp. 11–20. DOI: 10.12989/sem.2017.62.1.011.
21. Tyukalov, Yu.Ya. Finite element models in stresses for plane elasticity problems. Magazine of Civil Engineering. 2018. 77(1). Pp. 23–37. DOI: 10.18720/MCE.77.3.
22. Tyukalov, Yu.Ya. Finite element models in stresses for bending plates. Magazine of Civil Engineering. 2018. 82(6). Pp. 170–190. DOI: 10.18720/MCE.82.16.
23. Wriggers, P., Carstensen, C. Mixed finite element technologies. Springer verlag GMBH. 2009. 206 p. DOI: 10.1007/978-3-211-99094-0.
24. Qiu, W., Demkowicz, L. Mixed hp-finite element method for linear elasticity with weakly imposed symmetry: stability analysis // SIAM J. Numer. Anal. (SIAM Journal on Numerical Analysis) 2011. Vol. 49. 2. Pp. 619–641. DOI: 10.1137/100797539.
25. Stupishin, L.U., Nikitin, K.E. Mixed finite element for geometrically nonlinear orthotropic shallow shells of revolution // Advanced Materials Research. 2014. Vol. 919–921. Pp. 1299–1302. DOI: 10.4028/www.scientific.net/AMR.919-921.1299.
26. Mu, L., Wang, J., Ye, X. A hybridized formulation for the weak Galerkin mixed finite element method // Journal of Computational and Applied Mathematics. 2016. Vol. 307. Pp. 335–345. DOI: 10.1016/j.cam.2016.01.004.
27. Kulikov, G.M., Plotnikova, S.V. A hybrid-mixed four-node quadrilateral plate element based on sampling surfaces method for 3D stress analysis // International journal for numerical methods in engineering. 2016. Vol. 108. 1. Pp. 26–54. DOI 10.1002/nme.5201.
28. Ignatyev, A.V., Ignatyev, V.A. On the efficiency of the finite element method in the form of the classical mixed method. Procedia Engineering. 2016. Vol. 150. Pp. 1760–1765. DOI: 10.1016/j.proeng.2016.07.167.
29. Ignatyev, A.V., Ignatyev, V.A., Gamzatova, E.A. Analysis of thin plates with excluding the displacements of the finite element as an absolutely rigid body by the fem in the form of a classical mixed method. Izvestiya vuzov. Stroitelstvo. 2018. 711(3). Pp. 5–13. (rus)
30. Gaur, H. A New Stress Based Approach for Nonlinear Finite Element Analysis. Journal of Applied and Computational Mechanics. 2019. Vol. 5. 3. Pp. 563–576. DOI: 10.22055/JACM.2019.29045.1548.

31. Lalin, V.V., Rybakov, V.A., Ivanov, S.S., Azarov, A.A. Mixed finite-element method in Slivker's semi-shear thin-walled bar theory. Magazine of Civil Engineering. 2019. 89(5). Pp. 79–93. DOI: 10.18720/MCE.89.7.
32. Zienkiewicz, O.C. Constrained variational principles and penalty function methods in finite element analysis. Conference on the Numerical Solution of Differential Equations. Lecture Notes in Mathematics, 1974. Vol. 363. Pp. 207–214. DOI: 10.1007/bfb0069138.
33. Lukashevich, A.A. Sovremennyye chislennyye metody stroitelnoy mekhaniki [Modern numerical methods of structural mechanics]. Izd-vo KhGTU. Khabarovsk, 2003. 135 p. (rus)
34. Taylor, R.L., Zienkiewicz, O.C. Complementary energy with penalty functions in finite element analysis. Energy methods in finite element analysis. Chichester: Wiley, 1979. Pp. 153–173.
35. Vodopyanov, R.Yu., Titok, V.P., Artamonova, A.E., Romashkina, M.A. LIRA-SAPR software package. User manual. Educational examples. Edited by Gorodetsky, A.S. Electronic edition, 2017. 535 p. https://www.liraland.ru/files/lira2017/format-pdf/.

Contacts:

Anatoliy Lukashevich, aaluk@bk.ru

Received 31.05.2020. Approved after reviewing 05.04.2021. Accepted 05.04.2021.



Magazine of Civil Engineering

ISSN 2712-8172

journal homepage: http://engstroy.spbstu.ru/

DOI: 10.34910/MCE.110.5

Quantitative bounded method of special long-period ground motions

***Y. Cheng*[a], *Y.-R. Dong*[a,b]*, *Y.-Y. Wang*[a], *L. Qin*[a], *Y.-X. Li*[a], *G.-L. Bai*[b]**

[a] *School of Civil Engineering and Architecture, Hubei University of Arts and Science, Xiangyang, China*

[b] *School of Civil Engineering, Xi'an University of Architecture and Technology, Xi'an, China*

**E-mail: yaorong099@163.com*

Keywords: long-period ground motions, baseline drifting, frequency content characteristics, acceleration magnification factor, quantitative boundary parameter

Abstract. The resonance effect of special long-period ground motions to (super) high-rise buildings is significant, which is likely to cause serious damage to these long-period structures. Therefore, the influence of long-period ground motions cannot be ignored in the seismic design of long-period structures. To provide theoretical basis and quantitative criteria for the selection and evaluation of long-period ground motion records, a quantitative bounded method based on the normalized acceleration spectra is proposed. Firstly, two types of long-period ground motions with reliable information are selected for this research, and the baseline drifting on acceleration, velocity and displacement time-history curve are corrected. Then, the Fourier amplitude spectrum and Power spectral density amplitude of special long-period ground motions are analyzed. Lastly, a quantitative boundary parameter to distinguish near-fault pulse-like (NFPL) and far-field harmonic (FFH) ground motions from common ground motions are discussed. Study results are obtained as follows: The frequency distribution of special long-period ground motions is relatively concentrated in low-frequency band, and the frequency distribution of common ground motions is relatively dispersed in medium-high-frequency band. Power spectral density amplitude and Fourier amplitude spectrum are the specific performance of energy distribution about earthquake records from the aspect of frequency domain, and they have no interrelation with structural seismic response under earthquake excitation. The specific earthquake records whose weighted average value of acceleration amplification factor is less than 0.2 are known as common ground motions. The specific earthquake records whose weighted average value is between in 0.2~0.6 are known as NFPL ground motions. The specific earthquake records whose weighted average value is beyond 0.6 are known as FFH ground motions. It would provide reference for the selection of long-period ground motions during seismic analysis of long-period such as super high-rise building structures.

1. Introduction

In the recorded strong earthquake data, there are two types of special earthquake records that are considered to be long-period ground motions. One is near-fault pulse-like (NFPL) ground motions, and the other is far-field harmonic (FFH) ground motions. Studies have shown that these two types of special ground motions exhibit significant long-period (low-frequency) properties, so they can be called long-period ground motions [1–5]. Nowadays, with the rapid development of economic construction, long-period such as (super) high-rise structures have been widely built in major cities. Multiple earthquake damages indicate that long-period ground motions have a magnifying effect on long-period structures, and they are prone to severe destroy to long-period structures [6–12].

Cheng, Y., Dong, Y.-R., Wang, Y.-Y., Qin, L., Li, Y.-X., Bai, G.-L. Quantitative bounded method of special long-period ground motions. Magazine of Civil Engineering. 2022. 110(2). Article No. 11005. DOI: 10.34910/MCE.110.5

© Cheng, Y., Dong, Y.-R., Wang, Y.-Y., Qin, L., Li, Y.-X., Bai, G.-L., 2022. Published by Peter the Great St. Petersburg Polytechnic University.

This work is licensed under a CC BY-NC 4.0

Cheng et al. [13], who studied the basic characteristic parameters and influencing factors of long-period ground motion records, thought near-fault earthquake has high amplitude intensity and short strong-shock duration, and far-field earthquake has small peaks of acceleration, velocity, displacement time history and long strong-shock duration. Dong et al. [14], who analyzed the spectral characteristics and intensity indices for near-fault ground motions, suggested the peak ground velocity (PGV) index can be employed for medium-to-long period structures. Wang et al. [15] selected reasonable intensity indices as the input of structural seismic design under two types of long-period ground motions. Shih et al. [16] evaluated the relationship between groundwater and ground motions quantitatively in the frequency domain, and the spectral analysis becomes feasible to assess the effect of the groundwater level on the separation of FFH and NFPL movements. Zhao et al. [17] investigated the low-frequency characterizations of pulse-type ground motions through ground motion components instead of original records, and the ground motion components are obtained by a decomposed method based on multi-resolution analysis. Li et al. [18] proposed classification method for long period ground motions based on component decomposition with Hilbert-Huang transform. Shao et al. [19] researched the method to definite the long-period ground motion based on EMD with elastic spectrum.

Data analysis on strong earthquake records is an important part of earthquake engineering, and it is also the research foundation of various seismic engineering topics. At present, there are a small amount of research results on how to judge and select long-period ground motions, and they are mainly limited to qualitative analysis. However, response spectrum theory is an important tool to describe the relationship between earthquake excitation and structural response in the field of earthquake engineering and seismic design [20–22]. Response spectra become the focus of structural dynamic analysis and seismic design because it can directly show the maximum response of single degree of freedom (SDOF) system under earthquake action [23]. Therefore, it is necessary to quantify the definition of common ground motions and two types of special long-period ground motions from the perspective of response spectra.

Firstly, typical 189 long-period and 26 common earthquake records with reliable information are selected from Pacific Earthquake Engineering Research Center (PEER) and National Research Institute for Earth Science and Disaster Resilience (NIED). The types of Polynomial Linear and High-pass Filtering Butterworth are employed to correct the baseline of original earthquake records. Then, the Fourier amplitude spectrum and Power spectral density amplitude of ground motions are analyzed from the aspect of frequency domain. On the basic of normalized acceleration spectra, the boundary parameter distinguishing long-period ground motions from common ground motions is defined, and a quantitative evaluation index is proposed by calculating and analyzing the boundary parameters about a large number of NFPL and FFH ground motions. The quantitative boundary parameter would provide theoretical basis and quantitative criteria for the selection and evaluation of long-period earthquake records during seismic response analysis for high-rise building structures.

2. Methods

2.1. Selection of long-period ground motion records

Based on the property of long-period ground motions and selection principle of seismic waves [24–26], the earthquake records whose frequency distribution of Fourier amplitude spectrum are almost within 0.1~1.0 Hz are considered as long-period ground motions. 89 NFPL and 100 FFH ground motion records are selected from PEER and NIED. To deeply study the characteristic of long-period ground motions, 26 common ground motions are selected for a comparative analysis. The criteria of US NEHRP classification is adopted to calculate the site category of selected ground motions, and all earthquake records are classified as different site classifications. Tables 1–3 demonstrate the basic information of NFPL, FFH and common ground motion records, respectively.

Table 1. Basic information of NFPL ground motion records.

station /component	M_w	rupture distance	site class	station /component	M_w	rupture distance	site class	station /component	M_w	rupture distance	site class
1085_SCE018	6.7	5.2	C	953_MUL009	6.7	17.1	D	TCU116-NS	7.6	12.38	C
1085_SCE288	6.7	5.2	C	953_MUL279	6.7	17.1	D	CHY035-EW	7.6	12.65	C
1084_SCS052	6.7	5.3	D	1016_NYA090	6.7	18.5	C	CHY035-NS	7.6	12.65	C
1084_SCS142	6.7	5.3	D	1016_NYA180	6.7	18.5	C	TCU104-EW	7.6	12.87	C
1086_SYL090	6.7	5.3	C	1012_LA0000	6.7	19.1	C	TCU104-NS	7.6	12.87	C

station /component	M_w	rupture distance	site class	station /component	M_w	rupture distance	site class	station /component	M_w	rupture distance	site class
1086_SYL360	6.7	5.3	C	1012_LA0090	6.7	19.1	C	TCU109-EW	7.6	13.06	C
1045_WPI046	6.7	5.5	D	TCU068-EW	7.6	0.32	C	TCU109-NS	7.6	13.06	C
1045_WPI316	6.7	5.5	D	TCU068-NS	7.6	0.32	C	TCU128-EW	7.6	13.13	C
1013_LDM064	6.7	5.9	C	TCU065-EW	7.6	0.57	D	TCU128-NS	7.6	13.13	C
1013_LDM334	6.7	5.9	C	TCU065-NS	7.6	0.57	D	TCU074-EW	7.6	13.46	C
1044_NWH090	6.7	5.9	D	TCU052-EW	7.6	0.66	C	TCU074-NS	7.6	13.46	C
1044_NWH360	6.7	5.9	D	TCU052-NS	7.6	0.66	C	TCU048-EW	7.6	13.53	C
1063_RRS228	6.7	6.5	D	TCU102-EW	7.6	1.49	C	TCU048-NS	7.6	13.53	C
1063_RRS318	6.7	6.5	D	TCU102-NS	7.6	1.49	C	CHY034-EW	7.6	14.82	C
1050_PAC175	6.7	7	A	CHY080-EW	7.6	2.69	C	CHY034-NS	7.6	14.82	C
1050_PAC265	6.7	7	A	CHY080-NS	7.6	2.69	C	TCU123-EW	7.6	14.91	D
1052_PKC090	6.7	7.6	C	TCU103-EW	7.6	6.08	C	TCU123-NS	7.6	14.91	D
1052_PKC360	6.7	7.6	C	TCU087-NS	7.6	6.98	C	TCU107-EW	7.6	15.99	C
949_ARL090	6.7	8.7	D	TCU120-EW	7.6	7.4	C	TCU107-NS	7.6	15.99	C
949_ARL360	6.7	8.7	D	TCU136-EW	7.6	8.27	C	TCU064-EW	7.6	16.59	C
1082_RO3000	6.7	10.1	D	TCU136-NS	7.6	8.27	C	TCU064-NS	7.6	16.59	C
1082_RO3090	6.7	10.1	D	CHY006-EW	7.6	9.76	C	CHY104-EW	7.6	18.02	D
960_LOS000	6.7	12.4	D	CHY006-NS	7.6	9.76	C	CHY104-NS	7.6	18.02	D
960_LOS270	6.7	12.4	D	TCU138-NS	7.6	9.78	C	CHY025-EW	7.6	19.07	D
1083_GLE170	6.7	13.3	C	TCU063-EW	7.6	9.78	C	CHY025-NS	7.6	19.07	D
1083_GLE260	6.7	13.3	C	TCU063-NS	7.6	9.78	C	TCU036-EW	7.6	19.83	C
1080_KAT000	6.7	13.4	C	CHY029-EW	7.6	10.96	C	TCU036-NS	7.6	19.83	C
1080_KAT090	6.7	13.4	C	CHY029-NS	7.6	10.96	C	TCU039-EW	7.6	19.89	C
1087_TAR090	6.7	15.6	D	TCU100-NS	7.6	11.37	C	TCU039-NS	7.6	19.89	C
1087_TAR360	6.7	15.6	D	TCU116-EW	7.6	12.38	C				

Table 2. Basic information of FFH ground motion records.

station /component	M_w	epicenter distance	site class	station /component	M_w	epicenter distance	site class	station /component	M_w	epicenter distance	site class
EHMH07-EW2	7.3	203	D	NGN024-EW	7.3	721	D	YMT002-EW	9.0	236	D
EHMH07-NS2	7.3	203	D	NGN024-NS	7.3	721	D	YMT002-NS	9.0	236	D
EHM016-EW	7.3	213	D	IUBH03-EW	8.0	206	E	YMTH12-EW2	9.0	256	C
EHM016-NS	7.3	213	D	IUBH03-NS	8.0	206	E	YMTH12-NS2	9.0	256	C
SMNH09-EW2	7.3	233	C	HKD130-EW	8.0	241	C	FKSH03-EW2	9.0	279	D
SMNH09-NS2	7.3	233	C	HKD130-NS	8.0	241	C	FKSH03-NS2	9.0	279	D
EHMH04-EW2	7.3	249	D	ABSH04-EW2	8.0	280	C	NIG009-EW	9.0	310	E

station /component	M_w	epicenter distance	site class	station /component	M_w	epicenter distance	site class	station /component	M_w	epicenter distance	site class
EHMH04-NS2	7.3	249	D	ABSH04-NS2	8.0	280	C	NIG009-NS	9.0	310	E
HRS004-EW	7.3	260	C	HKD151-EW	8.0	318	D	AOMH10-EW2	9.0	336	D
HRS004-NS	7.3	260	C	HKD151-NS	8.0	318	D	AOMH10-NS2	9.0	336	D
KOCH13-EW2	7.3	285	C	AOM018-EW	8.0	343	C	AOM019-EW	9.0	366	E
KOCH13-NS2	7.3	285	C	AOM018-NS	8.0	343	C	AOM019-NS	9.0	366	E
OKYH06-EW2	7.3	333	C	HKD025-EW	8.0	374	D	CHBH20-EW2	9.0	416	A
OKYH06-NS2	7.3	333	C	HKD025-NS	8.0	374	D	CHBH20-NS2	9.0	416	A
TKS005-EW	7.3	360	D	AKT013-EW	8.0	399	C	NIGH17-EW2	9.0	443	C
TKS005-NS	7.3	360	D	AKT013-NS	8.0	399	C	NIGH17-NS2	9.0	443	C
TTR006-EW	7.3	404	D	AKT018-EW	8.0	437	D	YMN010-EW	9.0	472	C
TTR006-NS	7.3	404	D	AKT018-NS	8.0	437	D	YMN010-NS	9.0	472	C
OSK010-EW	7.3	454	D	YMT001-EW	8.0	482	E	YMNH13-EW2	9.0	500	B
OSK010-NS	7.3	454	D	YMT001-NS	8.0	482	E	YMNH13-NS2	9.0	500	B
NAR007-EW	7.3	490	C	YMTH14-EW2	8.0	513	D	HKD102-EW	9.0	531	D
NAR007-NS	7.3	490	C	YMTH14-NS2	8.0	513	D	HKD102-NS	9.0	531	D
KYTH04-EW2	7.3	523	B	YMT015-EW	8.0	548	E	SZOH53-EW2	9.0	562	B
KYTH04-NS2	7.3	523	B	YMT015-NS	8.0	548	E	SZOH53-NS2	9.0	562	B
MIEH03-EW2	7.3	557	C	FKS020-EW	8.0	580	E	AIC005-EW	9.0	599	D
MIEH03-NS2	7.3	557	C	FKS020-NS	8.0	580	E	AIC005-NS	9.0	599	D
MIEH07-EW2	7.3	587	C	FKSH21-EW2	8.0	640	C	AIC003-EW	9.0	636	E
MIEH07-NS2	7.3	587	C	FKSH21-NS2	8.0	640	C	AIC003-NS	9.0	636	E
AIC001-EW	7.3	620	E	NIGH11-EW2	8.0	687	C	HKD030-EW	9.0	676	D
AIC001-NS	7.3	620	E	NIGH11-NS2	8.0	687	C	HKD030-NS	9.0	676	D
AIC015-EW	7.3	654	D	NGNH28-EW2	8.0	763	B	ABSH01-EW2	9.0	714	B
AIC015-NS	7.3	654	D	NGNH28-NS2	8.0	763	B	ABSH01-NS2	9.0	714	B
GIFH24-EW2	7.3	683	B	MYG005-EW	9.0	208	D				
GIFH24-NS2	7.3	683	B	MYG005-NS	9.0	208	D				

Table 3. Basic information of common ground motion records.

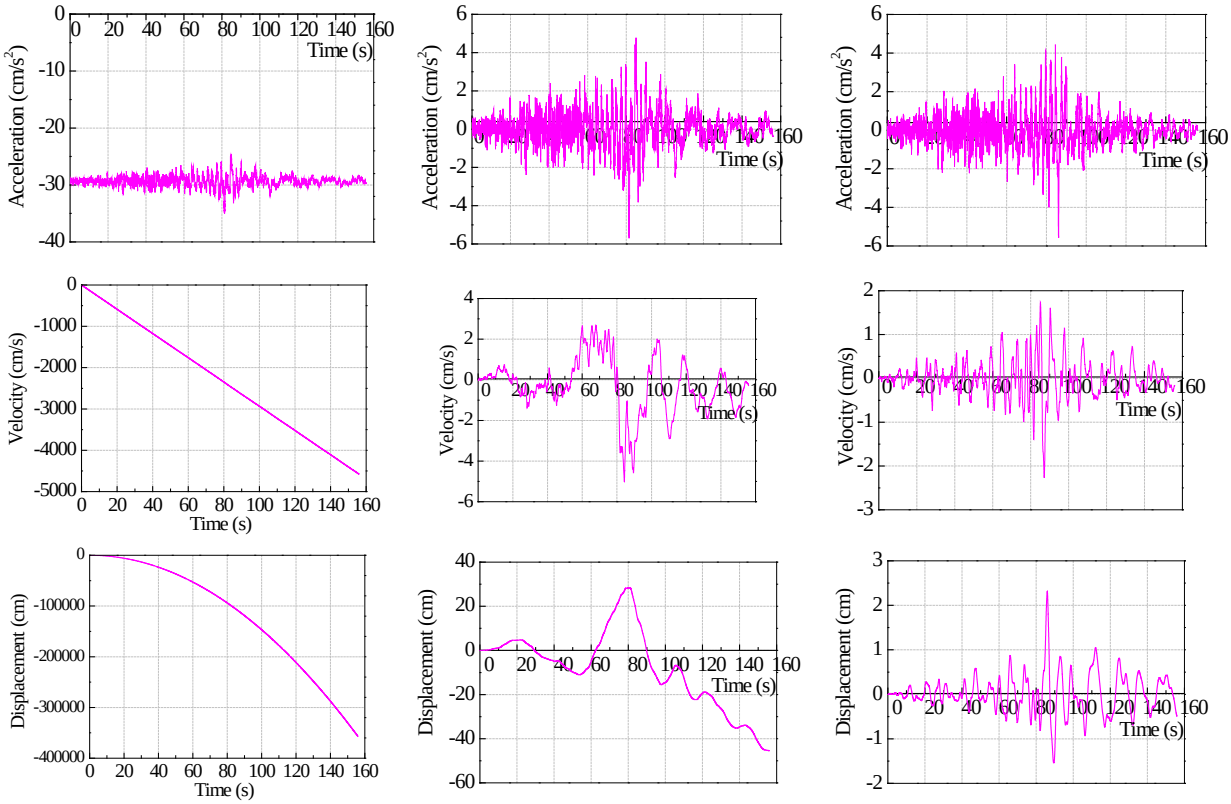
station /componen	M_w	rupture distanc	site clas	station /componen	M_w	rupture distanc	site clas	station /componen	M_w	rupture distanc	site clas
ELC000	5.0	34.98	D	TAF111	7.3	38.89	C	HCH090	6.9	27.6	D
ELC090	5.0	34.98	D	PAS180	7.3	125.59	C	HCH180	6.9	27.6	D
ELC180	6.5	6.09	D	PAS270	7.3	125.59	C	B-ICC000	6.5	18.2	D
ELC270	6.5	6.09	D	OSA000	6.9	21.35	D	B-ICC090	6.5	18.2	D
OKA000	6.9	86.94	C	OSA090	6.9	21.35	D	B-	6.5	13.03	D
OKA090	6.9	86.94	C	SHI000	6.9	19.15	D	B-	6.5	13.03	D
TAB-L1	7.3	2.05	B	SHI090	6.9	19.15	D	B-IVW090	6.5	23.85	E
TAB-T1	7.3	2.05	B	AGW000	6.9	24.57	D	B-IVW360	6.5	23.85	E
TAF021	7.3	38.89	C	AGW090	6.9	24.57	D				

2.2. Processing of long-period ground motion records

Earthquake records obtained from seismic stations not only contain ground vibration information purely caused by earthquake itself, but also much complex interference such as background noise and instrumental errors. And the long-period components of these interferences drift the baseline of time-history curve about earthquake records. This phenomenon of baseline drifting has no significant impact on

acceleration time-history (the error of acceleration peak is not beyond 3 %). However, the baseline drifting would be gradually accumulated with the numerical integration of acceleration and it eventually results in a great distortion of velocity and displacement time-history curve. To remove the influence on time-history curve by some non-seismic factors, the baseline of time-history curve about earthquake records should be corrected before they are used for further study.

Polynomial Linear is applied to adjust the baseline, and High-pass Filtering Butterworth is employed to correct the existed baseline drifting of original earthquake records. The low-frequency components of earthquake records are considered as much as possible to be retained during the filtering correction process. Taking as an example of a FFH ground motion record of AIC005-EW, Fig. 1a illustrates a time-history curve of original ground motions, Fig.1 b–c illustrate time-history curves after baseline adjustment and high-pass filter.



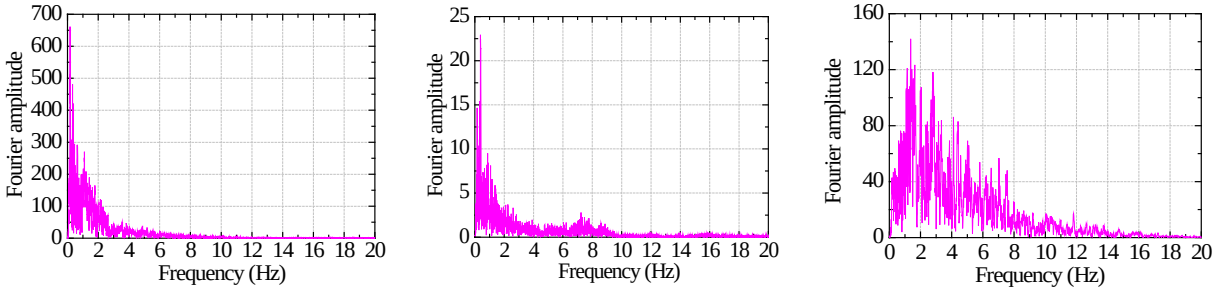
(a) original ground motion record **(b) after baseline adjustment** **(c) after high-pass filter**

Figure 1. Baseline correction of AIC005-EW.

2.3. Frequency content characteristics of long-period ground motions

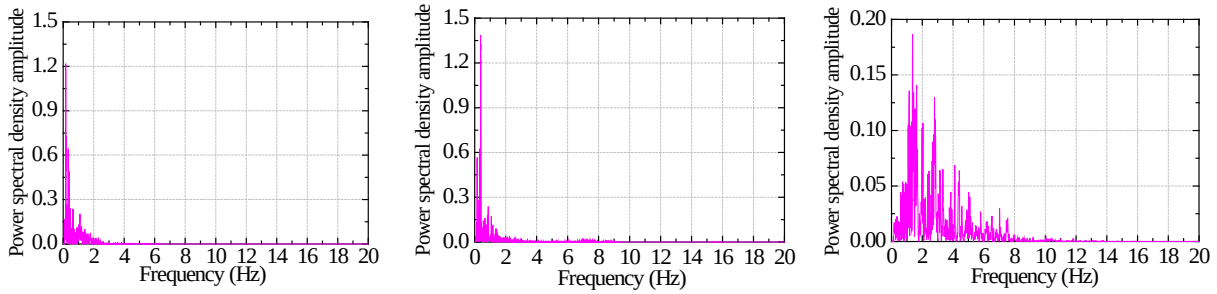
Some cases about structural seismic damage have been studied in recent years, and it is clear that the frequency content characteristic of ground motions has a significant impact on structural seismic response. If the predominant frequency of ground motions is within low-frequency band, it would cause a huge reaction on long-period structures. On the contrary, if the predominant frequency is within high-frequency band, it is more harmful to rigid structures. Therefore, the frequency characteristic is one of the most important aspects to reveal the basic property of ground motion records.

Fourier amplitude spectrum reflects the energy distribution of ground motions from the aspect of frequency domain, and it shows the energy carried by harmonic vibration at different frequency. Fourier amplitude spectrum, expressing what kinds of frequency components contained by ground motions, can clearly show amplitude content at each frequency component and maximum amplitude at a specific frequency component. Power spectral density amplitude, being defined as the mean square value of Fourier amplitude spectrum, is a physical quantity to describe stochastic process characteristic from the aspect of frequency domain. Power spectral density amplitude can also reflect the energy distribution of ground motion records along frequency axis.



(a) CHY104-EW **(b) AIC005-EW** **(c) TAF021**

Figure 2. Fourier amplitude spectrum.



(a) CHY104-EW **(b) AIC005-EW** **(c) TAF021**

Figure 3. Power spectral density amplitude.

Taking as examples of a NFPL ground motion of CHY104-EW, a FFH ground motion of AIC005-EW and a common ground motion of TAF021, Fig. 2–3 illustrate the Fourier amplitude spectrum and Power spectral density amplitude of ground motion records. The low-frequency components of CHY104-EW and AIC005-EW are very abundant. The energy distribution of CHY104-EW is mainly within 0.15~0.39 Hz, while the energy distribution of AIC005-EW is mainly within 0.15-0.42 Hz. It shows that the frequency distribution of long-period ground motion records is concentrated within relatively low-frequency band. The energy distribution of TAF021 is mainly within 1.07~2.84 Hz and it shows that the frequency distribution of common ground motions is concentrated within relatively high-frequency band. After a comparative analysis of Fig. 2 and Fig. 3, there is no essential difference between Power spectral density amplitude and Fourier amplitude spectrum, and both of them are the specific performance of energy distribution about earthquake records from the aspect of frequency domain. Power spectral density amplitude and Fourier amplitude spectrum are the physical properties of earthquake records themselves, and they have no interrelation with structural response under earthquake excitation.

2.4. Quantitative bounded method of long-period ground motions

Compared with common ground motions, long-period ground motions are characterized by abundant low-frequency components and long excellence period. In recent years, with the extensive study of long-period earthquakes, the definition about long-period ground motions is gradually developed from qualitative to semi-quantitative and quantitative. For example, the special earthquake records whose weighted average value of acceleration amplification factor within the period range of 2~10 s is larger than 0.4 can be bounded as the long-period ground motions [27], or the energy proportion of special earthquake records before 1 Hz can also be as the basis for defining long-period ground motions [28], and so on.

Fig. 4 demonstrates the comparison on normalized acceleration spectra (also known as magnification factor spectra) under three types of earthquake action. Acceleration amplitude is scaled to 1 cm/s^2 for calculating the normalized acceleration spectra of ground motions. Normalized acceleration spectra can eliminate the influence on the ordinate value of response spectra by earthquake intensity, and it also can reflect the response amplification of SDOF system under earthquake excitation. With reference to Fig. 4, it shows that the acceleration amplification factor of NFPL and FFH ground motions is larger than that of common ground motions in the period range of beyond 2 s. If the low-frequency components of earthquake records is much rich, it would bring more serious damage on long-period structures. Therefore, the boundary parameter combining the earthquake characteristic and structural seismic response could have a certain engineering significance.

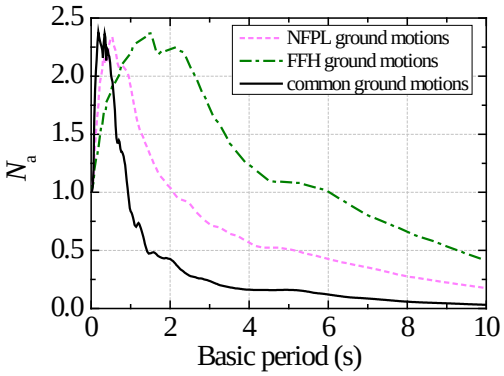


Figure 4. Normalized acceleration spectra.

According to equation (1), the weighted average value of acceleration amplification factor within the period range of 2~10s can be calculated.

$$\beta_l = \frac{\sum T_i^2 \left(\frac{S_a(T_i)}{PGA} \right)}{\sum T_i^2} \tag{1}$$

where, β_l is the weighted average value of spectra amplitude and the square of discrete period; T_i is the equidistant discrete period of acceleration response spectra with the damping ratio of 5 %, and T_i is within the period range of [2, 10]; $S_a(T_i)$ is the amplitude value of acceleration response spectra corresponding to T_i ; PGA is the peak of acceleration time history.

3. Results and Discussion

Table 4. Means, standard deviations and variation coefficients of weighted average value.

types of earthquake records	site class	weighted average value		
		mean	standard deviation	variation coefficient (%)
NFPL ground motions	C	0.388	0.0121	3.12
	D	0.325	0.0167	5.14
FFH ground motions	C	0.935	0.0223	2.39
	D	0.717	0.0356	4.97
	E	0.688	0.0274	3.98
common ground motions	C	0.077	0.0019	2.47
	D	0.051	0.0017	3.33

Table 4 demonstrates the means, standard deviations and variation coefficients about the weighted average value of acceleration amplification factor in various site classifications. The weighted average value under common ground motions is the smallest, NFPL ground motions is the second and FFH ground motions is the largest. On the whole, the means of the weighted average value under long-period ground motions are obviously larger than that under common ground motions. Therefore, the weighted average value can be considered as the quantitative bounded parameter to distinguish long-period ground motions from common ground motions. The variation coefficients in the D site classification is larger than that in the C site classification, which shows that the weighted average value in the D site classification is more discretized. Note that the statistical weighted average value of acceleration amplification factor in the same site classification would have a certain deviation. This is because the interaction between focal mechanism, earthquake magnitude, site-to-soil distance, propagation medium and path are not taken into account. At the same time, the calculated means are somewhat different when different strong-earthquake records are selected for statistical calculation. Therefore, the weighted average value of acceleration amplification factor can be determined based on the reliability requirements of structural seismic design in practical applications.

Table 5. Standard-deviation calculation of weighted average value.

types of earthquake records	site class	mean (μ)	standard deviation (σ)	μ-2σ	μ-σ	μ+σ	μ+2σ
NFPL ground motions	C	0.388	0.0121	0.3638	0.3759	0.4001	0.4122
	D	0.325	0.0167	0.2916	0.3083	0.3417	0.3584
FFH ground motions	C	0.935	0.0223	0.8904	0.9127	0.9573	0.9796
	D	0.717	0.0356	0.6458	0.6814	0.7526	0.7882
	E	0.688	0.0274	0.6332	0.6606	0.7154	0.7428
common ground motions	C	0.077	0.0019	0.0732	0.0751	0.0789	0.0808
	D	0.051	0.0017	0.0476	0.0493	0.0527	0.0544

Table 5 demonstrates the standard-deviation calculation of the weighted average value in various site classifications. The weighted average value of acceleration amplification factor from 2 s to 10 s can be regarded as a quantitative bounded parameter to distinguish long-period ground motions from common ground motions. According to the statistical results of 87 NFPL, 86 FFH and 24 common ground motion records, the specific earthquake records whose weighted average value of acceleration amplification factor is less than 0.2 with the dominant components of high-frequency and above are known as common ground motions. The specific earthquake records whose weighted average value is between in 0.2~0.6 with less high-frequency components and rich low-frequency components are known as NFPL ground motions. The specific earthquake records whose weighted average value is beyond 0.6 with the dominant components of low-frequency are known as FFH ground motions. Compared with NFPL ground motions, FFH ground motions have less high-frequency components. This is because that the high-frequency components are attenuated and low-frequency components are amplified by soft-soil site with the increase of propagation distance under FFH ground motions.

The Reference [26] drew a conclusion that, the ground motions are classified into long-period (β_l >0.4), moderate period (0.2 ≤ β_l ≤ 0.4) and short period (β_l < 0.2) ground motions[1]. Compared with these results, this study further divides long-period ground motions into NFPL and FFH ground motions. On this basis, the ground motions are classified into FFH (β_l > 0.6), NFPL (0.2 ≤ β_l ≤ 0.6) and common (β_l < 0.2) ground motions. This conclusion makes the classification of long-period ground motions more specific and close to the actual situation, and it also promotes the deep study of different mechanisms on structural damage caused by long-period ground motions.

The weighted average value of acceleration amplification factor from 2 s to 10 s is taken as a quantitative boundary parameter to distinguish NFPL and FFH ground motions from common ground motions, which would provide the theoretical basis and quantitative criteria for the selection and evaluation of long-period ground motion records during seismic response analysis for high-rise building structures.

4. Conclusion

Firstly, typical 189 long-period and 26 common ground motion records with reliable information are selected for this research. Then, the frequency content characteristics of long-period ground motion records are analyzed. Lastly, a quantitative boundary parameter to distinguish NFPL and FFH ground motions from common ground motions is proposed. The main conclusions are obtained as follows:

1. The frequency distribution of long-period ground motions is relatively concentrated in low-frequency band, and the frequency distribution of common ground motions is relatively dispersed in medium-high-frequency band. Power spectral density amplitude and Fourier amplitude spectrum are the specific performance of energy distribution about earthquake records from the aspect of frequency domain, and they have no interrelation with structural seismic response under earthquake excitation.

2. The specific earthquake records whose weighted average value of acceleration amplification factor is less than 0.2 are known as common ground motions. The specific earthquake records whose weighted average value is between in 0.2~0.6 are known as NFPL ground motions. The specific earthquake records whose weighted average value is beyond 0.6 are known as FFH ground motions.

[1] http://www.cq-vip.com/qk/92375x/201405/663002935.html

3. The high-frequency components of FFH ground motions is less than that of NFPL ground motions, because the high-frequency components are attenuated and low-frequency components are amplified by the soft-soil site under FFH ground motions. The quantitative boundary parameter would provide the theoretical basis and quantitative criteria for the selection and evaluation of long-period ground motion records during seismic response analysis for high-rise building structures.

5. Acknowledgments

The present work was supported by the Hubei Provincial Education Department's Science Research Program Funded Project (No. Q20212603) and Cultivation Special Project on National Natural Science Foundation of China (No. 2021kpgpzk01). These supports were greatly appreciated.

References

1. Takewaki, I., Fujita, K., Yoshitomi, S. Uncertainties in long-period ground motion and its impact on building structural design: case study of the 2011 Tohoku (Japan) earthquake. Engineering Structures. 2013. Vol. 49. Pp. 119–134. https://doi.org/10.1016/j.engstruct. 2012.10.038
2. Cheng, Y., Dong, Y.R., Bai, G.L., Qin, L., Xue, J.S., Li, Y.X. Study on standard response spectrum parameters of special long-period ground movements. Journal of Vibroengineering. 2021. Vol. 23. No. 1. Pp. 183–196. https://doi.org/10.21595/jve.2020.21618
3. Cheng, Y., Dong, Y.R., Qin, L., Wang, Y.Y., Li, Y.X. Seismic energy response of SDOF systems subjected to long-period ground motion records. Advances in Civil Engineering. 2021. Article ID 6655400, 20 pages. https://doi.org/10.1155/20-21/6655400
4. Yang, D.X., Pan, J.W., Li, G. Non-structure-specific intensity measure parameters and characteristic period of near-fault ground motions. Earthquake Engineering and Structural Dynamics. 2009. Vol. 38. No. 11. Pp. 1257–1280. https://doi.org/10.1002/eqe.889
5. Li, C.F., Zhang, Y., Zhao, J.B., Tang, H. Long-period ground motion characteristic of the 1999 Jiji (Chi-Chi), Taiwan, mainshock and aftershocks. Acta Seismologica Sinica. 2006. Vol. 19. No. 4. Pp. 448–460. https://doi.org/10.1007/s11589-004-0448-y
6. Takewaki, I., Murakami, S., Fujita, K., Yoshitomi, S., Tsuji, M. The 2011 off the Pacific coast of Tohoku earthquake and response of high-rise buildings under long-period ground motions. Soil Dynamics and Earthquake Engineering. 2011. Vol. 31. No. 11. Pp. 1511–1528. https:// doi.org/10.1016/j.soildyn.2011.06.001
7. Cheng, Y., Bai, G.L., Dong, Y.R. Spectrum characterization of two types of long-period ground motions and seismic behavior of frame-core wall structures under multidimensional earthquake records. The Structural Design of Tall and Special Buildings. 2018. Vol. 24. No. 16. Pp. e1539. https://doi.org/10.1002/tal.1539
8. Dong, Y.R., Xu, Z.D., Li, Q.Q., Zhu, C., He, Z.H. Design parameters and material-scale damage evolution of seismic upgraded RC frames by viscoelastic haunch bracing-dampers. Earthquake Engineering and Structural Dynamics. 2020. Pp. 1–16. https://doi.org/10.1002/ eqe.3406
9. Cheng, Y., Dong, Y.R., Bai, G.L., Wang, Y.Y. IDA-based seismic fragility of high-rise frame-core tube structure subjected to multi-dimensional long-period ground motions. Journal of Building Engineering. 2021. No. 43. Pp. 102917. https://doi.org/10.1016/j.jobe. 2021.102917
10. Chung, Y.L., Nagae, T., Hitaka, T., Nakashima, M. Seismic resistance capacity of high-rise buildings subjected to long-period ground motions: E-Defense shaking table test. Journal of Structural Engineering. 2010. Vol. 136. No. 6. Pp. 637–644. https://doi.org/10.1061/ (ASCE) ST. 943-541X.0000161
11. Ariga, T., Kanno, Y., Takewaki, I. Resonant behaviour of base-isolated high-rise buildings under long-period ground motions. The Structural Design of Tall and Special Buildings. 2006. Vol. 15. No. 3. Pp. 325–338. https://doi.org/10.1002/tal.298
12. Chen, Q.J., Yuan, W.Z., Li, Y.C., Cao, L.Y. Dynamic response characteristics of super high-rise buildings subjected to long-period ground motions. Journal of Central South University. 2013. Vol. 20. No. 5. Pp. 1341–1353. https://doi.org/10.1007/s11-771-013-1621-9
13. Cheng, Y., Bai, G.L. Basic characteristic parameters and influencing factors of long-period ground motion records. Journal of Vibroengineering. 2017. Vol. 19. No. 7. Pp. 5191–5207. https://doi.org/10.21595/jve.2017.18006
14. Dong, Y.R. Cheng, Y., Bai, G.L. Analysis of spectral characteristics and intensity indices for near-fault ground motions. Industrial Construction. 2015. Vol. 45. No. 7. Pp. 102–107. (Chinese). https://doi.org/10.13204/j.gyjz201507021
15. Wang, S.Z., Bai, G.L., Cheng, Y. Correlation analysis between long-period ground motion intensity indices and residual deformation of SDOF system. World Earthquake Engineering. 2018. Vol. 34. No. 1. Pp. 105–112. (Chinese)
16. Shih, D.C., Wu, Y.M., Chang, C.H. Significant coherence for groundwater and Rayleigh waves: Evidence in spectral response of groundwater level in Taiwan using 2011 Tohoku earthquake, Japan. Journal of Hydrology. 2013. No. 486. Pp. 57–70. http://dx.doi.org /10.1016/j.jhydrol.2013.01.013
17. Zhao, G.C., Xu, L., Xie, L. Study on low-frequency characterizations of pulse-type ground motions through multi-resolution analysis. Journal of Earthquake Engineering. 2016. Vol. 20. No. 6. Pp. 1011–1033. https://doi.org/10.1080/13632469.2015.1104761
18. Li, Y.M., Zhao, C.X., Tan, Q. Classification method for long period ground motions based on component decomposition with HHT. Journal of Vibration and Shock. 2018. Vol. 37. No. 7. Pp. 164–171+ 219. (Chinese)
19. Shao, Y.F, Bai, G.L., Jiang, L. Based on the EMD with the ground motion elastic spectrum to research the method to definite the long-period ground motion. World Earthquake Engineering. 2017. Vol. 33. No. 3. Pp. 95–104. (Chinese)
20. Kiureghian, A.D., Neuenhofer, A. Response spectrum method for multi-support seismic excitations. Earthquake Engineering and Structural Dynamics. 1992. Vol. 21. No. 8. Pp. 713–740. https://doi.org/10.1002/eqe.4290210805
21. Chopra, A.K., Goel, R.K. Capacity-demand-diagram methods based on inelastic design spectrum. Earthquake Spectra. 1999. Vol. 15. No. 4. Pp. 637–656.
22. Dong, Y.R., Xu, Z.D., Guo, Y.Q., Xu, Y.S., Chen, S., Li, Q.Q. Experimental study on viscoelastic dampers for structural seismic response control using a user-programmable hybrid simulation platform. Engineering Structures. 2020. No. 216. Pp. 110710. https:// doi.org/10.1016/j.engstruct.2020.110710

23. Chopra, A.K. Elastic response spectrum: A historical note. Earthquake Engineering and Structural Dynamics. 2007. Vol. 36. No. 1. Pp. 3–12. https://doi.org/10.1002/eqe.609
24. Tso, W.K., Zhu, T.J., Heidebrecht A.C. Engineering implication of ground motion A/V ratio. Soil Dynamics and Earthquake Engineering. 1992. Vol. 11. No. 3. Pp. 133–144. https:// doi.org /10.1016/0267-7261(92)90027-B
25. Fajfar, P., Vidic, T. Consistent inelastic design spectra: hysteretic and input energy. Earthquake Engineering and Structural Dynamics. 1994. Vol. 23. No. 5. Pp. 523–537. https:// doi.org/10.1002/eqe.4290230505
26. Loh, C.H., Wan, S., Liao W.I. Effects of hysteretic model on seismic demands: consideration of near-fault ground motions. The Structural Design of Tall and Special Buildings. 2002. Vol. 11. No. 3. Pp. 155–169. https://doi.org/10.1002/tal.182
27. Li, X.H., Wang, W.K., Wu, D., XU, X.L., LI, Z.J., LI, Y.X. The bounded method and characteristics analysis for long-period ground motions. Journal of Vibration Engineering. 2014. Vol. 27. No. 05. Pp. 685–692. (Chinese) https://doi.org/10.16385/j.cnki.issn.1004-4523.2014.05.004
28. Koketsu, K., Miyake, H.A. Seismological overview of long-period ground motion. Journal of Seismology. 2008. Vol. 12. No. 2. Pp. 133–143. https://doi.org/10.1007/s10950-007-9080-0

Contacts:

Yu Cheng, yucheng099@163.com
Yao-Rong Dong, yaorong099@163.com
Yuan-Yuan Wang, wyy1005@seu.edu.cn
Li Qin, 414042014@qq.com
Ye-Xue Li, warmhearted520@163.com
Guo-Liang Bai, baiglgh@xauat.edu.cn

Received 23.07.2020. Approved after reviewing 31.03.2021. Accepted 05.04.2021.



Magazine of Civil Engineering

ISSN 2712-8172

journal homepage: http://engstroy.spbstu.ru/

DOI: 10.34910/MCE.110.6

Numerical shear of post-tensioned beams with inverted-U shaped reinforcements

M. Khatib* [a], ***Z. Abou Saleh*** [b], ***O. Baalbaki*** [c], ***Z. Hamdan*** [d]

[a] *ISSEA-Cnam Lebanon, Maurice Barres, Beirut, Lebanon*

[b] *Rafik Hariri University, Damour, Lebanon*

[c] *Beirut Arab University, Beirut, Lebanon*

[d] *Lebanese University, Beirut, Lebanon*

**E-mail: milad.khatib@isae.edu.lb*

Keywords: finite element model, 3D modeling, bonded post-tensioned beams, shear stress, inverted-U shaped reinforcements, stirrups reinforcements

Abstract. Previous works verified that, compared to conventional stirrups reinforcements (or closed stirrups reinforcements), the inverted-U shaped reinforcements improve the performance of the flat slabs in terms of failure mode and load capacity. The primary goal of this research was to investigate the numerical advantage of the inverted-U shaped reinforcements in reinforcing post-tension beams (PTB) over the conventional one as well as comparing the results with the ACI provision. Several experiments and numerical analyses were conducted in order to increase the shear strength capacity of reinforced concrete beams using different shear reinforcement systems. Recently, the system's ability to experimentally improve the shear capacity of bonded post-tensioned beams was explored. In this study, two types of post-tensioned beams were tested using a finite element program (ANSYS 16.0) to help investigate the influence of inverted-U shaped reinforcements on the shear behavior of bonded post-tensioned beams. The numerical results indicated that the limitation on the nominal of shear reinforcements for bonded pre-stressed concrete beams in the ACI 318-14 was too conservative. Good correlation was found between the experimental and the numerical results.

1. Introduction

In 1872, the principle of prestressing the concrete was applied by Jackson for the first time in United States [1]. Later, several experimental tests were conducted on the behavior of bonded and unbonded post-tensioned concrete members such as: Dunker (1985) [2], Garden and Hollaway (1997) [3], Abou Saleh and Suaris (2007) [4], Kang and al. (2015) [5], Ellobody and Bailey (2016) [6], Xue and al. (2019) [7], Khatib and Abou Saleh (2020) [8], and others.

Normally, prestressed concrete can be constructed in three different ways: pre-tensioned prestressed concrete, bonded post-tensioned (PT) prestressed concrete, and unbonded PT prestressed concrete as cited by Kang and al. (2015) [8].

Since it is difficult to pinpoint an exact date for the initial development of the finite element analysis, a method initiated from necessity in order to explain and predict complex elasticity and structural analysis problems in civil and aeronautical engineering, its development can be traced back to the work done by Hrennikoff [9] and Courant in the early 1940s [10]. Numerical and theoretical models were previously developed by other researchers to study the behavior of bonded and unbonded post-tensioned concrete members.

Khatib, M., Abou Saleh, Z., Baalbaki, O., Hamdan, Z. Numerical shear of post-tensioned beams with inverted-U shaped reinforcements. Magazine of Civil Engineering. 2022. 110(2). Article No. 11006. DOI: 10.34910/MCE.110.6

© Khatib, M., Abou Saleh, Z., Baalbaki, O., Hamdan, Z., 2022. Published by Peter the Great St. Petersburg Polytechnic University.

This work is licensed under a CC BY-NC 4.0

Many articles and researches have been published addressing the optimization of concrete structures such as: Hopkins (1956) [11], Kim and Christopoulos (2008) [12], Ellobody and Bailey (2009) [13], Huang and al. (2010) [14], Kim and Lee (2012) [15], Kulkarni A. and Bhusare V (2016) [16], Khatib and al. (2016) [17], Abdul-Razzaq and al. (2018) [18], and Khatib and al. (2018) [19]. The techniques of optimization play an important role in the design of structures. One of the most important purposes of optimization is finding the best solutions from which a designer can realize the highest benefits and advantages within the available resources.

Generally, the beams may have major possible modes of failure (flexural failure, diagonal tension and shear failure), cracking, deflection, bending, and shear as discussed by Hawkins and al. [20] and recently by Slowik [21].

According to ACI 318 [22], the shear strength (V_c) for concrete section (with effective web width (b_w) and distance from extreme compression fiber to centroid of prestressing steel (d_p)) provided by pre-stressed reinforced concrete members. It was calculated in function of: modification factor related to the unit weight of concrete; λ, concrete compressive strength; f'_c, factored shear force; V_u, and factored moment; M_u. The shear strength (V_c) can be the lesser of the following:

$$V_c = \left(0.6\lambda\sqrt{f'_c} + 700 \cdot \frac{V_u d_p}{M_u} \right) \cdot b_w \cdot d_p, \tag{1}$$

where $\frac{V_u d_p}{M_u} \geq 1.0;$

The shear force at flexure-shear cracking $V_{ci} = 0.6\sqrt{f'_c} \cdot b_w \cdot d_p + V_c + \frac{V_i M_{cr}}{M_{\max}},$ (2)

where V_i is the factored shear force at section due to externally applied loads occurring simultaneously, M_{cr} is the cracked moment and M_{max} is the maximum moment.

The cracked moment (M_{cr}) for the section was calculated in function of: inertia of the section (I), concrete compressive strength (f'_c), average prestress value after losses at centroid of cross concrete section (f_{pe}), with unfactored dead load stress (f_d) at distance (y_t) from centroidal axis of gross section, neglecting reinforcement, to extreme fiber in tension as follows: $M_{cr} = \left(\frac{I}{y_t} \right) \left(6\sqrt{f'_c} + f_{pe} - f_d \right).$

In addition, for web shear (V_{CW}) in prestressed concrete members:

$$V_{cw} = \left(3.5\sqrt{f'_c} + 0.3 f_{pc} \right) \cdot b_w \cdot d_p + V_p. \tag{3}$$

where f_{pc} is the compressive stress in concrete after all prestress losses at centroid of cross section, and V_p is the vertical component of effective prestress force at the cross section.

However, the above equations of shear strength should not be less than those of shear strength provided by reinforced concrete members with calculated distance from extreme compression fiber to centroid of longitudinal tension reinforcement (d). V_c can be the lesser of the following:

$$\left(1.9\lambda\sqrt{f'_c} + 2500 V_n \frac{d_p}{M_u} \right) \cdot b_w \cdot d, \tag{4}$$

$$\left(1.9\lambda\sqrt{f'_c} + 2500 \right) \cdot b_w \cdot d, \tag{5}$$

with limitation:

$$\left(2\lambda\sqrt{f'_c} \right) \cdot b_w \cdot d \leq V_c \leq \left(5\lambda\sqrt{f'_c} \right) b_w \cdot d.$$

1.1. Shear reinforcement types

The following different systems of reinforcement were explained in order to highlight the differences between the conventional shear reinforcement system and the proposed one.

In 1899, Ritter stated that stirrups resisted tension, not horizontal shear. He also suggested the design of vertical stirrups (according to the equation:

$$V = \left(A_v f_v j_d\right)/S. \quad (6)$$

where: A_v is total cross sectional area of vertical stirrups

f_v is allowable stress in the stirrups

j_d is internal moment arm.

S is spacing of stirrups in the direction of the axis of the member.

Ritter's ideas were not widely accepted at that time, but his design for vertical stirrups is similar to that appearing in the design specifications of most countries today [23].

In the web of reinforced concrete beams, Taylor [24] specifically mentioned to the point that inclined cracks are prevented from spreading by using transversal reinforcements such as stirrups. Practically, shear reinforcement takes three forms: stirrups, inclined bent up bars, or a combination of both. However, in industry, vertical stirrups are most commonly used because of their simplicity in fabrication and installation [25] as shown in Fig. 1.



Figure 1. Vertical Stirrups Reinforcements [7].

In addition to a citation issued by ACI-ASCE Committee 445 [26], many earlier tests were carried out by Zwoyer and Seiss [27] then by Moody and al. [28] confirming that the vertical shear stirrups (V_s) intercept diagonal cracks, and the nominal shear stress in steel is limited to:

$$V_s \leq 8\sqrt{f_c'}. \quad (7)$$

This limitation was also approved later on by Xu and al. [29] and by Morsy and al. [30].

An inverted-U shaped reinforcing assembly sample (called Hairpin) was primarily conducted by Abou Saleh and Suaris (2007) [6]. Such a system is shown in Fig. 2.

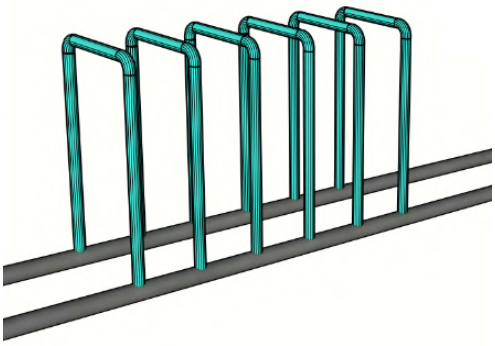


Figure 2. Inverted-U Shaped Reinforcements [7].

The use of such system improve experimentally the structural performance for an unbonded post-tensioned flat slab. The tested post-tensioned slabs provided with studs failed in pinching shear and the slabs provided with “Hairpin” shaped reinforcement failed in flexural. The test results with the stud reinforcement were almost equal to those predicted by the ACI equation. The slab with hairpin shaped reinforcement prevented the shear failure and showed about 27.5 % increase in slab capacity in comparison with the stud reinforcement [6].

According to the previous results, a proposed finite-element model was suggested in order to test the capability into predict the load–deflection relationships of the unbonded post-tensioned reinforced concrete slabs using finite element software. The outcomes of the conducted finite element analysis, utilizing ABAQUS software for the “Unbonded post-tensioned reinforced concrete slab provided with inverted U-shaped reinforcement”, are in line with that obtained experimentally, also the nominal shear strength that was compared to ACI provisions [17].

Recently, Khatib and Abou Saleh (2020) performed an experimental investigation for the enhancement of shear strength of bonded PTB provided with inverted-U shaped reinforcements [7]. The test results were compared with bonded PTB reinforced with conventional stirrups and correlated the results according to ACI provision.

The results indicate that the nominal shear stress (V_n) in bonded PTB provided with inverted-U shaped and stirrups reinforcements are respectively 14.4 $\sqrt{f_c'}$ psi (1.2 $\sqrt{f_c'}$ MPa) and 12.72 $\sqrt{f_c'}$ psi (1.06 $\sqrt{f_c'}$ MPa), which gives approximately 13 % increase in shear strength. Notice that no failure occurs in the welding due to its high proficiency and effectiveness.

Part of this paper presents the results of an experimental investigation for both the bonded PTB with inverted-U shaped and stirrups reinforcements [7]. These results were compared to the same model using a finite element software ANSYS 16.0 [31].

The primary goal of this research was to conduct a numerical evaluation of the shear strength behavior of bonded PTB with stirrups on one side and inverted-U shaped reinforcements on the other. The beams were also analyzed to compare the results to those obtained experimentally.

The aim of the study was to investigate the advantage of an inverted-U shaped system over a conventional one. The numerical model was used to correlate between the experimental results with those obtained numerically to give the proposed system a proper and absolute validity.

Recently, an experimental investigation for the improvement of shear strength of bonded PTB provided with inverted-U shaped reinforcements was conducted against other bonded PTB with stirrups reinforcements. The dimensions, pre-stressing strands, and shear reinforcements of the beams were chosen to yield a nominal shear stress of that is equivalent to 1.25 $\sqrt{f_c'}$, which approximately corresponds to an 18 % increase in shear strength. This increase is higher than that presented by the ACI for conventional reinforcements [7].

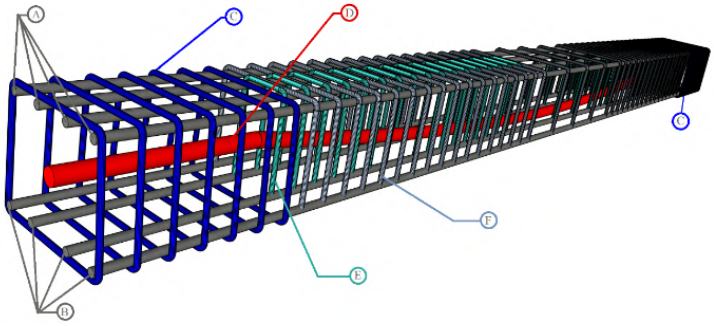
The test results indicate that the failure load for the inverted-U shaped specimens were slightly below the expected load (83 tons), which would ensure a shear failure mode of the bonded PTB [7]. According to ACI 318 [22], the beams were designed to ensure shear failure by checking that the obtained load from shear is less than that obtained due to bending. The tests were conducted by applying two concentrated point loads on the bonded PTB as shown in Fig. 3.



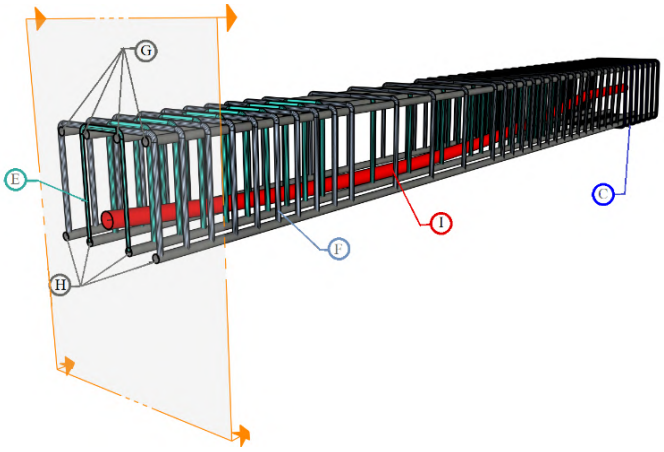
Figure 3. Tested Bonded Post-Tensioned Beam [7].

The concrete compressive strength applied was equal to 30 MPa. The seven prestressing wire strands conforming to ASTM standards A421 were 12.7 mm in diameter and at a specified ultimate strength of 1860 MPa.

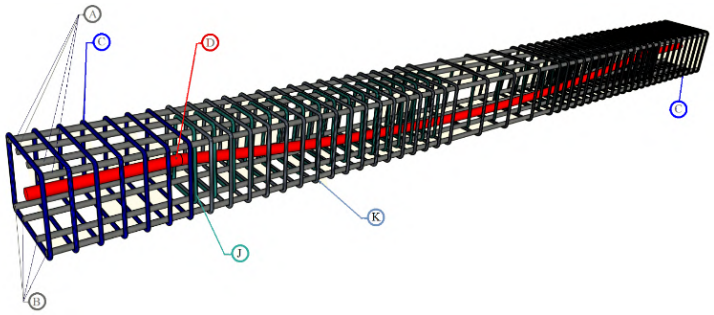
The inverted-U shaped and stirrups reinforcements were fabricated using 10 mm diameter rebar that yielded a specified strength of 420 MPa. The distribution of the rebar and shear reinforcements are as shown in Fig. 4.



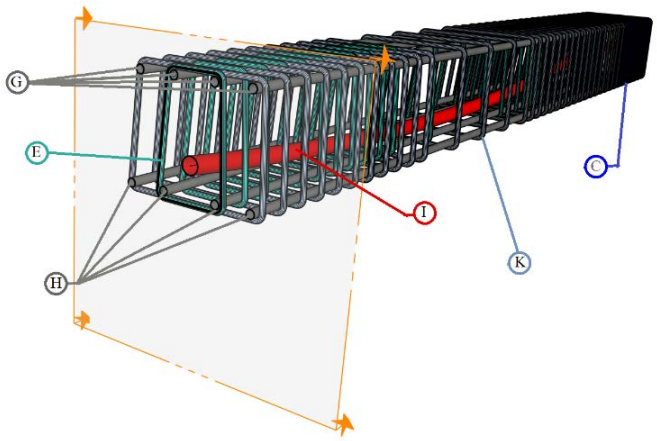
(a) Arrangement of Inverted-U Shaped Reinforcements and Rebars



(b) Cross-Section for the Inverted-U Shaped Reinforcements.



(c) Arrangement of Closed Stirrups Reinforcements and Rebars



(d) Cross-Section for the Closed Stirrups Reinforcements

Figure 4. Arrangement of Shear Reinforcements and Reinforcements [7]
Where A: Top Rebars, B: Bottom Rebars, C: Steel Cage, D: Strands, E: Internal Inverted-U, F: External Inverted-U, G: Cross-Section in Top Rebars, H: Cross-Section in Bottom Rebars, I: Cross-Section in Strand, J: Internal Stirrups, K: External Stirrups.

In general, all tested specimens failed in shear mode. The experimental results were presented in Table.1.

Table 1. The experimental shear test results compared with ACI provision.

Specimen Designation	Test results				ACI Equation
	Failure loads Kips/ kN	Average failure load Kips/kN	Spacing between point Load in/mm	Nominal shear stress. Psi/MPa	Nominal shear stress Psi/MPa
PTB-A-1	187.98/836.2	181.92/ 809.24	47.24/1200	$14.40\sqrt{f_c'}$ /$1.20\sqrt{f_c'}$	N. A.
PTB-A-2	175.86/782.30		43.3/ 1100		
PTB-B-1	166.31/739.80	166.79/ 714.96	47.24/1200	$12.7\sqrt{f_c'}$ /$1.06\sqrt{f_c'}$	$10.8\sqrt{f_c'}$ /0. $9\sqrt{f_c'}$
PTB-B-2	155.14/690.11		43.3/1100		

These results indicate that the nominal shear stress in inverted-U shaped and stirrups reinforcements are respectively $14.4\sqrt{f_c'}$ psi ($1.2\sqrt{f_c'}$ MPa) and $12.72\sqrt{f_c'}$ psi ($1.06\sqrt{f_c'}$ MPa), which yield an approximate 13 % increase in shearing strength [7].

Good correlations exist between the designed and the actual experimental results. Furthermore, the test results indicate that the failure load of the inverted-U shaped specimens were a little below the expected load; thus, resulting in a shear failure mode of the bonded PTB.

Moreover, the average load deflection curves for the two types approve that the obtained results concerning the use of the inverted-U shaped reinforcements are better than those provided with the conventional closed stirrups reinforcements as shown in Fig. 5 [7].

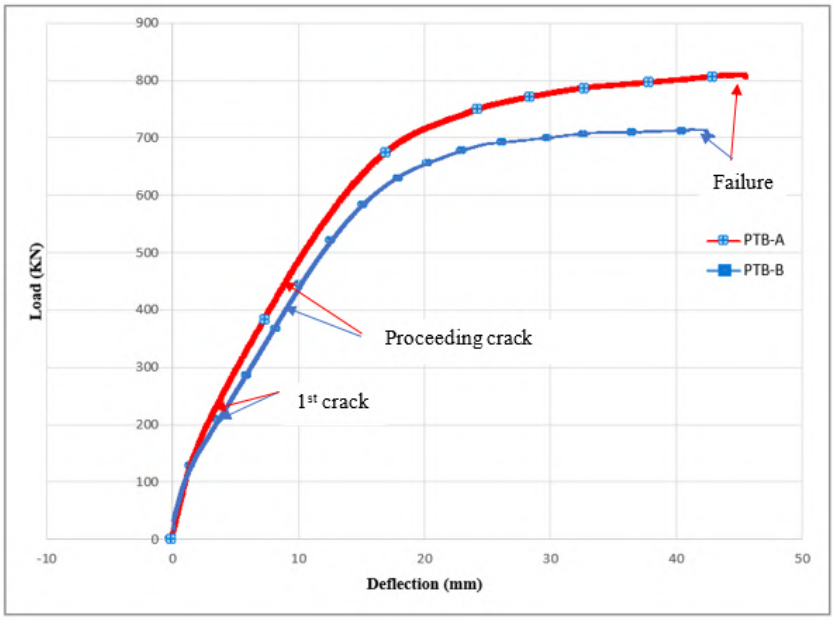


Figure 5. Load Deflection Curves for PTB – A & PTB – B (Average Values) [7].

The post-cracking stiffness is an important parameter in determining the proper distribution of forces in the analysis of PTB. It can be calculated as the triangular area under load deflection curve (linear elastic region). Although, different parameters can affect the energy absorption values, such as concrete compressive strength and steel reinforcement ratios, the energy absorption can be considered as the total area under the load deflection curve.

Refer to Fig. 5 both of post cracking stiffness and energy absorption for PTB-A show an effective enhancement comparing to PTB-B as shown in Table 2.

Table 2. The experimental enhancement results.

Specimen Designation	Average failure load Kips/kN	Nominal shear stress Psi/MPa	Post-Cracking Stiffness	Energy Absorption
PTB-A	181.92/809.24	$14.40\sqrt{f_c'}$ /$1.20\sqrt{f_c'}$	45.96	252.66
PTB-B	166.79/714.96	$12.7\sqrt{f_c'}$ /$1.0\sqrt{f_c'}$	41.88	207.48
% Enhancement	9.07%	13.4 %	9.75 %	21.77 %

2. Methods

Ever since the finite element was first introduced by Ngo and Scordelis (1967) [32] and applied to the analysis of reinforced beams, a huge number of methodologies for modeling the behavior of concrete as a material or the behavior of reinforced concrete structures have been established.

The obtained experimental results [7], mentioned earlier, were compared with the same model using a finite element software “ANSYS 16.0” [31]. The objective of this comparison is to validate the experimental results and highlight the effectiveness of the proposed system. Moreover, the modeled beams were analyzed to compare the obtained experimental test results.

The ANSYS 16.0 program [31] is capable of simulating structural analysis problems in a wide range of engineering disciplines, deformations, stresses, strains, and reaction forces. The analysis of a structure with ANSYS 16.0 is performed through the following pre-processing steps: The first process is defining the finite element model and the environmental factors applied to it. The second is analyzing the solver which

is the solution of the finite element model and finally post-processing the results like deformations, contours for displacement, etc…, using visualization tools.

An approach to modeling bonded PTB will usually aid in making better and improved engineering decisions about preparing the geometry, which includes beams, cables, reinforcement rebar, inverted-U shaped and stirrups reinforcements.

The finite element analysis calibration study included modeling bonded PTB with the dimensions and properties. In order to model them using ANSYS 16.0, there are multiple tasks that have to be completed for it to run properly. Models can be presented using either a command prompt line input or a Graphical User Interface.

For this model, the graphical user interface was utilized. This section describes the different tasks and entries used to model the finite element calibration. The boundary conditions and load application were identical to those used in the tests.

The main evaluation for a theoretical model is testing two types of bonded PTB: PT-1 (provided with inverted-U shaped reinforcements) and PT-2 (provided with stirrups reinforcements). Both types are analyzed using ANSYS 16.0.

The PTB was designed following the recommendations of PTI (Post Tensioning Institute) manual, so the profile of the strands is a fixed parameter and cannot be changed, because the profile was chosen to ensure the maximum benefit from the post-tension system. Concerning the level of force, in this study, it does not make any sense to change it. Since during the experimental tests, it was chosen the level to ensure the maximum efficiency force. However, the concrete compressive strength was changed to study its effect on the PTB.

2.1. Modeling of post-tensioned beams

The model is considered vertically symmetrical at mid span as performed in the previous test. The test specimens were 3.4 m × 0.3 m × 0.25 m. The concrete beam was modeled by drawing the area into the YZ plan and extruding it into the X direction as shown in Fig. 6.

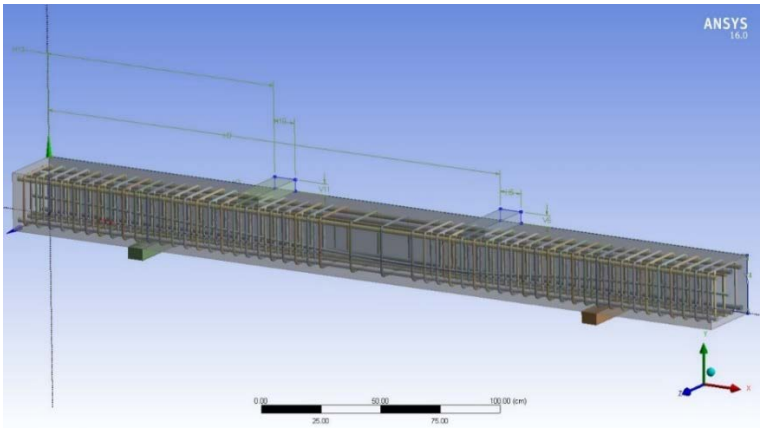


Figure 6. Modeling of PTB.

The element is a 10-node element model with a higher 3D order (SOLID187) as shown schematically in Fig. 7.

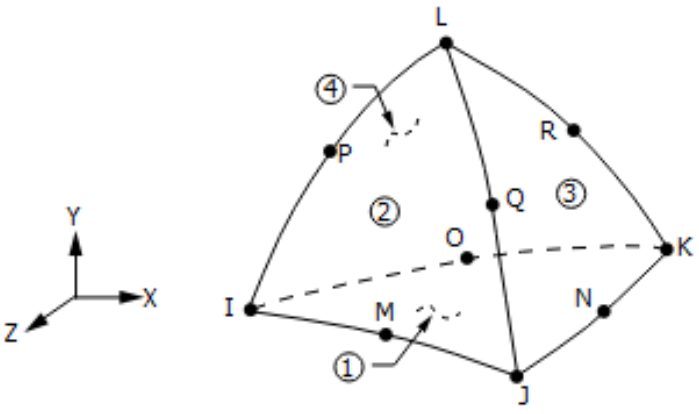


Figure 7. Solid 187 Element Model.

It has a quadratic displacement behavior and is well suited to modeling irregular meshes (such as those produced from various CAD/CAM systems). This element had three degrees of freedom at each node: translations in the nodal x, y, and z directions. The element has plasticity, hyperelasticity, creep, stress stiffening, large deflection, and large strain capabilities.

It also has a mixed formulation capability for simulating deformations of both partially incompressible elastoplastic materials and fully incompressible hyper-elastic ones. The element is capable of plastic deforming, cracking in three orthogonal directions, and crushing.

Four longitudinal reinforcements of 20 mm in diameter were placed at the top and bottom of the concrete beams as described before in the experiment investigation (Fig. 8).

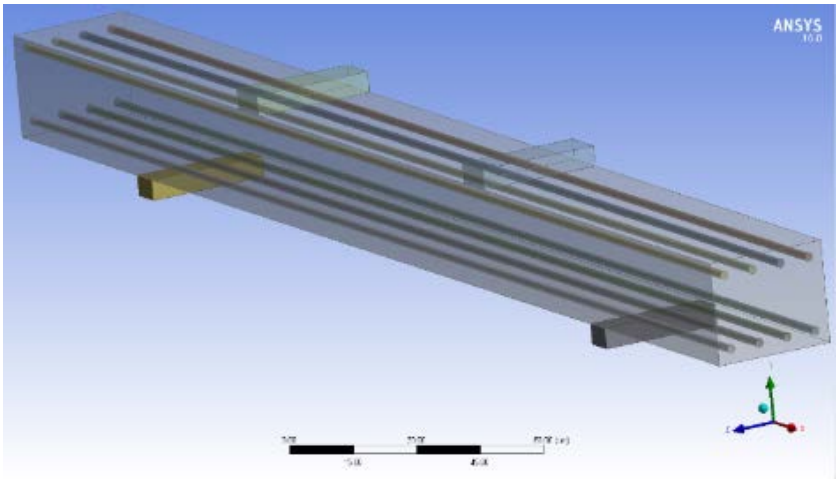


Figure 8. Rebar in Bonded PTB.

The shear reinforcements were located at the supports (max. shear region) of the beam, around the loaded or reaction area. Sixteen inverted-U shaped reinforcements of dimensions (21 cm×26 cm×21 cm) along with another sixteen of dimensions (21 cm×8 cm×21 cm) were used in the first beam type PT-1 as shown in Fig. 9.

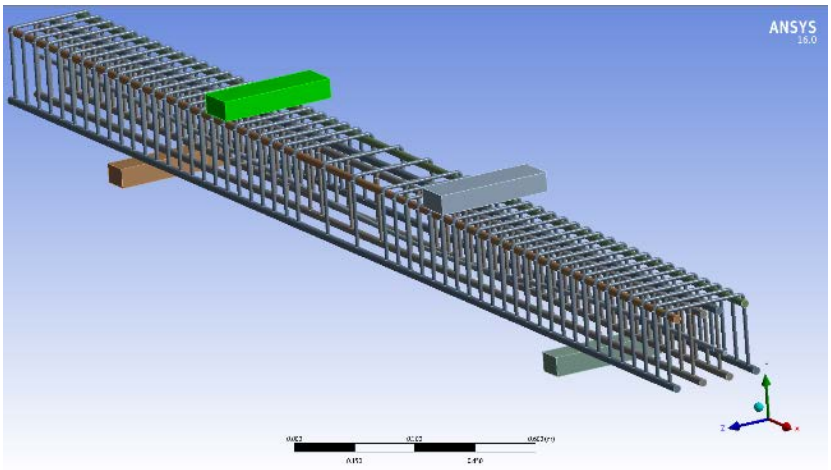


Figure 9. Inverted-U Shaped Distribution in Bonded PTB.

Also, another 16 closed stirrups reinforcements of dimensions (21 cm×26 cm) plus 16 closed stirrups reinforcements of dimensions (21 cm × 8 cm) were prepared for the second type of beam (PT-2) as shown in Fig. 10.

One sector was provided into the XZ plane in a longitudinal direction to model a cable. The cable geometry was entered with a curvilinear body and anchored at the ends through a thin cylindrical joint as shown in Fig. 11.

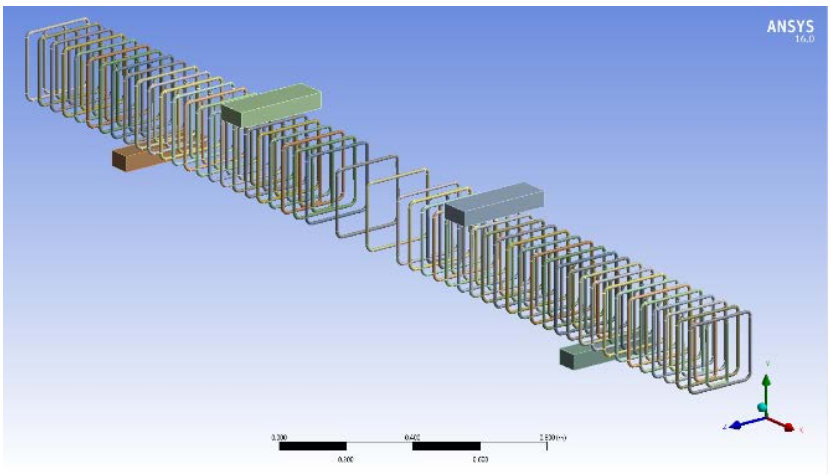


Figure 10. Stirrups Distribution in Bonded PTB.

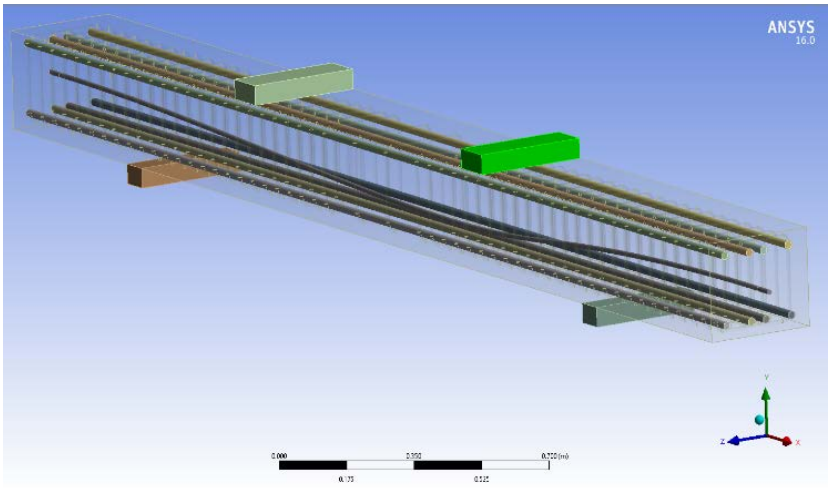


Figure 11. Layout of Post-Tensioned Cable.

2.2. Modeling of material properties

The material properties adopted for the discrete model concerning concrete, rebar steel, shear reinforcements (inverted-U shaped and stirrups reinforcements) used were taken from the accomplished experiments.

Concrete is modeled with the help of a solid element, SOLID186. In tension, the stress–strain curve is thus presumed to be linear elastic until it reaches the uniaxial tensile strength of the concrete. Thus, the concrete element eventually cracks.

By default, there is a model for concrete, but for the nonlinear analysis purpose, the plastic behavior model should be added. The simple one is the bilinear kinematic hardening model. But in order to get a better performance, the multilinear model is used and the values as stress-strain relationship are added as shown below in Table 3 and Fig. 12. The other concrete material values are listed in Table 4.

Table 3. Concrete stress strain values.

Plastic Strain	Stress (MPa)
0	1E-09
0.0006	15
0.0009	21.08
0.0012	25.27
0.0015	27.96
0.0018	29.42
0.0021	29.96
0.00219	30
0.003	30

Table 4. Concrete properties.

Properties	Values
Young's Modulus	25000 Mpa
Poison's ratio	0.1
Tensile Yield Strength	3.42 MPa

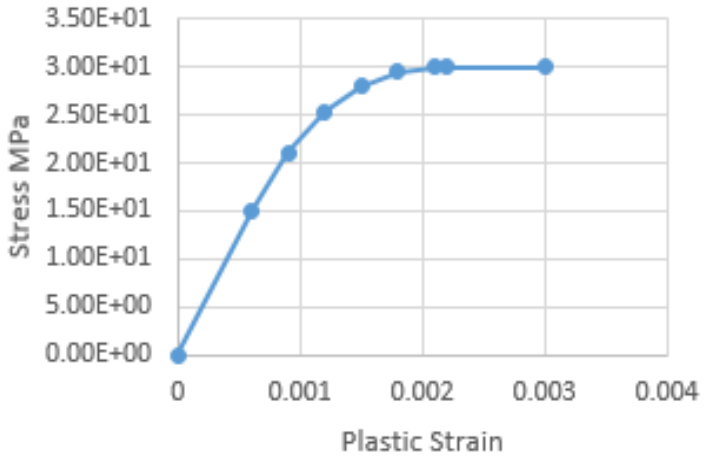


Figure 12. Stress-Strain Relationship for Concrete.

ANSYS 16.0 supplies a huge number of material libraries. Structural steel is one of them. The values were modified so that it would be similar to that used in the experimental analysis then added a plastic behavior model for the nonlinear analysis as listed in Table 5 by using the simpler one which is the bilinear isotropic hardening model. The values for yielding strength (420 MPa) and tangent modulus (6700 MPa) are added as shown in Fig.13.

Table 5. Rebars Properties.

Properties	Values
Young's Modulus	1.96*105 MPa
Poison's ratio	0.28
Tensile Yield Strength	420 MPa
Tangent Modulus	6700 MPa
Tensile Ultimate Strength	525 MPa

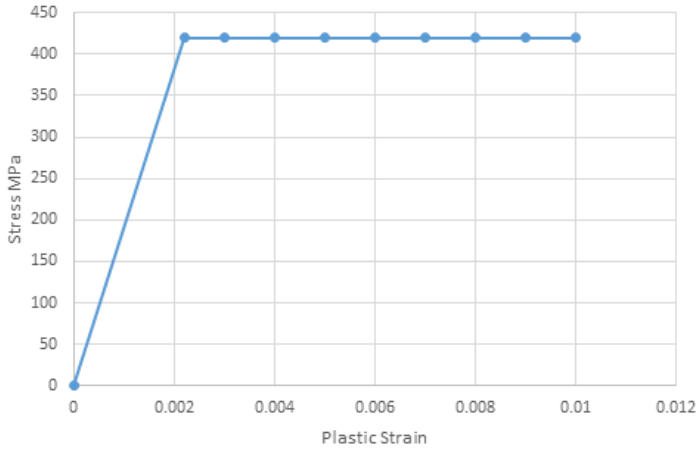


Figure 13. Stress-Strain Relationship for Steel.

The steel element model in the "Engineering Data Sources" was duplicated and renamed it as prestressed cables. The values were modified to have the same material properties used in the experimental analysis as shown in Table 6.

Table 6. Prestressed Cables Properties.

Properties	Values
Young's Modulus	2*105 MPa
Poison's ratio	0.3
Tensile Yield Strength	

2.3. Meshing

The Solid186 element was used to mesh the PTB. This properly sets width and length of the elements in the rebar and lets the cables be consistent with the elements and nodes in the concrete portions of the model. The necessary element divisions are noted. The model was meshed as shown in Fig. 14 using "Curvature" option in "Advanced size function", "Coarse" option for "Relevance Center with Medium Smoothing" and "Fast Transition" so that both the rebar and concrete elements share the same nodes. The same goes for cables and concrete.

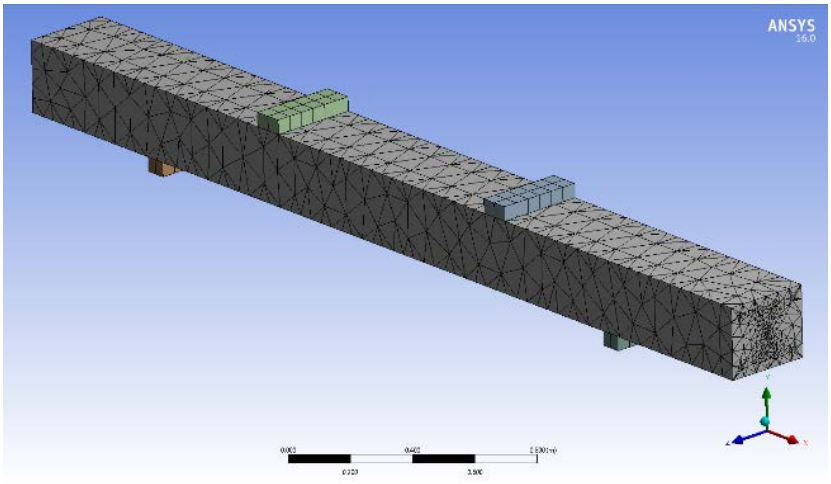


Figure 14. Meshed Bonded PTB.

An internal closed view for the meshed inverted-U shaped reinforcements and post-tensioned cables was shown in Fig. 15.

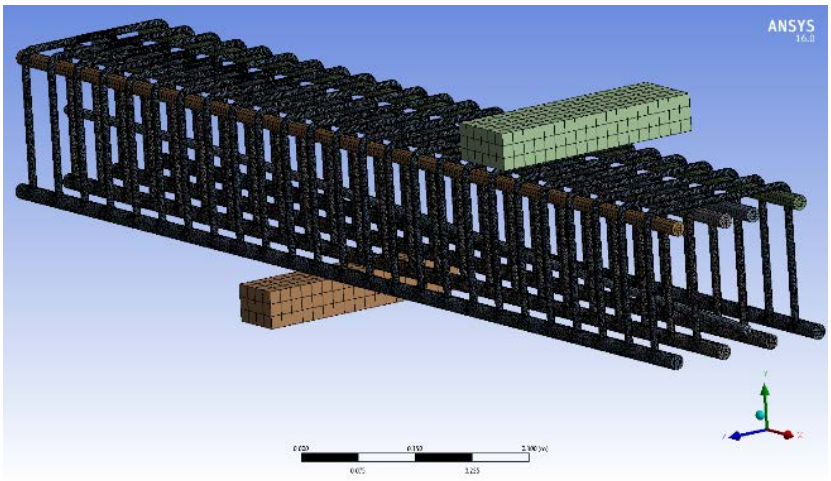


Figure 15. Internal Closed Meshed View for PT-1.

Another internal view for the meshed stirrups and post-tensioned cables was presented in Fig. 16.

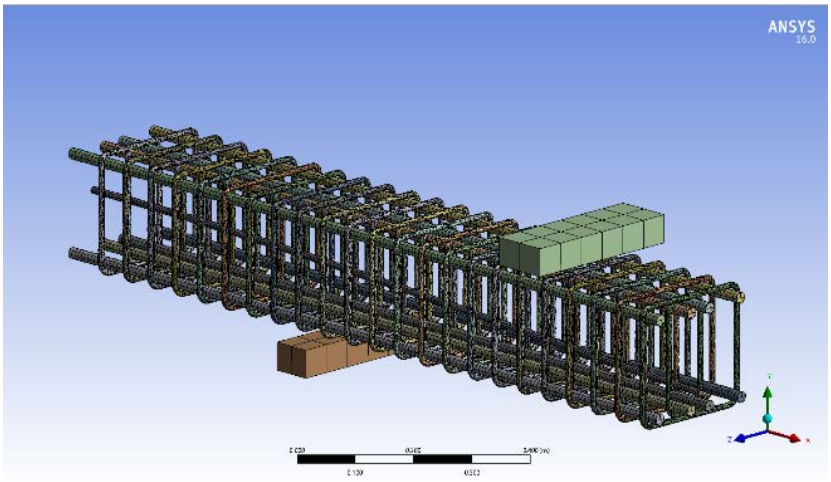


Figure 16. Internal Closed Meshed View for PT-2.

2.4. Loads and boundary conditions

The load was applied downwards at two separated points 30 cm from the center of the PTB. Two other different points, which were 200 cm apart from each other, were used to be the supports of the PTB. The beam also had a 70 cm overhanging on each side as shown in Fig. 17.

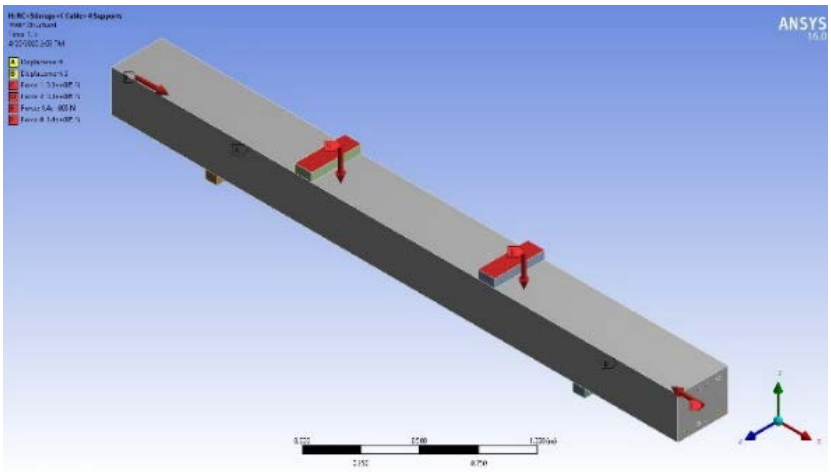


Figure 17. Bonded PTB Loaded.

3. Results and Discussion

The Analysis Settings was specifying to ON for the Large deflection and the numerical analysis started running. Numerical results of shear behavior of bonded PTB with inverted-U shaped and stirrups reinforcements were presented in this paper. These results state that both models failed in shear.

The initial cracking of the PTB provided with inverted-U (PT-1) appeared at a load P = 198 kN and the corresponding deflection is 3 mm. Smooth graded crack occurs as more load is applied to the PT-1. The second crack appeared at a load P = 431 kN with corresponding deflection equal to 8.5 mm. Thus, larger deflection takes place at mid-span, and the successive appearance cracking of the PT-1 means that significant cracks appear at beyond yielding of steel reinforcement. At 845.16 kN the PTB is at the verge of failure i.e. the cracking extends towards the top and record a deflection equals to 46 mm.

From X–Y plot results in Fig. 18 and the directional deformation colored contour bands for the PTB shown in Fig. 20. a,b a smooth graded crack occurred as the load increased and up to a 198 kN, the linear elastic material behavior for both steel reinforcement and concrete defines the flexural rigidity. When concrete stresses exceed modulus of rupture, cracked transformed moment of inertia in addition to linear elastic steel and concrete behavior defines the flexural rigidity of the beam, then the nonlinear concrete behavior takes place, at this stage deflection was computed based on curvature.

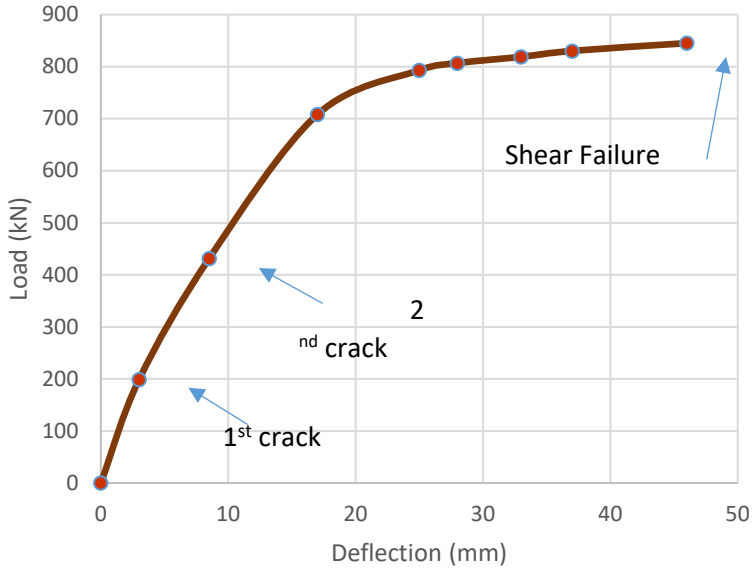


Figure 18. Load Deflection Curves for Numerical PTB (PT-1).

From the results obtained (Fig. 19) the bonded post-tensioned reinforced concrete beam provided with closed stirrups (PTB-2) crack initially at a load P = 200 kN with a corresponding deflection equals to 3.2 mm. It is noticed that at P = 400 kN the cracks develop in a sudden way caused a 9.5 mm as deflection, this implies that the tensile stress relaxation is not functioning properly. Cracking increases and the maximum load reached P = 756.20 kN caused a crushing in the top of the PTB model with deflection equals to 49.1 mm.

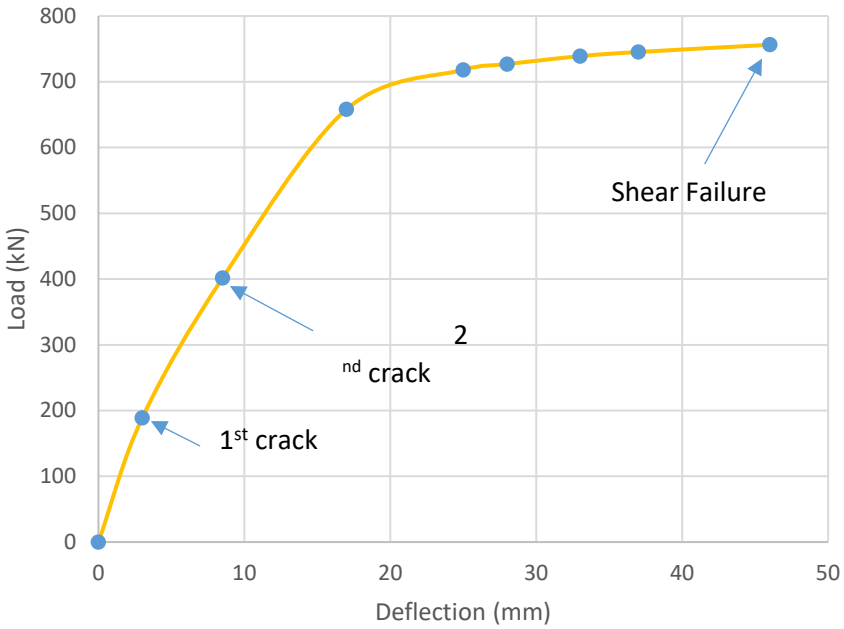
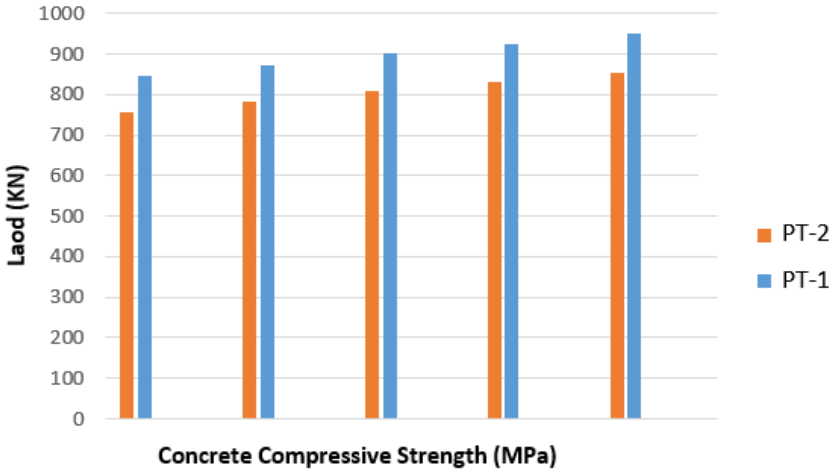


Figure 19. Load Deflection Curves for Numerical PTB (PT-2).

In order to investigate numerically the effect of the concrete compressive strength $\left(f_c'\right)$ on the two types of PTB (PT-1 & PT-2), several values were also studied (35 MPa, 40 MPa, 45 Mpa and 50 MPa). It was very clear, for both cases of PTB (PT-1 & PT-2) that with the increase of $\left(f_c'\right)$, the shear failure reach a higher value than the previous one as shown in Fig. 20.



	30	35	40	45	50
PT-1	845.16	873.54	900.62	926.22	950.14
PT-2	756.20	781.60	807.85	830.80	852.26

Figure 20. Load-Concrete Compressive Strength Relationship.

The directional deformation results appear as colored bands on the two types of bonded PTB (PT-1 & PT-2) as shown in Fig. 21.

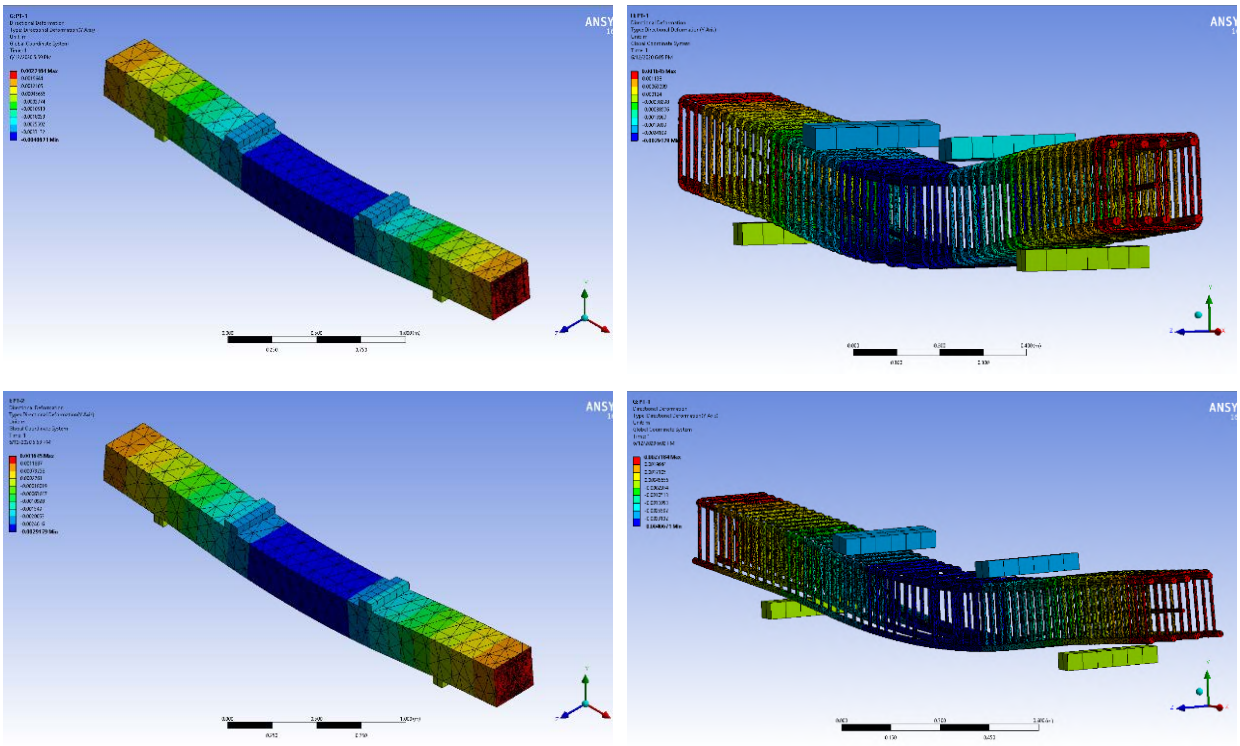


Figure 21. Top-left: Last Directional Deformation Beam Colored Bands for PT-1; Top-right: Internal View for Last Directional Deformation Colored Bands for PT-1; Bottom-left: Last Directional Deformation Beam Colored Bands for PT-2; Bottom-right: Internal View for Last Directional Deformation Colored Bands for PT-2.

The numerical results of bonded PTB with shear stirrups were almost equal to those predicted by the ACI equation. The comparisons were made between load deflection curves at mid-span and failure load. The results of the finite element analysis were calculated at the same location as the experimental test of the beams.

The bonded PTB capacity with the inverted-U shaped reinforcements was about 11.76 % higher than the bonded PTB with the stirrups. An enhancement was observed in the ductility computed as the

percentage difference in the max deflection between the two beams. The numerical results have shown that the use of inverted-U shaped reinforcements structurally behave as good if not better as shear reinforcements than stirrups do.

The accuracy of the finite element models was assessed by comparison with the experimental results that appear to be in good agreement. The load-deflection curves from the finite element analysis agree well with the experimental results in the linear range till peak load as appears in Table 7 and Fig. 22.

Table 7. Comparison of Numerical and Experimental PTB Results with ACI Provision.

Specimen designation	Average failure load Kips/ kN	Test Results Nominal shear stress psi /MPa	ACI Equation Nominal shear stress psi /MPa
PTB-A	181.92/ 809.24	$14.40\sqrt{f_c'}$ /$1.20\sqrt{f_c'}$	N. A.
PTB-B	166.79/ 714.96	$12.72\sqrt{f_c'}$ /$1.06\sqrt{f_c'}$	$10.8\sqrt{f_c'}$ /$0.9\sqrt{f_c'}$
Numerical Results			
PT-1	190 / 845.16	$15.04\sqrt{f_c'}$ / $1.25\sqrt{f_c'}$	N. A.
PT-2	170 / 756.20	$12.96\sqrt{f_c'}$ / $1.10\sqrt{f_c'}$	$10.8\sqrt{f_c'}$ /$0.9\sqrt{f_c'}$

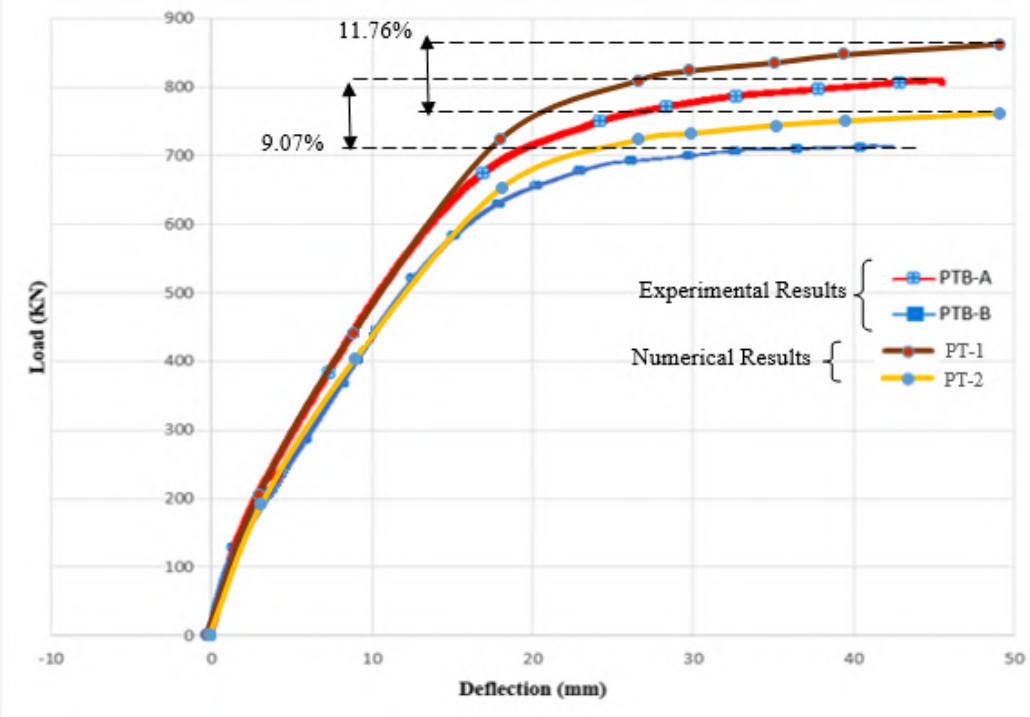


Figure 22. Load Deflection Curves for Experimental PTB (PTB-A and PTB-B) and Numerical PTB (PT-1 and PT-2).

The obtained numerical results show improvement values as much the experimental ones. The percentage enhancement concerning Average load failure, Nominal shear stress, Post-Cracking Stiffness and Energy Absorption were shown in Table 8.

Table 8. Comparison of Enhancement for Numerical and Experimental PTB Results.

Specimen Designation	Average failure load Kips/ kN	Nominal shear stress psi /MPa	Post-Cracking Stiffness	Energy Absorption
		Test Results		
PTB-A	181.92/ 809.24	$14.40\sqrt{f_c'}$ /$1.20\sqrt{f_c'}$	45.96	252.66
PTB-B	166.79/ 714.96	$12.72\sqrt{f_c'}$ /$1.06\sqrt{f_c'}$	41.88	207.48
%Enhancement	9.07 %	13.4 %	9.75 %	21.77 %
		Numerical Results		
PT-1	190/845.16	$15.04\sqrt{f_c'}$ /$1.25\sqrt{f_c'}$	57.28	275.25
PT-2	170/756.20	$12.96\sqrt{f_c'}$ /$1.10\sqrt{f_c'}$	52.87	229.56
%Enhancement	11.76 %	16.04 %	8.34 %	19.90 %

The numerical results give values higher than the experimental ones; however, the properties of concrete during the achieved experiments were possibly not as similar as estimated. According to the numerical results obtained, the proposed finite element model proves the capability to accurately predict the load deflection relationships of the bonded PTB. To obtain new equations governing the design of inverted-U shaped reinforcements, further research is needed.

4. Conclusion

A nonlinear finite element model, ANSYS 16.0, was developed and presented for the analysis of two bonded PTB. The first was provided with inverted-U shaped reinforcements while the second was provided with closed stirrups reinforcements. The interface between the tendon and the surrounding concrete was modeled allowing the tendon to retain its profile shape during the deformation of the beam. The comparison between the experimental and numerical results showed that the model can predict the behavior of bonded PTB. The numerical results allow to draw following conclusions:

1. The outcomes of the conducted finite element analysis, utilizing ANSYS 16.0 software for the bonded PTB provided with inverted-U shaped and stirrups reinforcements are in good agreement in terms of load deflection relationship with that obtained experimentally.

2. Structural modeling using SOLID187 finite element utilizing ANSYS 16.0 software properly simulate the behavior of bonded PTB provided with inverted-U shaped and stirrups reinforcements.

3. It was planned that the testing results should give values higher than the numerical ones; however, the properties of concrete during the testing process were perhaps not as homogenous as expected.

4. The numerical model of bonded PTB provided with inverted-U shaped reinforcements failed in shear mode with an increase in capacity of about 11.76 % above the numerical model of bonded PTB provided with stirrups before collapsing.

5. The nominal shear stress for bonded PTB provided with inverted-U shaped reinforcement was equal to $1.25\sqrt{f_c'}$ MPa and could actually be as high as the bonded PTB provided with stirrups by 16.05 %.

References

1. Nawy, E.G. Prestressed Concrete: A Fundamental Approach (5th ed). Pearson/Prentice Hall, 2012. [Online].
2. Dunker, K.F. Strengthening of simple span composite bridges by post-tensioning [Iowa State University, Digital Repository], 1985. DOI: 10.31274/rtd-180813-13333
3. Garden, H.N., Hollaway, L.C. An Experimental Study of the strengthening of Reinforced Concrete Beams using Prestressed Carbon Composite Plates. Proceedings of 7th Int. Conf. Structural Faults and Repair. Edinburgh, 1997. V. 2. Pp. 191–199.
4. Abou Saleh, Z., Sauris, W. Reinforcing Assemblies and Reinforced Concrete Structures. Patent USA US20080263978A1, 2008.
5. Kang, T., Huang Y., Shin M., Lee J., Sir Cho A. Experimental and Numerical Assessment of Bonded and Unbonded Post-Tensioned Concrete Members. ACI Structural Journal. 2015. 112 (6). Pp. 735–748. DOI: 10.14359/51688194
6. Ellobody, E., Bailey, C. Behaviour of Unbonded Post-Tensioned One-Way Concrete Slabs. Advances in Structural Engineering Journal. 2016. 11(01). Pp. 107–120. DOI: 10.1260/136943308784069504

7. Xue, W., Tan, Y., Peng, F. Experimental Study on Damaged Prestressed Concrete Beams Using External Post-Tensioned Tendons. ACI Structural Journal. 2019. 117(1). Pp. 159–168. DOI: 10.14359/51718019
8. Khatib, M., Abou Saleh, Z. Enhancement of Shear Strength of Bonded Post-Tensioned Beams Using Inverted-U Shaped Reinforcements. Case Studies in Construction Materials Journal. 2020. Vol. 13. DOI: 10.1016/j.cscm.2020.e00370
9. Hrennikoff, A. Solution of Problems by the Frame Work Method. Journal of Applied Mechanics. 1941. 8(4). Pp.169–175.
10. Courant, R. Variational Methods for the Solution of Problems of Equilibrium and Variations. Bulletin of the American Mathematical Society. 1943. No. 49. Pp. 1–23.
11. Hampshire, J.K., Topping, B.H.V., Chan, H.C. Three Node Triangular Bending Elements with One Degree of Freedom per Node. Engineering Computations. 1992. 9 (1). Pp. 49–62. DOI: 10.1108/eb023848
12. Kim, H., Christopoulos, C. Numerical models and ductile ultimate deformation response of post-tensioned self-centering moment connections. Earthquake Engineering Structural Dynamic. 2008. 38(1). Pp. 1–21. DOI: 10.1002/eqe.836
13. Ellobody, E., Bailey, C. G. Modelling of Unbonded Post-Tensioned Concrete Slabs under Fire Conditions. Fire Safety Journal. 2009. Vol. 44. Pp. 159–167. DOI: 10.1016/j.firesaf.2008.05.007
14. Huang, Y., Kang, T.H.-K., Ramseyer, C., Rha, C. Background to multi-scale modelling of unbonded Post-Tensioned concrete structures. International Journal Theoretical and Applied Multiscale Mechanicsю 2010. 1(3). Pp. 219–235.
15. Kim, K.S., Lee, D. Nonlinear analysis method for continuous post-tensioned concrete members with unbonded tendons. Engineering Structures. 2012. 40 (1). Pp. 487–500. DOI: 10.1016/j.engstruct.2012.03.021
16. Kulkarni, A., Bhusare V. Structural optimization of reinforced concrete structures. International Journal of Engineering Research. 2016. 5 (07). DOI: 10.17577/IJERTV5IS070156
17. Khatib, M., Abou Saleh, Z., Baalbaki, O. Punching Shear Analysis of Bonded Post-Tensioned Slabs with Inverted-U Shaped Reinforcements. Proceedings 9th Alexandria International Conference on Structural and Geotechnical Engineering. AICSGE 9. Alexandria, 2016. Pp. RC 16-RC 17.
18. Mohammed, A. H., Abdul-Razzaq, K. S., Mohammedali, T. K., Nassani K., D. E., Hussein, A. K. Finite Element Modeling of Post-Tensioned Two-Way Concrete Slabs under Flexural Loading. Civil Engineering Journalю 2018. 4(1). DOI: 10.28991/cej-030964
19. Khatib, M., Abou Saleh, Z., Baalbaki, O., Temsah, Y. Numerical Punching Shear Analysis of Unbonded Post-Tensioned Slabs with Inverted-U Shaped. KSCE Journal of Civil Engineeringю 2018. 22(11). DOI: 10.1007/s12205-018-1505-5
20. Hawkins, N., Kuchma, D., Mast, R., Marsh, M.L., Reineck, K.-H. Simplified Shear Design of Structural Concrete Members: Appendixes, 2005. [Online] URL: https://onlinepubs.trb.org/onlinepubs/nchrp/nchrp_w78.pdf. (13.11.2020)
21. Słowik, M. The analysis of failure in concrete and reinforced concrete beams with different reinforcement ratio. Archive of Applied Mechanicsю 2019. 89 (5). DOI: 10.1007/s00419-018-1476-5
22. ACI Committee 318. Building Code Requirements for Structural Concrete (ACI 318-05) and Commentary (ACI 318R-05), 2005.
23. Report of ACI ASCE Committee 326 (now 426). Shear and Diagonal Tension, 2008. [Online] URL: https://www.scribd.com/document/340287092/Report-of-ACI-ASCE-Committee-326-Shear-and-Diagonal-Tension-Part-3-Siabs-and-Footings-Chapter-8-March1962 (13.11.2020)
24. Taylor, R. The Design Of Stirrups In Reinforced Concrete Beams. Architectural Science Review. 1964. 7 (3). DOI: 10.1080/00038628.1964.9696122
25. Al-Nasra, M., Asha, N. Shear Reinforcements in the Reinforced Concrete Beams. American Journal of Engineering Research. 2013. 2(10).
26. Muttoni, A., Fernández Ruiz, M., Simões, J.T. The theoretical principles of the critical shear crack theory for punching shear failures and derivation of consistent closed-form design expressions. Structural Concrete. 2018. 19(1). DOI: 10.1002/suco.201700088
27. Zwoyer, E.M., Seiss, C.P. Ultimate Strength in Shear of Simply-Supported Prestressed Concrete Beams Without Web Reinforcements. ACI Journal. 1954. 26 (2). Pp. 181–200.
28. Moody, K.G., Viest, M., Elstner, R.C., Hognestad, E. Shear Strength of Reinforced Concrete Beams – Part 1: Tests of Simple Beams. ACI JOURNAL. 1954. 51(4). Pp. 317–332.
29. Xu, S., Zhang, Z., Li, R., Qiu, B. Experimental Study on the Shear Behavior of RC Beams with Corroded Stirrups. Journal of Advanced Concrete Technology. 2017. 15(4). DOI: 10.3151/jact.15.178
30. Morsy, N.S., Sherif, A.G., Shoeib, A.E., Agamy, M.H. Experimental Study of Enhancing the Shear Strength of Hidden/Shallow Beams by Using Shear Reinforcement. 2018. DOI: 10.11159/icsenm18.116
31. ANSYS, I. Theory Reference for the Mechanical APDL and Mechanical Applications: Vol. Release 12, 2009
32. Ngo D., Scordelis A.C. Finite Element Analysis of Reinforced Concrete Beams. ACI Journal. 1967. No. 3. Pp. 152–163.

Contacts:

Milad Khatib, milad.khatib@isae.edu.lb

Zaher Abou Saleh, abousalehza@rhu.edu.lb

Oussama Baalbaki, obaalbaki@bau.edu.lb

Ziad Hamdan, ziad.hamdan.2@ul.edu.lb

Received 27.07.2020. Approved after reviewing 13.04.2021. Accepted 14.04.2021.



Magazine of Civil Engineering

ISSN 2712-8172

journal homepage: http://engstroy.spbstu.ru/

DOI: 10.34910/MCE.110.7

Application of artificial neural networks for prediction of concrete properties

N.A. Abdulla
University of Salahaddin, Erbil, Iraq
E-mail: anwzad@yahoo.com

Keywords: slump, aggregate/cement ratio, artificial neural network, concrete stress, strain at peak stress, regression analysis

Abstract. The effect of different mix ratios on the mechanical properties of concrete was investigated. The strength and deformation in terms of the strain of normal strength concrete were evaluated under concentric loading. The artificial neural network (ANN) technique was used for predicting the compressive stress and strain at peak stress of concrete. The input parameters for ANN architectures included water/cement ratio, aggregate/cement ratio, and slump values. An equation for predicting the strain of concrete at peak stress was proposed based on ANN output values for compressive stress and strain at peak stress. The capability and performance of the proposed equation are compared with actual experimental results and predictions from existing fifty-three empirical equations, including several design codes and various strain models for normal and high strength concretes, using several statistical indexes. The results showed that ANN technique have good potential for predicting the compressive strength and strain at peak stress of concrete, yielding close predictions and good agreement with the original ones.

1. Introduction

In the last nine decades, considerable effort has been spent to understand the inelastic behavior of concrete and the resulting shape of the stress-strain curve. The compressive strength and the strain at peak stress of concrete were found to have a significant interrelationship. Several studies have reported the axial strain capacity to increase significantly in concretes with improved compressive strength. Modern technology and new additives assisted in the improvement of concrete properties. Several parameters influence the strain at peak stress, including water/binder ratio and workability. One measure of quality control and uniformity of concrete from batch to batch is the slump test. Workability extends the fresh use of concrete to achieve full compaction, increase the resistance to bleeding, harshness, and segregation. A significant component that makes up concrete and contributes to its physical improvements is aggregate. A high aggregate/cement ratio indicates lower compressive strength and vice versa.

Some design codes have adopted a constant value for the strain at peak stress of concrete tested under axial compression load. However, such approaches may not yield acceptable results with more minor errors since the compressive strength of concrete and its strain at peak stress are influenced by several parameters such as mixed ingredients, specimen geometry, testing conditions, and environmental conditions.

Several studies have highlighted the potential use of artificial neural networks (ANN) to predict the compressive strength of concrete. In a research, ANN procedure was employed for evaluating the compressive strength of concretes containing metakaolin and silica fume [1] using the experimental test results from 195 specimens produced with 33 different mixture proportions. The obtained test data was used in the multi-layer feed-forward neural network models and were arranged in a format of eight input parameters. In another study, ANNs and genetic programming (GP) were used for predicting the strength of concrete [2]. The ANN model with the training function, Levenberg-Marquardt (LM), was found to be a

Abdulla, N.A. Application of artificial neural networks for prediction of concrete properties. Magazine of Civil Engineering. 2022. 110(2). Article No. 11007. DOI: 10.34910/MCE.110.7

© Abdulla, N., 2022. Published by Peter the Great St. Petersburg Polytechnic University.

This work is licensed under a CC BY-NC 4.0

useful tool for compressive strength predictions of concrete. Lai and Serra [3] used the ANN model for assessing the compressive strength of cement conglomerates by constructing models in which a variety of different mix-design parameters associated with cement conglomerates were considered.

Unlike normal concrete, high-strength concrete (HSC) has been reported to be a highly sophisticated material that makes its modeling difficult. ANN models [4] have shown to be a powerful tool for calculating the compressive strength and slump of HSC. The ANN models for compressive strength and slump were constructed, trained, and tested using a database of 187 test results arranged in a format of seven input parameters. The mean absolute percentage error found to be less than 1 % for compressive strength and 5 % for slump values, and the corresponding R^2 values were 99.93 % and 99.34 %, respectively. Naderpour and Mirrashid [5] utilized the ANN technique to assess the effect of micro-silica and calcium in silicate minerals on the compressive strength of mortars. The ANN modeling showed high accuracy, functional ability, and acceptable performance in predicting the compressive strength of the tested mortars. Asteris et al. [6] reported ANN to be a proper simulation technique for predicting concrete properties. Duan et al. [7] suggested an ANN model-based explicit formulation for predicting the loss in compressive strength of recycled aggregate concrete. The authors used one hundred forty-six available sets of data from sixteen different published literature sources to construct ANN models with fourteen input parameters. They concluded that with varying the types and sources of recycled aggregates, ANN showed excellent potential as a technique for evaluating the compressive strength of recycled aggregate concretes.

An experimental program [8] consisting of a direct and indirect evaluation of unconfined compressive strength (UCS) of sixty-six granite and limestone sample sets of rocks was carried out. Point load index test, Schmidt hammer rebound number, p-wave velocity test, and dry density test were used as inputs of the network while the output was the UCS values. A PSO-based ANN techniques hybrid model was proposed. Several studies have reported the predictions of the alternative evaluation methods to be often closer to the experimental test data than the predictions from design codes [9]. ANN method performed better and yielded more accurate predictions than the Multiple Linear Regression (MLR) technique for both slump and compressive strength of concrete [10]. From the above review, most of the previous studies were on the compressive strength of concrete, and the application of the ANN technique to predict the concrete deformation in terms of strain at peak stress still needs to be covered.

The objectives of the present study are to evaluate the previously published models relating the strain at peak stress to the compressive strength; to perform experimental tests to assess the stress-strain relationship parameters, compressive strength and its corresponding compressive strain at maximum stress, of normal strength concrete; to use ANN technique to predict the above two parameters based on the experimental results. Finally, the paper sets to develop a model to predict the strain at peak stress based on regression analysis of ANN predicted values.

2. Materials and Methods

2.1. Materials

The following ingredients were used for the twelve concrete mixtures: water, coarse river aggregate, fine river aggregate, and cement.

Ordinary Portland cement with a specific gravity of 3.15 and conforming to ASTM C150 Type I was used for making concrete.

The coarse aggregate for all the mixes was rounded and well-graded river gravel with a maximum aggregate size of 20 mm and specific gravity of 2.72.

The fine aggregate was river sand from the Eski-kalak region north of Iraq with a maximum size of 4.75mm and specific gravity of 2.7.

The quantity of coarse aggregate was adjusted, yielding twelve mixes with aggregate/cement (a/c) ratios ranging from 3 to 8 in increments of 0.5. Tap water was used to hydrate the ordinary Portland cement in a drum-type rotary mixer. All the mix details are summarized in Table 1.

2.2. Methods of Testing

2.2.1. Fresh concrete

The slump test was used to evaluate the consistency of fresh concrete and the effect of change in the mix on fresh concrete properties. The truncated steel cone was filled with the fresh concrete in three equal layers, and each layer was tamped twenty-five times with a steel rod to ensure compaction. The workability of new concrete decreased as the a/c ratio increased, resulting in harsh combinations with increased compaction difficulties. The details of slump results are presented in Table 1. The unit weight of

fresh concrete was measured and computed in Table 1. In general, as the amount of fine material or sand decreased, the unit weight decreased, too.

2.2.2. Hardened concrete

After 28 days of curing, the rough surface of concrete cylinders was capped with a filling material. The specimens were tested in compression under a displacement control mode at a rate of approximately 0.5 mm/min. The relative displacement between the upper and lower loading platens was measured using two linear variable differential transformer (LVDT) and one dial gauge (Fig. 1). Two electrical strain gauges on the surface of cylinders used for longitudinal and lateral strain measurements. There was an inverse relationship between compressive strength and the three test parameters for hardened concrete depending on variations in constituent materials, Table 1.

2.3. Intelligent systems and methods

2.3.1. Artificial neural networks

The neural network modeling process involves five main aspects: data acquisition, analysis, and problem representation; architecture determination; learning process determination; training of the networks; and testing of the trained system for generalization evaluation [1, 11]. ANN procedure handles severe problems via the interaction between nodes (artificial neurons). The ANN model has elements arranged in layers and trained with the data from the experimental results. The first layers of nodes (neurons) get data from the outside environment and transfer it to the nodes of the hidden layer without performing any computation, where the data is processed to draw out useful features. Weights interconnect other nodes in other layers. The output layer neurons produce network predictions. In a three-layer ANN, training data relates between input and output nodes. Due to the ability of neurons to pass and remember the data from experimental results during the training process, the network can learn, categorize, and predict values.

Table 1. Mix details and properties of fresh and hardened concrete.

Specimen	Mix ratio	w/c ratio	Aggregate/ cement ratio	Slump (mm)	γ (kg/m^3)	f_c (MPa)	ε_c
1-1	1:2:1	0.435	3.0	12	2400	38.7	0.00197
1-2	1:2:1	0.435	3.0	12		38.9	0.0019
1-3	1:2:1	0.435	3.0	12		38.5	0.00192
2-1	1:2:1.5	0.450	3.5	10	2400	36.5	0.00187
2-2	1:2:1.5	0.450	3.5	10		38.1	0.00188
2-3	1:2:1.5	0.450	3.5	10		37.5	0.0018
3-1	1:2:2	0.485	4.0	9.5	2380	34.6	0.00179
3-2	1:2:2	0.485	4.0	9.5		34.3	0.00188
3-3	1:2:2	0.485	4.0	9.5		33.7	0.00182
4-1	1:2:2.5	0.505	4.5	9.5	2375	34	0.00177
4-2	1:2:2.5	0.505	4.5	9.5		32	0.00173
4-3	1:2:2.5	0.505	4.5	9.5		32.7	0.00179
5-1	1:2:3	0.51	5.0	8	2370	31.1	0.00168
5-2	1:2:3	0.51	5.0	8		33.3	0.00176
5-3	1:2:3	0.51	5.0	8		32.2	0.00169
6-1	1:2:3.5	0.51	5.5	7	2355	30.8	0.00172
6-2	1:2:3.5	0.51	5.5	7		32	0.00174
6-3	1:2:3.5	0.51	5.5	7		30.8	0.00171
7-1	1:2:4	0.52	6.0	5	2340	28.5	0.00169
7-2	1:2:4	0.52	6.0	5		29.7	0.00176
7-3	1:2:4	0.52	6.0	5		27.6	0.00169
8-1	1:2:4.5	0.535	6.5	5	2325	25.2	0.00157
8-2	1:2:4.5	0.535	6.5	5		24.8	0.00172
8-3	1:2:4.5	0.535	6.5	5		26.5	0.00182
9-1	1:2:5	0.56	7.0	4	2300	20.6	0.00164

Specimen	Mix ratio	w/c ratio	Aggregate/ cement ratio	Slump (mm)	γ (kg/m^3)	f_c (MPa)	ε_c
9-2	1:2:5	0.56	7.0	4		19.6	0.00165
9-3	1:2:5	0.56	7.0	4		21.6	0.00165
10-1	1:2:5.5	0.585	7.5	2.5	2245	19.9	0.00169
10-2	1:2:5.5	0.585	7.5	2.5		18.2	0.00151
10-3	1:2:5.5	0.585	7.5	2.5		19.5	0.00158
11-1	1:2:6	0.6	8.0	0.0	2270	16.3	0.00153
11-2	1:2:6	0.6	8.0	0.0		16.1	0.00154
11-3	1:2:6	0.6	8.0	0.0		17.7	0.00169
12-1	1:2:6.5	0.605	8.5	0.0	2225	15.6	0.00153
12-2	1:2:6.5	0.605	8.5	0.0		16.85	0.00164
12-3	1:2:6.5	0.605	8.5	0.0		16.4	0.00167

A typical node (AN) designed to carry out specific tasks, as shown schematically in Fig. 2. The network supplied with the values of parameters x_j (selected parameters related to the strength characteristics of the concrete) [9]. Each parameter assigned weight w_{ji} and bias Θ_i and this yields the sum n_i of the multiplication:

$$n_i = \sum\left(x_j\right)\left(w_{ji}\right) + \theta_i \tag{1}$$

The n_i is integrated into an established activation function (g):



Figure 1. Testing of concrete specimens.

$$y_i = g_i = g\left(\sum\left(x_i\right)\left(w_{ji}\right) + \theta_i\right) \tag{2}$$

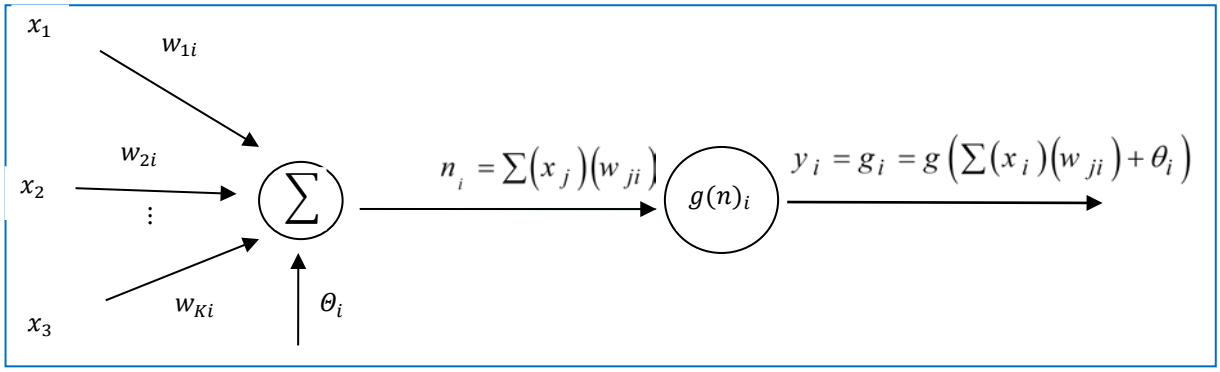


Figure 2. A simple neuron model.

And the result is the output O_i of the AN. Several layers assembled to establish the artificial neural networks used in the present study. The randomly assigned values of the weights and bias undergo iterative training to yield the final results. The architecture of the ANN established through a trial-and-error process related to the type of activation function and the number of neurons in each hidden layer. The goal of this process is to reduce the gap between the ANN output O_i values and the target values T_i [12, 13, 1]. A measure of the deviation of O_i from T_i is given by:

$$E = \frac{1}{2}\sum(T_i - O_i)^2 \quad (3)$$

2.3.2. Adopted ANN models

The three-layer feed-forward type of ANNs was adopted in the present study, Figs. 3 to evaluate the peak stress and Fig.4 to assess the strain at peak stress. The transferred information is processed to extract useful features to reconstruct the architecture from the input space to the output space [15]. If convergence is not achieved, the calculation repeated. Weights fully interconnect the neighboring layers. The network architecture is dictated by the interconnected input, hidden, and output neurons. The weights and processing function of each neuron influence the output layer.

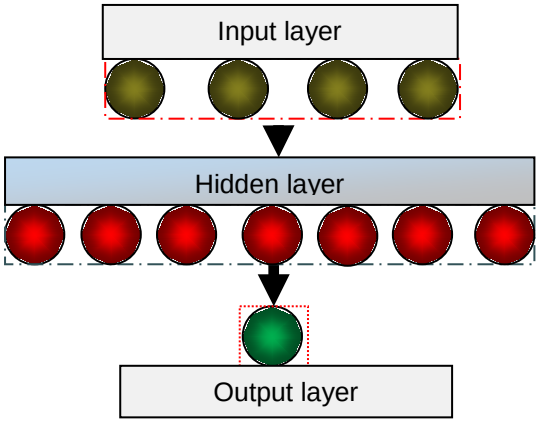


Figure 3. Architecture of ANN model to evaluate peak stress.

Most studies adopted a neural network with one hidden layer that was found sufficient to solve most problems in civil engineering [16–18]. When considering computational efforts required for more hidden layers and an additional number of neurons, one hidden layer reported to be sufficient to produce an acceptable ANN model [19] and to predict the elastic modulus of concrete. When increasing the number of hidden layers, a marginal change in results was obtained [20]. Two ANN models, ANN-1 and ANN-2, with one hidden layer were constructed, trained, and tested using the current experimental test results. The experimental test data was based on two different mix parameters (i.e., w/c and a/c ratios) in addition to slump results. The experimental data was divided into three subcategories of training, validation, and test. Subsequently, the network was trained to minimize the error between the experimental and ANN predicted values.

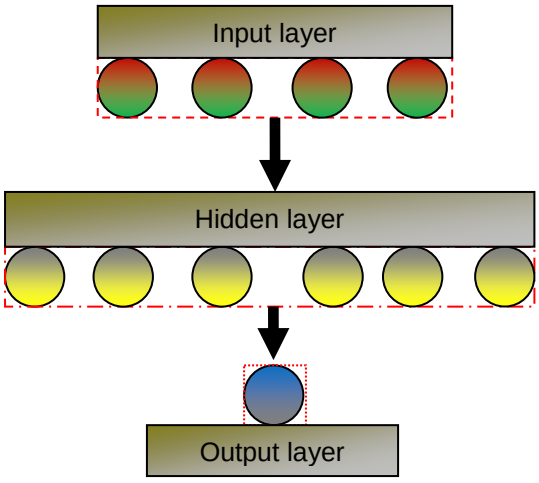


Figure 4. Architecture of ANN model to evaluate strain at peak stress.

The two concrete mix parameters (w/c ratio and a/c ratio) and slump values were used as the four input variables and the bias. The compressive strength and strain at peak stress were the output parameters for the two models, as shown in Figs. 3 and 4, respectively. The hidden layer of the ANN-1 Model to evaluate peak stress (Fig. 3) consisted of seven neurons. In contrast, the same number for the ANN-2 Model to evaluate strain consisted of six neurons (Fig. 4).

3. Results and Discussions

3.1. Strain models

The size and shape of the specimen and concrete physical characteristics influence the strain at peak stress of concrete [21]. Strain is needed to determine the response of a structure to crack control and assess cracking risk [22]. Generally concrete strain is expressed as a function of compressive strength in standard codes and empirical expressions. Different function forms of $\varepsilon_c - f_c$ relationship is found in the literature which can be classified into three groups. The experimental test results were checked against the three groups containing fifty-three existing expressions for strain at peak stress [21–68]. It included the following:

3.3.1. Group one (G-1) with polynomial function

In models with polynomial functions [21, 22, 27], the compressive strength is raised to a non-negative integer power. The leading term or the highest power of the variable in the polynomial function was 3. Among the three models in group one is the model by Tasdemir et al. [22], which was based on tests on concrete with a wide range of strengths from 6 to 105 N/mm^2. Using a total of 228 test results for specimens tested under uniaxial compressive loading conditions, the authors reported a polynomial function to best fit the experimental data with a reasonably good correlation coefficient of 0.75, Table 2.

3.3.2. Group two (G-2) with linear function

Twenty-one models [24–26, 28, 30, 32, 33, 35, 36, 38–40, 47, 49, 54, 56, 59, 60, 62, 63, 65] among the fifty-three models have a linear function. Group two linear models with large database include two models; Chen et al. [60] and Chen et al. [63] with 380 test data from 15 studies.

3.3.3. Group three (G-3) with power functions

The largest group with twenty-nine models [23, 29, 32, 34, 37, 39, 41–46, 48, 50–53, 55, 57, 58, 61, 64, 66a, 67, 68]. Several of these models based on a large database, including De Nicolo et al. [39] using 17 studies, Arıoğlu [42] with 41 sets of test data from 8 studies, Wee et al.[44] with 163 test data, Mansur et al. [48] with 54 test data, Lu and Zhao [55] with 75 test data, Ding et al. [57] with 165 test data, Kumar et al. [58] with 162 test results, Lim and Ozbakkaloglu [61] with 147 test data, Hoang and Fehling [67] with 132 test data from 6 studies. All the equations with a power function have a variable base as a compressive strength raised to power with a small, even positive number. The power ranges from 0.19 [66] (a) to 0.53 [52] and [66]c for most of the studies. However, the model [67] uses power as high as 0.96. On the other hand, the model [68] incorporates negative power (-2.256).

Other studies, not included in Table 2, employed constant values of strain such as 0.002 [44, 69], 0.0022 [70–73], 0.0024 [74], and 0.003 [75, 76]. The ε_c =0.003 was suggested to be used for design purposes, for concrete compressive strengths up to 124MPa [75, 76].

Table 2. Models used to predict the strain at peak stresses.

Year	Source	Model	Strength range MPa	No. of test data	Comments
1993	Collins et al. [21]	$\varepsilon_c = \frac{f_c\left(0.0588 f_c + 0.8\right)}{\left(3220 {f_c}^{0.5} + 6900\right)\left(0.0588 f_c - 0.2\right)}$ ε_c is strain at peak stress f_c is compressive strength	21 to 83MPa	14	
1998	Tasdemir et al.[22]	$\varepsilon_c = \left(-0.067 \frac{{f_c}^2}{{f_c}^*} + 29.9 \frac{f_c}{{f_c}^*} + 1053\right) 10^{-6}$ f^* = 1 MPa	6 to 105MPa	228 from 12 studies	R^2= 0.75

Year	Source	Model	Strength range MPa	No. of test data	Comments
1936	Emperger [23]	$\varepsilon_c = \left(0.0445\left(f_c\right)^{0.5}\right)10^{-2}$			For concrete with a low level of sand
1950	Ros [24]	$\varepsilon_c = \left(0.0546 + 0.003713 f_c\right)10^{-2}$			
1955	Hognestad et al. [25]	$\varepsilon_c = \left(0.004 + \frac{f_c}{6.5_c}\ 10^{-6}\right)$	5 to 52.4	26	
1962	Liebenberg [26]	$\varepsilon_c = \left(0.004 + \frac{f_c}{(0.73)(8.3)}10^{-6}\right)$	7 to 69		
1964	Saenz [27]	$\varepsilon_c = 0.12\left(f_c\right)^{0.25}\left[9 - \left(f_c\right)^{0.25}\right]10^{-3}$			
1967	Soliman et al.[28]	$\varepsilon_c = 2\left(f_c\right) / 25097^{*}$ *MPa		16	
1970	Popovics [29]	$\varepsilon_c = 0.000735\left(f_c\right)^{0.25}$			
1970	Tadros [30]	$\varepsilon_c = \left(1.6 + 0.01 f_c\right)10^{-3}$			
1973	Popovics [31]	$\varepsilon_c = 0.000937\left(f_c\right)^{0.25}$			Curve fitting using data from another reference
1976	Bashur and Darwin[32]	$\varepsilon_c = \frac{f_c}{363000 + 400 f_c}$ (f_c in psi)	(f_c in psi)		Curve fitting using data from another
1982	Ahmad-Shah [33]	$\varepsilon_c = 0.001648 + 1.65\left(f_c\right)10^{-5}$	20 to 75		
1984	Tomaszewicz [34]	$\varepsilon_c = 700\left(f_c\right)^{0.31}10^{-6}$	f_c≤ 85MPa		High-strength
1985	Shah-Fafitis [35]	$\varepsilon_c = 1.491\left(10^{-5}\right)\left(f_c\right) + 0.00195$			
1986	Carreira-Chu [36]	$\varepsilon_c = 0.71\left(10^{-5}\right)\left(f_c\right) + 0.00168$	8.96 to 52.4	9	Data from two studies
1990	Ali et al. [37]	$\varepsilon_c = 0.000875\left(f_c\right)^{0.25}$	16.7 to 43.5	12	
1994	Hsu and Hsu [38]	$\varepsilon_c = 1.29\left(10^{-5}\right)\left(f_c\right) + 2.114\left(10^{-3}\right)$	65.8 to 91.4	14	
1994	De Nicolo et al. [39]	$\varepsilon_c = 0.00076 + \left[\left(0.626\frac{f_c}{f^{*}} - 4.33\right)10^{-7}\right]^{0.5}$	10 MPa≤ f_c≤ 100 MPa	Not given 17 studies	
	Brandtzaeg [39]	$_c = \frac{f_c}{46.886 + 2.6 f_c}10^{-2}$			
1995	Almusallam and Alsayed [40]	$\varepsilon_c = \left(0.398 f_c + 18.147\right)10^{-4}$	20 to 110MPa		
1995	CEB-FIB [41]	$\varepsilon_c = \left(0.7 f_c\right)^{0.31}\left(10^{-3}\right)$	fc≤ 100MPa		
1995	Arıoğlu [42]	$\varepsilon_c = 1.753\left(f_c\right)^{0.27756}\left(V\right)^{-0.09314}$	V=volume	41 from 8 studies	R^2= 0.874

Year	Source	Model	Strength range MPa	No. of test data	Comments
1996	Attard and Setunge [43]	$\varepsilon_c = \frac{3.78 f_c}{E_c \sqrt[4]{f_c}}$	> 40MPa		
1996	Wee et al.[44]	$\varepsilon_c = 0.00078 (f_c)^{0.25}$		163	
1997	Guo [45]	$\varepsilon_c = \left(700 + 172 \left(\sqrt[2]{f_c}\right)\right) 10^{-3}$	Up to 120MPa		
1998	Xu [46]	$\varepsilon_c = \left(966 + 155.64 \left(\sqrt[2]{f_c - 13.77}\right)\right) 10^{-3}$			high-performance concrete
1999	CEB-FIB [47]	$\varepsilon_c = \left(1.7 + \frac{f_c}{f_{cmo}}\right) 10^{-3}$	f_{cmo}=70, f_c≤100MPa f_c≤100MPa		
1999	Mansur et al. [48] a	$\varepsilon_c = 0.0005 (f_c)^{0.35}$	70 to 120MPa	54	For cylinders
1999	Mansur et al. [48] b	$\varepsilon_c = 0.00048 (f_c)^{0.35}$	70 to 120MPa	54	For prisms
2002	Lee [49] c	$\varepsilon_c = \frac{f_c}{(46.886 + 2.6 f_c) 10^2}$	75 to 78	20 HPC	
2003	NS 3473[50]	$\varepsilon_c = \frac{0.7}{1000} (f_c)^{0.31}$	f_c=peak stress		
2003	Yu and Ding [51]	$\varepsilon_c = \left(383 f_{cu}^{7/18}\right) 10^{-6}$			$f_c = 0.4 f_{cu}^{7/6}$
2004	EC2 [52]	$\varepsilon_c = 2 + 0.085 (f_c - 50)^{0.53}$	50MPa≤f_c≤ 100MPa		0.002 for f_c<50MPa
2004	Tasnimi [53]	$\varepsilon_c = \left(65.57 f_c^{0.44} - 6.748\right) 10^{-5}$			
2006	Mertol [54]	$\varepsilon_c = 0.0033 - 13.793 \left(10^{-5}\right) f_c$	69 to 124	21	
2008	Lu and Zhao [55]	$\varepsilon_c = 430 (f_c)^{0.38} \left(10^{-6}\right)$	42.7 to 125.6	75	
2010	Arslan and Cihanli[56]	$\varepsilon_c = 0.002 + \left(\frac{0.001 (f_c - 20)}{70}\right)$	50MPa≤f_c< 100MPa		
2011	Ding et al. [57] a	$\varepsilon_c = 520 (f_c)^{1/3} \left(10^{-3}\right)$	20 to 150MPa from five studies	165groups	
2011	Ding et al. [57] b	$\varepsilon_c = 383 (f_{cu})^{7/18} \left(10^{-6}\right)$	30 to 150MPa from four	58 groups	$f_c = 0.4 f_{cu}^{7/6}$
2011	Kumar et al. [58]	$\varepsilon_c = 0.0006 (f_c)^{1/3} \left(10^{-3}\right)$	35 to 70MPa	162 cylinders	self-compacting concrete
2013	Hussin et al. [59]	$\varepsilon_c = 2 (f_c) \left(10^{-5}\right) + 0.0008$	9.25 to 38	26	
2013	Chen et al.[60]	$\varepsilon_c = 1.74 (f_c) \left(10^{-6}\right) + (2.41) \left(10^{-3}\right)$	HSC considering size effect	380 from 15 studies	COV=0.176

Year	Source	Model	Strength range MPa	No. of test data	Comments
2014	Lim and Ozbakkaloglu[61]	$\varepsilon_c = \left(f_{co}^{\,0.225k_d}\right)\left(10^{-3}\right)k_s k_a$ $k_s = 1, k_a = 1$	10MPa≤f_c≤ 150MPa	147	R^2=0.626 NWC
2015	Ahmed et al.[62]	$\varepsilon_c = 0.00003\left(f_c\right) + 0.001$	5.9 to 26.5	78	R^2=0.49
2015	Chen et al.[63]	$\varepsilon_c = 4.76\left(f_c\right)10^{-6} + \left(2.13\right)10^{-3}$	20 to 105	380 from 15 studies	COV=0.14
2016	Wang et al. [64]	$\varepsilon_c = 0.5\left(1.95 + 0.01491 f_c + 0.763\sqrt[4]{f_c}\right)$	f_c≤200MPa		
2016	Shanaka [65]	$\varepsilon_c = 1.1\left(\frac{f_c}{E_c}\right)$	95 to 147MPa	18	
2016	Nematzadeh et al.[66] a	$\varepsilon_c = \left(1074 f_c^{\,0.19}\right)10^{-6}$	17.9-52.6MPa RC	30	R^2=0.62, reference concrete (RC)
2016	Nematzadeh et al.[66] b	$\varepsilon_c = 402\left(10^{-6}\right)\left(f_c^{\,0.41}\right)$	43-83MPa LPCC	30	R^2=0.55, long-term pressure-compressed concrete
2016	Nematzadeh et al.[66] c	$\varepsilon_c = 225\left(10^{-6}\right)\left(f_c^{\,0.53}\right)$	44-91MPa SPCC	30	R^2=0.74,Short-term pressure-compressed concrete
2017	Hoang and Fehling[67]	$\varepsilon_c = 0.0257\left(10^{-2}\right)\left(f_c^{\,0.96}\right)$	100≤f_c ≤150MPa	132 from 6 studies	R^2=0.86, UHPC; Ultra-high performance concrete
2017	Aslam et al.[68]	$\varepsilon_c = 18.938\left(f_c\right)^{-2.256}$	42.5 to 52	9 *LWA*	R^2=0.96
	Proposed	$\varepsilon_c = 0.001\left(f_c\right)^{0.17}$	16.1 to 38.9MPa	36	R^2=0.82

3.2. ANN models

A total of 36 data sets with minimum and maximum concrete strengths of 15.6 MPa and 38.9MPa were unequally divided and used for training (approximately 80% of modeling) and the rest for testing (about 20%) of the model. The ANN approach considers several parameters affecting the strength of

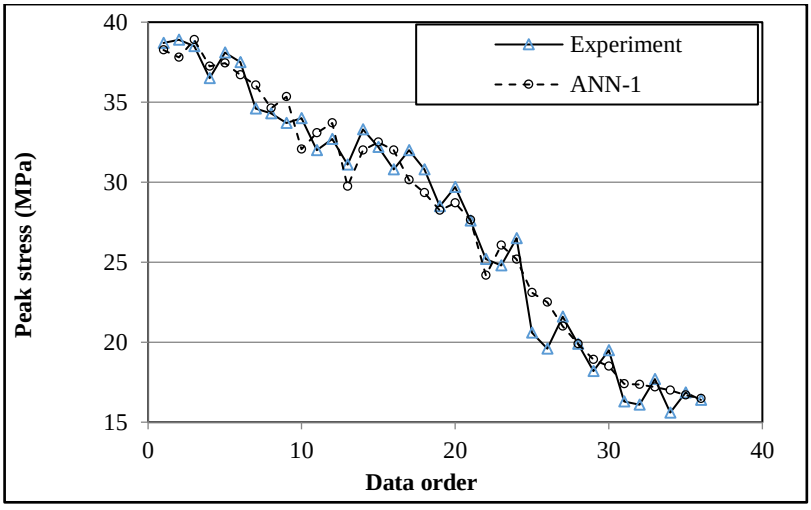


Figure 5. Comparison of predicted peak stress (ANN-1) with experimental peak stress.

concrete at the same time [19]. The experimental compressive strength and predicted strength values using the ANN-1 model were plotted in Fig.5. A similar procedure followed for strain at peak stress, using ANN-2 model, as shown in Fig. 6. The results showed that, on average, the peak stress decreased as aggregate/cement ratio and w/c ratio increased.

In Figure 6, the trend for the experimental strain was more to increase with a decrease in the aggregate/cement ratio, and this follows the same trend for predicted strain at peak stress using the ANN-2 model. ANN models have captured the inter-relationships between input and output data pairs. The curves plotted in Fig. 5 for peak stress and Fig. 6 for corresponding strain demonstrate that the neural network was effective in learning the relationship between the different input parameters and the outputs, compressive strength, and strain at peak stress. The error between the predicted and experimental values then was computed. The output error can be minimized by modifications on the weights and bias at each neuron. The connections which could be positive or negative were not shown in Figs. 3 and 4. Instead, all the connection weights and biases used to predict the peak stress of concrete were computed in Table 3, and the connection weights and biases used to predict the strain at peak stress of concrete were summarized in Table 4.

Table 3. Connection weights and biases used to predict the strength of concrete.

Neuron	w/c	a/c	Slump	(Bias)
1	-0.423	0.242	0.205	-0.152
2	.171	.039	-.208	.338
3	-.284	-.205	.190	.380
4	-.868	-.319	-.083	.046
5	.347	.293	-.109	.230
6	.437	.404	.066	.075

Neuron	1	2	3	4	5	6	(Bias)
fco	0.144	-0.177	0.326	0.673	0.027	-0.481	-0.010

Table 4. Connection weights and biases used to predict the peak strain of concrete.

Neuron	w/c	a/c	slump	(Bias)
1	-.346	-.246	.509	-.732
2	-.729	.447	.136	-.078
3	.703	-.697	.174	-.034
4	.568	-.286	.072	.132
5	.053	-.340	-.915	.951

Neuron	1	2	3	4	5	(Bias)
Strain	0.538	0.709	-0.820	-0.441	-1.176	1.013

In normal strength concretes the elastic mismatch of aggregate and the matrix is significant, leading to large tangential, radial, and shear stresses at the paste-aggregate interface [22]. In the current study, the predicted peak strain values, using ANN-2 model, were plotted versus the corresponding predicted maximum stress, using the ANN-1 model and the graph was fitted with a nonlinear curve to find the relationship between the two variables. Consequently, an equation obtained and proposed for peak strain predictions, as summarized in Table 2.

3.3. Statistical indices

Several standard statistics used to assess the performances of the existing fifty-three equations for the strain at peak stress which include:

3.3.1. Normalized root-mean-square error (NRMSE)

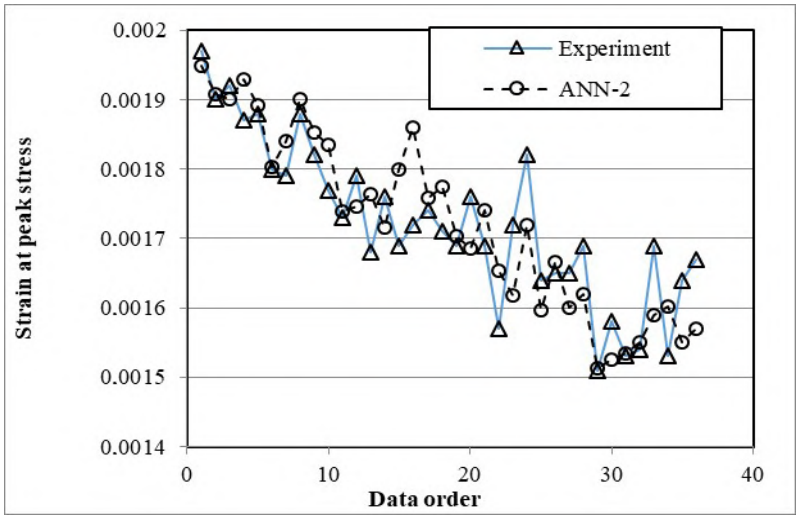


Figure. 6. Comparison of predicted strain at peak stress (ANN-2) with the corresponding experimental values.

$$NRMSE = \frac{\sqrt{\sum_{i=1}^{N}\left(\exp._i - model_i\right)^2}}{\sum_{i=1}^{N}\exp._i} \quad (4)$$

Where the model prediction is expressed by ($model._i$), the experimental value is represented by ($exp.i$), and N is the total number of data.

3.3.2. Average absolute error (AAE)

$$AAE = \frac{\sum_{i=1}^{N}\left|\frac{model_i - \exp._i}{\exp._i}\right|}{N} \quad (5)$$

Lower AAE values indicate excellent model performance.

3.3.3. Nash–Sutcliffe efficiency (E)

$$E = 1 - \frac{\sum_{i=1}^{N}\left(\exp._i - model_i\right)^2}{\sum_{i=1}^{N}\left(\exp._i - aver.\exp._i\right)^2} \quad (6)$$

An E value of over 0.80 is considered good.

3.3.4. Modified Nash–Sutcliffe efficiency (E1)

$$E1 = 1 - \frac{\sum\left|\exp._i - model_i\right|}{\sum\left|\exp._i - aver.\exp._i\right|} \quad (7)$$

The Modified Nash–Sutcliffe efficiency is based on absolute deviations instead of squares of the deviations.

3.3.5. Coefficient of correlation (R^2)

$$R^2 = \left(\frac{\sum_{i=1}^{N}\left(\exp._i - aver.\exp._i\right)\left(model_i - model_i aver\right)}{\sum_{i=1}^{N}\left(\exp._i - aver.\exp._i\right)^2 \sum_{i=1}^{N}\left(model_i - model_i aver\right)^2}\right)^2 \quad (8)$$

R^2 is the rate of association between the two variables, and many outliers result in weak R^2. The statistical measures also used to determine the performance of the two trained ANN models.

3.4. Strain at peak stress

The fifty-three existing strain models found in the literature [21-68] and the proposed ANN-based model were used to predict the strains (ε_c) at the peak stress and were compared with the experimental results. All the models for the strain at peak stress prediction summarized in Table 2 including the proposed ANN-based model. Some models have limitations that make these models not applicable to the strength range of the present study, but were included for comparison purposes. The predicted strains and the best fitting line or curve for each model shown in Fig. 7 for G-1 models with polynomial functions. Also shown in Fig.7 is the predictions by the proposed ANN-based model. A significant trend is observed as the compressive stress of concrete increases, the strain at peak stress increases, too [21, 22, 27]. The same thing is correct for the proposed equation. Model [22] exhibit good predictions for concrete strengths up to 25MPa. However, at strengths beyond 25Mpa the error increases. The model [27] show a reasonable performance for all the strength range tested in the present study. The third model in G-1 over predicts the strain values, Fig.7. The proposed strain equation out performed all the three models in G-1 with very good predictions, Fig.7.

Fig. 8 shows predictions and best-fitting lines for the models with linear function in addition to the proposed model. The predicted strains spread over a wide strain range, 0.0001 to 0.004. The best-fitting lines or curves for some of the models [28, 40,49, 54] become steeper away from the origin. All models prediction show an increase in compressive strength, except the EC2 model, which shows a reverse trend because it is proposed for strengths higher than 50 MPa, which is beyond the experimental strength range covered in the present study. As can be seen, most of the models overestimated the strain values, and some models largely over-predicted the experimental strain values [25, 26, 40]. Using model [24], a better prediction of strain at lower values of f_c is observed. The opposite can be said for other models [28].

The predictions of models using power functions are displayed in Fig. 9. The predictions with best-fitting curves in Fig. 9 compared with Fig. 8 are more compact with fewer models overestimating the predicted strain values, except for model 67 which was proposed for ultra-high-strength concrete. In contrast to models with a linear function, only a couple of models with power functions underestimated the values for the strain at peak stress, [57]a and [66]c. Some models showed a better prediction of strain at lower values of f_c, example model [23]. This trend is reversed in the predictions of other models, such as model [55]. Over all, the models with linear functions, Fig. 8, displayed more change in the best-fitting line slope than models in Fig.9. Most existing model predictions are higher than the test data and the proposed model, this is ascribed to the fact that these models were developed for concretes with higher strength.

3.5. $\varepsilon_{c\,Pre}/\varepsilon_{c\,Exp}$ ratio

To further assess the performance of the fifty-three existing models and the proposed model, the ratio of the predicted strain ($\varepsilon_{c\,Pre}$) to the experimental strain ($\varepsilon_{c\,Exp}$) at peak stress was computed and shown in Table 5. Five statistical indexes used to evaluate the percentage of error or the degree of association between the experimental test results and their corresponding predicted values. The difference between the experimental and predicted values of the strain at peak stress was summarized in Table 6. Other statistical indexes including minimum predictions (Min.), maximum predictions (Max.), mean, standard deviation (STD), and coefficient of variance (COV) are also shown in Table 6. Lower values of NRMSE and AAE show good performance of the models. In contrast, higher values of E, $E1$, and R^2 show less error measured between the predicted and experimental values.

Statistics on the performance of fifty-three existing models and the proposed model illustrate that the values of NRMSE ranged from 0.0011(proposed model) to 0.27 [68] and for AAE ranged from 3.46% (proposed model) to 785.81% [68]. A similar observation made for the other indexes. The six models with least values of NRMSE and AAE included the proposed model, [44], [51], [58], [33], and [27] with values of 0.0011, 0.0014, 0.0019, 0.0018, 0.0021, 0.0025 and 3.46%, 4.445% , 5.34%, 5.712%, 6.072%, 6.761% respectively. Among the six models with the least values of NRMSE and AAE, four models have power function, one model with a linear function, and one model with a polynomial function. This indicates that models with power functions showed better performance compared with the other two types of models. Ahmed-Shah's [33] model with a linear function yielded nearly a horizontal best-fitting line and shows reasonable predictions with NRMSE and AAE values of 0.0025 and 6.761%, respectively. For the range of strength considered in the present study, the constant value of the model [33] controls the outcome of the strain values with the variable parameter (f_c) having a minor role. The model [44] with AAE values of 4.445% displayed reasonable predictions of strain. The proposed model with AAE values of 3.46% yielded the lowest AAE values with predictions of strain at peak stress very close to the experimental strain values. The proposed model showed good performance with the highest values of E and E1. Furthermore, the

proposed model yielded the lowest values of NRMSE among all the models, as shown in Fig. 10. The R^2 value for the proposed model (0.708) was slightly lower than for models [35, 36] with similar values of 0.736, Table 6. Few equations found to reasonably predict the strains at peak stress for the different concrete mixtures. As it was explained before, several existing strain models have been calibrated for high-strength concrete and show poor performance when used to predict the strain of normal strength concrete. Furthermore, most of these models derived from simple regression analysis based on test results carried out by the generators of the models and applicable for a particular type of concrete. Several of these expressions are valid within limited ranges of strength and not for other varieties. The complex relations developed between the mix proportions of concrete and the compressive strength can be captured better by the ANN-based model, which trained to yield low mean squared error and absolute average error between the experimental results and the network predicted values.

Table 5. The ratio of $\varepsilon_{c\ Pre}/\varepsilon_{c\ Exp}$ using existing fifty-three models and the proposed model.

	$\varepsilon_{c\ Pre}/\varepsilon_{c\ Exp}$														
Specimen	[21]	[22]	[23]	[24]	[25]	[26]	[27]	[28]	[29]	[30]	[31]	[32]	[33]	[34]	[35]
1-1	1.081	1.071	1.405	1.007	2.033	2.034	0.988	1.565	0.931	1.009	1.186	1.092	1.161	1.104	1.283
1-2	1.122	1.113	1.461	1.048	2.108	2.108	1.026	1.632	0.966	1.047	1.232	1.133	1.205	1.146	1.332
1-3	1.107	1.096	1.438	1.029	2.086	2.086	1.013	1.598	0.954	1.034	1.216	1.12	1.189	1.131	1.315
2-1	1.121	1.099	1.438	1.017	2.142	2.142	1.032	1.555	0.966	1.051	1.232	1.141	1.203	1.142	1.334
2-2	1.128	1.114	1.461	1.043	2.131	2.131	1.033	1.615	0.971	1.054	1.238	1.142	1.211	1.151	1.339
2-3	1.173	1.156	1.514	1.077	2.225	2.225	1.077	1.66	1.01	1.097	1.288	1.19	1.259	1.196	1.394
3-1	1.156	1.121	1.462	1.023	2.238	2.238	1.069	1.54	0.996	1.087	1.27	1.183	1.24	1.173	1.378
3-2	1.098	1.064	1.386	0.968	2.13	2.13	1.016	1.454	0.946	1.034	1.206	1.125	1.178	1.114	1.309
3-3	1.13	1.09	1.419	0.988	2.201	2.201	1.047	1.476	0.973	1.064	1.24	1.158	1.211	1.144	1.348
4-1	1.164	1.126	1.466	1.022	2.263	2.263	1.078	1.531	1.003	1.096	1.278	1.193	1.248	1.18	1.388
4-2	1.174	1.122	1.455	1.002	2.315	2.315	1.092	1.474	1.01	1.11	1.288	1.209	1.258	1.185	1.403
4-3	1.141	1.094	1.422	0.983	2.237	2.237	1.059	1.456	0.982	1.077	1.252	1.172	1.222	1.153	1.362
5-1	1.202	1.142	1.477	1.012	2.384	2.384	1.12	1.475	1.033	1.138	1.317	1.239	1.286	1.209	1.437
5-2	1.165	1.122	1.459	1.013	2.276	2.276	1.081	1.508	1.003	1.098	1.279	1.196	1.249	1.179	1.39
5-3	1.204	1.152	1.494	1.031	2.37	2.37	1.119	1.518	1.036	1.137	1.321	1.239	1.29	1.215	1.438
6-1	1.172	1.111	1.436	0.982	2.328	2.328	1.092	1.427	1.007	1.109	1.283	1.208	1.254	1.178	1.401
6-2	1.168	1.116	1.447	0.997	2.302	2.302	1.086	1.466	1.005	1.103	1.281	1.202	1.251	1.178	1.395
6-3	1.179	1.117	1.444	0.988	2.342	2.342	1.098	1.435	1.013	1.116	1.291	1.215	1.261	1.185	1.409
7-1	1.174	1.095	1.406	0.949	2.369	2.369	1.097	1.344	1.005	1.115	1.281	1.213	1.253	1.17	1.405
7-2	1.137	1.069	1.378	0.937	2.275	2.275	1.061	1.345	0.975	1.078	1.243	1.173	1.215	1.138	1.36
7-3	1.168	1.081	1.383	0.929	2.369	2.369	1.092	1.301	0.997	1.11	1.271	1.206	1.245	1.158	1.397
8-1	1.239	1.124	1.423	0.944	2.55	2.55	1.158	1.279	1.049	1.18	1.337	1.276	1.315	1.212	1.481
8-2	1.128	1.019	1.288	0.853	2.328	2.328	1.054	1.149	0.954	1.074	1.216	1.161	1.196	1.101	1.349
8-3	1.077	0.988	1.259	0.841	2.2	2.2	1.007	1.16	0.916	1.025	1.168	1.111	1.146	1.062	1.289
9-1	1.161	1	1.232	0.799	2.441	2.441	1.071	1.001	0.955	1.101	1.217	1.169	1.212	1.09	1.376
9-2	1.151	0.978	1.194	0.772	2.426	2.426	1.055	0.947	0.937	1.088	1.195	1.148	1.195	1.067	1.359
9-3	1.158	1.011	1.253	0.817	2.426	2.426	1.073	1.043	0.96	1.101	1.224	1.175	1.215	1.1	1.377
10-1	1.125	0.959	1.175	0.76	2.369	2.369	1.033	0.938	0.919	1.064	1.171	1.125	1.169	1.047	1.329
10-2	1.255	1.043	1.257	0.809	2.651	2.651	1.138	0.961	1.005	1.18	1.282	1.232	1.29	1.14	1.471
10-3	1.202	1.019	1.244	0.804	2.534	2.534	1.101	0.984	0.978	1.136	1.246	1.198	1.247	1.113	1.418
11-1	1.241	0.995	1.174	0.752	2.616	2.616	1.102	0.849	0.965	1.152	1.231	1.181	1.253	1.087	1.433

	$\varepsilon_{c\,Pre}/\varepsilon_{c\,Exp}$														
Specimen	[21]	[22]	[23]	[24]	[25]	[26]	[27]	[28]	[29]	[30]	[31]	[32]	[33]	[34]	[35]
11-2	1.234	0.985	1.159	0.743	2.599	2.599	1.092	0.833	0.956	1.144	1.219	1.169	1.243	1.076	1.422
11-3	1.121	0.924	1.108	0.712	2.368	2.368	1.012	0.835	0.892	1.051	1.137	1.093	1.148	1.009	1.31
12-1	1.244	0.982	1.149	0.735	2.616	2.616	1.093	0.813	0.955	1.148	1.217	1.166	1.245	1.072	1.427
12-2	1.157	0.938	1.114	0.714	2.441	2.441	1.034	0.819	0.908	1.078	1.158	1.112	1.174	1.024	1.342
12-3	1.137	0.913	1.079	0.692	2.397	2.397	1.01	0.783	0.886	1.056	1.129	1.084	1.149	0.998	1.314

Table 5 continued.

	$\varepsilon_{c\,Pre}/\varepsilon_{c\,Exp}$														
Specimen	[36]	[37]	[38]	[39]	[39]b	[40]	[41]	[42]	[43]	[44]	[45]	[46]	[47]	[48]a	[48]b
1-1	0.992	1.108	1.327	1.102	1.332	1.703	1.104	1.237	1.218	0.988	0.898	0.885	1.144	0.912	0.876
1-2	1.03	1.15	1.377	1.145	1.383	1.77	1.146	1.284	1.265	1.025	0.933	0.919	1.187	0.948	0.91
1-3	1.017	1.135	1.36	1.128	1.364	1.743	1.131	1.267	1.247	1.012	0.92	0.906	1.172	0.935	0.897
2-1	1.037	1.15	1.382	1.134	1.377	1.747	1.142	1.282	1.255	1.025	0.93	0.913	1.188	0.942	0.904
2-2	1.038	1.156	1.386	1.147	1.389	1.772	1.151	1.29	1.269	1.031	0.937	0.922	1.194	0.951	0.913
2-3	1.081	1.203	1.443	1.191	1.443	1.837	1.196	1.342	1.317	1.072	0.974	0.958	1.242	0.988	0.948
3-1	1.076	1.186	1.43	1.16	1.413	1.783	1.173	1.32	1.285	1.057	0.956	0.937	1.226	0.966	0.927
3-2	1.023	1.126	1.36	1.101	1.341	1.691	1.114	1.253	1.219	1.004	0.908	0.889	1.165	0.917	0.88
3-3	1.055	1.158	1.4	1.129	1.377	1.734	1.144	1.288	1.251	1.033	0.933	0.913	1.199	0.941	0.903
4-1	1.086	1.194	1.442	1.165	1.42	1.79	1.18	1.328	1.291	1.064	0.962	0.941	1.235	0.971	0.932
4-2	1.102	1.203	1.461	1.164	1.422	1.785	1.185	1.336	1.29	1.072	0.967	0.943	1.247	0.972	0.933
4-3	1.068	1.169	1.417	1.134	1.385	1.741	1.153	1.299	1.257	1.042	0.941	0.918	1.211	0.947	0.909
5-1	1.131	1.23	1.497	1.185	1.449	1.817	1.209	1.365	1.314	1.096	0.988	0.961	1.276	0.991	0.951
5-2	1.089	1.194	1.445	1.162	1.418	1.784	1.179	1.328	1.288	1.065	0.962	0.94	1.236	0.969	0.93
5-3	1.129	1.233	1.497	1.194	1.459	1.832	1.215	1.37	1.324	1.099	0.992	0.967	1.278	0.997	0.957
6-1	1.104	1.198	1.46	1.153	1.41	1.768	1.178	1.33	1.279	1.068	0.962	0.935	1.244	0.965	0.926
6-2	1.096	1.196	1.452	1.157	1.414	1.775	1.178	1.328	1.283	1.066	0.961	0.937	1.24	0.967	0.928
6-3	1.11	1.205	1.469	1.159	1.419	1.778	1.185	1.337	1.286	1.075	0.968	0.941	1.251	0.97	0.932
7-1	1.114	1.196	1.468	1.137	1.394	1.745	1.17	1.324	1.263	1.066	0.958	0.925	1.247	0.956	0.917
7-2	1.074	1.161	1.419	1.11	1.36	1.703	1.138	1.286	1.232	1.035	0.93	0.902	1.207	0.931	0.894
7-3	1.11	1.187	1.462	1.123	1.376	1.724	1.158	1.313	1.247	1.058	0.949	0.914	1.239	0.945	0.907
8-1	1.184	1.249	1.554	1.165	1.428	1.795	1.212	1.378	1.295	1.113	0.996	0.95	1.312	0.985	0.946
8-2	1.079	1.135	1.415	1.057	1.295	1.629	1.101	1.252	1.175	1.012	0.905	0.862	1.194	0.894	0.859

8-3	1.026	1.091	1.349	1.026	1.258	1.577	1.062	1.205	1.14	0.972	0.871	0.836	1.142	0.865	0.83
9-1	1.114	1.137	1.451	1.028	1.251	1.606	1.09	1.247	1.143	1.013	0.903	0.837	1.216	0.879	0.844
9-2	1.103	1.116	1.434	1.001	1.214	1.573	1.067	1.223	1.114	0.995	0.886	0.813	1.2	0.859	0.824
9-3	1.111	1.143	1.45	1.042	1.27	1.621	1.1	1.256	1.158	1.019	0.909	0.849	1.217	0.888	0.853
10-1	1.078	1.094	1.403	0.983	1.194	1.542	1.047	1.199	1.094	0.975	0.868	0.8	1.174	0.843	0.809
10-2	1.198	1.197	1.555	1.06	1.279	1.681	1.14	1.309	1.18	1.067	0.95	0.857	1.298	0.914	0.878
10-3	1.151	1.164	1.497	1.043	1.265	1.64	1.113	1.275	1.16	1.037	0.924	0.847	1.252	0.895	0.859
11-1	1.174	1.149	1.519	0.998	1.193	1.61	1.087	1.253	1.112	1.024	0.911	0.793	1.263	0.868	0.833
11-2	1.165	1.138	1.508	0.986	1.178	1.594	1.076	1.24	1.1	1.015	0.903	0.782	1.253	0.859	0.824
11-3	1.068	1.062	1.386	0.936	1.127	1.491	1.009	1.16	1.042	0.947	0.842	0.754	1.156	0.809	0.777
12-1	1.17	1.137	1.513	0.979	1.166	1.592	1.072	1.238	1.092	1.013	0.902	0.769	1.257	0.855	0.821
12-2	1.097	1.081	1.422	0.944	1.133	1.515	1.024	1.179	1.052	0.964	0.857	0.756	1.183	0.819	0.787
12-3	1.076	1.054	1.393	0.916	1.097	1.477	0.998	1.15	1.022	0.94	0.836	0.73	1.158	0.797	0.765

Table 5 continued.

	$\varepsilon_{c\,Pre}/\varepsilon_{c\,Exp}$											
Specimen	[49]	[50]	[51]	[52]	[53]	[54]	[55]	[56]	[57] a	[57] b	[58]	[59]
1-1	1.332	1.104	0.939	1.171	1.629	1.034	0.876	1.151	0.892	0.806	1.018	0.799
1-2	1.383	1.146	0.975	1.213	1.692	1.087	0.91	1.195	0.926	0.837	1.057	0.831
1-3	1.364	1.131	0.962	1.203	1.667	1.047	0.897	1.179	0.913	0.825	1.042	0.818
2-1	1.377	1.142	0.97	1.25	1.671	0.928	0.902	1.196	0.921	0.83	1.052	0.818
2-2	1.389	1.151	0.979	1.232	1.695	1.04	0.912	1.201	0.93	0.839	1.061	0.831
2-3	1.443	1.196	1.017	1.291	1.757	1.04	0.947	1.25	0.966	0.871	1.102	0.861
3-1	1.413	1.173	0.995	1.32	1.704	0.823	0.924	1.234	0.946	0.849	1.079	0.834
3-2	1.341	1.114	0.945	1.258	1.616	0.761	0.876	1.172	0.898	0.806	1.025	0.79
3-3	1.377	1.144	0.971	1.304	1.656	0.741	0.899	1.206	0.922	0.826	1.052	0.81
4-1	1.42	1.18	1.001	1.339	1.71	0.785	0.928	1.243	0.951	0.853	1.085	0.836
4-2	1.422	1.185	1.004	1.383	1.703	0.644	0.928	1.255	0.953	0.852	1.088	0.832
4-3	1.385	1.153	0.977	1.332	1.662	0.676	0.904	1.219	0.928	0.83	1.059	0.812
5-1	1.449	1.209	1.024	1.431	1.731	0.589	0.945	1.285	0.972	0.868	1.11	0.846
5-2	1.418	1.179	1	1.351	1.704	0.735	0.926	1.244	0.949	0.851	1.084	0.833
5-3	1.459	1.215	1.029	1.415	1.748	0.675	0.952	1.287	0.978	0.874	1.116	0.854
6-1	1.41	1.178	0.997	1.399	1.683	0.551	0.92	1.252	0.947	0.844	1.081	0.823
6-2	1.414	1.178	0.998	1.375	1.693	0.64	0.922	1.248	0.948	0.847	1.082	0.828

	$\varepsilon_{c\,Pre}/\varepsilon_{c\,Exp}$											
Specimen	[49]	[50]	[51]	[52]	[53]	[54]	[55]	[56]	[57] a	[57] b	[58]	[59]
6-3	1.419	1.185	1.002	1.408	1.693	0.555	0.925	1.26	0.952	0.849	1.087	0.828
7-1	1.394	1.17	0.988	1.439	1.654	0.373	0.909	1.255	0.939	0.834	1.072	0.811
7-2	1.36	1.138	0.962	1.375	1.618	0.453	0.886	1.215	0.914	0.814	1.044	0.792
7-3	1.376	1.158	0.978	1.445	1.63	0.3	0.898	1.248	0.929	0.824	1.061	0.8
8-1	1.428	1.212	1.021	1.571	1.685	0.112	0.933	1.321	0.97	0.856	1.108	0.831
8-2	1.295	1.101	0.927	1.436	1.527	0.07	0.847	1.203	0.881	0.776	1.006	0.753
8-3	1.258	1.062	0.896	1.348	1.486	0.195	0.821	1.15	0.851	0.753	0.972	0.731
9-1	1.251	1.09	0.914	1.531	1.472	0.28	0.828	1.225	0.868	0.757	0.993	0.739
9-2	1.214	1.067	0.894	1.527	1.431	0.362	0.807	1.209	0.849	0.738	0.971	0.722
9-3	1.27	1.1	0.923	1.516	1.495	0.194	0.838	1.226	0.877	0.767	1.002	0.747
10-1	1.194	1.047	0.877	1.489	1.407	0.329	0.793	1.183	0.833	0.725	0.953	0.709
10-2	1.279	1.14	0.953	1.677	1.512	0.523	0.858	1.307	0.905	0.784	1.035	0.771
10-3	1.265	1.113	0.932	1.595	1.491	0.386	0.841	1.261	0.885	0.77	1.012	0.753
11-1	1.193	1.087	0.906	1.666	1.419	0.687	0.812	1.273	0.861	0.741	0.985	0.736
11-2	1.178	1.076	0.897	1.656	1.402	0.701	0.803	1.263	0.852	0.733	0.975	0.729
11-3	1.127	1.009	0.843	1.501	1.334	0.508	0.758	1.164	0.801	0.693	0.916	0.683
12-1	1.166	1.072	0.893	1.67	1.391	0.751	0.798	1.266	0.848	0.729	0.971	0.727
12-2	1.133	1.024	0.855	1.551	1.344	0.595	0.767	1.192	0.812	0.7	0.929	0.693
12-3	1.097	0.998	0.832	1.525	1.304	0.622	0.745	1.167	0.79	0.681	0.904	0.675

Table 5 continued.

	$\varepsilon_{c\,Pre}/\varepsilon_{c\,Exp}$											
Specimen	[60]	[61]	[62]	[63]	[64]	[65]	[66] a	[66] b	[66] c	[67]	[68]	Proposed
1-1	1.258	1.155	1.097	1.175	1.124	0.784	1.092	0.914	0.793	4.362	2.518	0.945
1-2	1.304	1.199	1.141	1.219	1.167	0.816	1.133	1.133	0.824	4.545	2.58	0.981
1-3	1.29	1.184	1.122	1.205	1.152	0.802	1.119	1.119	0.811	4.453	2.614	0.969
2-1	1.323	1.201	1.12	1.232	1.168	0.796	1.138	1.138	0.81	4.344	3.027	0.986
2-2	1.317	1.207	1.14	1.229	1.174	0.814	1.141	1.141	0.824	4.503	2.733	0.988
2-3	1.375	1.256	1.181	1.283	1.221	0.842	1.188	1.188	0.853	4.632	2.958	1.029
3-1	1.38	1.24	1.139	1.282	1.206	0.805	1.176	1.176	0.822	4.311	3.567	1.02
3-2	1.314	1.178	1.079	1.22	1.146	0.762	1.118	1.118	0.779	4.071	3.464	0.97
3-3	1.356	1.212	1.105	1.258	1.179	0.778	1.151	1.151	0.798	4.134	3.723	0.999

	$\varepsilon_{c\,Pre}/\varepsilon_{c\,Exp}$											
Specimen	[60]	[61]	[62]	[63]	[64]	[65]	[66] a	[66] b	[66] c	[67]	[68]	Proposed
4-1	1.395	1.249	1.141	1.295	1.215	0.805	1.186	1.186	0.824	4.287	3.753	1.029
4-2	1.425	1.261	1.133	1.319	1.226	0.792	1.199	1.199	0.816	4.138	4.402	1.042
4-3	1.378	1.224	1.107	1.277	1.191	0.776	1.164	1.164	0.798	4.084	4.052	1.011
5-1	1.467	1.29	1.151	1.356	1.255	0.801	1.228	1.228	0.828	4.146	4.835	1.068
5-2	1.402	1.25	1.136	1.3	1.216	0.799	1.188	1.188	0.82	4.226	3.955	1.031
5-3	1.459	1.292	1.163	1.351	1.257	0.814	1.229	1.229	0.838	4.262	4.443	1.068
6-1	1.432	1.257	1.119	1.324	1.223	0.778	1.198	1.198	0.805	4.012	4.827	1.041
6-2	1.417	1.253	1.126	1.312	1.219	0.788	1.192	1.192	0.812	4.115	4.377	1.036
6-3	1.441	1.265	1.125	1.331	1.23	0.782	1.205	1.205	0.809	4.036	4.855	1.047
7-1	1.455	1.257	1.098	1.341	1.224	0.753	1.201	1.201	0.786	3.791	5.852	1.046
7-2	1.399	1.219	1.074	1.291	1.186	0.743	1.162	1.162	0.771	3.787	5.12	1.011
7-3	1.454	1.248	1.082	1.338	1.216	0.738	1.194	1.194	0.773	3.676	6.292	1.04
8-1	1.563	1.316	1.118	1.433	1.285	0.749	1.263	1.263	0.793	3.626	8.315	1.102
8-2	1.426	1.197	1.014	1.307	1.169	0.677	1.149	1.149	0.717	3.259	7.869	1.004
8-3	1.35	1.149	0.986	1.24	1.12	0.668	1.1	1.1	0.702	3.282	6.404	0.959
9-1	1.491	1.204	0.987	1.359	1.184	0.629	1.164	1.164	0.682	2.86	12.54	1.02
9-2	1.481	1.184	0.962	1.347	1.166	0.605	1.146	1.146	0.66	2.71	13.95	1.005
9-3	1.483	1.21	0.999	1.353	1.187	0.645	1.167	1.167	0.695	2.975	11.2	1.022
10-1	1.447	1.16	0.945	1.316	1.141	0.597	1.122	1.122	0.65	2.685	13.16	0.984
10-2	1.617	1.272	1.024	1.468	1.257	0.629	1.234	1.234	0.693	2.758	18.02	1.085
10-3	1.547	1.235	1.003	1.407	1.216	0.63	1.195	1.195	0.687	2.816	14.74	1.049
11-1	1.594	1.225	0.973	1.443	1.218	0.577	1.193	1.193	0.646	2.449	22.8	1.05
11-2	1.583	1.213	0.963	1.433	1.207	0.569	1.182	1.182	0.637	2.404	23.29	1.041
11-3	1.444	1.13	0.906	1.31	1.118	0.552	1.097	1.097	0.611	2.399	17.14	0.964
12-1	1.593	1.213	0.959	1.441	1.209	0.56	1.183	1.183	0.631	2.348	25.17	1.043
12-2	1.487	1.151	0.918	1.348	1.142	0.551	1.12	1.12	0.613	2.358	19.74	0.986
12-3	1.46	1.124	0.893	1.322	1.117	0.531	1.094	1.094	0.593	2.257	20.6	0.963

When R^2 equals the value of one that does not mean a perfect prediction because other indices influence the selection. In Table 6, the predictions of two strain models [36, 62] yielded equal values of R^2 (0.736) but with higher values of AAE (9.4% and 9.02%) and lower values of E1 (0.99 and 0.988) compared with 3.46% and 0.998 for the proposed model. Therefore, for this kind of evaluation, R^2 is not the most critical index.

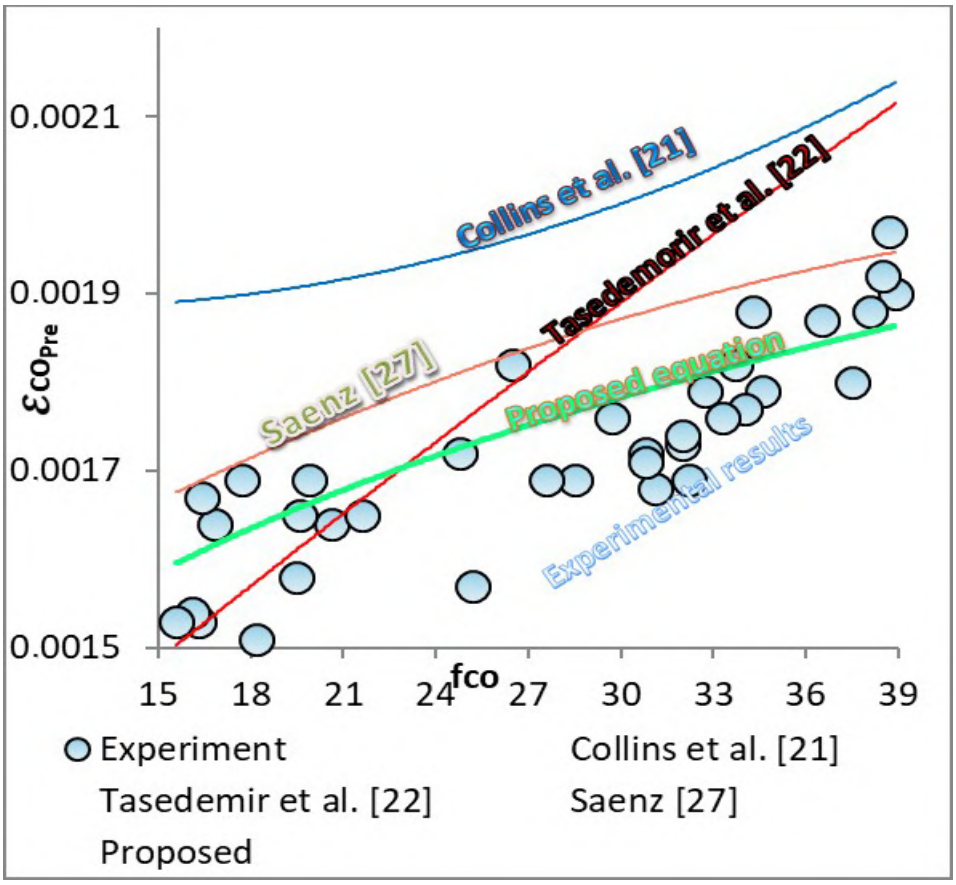


Figure. 7. Predicted strain at peak stress versus the f_c for G-1 strain models with polynomial functions.

3.6. Applicability of strain models

The five best performing models [27, 33, 44, 51, 58] and the proposed ANN-based model were checked against the test results reported by Woldemariam et al. [77] for concrete strain at peak stress, specimens C1 (ε_c =0.0021), C2 (ε_c =0.0026), C3 (ε_c =0.0029), C4 (ε_c =0.0031), C5 (ε_c =0.0033), respectively. The values of AAE in percentage were 38.7 [27], 39.6 [33], 43.21 [44], 49.7 [58], and 41.5 for the proposed model, respectively. The corresponding values of NRMSE were close, 0.021 [27], 0.022 [33], 0.021 [44], 0.026 [58], and 0.022 for the proposed model, respectively. However, it was slightly higher for model [51] with a value of 0.026, (Fig. 11). For the coefficient of correlation, the corresponding values were (0.985, 0.945, 0.98, 0.992, 0.992) for the five models [27, 33, 44, 51, 58] and 0.988 for the proposed model. However, other statistical measures show more measured errors (standard deviations with values of 0.07, 0.102, 0.052, 0.034, and 0.037 for the five models and 0.068 for the proposed model), Fig. 11.

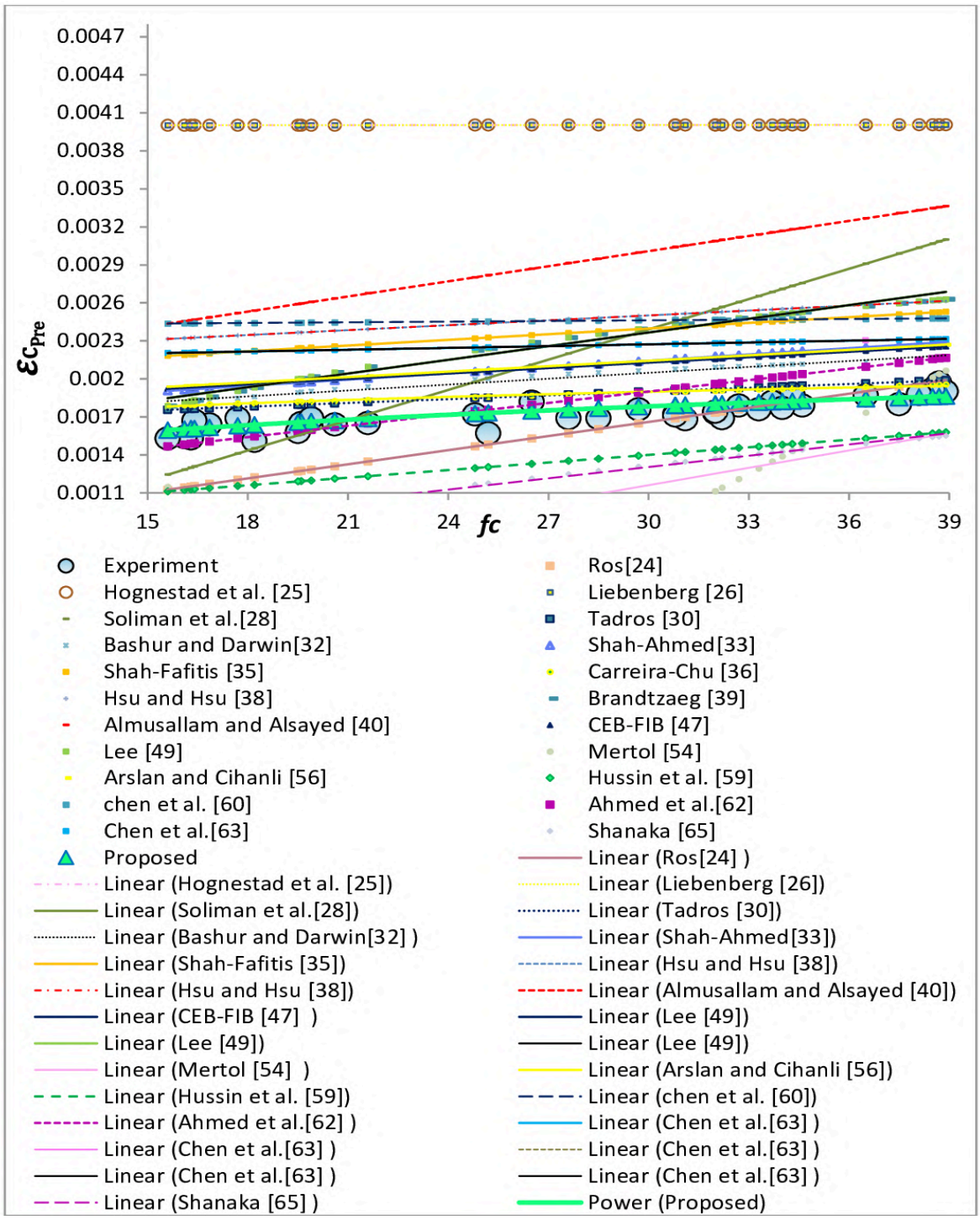


Figure. 8. Predicted strain at peak stress versus the f_c for G-2 strain models with linear functions.

The corresponding values of covariance are 0.005, 0.01, 0.003, 0.001, and 0.0014 for the five models [27, 33, 44, 51, 58] and 0.004 for the proposed model, respectively. Therefore the efficiency of the models in predicting the strain at peak stress can be better represented by the four indexes AAE, NRMSE, E, and E1 compared with the R^2 index.

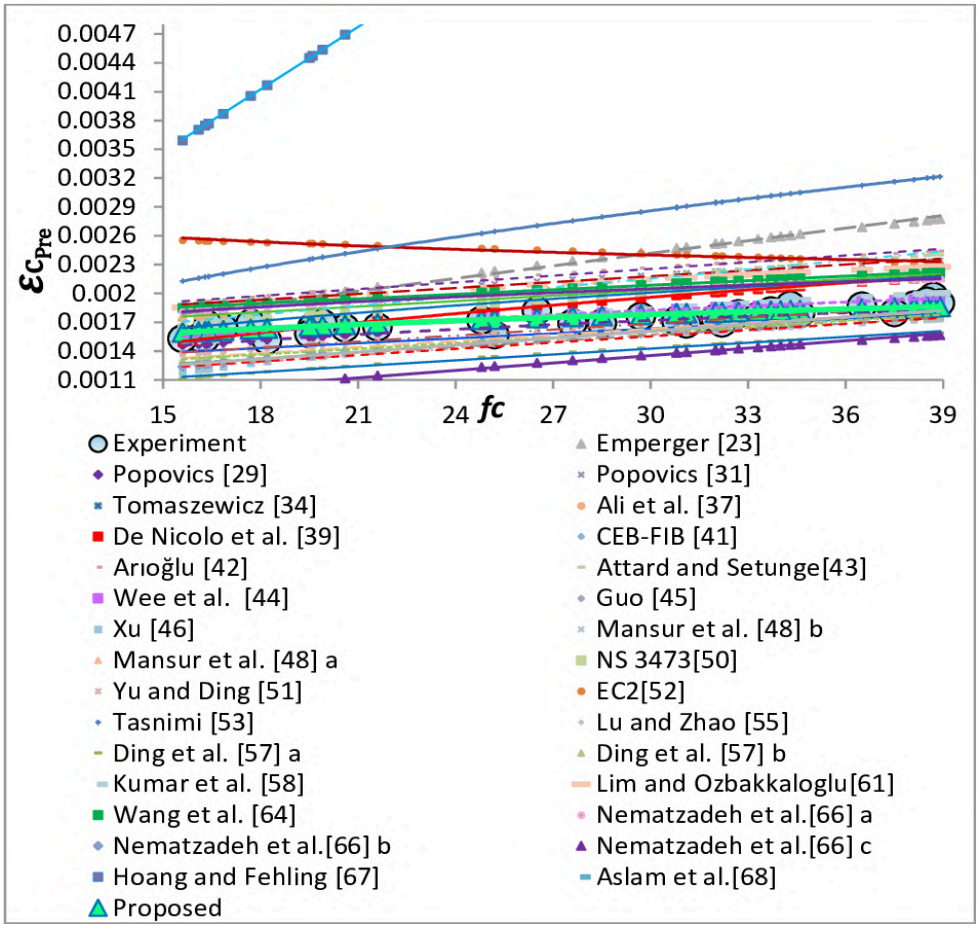


Figure. 9. Predicted strain at peak stress versus the f_c for G-3 strain models with power functions.

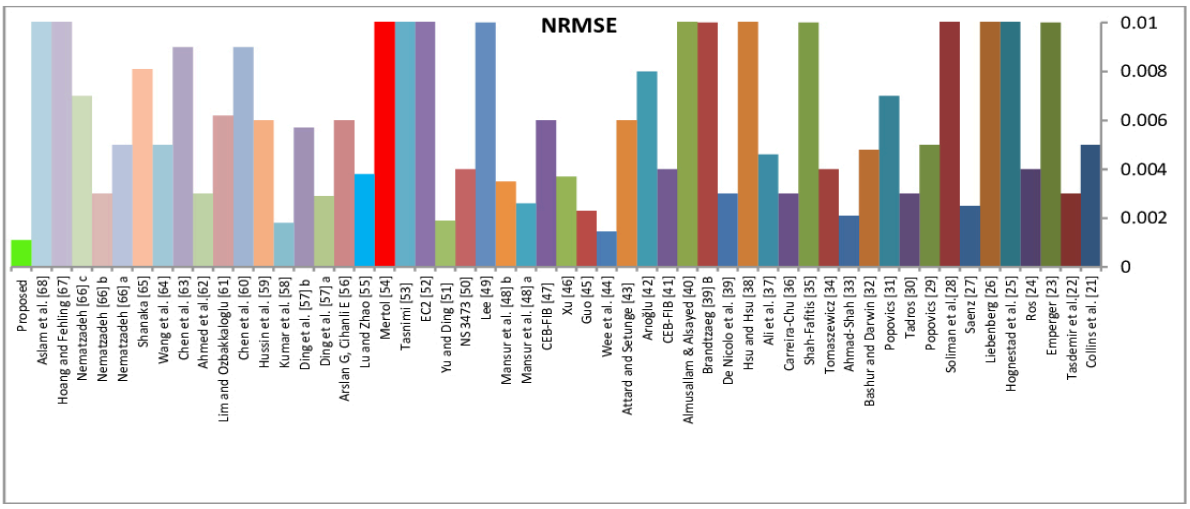
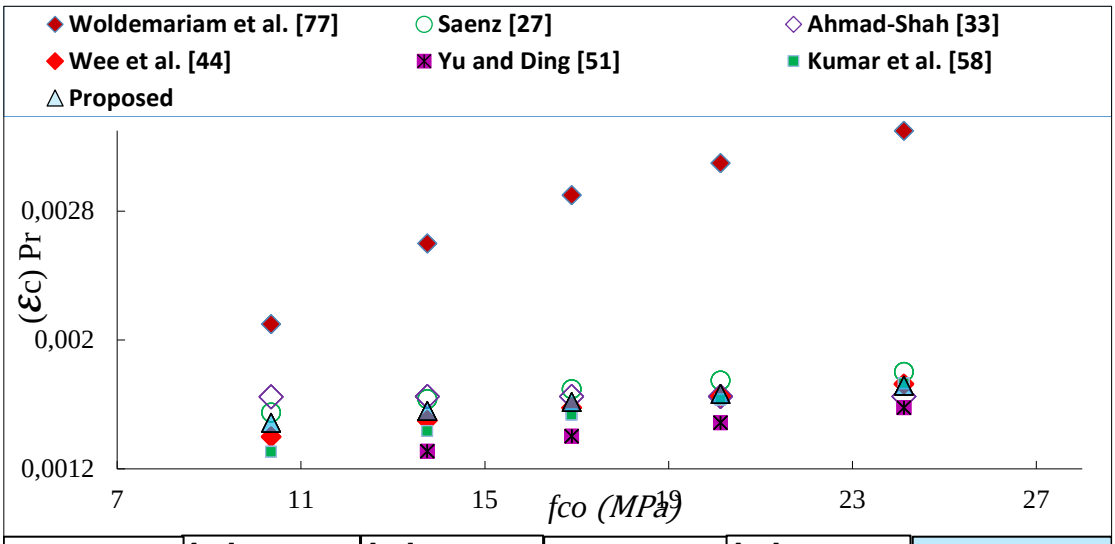


Figure 10. NRMSE values in model predictions of strain at peak stress [21-68] and the proposed model.

Table 6. Performance of the strain models using statistical indexes.

Model	*Min.*	*Max.*	*Mean*	*COV*	*STD*	*NRMSE*	*AAE(%)*	*E*	*E1*	R^2
Collins et al. [21]	1.077	1.255	1.161	0.002	0.045	0.005	16.09	0.973	0.837	0.744
Tasdemir et al.[22]	0.913	1.156	1.060	0.005	0.069	0.003	7.85	0.991	0.918	0.732
Emperger [23]	1.079	1.514	1.343	0.017	0.131	0.010	34.33	0.854	0.642	0.720
Ros [24]	0.929	1.446	1.118	0.025	0.158	0.004	10.70	0.980	0.894	0.736
Hognestad et al. [25]	2.033	2.651	2.336	0.024	0.157	0.037	133.6	-0.818	-0.36	0.706
Liebenberg [26]	2.034	2.651	2.336	0.024	0.157	0.037	133.6	-0.818	-0.36	0.706
Saenz [27]	0.988	1.158	1.067	0.002	0.040	0.0025	6.761	0.994	0.932	0.701

Model	*Min.*	*Max.*	*Mean*	*COV*	*STD*	*NRMSE*	*AAE(%)*	*E*	*E1*	R^2
Soliman et al.[28]	0.783	1.660	1.271	0.083	0.290	0.0110	34.02	0.823	0.64	0.736
Popovics [29]	1.054	1.249	1.158	0.002	0.047	0.005	15.79	0.972	0.838	0.711
Tadros [30]	1.009	1.18	1.093	0.002	0.042	0.003	9.29	0.99	0.907	0.736
Popovics [31]	1.129	1.337	1.24	0.002	0.050	0.007	24.00	0.938	0.735	0.711
Bashur and Darwin [32]	1.084	1.276	1.171	0.002	0.045	0.0048	17.10	0.968	0.826	0.675
Ahmad-Shah [33]	0.839	1.093	0.963	0.004	0.064	0.0021	6.08	0.994	0.936	0.736
Tomaszewicz [34]	0.998	1.215	1.129	0.003	0.058	0.004	12.87	0.979	0.867	0.713
Shah-Fafitis [35]	1.283	1.481	1.375	0.002	0.049	0.01	37.53	0.855	0.616	0.736
Carreira-Chu [36]	0.992	1.198	1.093	0.002	0.049	0.003	9.37	0.99	0.907	0.736
Ali et al. [37]	1.054	1.249	1.158	0.002	0.047	0.0046	15.8	0.972	0.834	0.711
Hsu and Hsu [38]	1.327	1.555	1.439	0.003	0.056	0.0121	43.9	0.803	0.522	0.736
De Nicolo et al. [39]	0.916	1.194	1.09	0.006	0.08	0.003	10.44	0.984	0.891	0.714
Brandtzaeg [39] B	1.097	1.459	1.325	0.011	0.104	0.01	32.47	0.876	0.663	0.693
Almusallam & Alsayed [40]	1.477	1.837	1.694	0.01	0.101	0.02	69.35	0.484	0.284	0.736
CEB-FIB [41]	0.998	1.215	1.129	0.003	0.058	0.004	12.87	0.979	0.867	0.713
Arıoğlu [42]	1.15	1.378	1.28	0.003	0.057	0.008	27.97	0.915	0.712	0.712.
Attard and Setunge [43]	1.022	1.324	1.21	0.007	0.086	0.006	20.99	0.945	0.781	0.711
Wee et al. [44]	0.94	1.113	1.032	0.002	0.042	0.001	4.45	0.997	0.955	0.711
Guo [45]	0.836	0.996	0.927	0.002	0.041	0.0023	7.24	0.993	0.925	0.72
Xu [46]	0.73	0.967	0.88	.0045	0.068	0.0037	11.95	0.982	0.879	0.697
CEB-FIB [47]	1.142	1.312	1.22	0.002	0.043	0.006	21.96	0.95	0.776	0.736
Mansur et al. [48] a	0.797	0.997	0.92	0.003	0.055	0.0026	8.04	0.991	0.919	0.715
Mansur et al. [48] b	0.765	0.957	0.883	0.003	0.053	0.0035	11.71	0.984	0.881	0.715
Lee [49]	1.097	1.459	1.325	0.011	0.104	0.01	32.47	0.876	0.663	0.693
NS 3473 [50]	0.998	1.215	1.129	0.003	0.058	0.004	12.87	0.979	0.867	0.713
Yu and Ding [51]	0.832	1.029	0.952	0.0028	0.053	0.0019	5.34	0.995	0.946	0.714
EC2 [52]	1.171	1.677	1.422	0.019	0.139	0.012	42.20	0.812	0.575	0.755
Tasnimi [53]	1.304	1.757	1.584	0.018	0.134	0.017	58.38	0.618	0.395	0.718
Mertol [54]	0.072	1.087	0.605	0.073	0.727	0.013	40.85	0.775	0.589	0.436
Lu and Zhao [55]	0.745	0.952	0.873	0.0033	0.058	0.0038	12.69	0.981	0.871	0.716
Arslan G, Cihanli E [56]	1.15	1.321	1.228	0.002	0.043	0.006	22.79	0.946	0.767	0.736
Ding et al. [57] a	0.79	0.978	0.904	0.0025	0.051	0.0029	9.57	0.988	0.903	0.714
Ding et al. [57] b	0.68	0.874	0.801	0.003	0.055	0.0057	19.92	0.957	0.797	0.716
Kumar et al. [58]	0.904	1.117	1.033	0.0032	0.057	0.0018	5.71	0.995	0.941	0.714
Hussin et al. [59]	0.675	0.861	0.786	0.003	0.053	0.006	21.43	0.951	0.781	0.736
Chen et al. [60]	1.175	1.468	1.318	0.005	0.071	0.009	31.84	0.896	0.677	0.736
Lim and Ozbakkaloglu [61]	1.123	1.316	1.219	0.0021	0.046	0.0062	21.89	0.949	0.776	0.71
Ahmed et al.[62]	0.893	1.181	1.062	0.007	0.083	0.003	9.02	0.988	0.906	0.736
Chen et al. [63]	1.175	1.468	1.318	0.005	0.071	0.009	31.84	0.896	0.677	0.736
Wang et al. [64]	1.117	1.285	1.193	0.002	0.042	0.005	19.25	0.961	0.803	0.724
Shanaka [65]	0.531	0.842	0.715	0.0094	0.097	0.0081	28.51	0.912	0.711	0.722
Nematzadeh [66] a	1.091	1.2629	1.167	0.0017	0.042	0.005	16.7	0.97	0.83	0.709
Nematzadeh [66] b	0.757	0.9875	0.901	0.0044	0.067	0.003	9.88	0.986	0.901	0.717
Nematzadeh [66] c	0.593	0.8533	0.750	0.0061	0.079	0.007	24.99	0.932	0.746	0.721
Hoang and Fehling [67]	2.257	4.632	3.586	0.602	0.782	0.077	258.6	-6.96	-1.7	0.735
Aslam et al. [68]	2.518	25.17	8.858	47.28	6.924	0.27	785.8	-96.51	-6.71	0.598
Proposed	0.945	1.102	1.018	0.001	0.037	0.0011	3.46	0.998	0.965	0.708



[27]	[33]	[44]	[51]	[58]	Proposed
NRMSE=0.021	NRMSE=0.022	NRMSE=0.021	NRMSE=0.026	NRMSE=0.023	NRMSE=0.022
AAE=38.7%	AAE=39.6%	AAE=43.21%	AAE=49.7%	AAE=44.9%	AAE=41.5%
E=0.828	E=0.78	E=0.795	E=0.737	E=0.784	E=0.804
E1=0.59	E1=0.58	E1=0.55	E1=0.54	E1=0.534	E1=0.56
R^2 =0.985	R^2 =0.945	R^2 =0.98	R^2 =0.992	R^2 =0.992	R^2 =0.988
STD=0.07	STD=0.102	STD=0.052	STD=0.034	STD=0.037	STD=0.068
COV=0.005	COV=0.01	COV=0.003	COV=0.001	COV=0.0014	COV=0.004

Figure 11. Strain predictions of test results of [77] using models [27, 33, 44, 51, 58] and the proposed model.

4. Conclusions

1. Several parameters such as aggregate/cement ratio, w/c ratio, and slump values that influence the compressive strength and strain at peak stress of concrete were considered as input for the two ANN models.

2. The developed ANN models successfully yielded good predictions of the test results presented in the current study.

3. The AAE value was found to be less than 3.46% for the proposed model, and the NRMSE value was the lowest, 0.0011.

4. The predicted strains obtained from the regression of ANN output data for stress and strain at peak stress were more accurate than those obtained from the fifty-three existing expressions for predicting the strain at peak stress.

5. Both the NRMSE and AAE indexes allow the assessing of the performance of the strain models for the present study more properly than the R^2 index. ANN procedure is a valuable modeling technique for practicing engineers interested in concrete technology.

6. The models with power function show better performance in predicting the strain at peak stress than models with linear or polynomial functions.

New research should be carried out along these lines to include input parameters outside the range considered in the present study and to improve the prediction capability of the proposed model and its application to test data with higher strengths.

References

1. Saridemir, M. Prediction of compressive strength of concretes containing metakaolin and silica fume by Artificial Neural Networks. Advances in Engineering Software. 2009. 40. Pp. 350–355. DOI: 10.1016/j.advengsoft.2008.05.002
2. Chopra, P., Sharma, R.K., Kumar, M. Prediction of compressive strength of concrete using artificial neural network and genetic programming. Advances in Materials Science and Engineering. 2016. ID 7648467. Pp. 1–10. DOI: 10.1155/2016/7648467
3. Lai, S., Serra, M. Concrete strength prediction neural network. Construction and Building Materials. 1997. 11(2). Pp. 93–98. DOI: 10.1016/S0950-0618(97)00007-X
4. Oztas, A., Pala, M., Ozbay, E., Kanca, E., Caglar, N., Bhatti, M. A. Predicting the compressive strength and slump of high strength concrete using neural network. Construction and Building Materials. 2016. 20. Pp. 769–775. DOI: 10. 1016/j. conbuildmat.2005.01.054
5. Naderpour, H., Mirrashid, M. An innovative approach for compressive strength estimation of mortars having calcium inosilicate minerals. Journal of Building Engineering. 2018. 19. Pp. 205–215. DOI: 10.1016/j.jobe.2018.05.012

6. Asteris, P.G., Kolovos, K.G., Douvika, M.G., Roinos, K. Prediction of self-compacting concrete strength using artificial neural networks. European Journal of Environmental and Civil Engineering. 2016. 20(1). Pp. 102–122.DOI: .org/10. 1080/19648189.2016.1246693
7. Duan, Z. H., Kou, S. C., Poon, C. S. Prediction of compressive strength of recycled aggregate concrete using artificial neural networks. Construction and Building Materials. 2013. 40. Pp. 1200–1206. DOI: 10.1016/j.conbuildmat.2012.04.063
8. Momeni, E., Armaghani, D. J., Hajihassani, M. Prediction of uniaxial compressive strength of rock samples using hybrid particle swarm optimization-based artificial neural networks. Measurement. 2015. 60. Pp. 50–63. DOI: 10.1016/j.measurement.2014.09.075
9. Ahmad, A., Kotsovou, G., Cotsovos, D.M., Lagaros, N.D. Assessing the accuracy of RC design code predictions through the use of artificial neural networks. International Journal of Advanced Structural Engineering. 2018. 10(4). Pp. 349–365. DOI: 10.1007/s40091-018-0202-4
10. Charhate, S., Subhedar, M., Adsul, N. Prediction of Concrete Properties Using Multiple Linear Regression and Artificial Neural Network. Journal of Soft Computing in Civil Engineering. 2018. 2-3. Pp. 27–3. DOI: 10.22115/scce.2018.112140.1041
11. Pala, M., Ozbay, E., Oztas, A., Yuce, M. I. Appraisal of long-term effects of fly ash and silica fume on compressive strength of concrete by neural networks. Construction and Building Materials. 2007. 21(2). Pp. 384–394.DOI: 10.1016/j. conbuildmat.2005.08.009
12. Svozil, D., Kvasnicka, V., Pospichal, J. Introduction to multi-layer feed-forward neural networks. Chemometrics and Intelligent Laboratory Systems. 1997. 39. Pp. 43–62.
13. Basher, I.A., Hajmeer, M. Artificial neural networks: fundamentals, computing, design, and application. Journal of Microbial Methods. 2000. 43. Pp. 3–31. DOI: 10.1016/s0167-7012(00)00201-3
14. Abdulla, N.A. Concrete encased with engineering plastics. Journal of Civil Engineering and Construction. 2020. 9 (1). Pp. 31–41. DOI: 10.32732/jcec.2020.9.1.31
15. Adhikary, B.B., Mutsuyoshi, H. Prediction of shear strength of steel fiber RC beams using neural networks. Construction and Building Materials. 2006. 20(9). Pp. 801–11. DOI:10.1016/j.conbuildmat.2005.01.047
16. Nikbin, I.M., Rahimi, S., Allahyari, H. A new empirical formula for prediction of fracture energy of concrete based on the artificial neural network. Engineering Fracture Mechanics. 2017. 186. Pp.466–82.DOI: 10.1016/j.engfracmech.2017.11.010
17. Naderpour, H., Kheyroddin, A., Amiri, G.G. Prediction of FRP-confined compressive strength of concrete using artificial neural networks. Composite Structures. 2010. 92. Pp. 2817–29. DOI: 10.1016/j.compstruct.2010.04.008
18. Kassem, A. A., Raheem, A. M., Khidir, K. M., Alkattan, M. Predicting of daily Khazir basin flow using SWAT and hybrid SWAT-ANN Models. Ain Shams Engineering Journal. 2019. DOI: 10.1016/j.asej.2019.10.011
19. Demir, F. Prediction of elastic modulus of normal and high strength concrete by artificial neural networks. Construction and Building Materials. 2008. 22(7). Pp. 1428–1435. DOI: 10.1016/j.conbuildmat.2007.04.004
20. Maghreb, M., Sammut, C., Waller, T. Predicting the duration of concrete operations via artificial neural network and by focusing on supply chain parameters. Building Research Journal. 2014. 61(1). Pp. 1–14. DOI: 10.2478/brj-2014-0001
21. Collins, P.M., Mitchell, D., Macgregor, J.G. Structural design considerations for high-strength concrete. Concrete International. 1993. Pp. 27-34.
22. Tasdemir, M., Tasdemir, C., Akyüz, S., Jefferson, A., Lydon, F., Barr, B., Evaluation of strains at peak stresses in concrete: a three-phase composite model approach. Cement and Concrete Composites. 1998. 20 (4). Pp. 301–318. DOI: 10.1016/S0958-9465(98)00012-2
23. Emperger, F.V. Der Beiwert n. Beton und Eisen. 1936. 35(19). Pp. 324–332.
24. Ros, M. Material-technological foundation and problems of reinforced concrete. Bericht No. 162 (Eidgenossische Material prfifungs und Versuchs anstalt f/Jr Industrie, Bauwesen and Gewerbe, Zurich, Switzerland 1950.
25. Hognestad, E., Hanson, N.W., Mchenry, D. Concrete stress distribution in ultimate strength design. Journal of the American Concrete Institute. 1955. 27 (4). Pp. 455–479.
26. Liebenberg, A.C. A stress-strain function for concrete subjected to short-term loading, Magazine of concrete Research. 1962. 14. Pp. 85–99.
27. Saenz, L.P. Discussion of a paper by Desayi P, Krishnan S. Equation for the stress-strain curve of concrete. Ibid. 1964. 61(9). Pp. 1229–1235.
28. Soliman, M.T.M. The flexural stress-strain relationship of concrete confined by rectangular transverse reinforcement, Magazine of Concrete Research. 1967. 19(61). Pp. 223–238. DOI: 10.1680/macr.1967.19.61.223
29. Popovics, S. A review of stress-strain relationships for concrete. ACI Journal. 1970. 67(3). Pp. 243-248.
30. Tadros, G.S. Plastic rotation of reinforced concrete members subjected to bending, axial load, and shear. Ph.D. Thesis, University of Calgary. 1970.
31. Popovics, S. A numerical approach to the complete Stress-strain curve of concrete, Cement, and Concrete Research. 1973. 3. Pp. 583–599
32. Fuad K. Bashur David Darwin. Nonlinear model for reinforced concrete slabs. A Report on a Research Project Sponsored by THE National Science Foundation Research Grant Eng76-09444 University of Kansas Lawrence, Kansas December 1976
33. Ahmad, S.H., Shah, S.P. Behavior of hoop confined concrete under high strain rates. ACI Journal. 1982. 82. Pp. 634–647.
34. Tomaszewicz, A. Betongens Arbeidsdiagram: SINTEF Rep. No. STF 65A84605, Trondheim. 1984.
35. Shah, S.P., Fafitis, A. Predictions of ultimate behavior of confined columns subjected to large deformations. Ibid. 1985. 82(4). Pp. 423–433.
36. Carreira, D.J., Chu, K. H. Stress-Strain relationship for plain concrete in compression. Journal of American Concrete Institute. 1986. 82(6). Pp. 797–804
37. Ali AM, Farid BJ, Al-Janabi AJM. Stress-strain relationship for concrete in compression made of local materials. Engineering Science. 1990. 2(1). Pp. 183–194
38. Hsu LS, Hsu CT. Complete stress-strain behavior of high-strength concrete under compression. Magazine of Concrete Research. 1994. 46(169). Pp. 301–12
39. De Nicolo, B., Pani, L., Pozzo, E. Strain of concrete at peak compressive stress for a wide range of compressive strengths. Materials and Structures**.** 1994. 27(4). Pp. 206–210. DOI: org/10.1007/BF02473034
40. Al Musallam, T. H., Al Sayed, S. H. Stress-strain relationship of normal, high, and lightweight concrete. Magazine of Concrete Research. 1995. 47(170). Pp. 39–44. DOI: https://doi.org/10.1680/macr.1995.47.170.39

41. CEB-FIB. High-Performance Concrete-Recommended Extensions to the Model code 90, Research Needs. International Federation for Structural Concrete (fib), Lausanne, Switzerland. 1995.
42. Arıoğlu, E. Strain of Concrete at Peak Compressive Stress for a Wide Range of Compressive Strengths. Discussion on paper by B. de Nicolo, L. Panni, E. Pozzo, Materials and Structures, RILEM. 1995. 28(184). Pp. 611–614
43. Attard M. M., Setunge, S. Stress-strain relationship of confined and unconfined concrete. ACI Materials journal.1996. 93(5). Pp. 432–442
44. Wee, T.H., Chin, M.S., Mansur, M.A. Stress-strain relationship of high-strength Concrete in compression. Journal of Materials in Civil Engineering. 1996. 8(12). Pp. 70–76. DOI: 10.1061/(ASCE)0899-1561(1996)8:2(70)
45. Guo, Z.H. Strength and deformation of concrete (test foundation and constitutive relationship). Beijing: Tsinghua University Press, China. 1997 (in Chinese)
46. Xu, L.Y. Experimental research on stress-strain curves of high-performance concrete and compact, reinforced high-performance concrete in tension. Dissertation for the Doctoral Degree. Wuhan: Wuhan University of Hydraulic and Electric Engineering. 1998 (in Chinese)
47. CEB-FIB. Structural Concrete-Textbook on behavior, design, and performances (Updated knowledge of CEB/FIP Model Code 1990), International Federation for Structural Concrete (fib), Lausanne, Switzerland. 1990.
48. Mansur M.A., Chin M. S., Wee T. H. Stress-strain relationship of confined high strength plain and fiber concrete– closure. Journal of Materials in Civil Engineering. 1999. 11(4). Pp. 364-364.
49. Lee, I. Complete stress-strain characteristics of high-performance concrete Ph.D. thesis. New Jersey Institute of Technology. 2002.
50. NS 3473. Concrete structures-design and detailing rules. Norwegian Standards. 2003.
51. Yu, Z. W., Ding, F. X. Calculation method of compressive mechanical properties of concrete. Journal Building Structures. 2003. 24(4). Pp. 41–46 (In Chinese)
52. Euro code. Design of concrete structures–Part 1-1: General rules and rules for building. European Committee for Standardization (CEN), Brussels, Belgium. 2004.
53. Tasnimi, A.A. Mathematical model for complete stress-strain curve prediction of normal, lightweight, and high-strength concretes. Magazine of Concrete Research. 2004. 56(1). Pp. 23-34. DOI: 10.1680/macr.2004.56.1.23
54. Mertol, H.C. Behavior of high-strength concrete members subjected to combined flexure and axial compression loadings. Ph.D. thesis. Raleigh, North Carolina. 2006.
55. Lu Z. H., Zhao, Y.G. An improved analytical constitutive relation for normal weight high-strength concrete. International Journal of Modern Physics B. 2008. 22(31–32). Pp. 5425–30.
56. Arslan, G., Cihanli, E. Curvature ductility prediction of reinforced high-strength concrete beam sections. Journal of Civil Engineering and Management. 2010. 16(4). Pp. 462–470. DOI: doi.org/10.3846/jcem.2010.52
57. Ding, F., Ying, X., Zhou, L., Yu Z. Unified calculation method, and its application in determining the uniaxial mechanical properties of concrete. Frontiers in Architectural and Civil Engineering. 2011. 5(3). Pp. 381–393. DOI 10.1007/s11709-011-0118-6
58. Kumar R., Singh, B., Bhargava, P. Flexural capacity predictions of SCC beams using stress-strain relationship in axial compression. Magazine of Concrete Research. 2011. 63(1). Pp. 49–59. DOI: 10.1680/macr.2011.63.1.49
59. Hussin, M., Zhuge, Y., Bullen, F., Lokuge, W. A mathematical model for complete stress-strain curve prediction of permeable concrete. Proceedings of the 22nd Australasian Conference on the Mechanics of Structures and Materials (ACMSM 22). Taylor & Francis (CRC Press) / Balkema. 2013. Pp. 293-298.
60. Chen, Y., Visintin, P., Oehlers, D. J. Mechanism orientated stress-strain model for unconfined concrete. Departmental Rep. R-181, School of Civil, Environmental and Mining Engineering University of Adelaide, SA, Australia. 2013.
61. Lim, J.C., Ozbakkaloglu, T. Stress–strain model for normal- and lightweight concretes under uniaxial and triaxial compression. Construction and Building Materials. 2014. 71. Pp. 492–509
62. Ahmad, S., Pilakoutas, K., Khan, Q.Z, Neocleous, K. Stress-Strain Model for Low-Strength Concrete in Uni-Axial Compression. Arabian Journal of Science and Engineering. 2015. 40**.** Pp. 313–328. https://doi.org/10.1007/s13369-014-1411-1
63. Chen, Y., Visintin, P., Oehlers, D.J., Alengaram, U.J. Size-Dependent Stress-Strain Model for Unconfined Concrete. Journal of Structural Engineering. 2015. 140. DOI: 10.1061/(ASCE)ST.1943-541X.0000869
64. Wang, Z., Wang, J., Liu, T., Zhang, F. Modeling seismic performance of high strength steel-ultra-high-performance concrete piers with modified Kent-Park model using fiber elements. Advanced Mechanical Engineering. 2016. 8(2). Pp.1–13. DOI: 10.1177/1687814016633411
65. Shanaka, K. Ductility Design of Very-High Strength Reinforced Concrete Columns (100–150 MPa). Ph.D. thesis. The University of Melbourne. 2016
66. Nematzadeh, M., Salari, A., Ghadami, J., Naghipour, M. Stress-strain behavior of freshly compressed concrete under axial compression with a practical equation. Construction and Building Materials. 2016. 115. Pp. 402–423. DOI: 10.1016/j.conbuildmat.2016.04.045
67. Hoang, A.L., Fehling, E. Influence of steel fiber content and aspect ratio on the uniaxial tensile and compressive behavior of ultra-high-performance concrete. Construction and Building Materials. 2017. 153. Pp. 790–806. DOI: 10.1016/j.conbuildmat.2017.07.130
68. Aslam, M., Shafigh, P., Nomeli, M.A., Jumaat, M.Z. Manufacturing of high-strength lightweight aggregate concrete using blended coarse lightweight aggregates. Journal of building Engineering. 2017. 13. Pp. 53-62. DOI: 10.1016/j.conbuildmat.2017.07.130
69. CEB-FIP Model Code 1990 // Bulletin d'lnformation No. 203, Chap. 2. 1991.
70. Z. Guo, X. Zhang. Investigation of complete stress-deformation curves for concrete in tension. ACI Materials Journal. 1987. 84. Pp. 278–285
71. Sargin, M., Ghosh, S.K. Handa, V.K. Effects of lateral reinforcement upon the strength and deformation properties of concrete. Magazine of Concrete Research. 1971. 23 (75–76). Pp. 99–110
72. Xie, N., Liu, W. Determining tensile properties of mass concrete by direct tensile test. ACI Materials journal. 1989. 86. Pp. 214–219
73. Phillips, D.V. Zhang, B. Direct tension tests on notched and unnotched plain concrete specimens. Magazine of concrete research. 1993. 45. Pp. 25–35
74. Kaklauskas, G. Practical techniques for determining of Average stress-strain relationships for concrete from experimental data Of RC bending members. Statyba. 1998. 4(1). Pp. 20-28, DOI: 10.1080/13921525. 1998.10531375
75. Jensen, V. P. The Plasticity Ratio of Concrete and Its Effect on the Ultimate Strength of Beams. Journal of the American Concrete Institute. 1943. 14(6). Pp. 565-582

76. Thorenfeldt, E., Tomaszewicz, A., Jensen, J. J. Mechanical Properties of High-Strength Concrete and Application in Design. Proceedings of Utilization of High Strength Concrete Symposium, Stavanger, Norway. 1987. Pp. 149–159
77. Woldemariam, A. M., Oyawa, W. O., Nyomboi, T. Structural performance of UPVC confined concrete equivalent cylinders under axial compression loads. Buildings. 2019. 9(4). Pp. 82. DOI: 10.3390/buildings9040082.

Contacts:

Nwzad Abduljabar Abdulla, anwzad@yahoo.com

Received 27.05.2020. Approved after reviewing 11.05.2021. Accepted 12.05.2021.



Magazine of Civil Engineering

ISSN 2712-8172

journal homepage: http://engstroy.spbstu.ru/

DOI: 10.34910/MCE.110.8

The site effect investigation using nonlinear and Iranian seismic code methods in Babol city

S. Rezaei* , ***A. Hasanzadeh***

Babol Noshirvani University of Technology, Babol, Mazandaran, Iran

**E-mail: S_Rezaei1366@yahoo.com*

Keywords: earthquake, site effect, nonlinear method, seismic code, design spectrum, response spectra

Abstract. Site effect is known as one of the important issues in geotechnical earthquake engineering. The site effect can change the characteristics of seismic waves and amplify the vibrations which results in the casualties and financial damages. Nonlinear method is an appropriate numerical method for site effect analysis due to its accuracy and its close results compared to the actual soil behavior. Thus, in this research, nonlinear analysis was applied for evaluation of site effect and for achievement of a suitable design spectrum in Babol city located in the north of Iran. For this purpose, first, seismic, geophysical and geotechnical data of Babol city were provided. Then, by modeling the subsurface conditions, the tripartite response spectra were found for different areas of Babol. According to the obtained results, the behaviors of tripartite response spectra are fundamentally different in some frequency ranges. In addition, the shape factors obtained from site analysis for different parts of Babol city were compared with the shape factor of the design spectrum presented by Iranian seismic code. This comparison indicated that the response spectrum obtained through analysis differs from the Iranian seismic code design spectrum. Finally, it can be concluded that the structures designed according to Iranian seismic code are neither safe nor economic in some areas. This issue shows the necessity for more serious consideration of site effect phenomenon in Iranian seismic code.

1. Introduction

One of the most important issues in seismic study of an area is evaluation of the site effect on the characteristics of seismic waves. The occurrence of catastrophic earthquakes such as Caracas 1967, San Fernando 1971, Mexico City 1985, Loma Prieta 1989, Manjil–Rudbar 1990, Izmit 1999, Bam 2003, Sichuan 2008, Tohoku 2011 and Chiapas 2017 revealed the significant effect of geotechnical conditions on the earthquake characteristics [1–3]. By studying the influence of soil on the earthquake-induced damage, it was found that soil behavior can be an important factor in causing damage in different ways. When the natural period of the site is the same as the natural period of the structure, the resonance phenomenon occurs. In this case, the ground motions caused by the earthquake are amplified and will be applied to the structure with a greater acceleration. Besides, site effect can increase vibration duration and change its frequency content. Another factor that impacts the amount of earthquake-induced damage is the dominant period and amplification factor of site. The dominant period of site is the period associated with the highest peak on the acceleration spectrum. Physically, the main factor causing the amplification of ground motions in soft deposits is the trapping of the seismic waves between deposits and the bedrock [4–7].

Nowadays, all the developed countries have incorporated the site effect phenomenon into their seismic codes. There are different soil classifications in codes considering the mechanical and dynamic properties, liquefaction and collapse potential of soils [8–10].

In Iranian seismic code (standard No. 2800), site effect has been considered using the design spectrum shape factor (B_1). This parameter is dependent on the period of structure, soil type and seismic

Rezaei, S., Hasanzadeh, A. The site effect investigation using nonlinear and Iranian seismic code methods in Babol city. Magazine of Civil Engineering. 2022. 110(2). Article No. 11008. DOI: 10.34910/MCE.110.8

© Rezaei, S., Hasanzadeh, A., 2022. Published by Peter the Great St. Petersburg Polytechnic University.

This work is licensed under a CC BY-NC 4.0

hazard level of the region [11]. The results of previous investigations showed that the shape factor presented in standard No. 2800 has some shortcomings and does not well represent the site effect on a given structure. Some of the problems in this standard are as follows:

1. The design spectrum shape factor does not take into account the amplification effect for short-period earthquakes.
2. The design spectrum shape factor does not consider the nonlinear response of the site, particularly in soft clayey soils.
3. Different parts of standard No. 2800 has been directly derived from the Uniform Building Code (UBC) which has undergone major changes itself and in its new edition the effects of the site are taken into account more seriously.
4. The effects of near-field earthquakes were not considered in standard No. 2800.
5. Standard No. 2800 does not address earthquake directivity effects.
6. The major geotechnical features such as soil layering, profile thickness and shear strength of soft soil were not accurately addressed in standard No. 2800 [12–18].

Since Iran is located in a seismic zone with the possibility of occurrence of destructive earthquakes, serious attention to the earthquake effect in the design and construction of structures seems necessary. Overall revision of United States building code induced other seismic countries to take a new look at the effect of site on the base shear [11, 17–19]. By studying various codes, it can be found that in addition to the Vs_{30} parameter (the average seismic shear wave velocity from the surface to a depth of 30 meters), other parameters such as the depth of the seismic bedrock, material type, vibration intensity, site period and deposit depth have been used to consider the site effect [17–19].

In the new edition of standard No. 2800, application of site-specific design spectrum has been recommended. This spectrum depends on several factors such as seismic, geological and tectonic characteristics of the site. Since application of site-specific design spectrum is only necessary for the design of particular structures, engineers do not take it into account for the design of common buildings [11]. Thus, it is essential to conduct a comprehensive study to reveal the importance of site-specific design spectrum. In other words, using site analyses, the effective factors on the structures can be found and different approaches to confront the destructive effects of earthquakes in the design of structures can be suggested.

Generally, there are two approaches for evaluation of site effect including field and numerical methods. Field methods include all geotechnical, seismic, geophysical and geological activities that are carried out in the field. Numerical methods mainly use the information of field methods (earthquake record, borehole log, shear wave velocity, etc.) as primary data for the detailed analyses [20, 21].Numerical methods of site effect analysis are divided into several methods based on different factors such as model and domain of analysis, pore water pressure, problem dimensions and characteristics of materials [22].

The application of an elastic model is appropriate when behavior of soil is anticipated to remain within the small strain range ($<10^{-5}$). For the medium strain range (10^{-3}), the behavior of soil gets elasto-plastic and shear modulus reduces with the increase of the shear strain. The damping ratio and shear modulus do not alter with the progression of cycles in this strain level (non-degraded hysteresis). In the case of shear strain level greater than 10^{-2}, the characteristics of soil tend to alter significantly not only with shear strain but also with the progression of cycles. This behavior is called as the degraded hysteresis [16, 22]. During destructive earthquakes, large strains occur in the soil. Under these conditions, nonlinear analysis can accurately present the actual soil behavior as well as irreversible deformations.

Thus, in this study, nonlinear analysis is performed for evaluation of site effect considering site-specific design spectrum. For this purpose, in the city of Babol, geophysical data by performing down-hole tests and geotechnical data using 90 boreholes were provided and employed. The results of analyses are presented as tripartite response spectra. At the next step, the shape factors of design spectra obtained by numerical analyses are compared with the one presented in standard No. 2800. Finally, using standard No. 2800 and the results of this investigation, structures with different stories are modeled and their structural design characteristics (base shear and drift) are compared to reveal the importance of considering site effect on structures.

2. Methods

Evaluation of previous earthquakes has shown that geotechnical conditions can significantly affect the damage distribution in residential areas. The results found by different researchers have proved that soft deposits are problematic for high structures and far-field earthquakes. In addition, stiff deposits are dangerous for short structures and near-field earthquakes due to the amplification of ground motion. In

other words, it can be stated that soil acts like a filter and changes the characteristics of ground motion during earthquake [22–25]. Density, age, thickness and other geotechnical properties of soil can alter the characteristics of seismic waves so that site effect can increase intensity up to 3 degrees in Mercalli scale [26–32]. Thus, the importance of site effect evaluation and its application in building codes becomes more pronounced.

The study area in the present research is Babol city in Iran. This city is situated in a high seismic area due to its location in front of Alborz Mountain, which is tectonically an active region. The tectonic of Alborz Mountain is controlled by boundary conditions due to convergent motion between Arabia and Eurasia, which probably started in the Cretaceous [16, 24]. The texture and thickness of deposits in Babol city are mainly affected by the sedimentation of Babolrood River and the coastal deposits of Caspian Sea. Fig. 1 shows the study area and location of boreholes. In this study, 57 geotechnical boreholes with variable depths (5 to 40 m) were collected from different sources. Moreover, 33 boreholes were drilled for better evaluation of subsurface conditions.

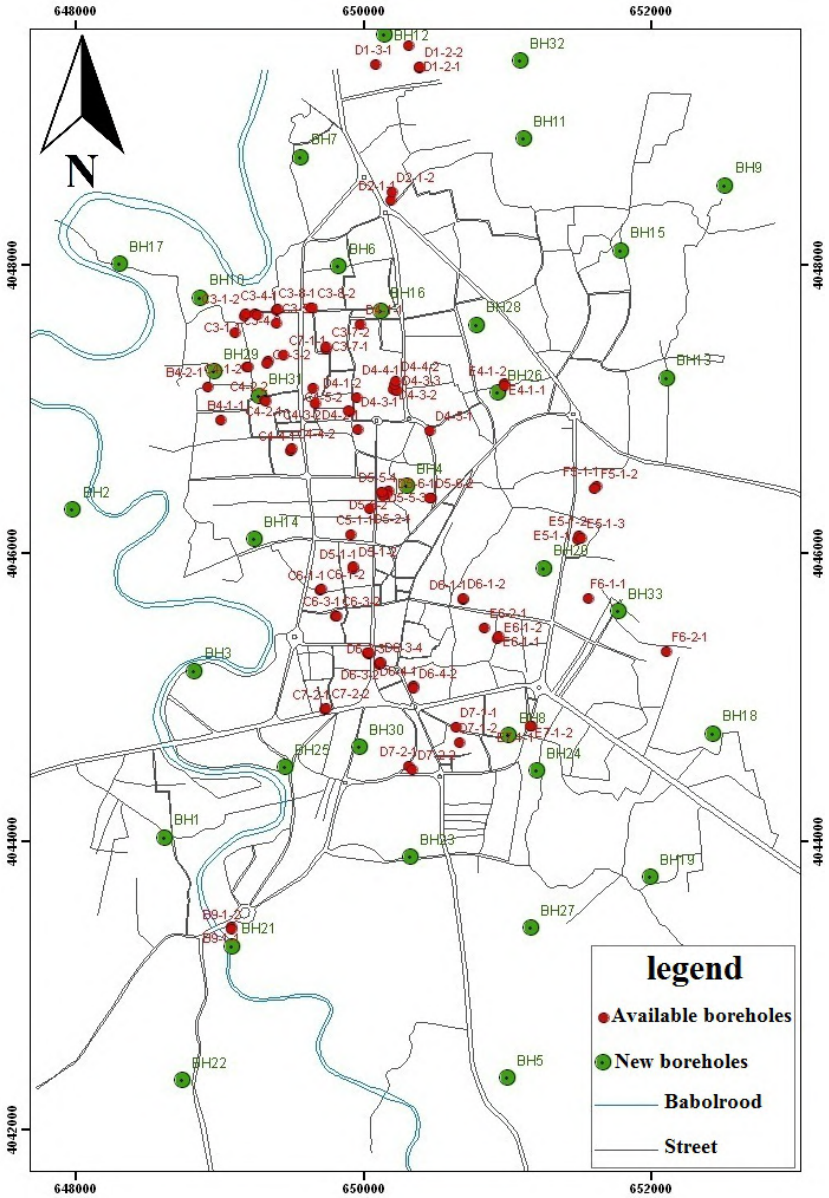


Figure 1. The study area and location of boreholes.

Using geotechnical data and Rockworks software, soil layering in the study area was obtained for various depths. For example, Fig. 2 shows the distribution of soil texture at the ground level.

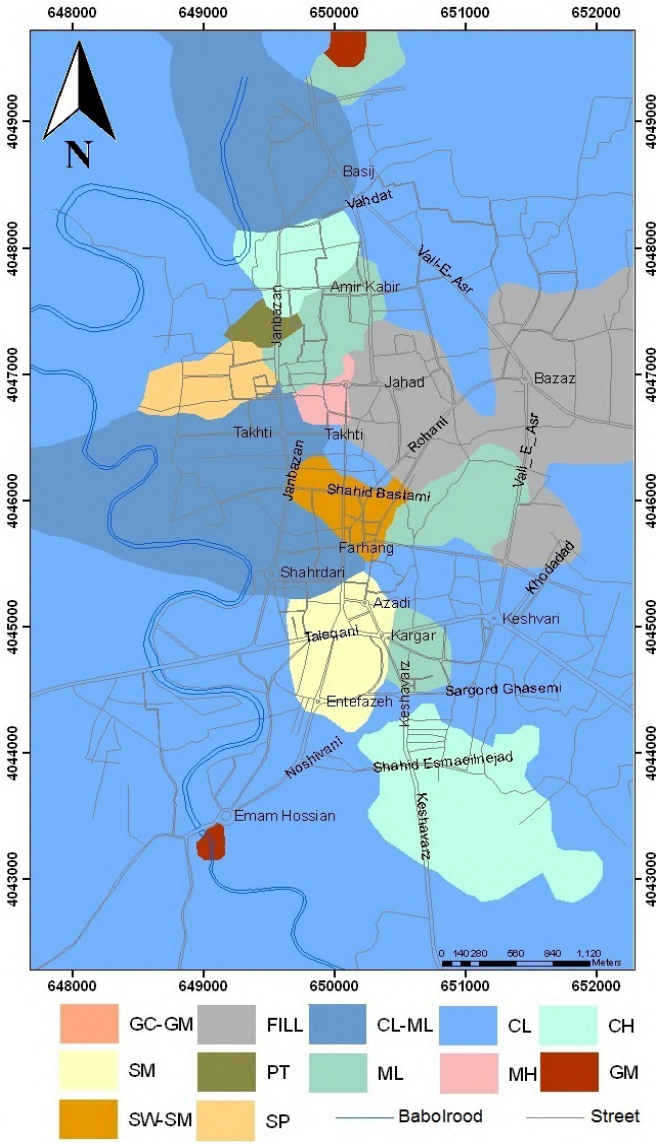


Figure 2. Distribution of soil texture at the ground level in Babol city.

Using these data, the geological model of the study area was provided which is used for numerical analysis. In addition, the results of the laboratory (direct shear, unconfined compression and Atterberg tests) and field (Standard Penetration Test) tests showed that the study area is consisted mainly of fine-grained soil with low relative density (Standard Penetration Test number <10, unconfined compressive strength <60 kPa). The study area and its surroundings up to 150 km radius are located in two seismic zones of Rasht-Gorgan and Central Alborz. Table 1 presents the major faults within the 150 km radius of the study area.

Table 1. Characteristics of faults around the study area [24].

Fault name	Distance to study area (km)	Fault length (km)	Fault mechanism
Firooz Abad	85	112	thrust fault
Alborz	44	300	thrust fault
Khazar	16	550	thrust fault
Attari	91	85	thrust fault
Astane	93	75	thrust fault
Garmsar	136	70	thrust fault
Kandovan	100	64	thrust fault
Masha	91	400	thrust fault
North of Tehran	115	108	thrust fault
Ivanaki	143	75	thrust fault
Firoozkooh	84	40	thrust fault
Basham	96	71	thrust fault
Ourim	72	44	thrust fault
Damghan	136	100	thrust fault
Robat Karim	184	90	thrust fault
Bayjan	60	45	thrust fault

The study area has repeatedly experienced earthquakes such as Qumis (22 December 856), Rey-Taleghan (23 February 958), Damavand-Shemiranat (27 March 1830), Ah-Mubarakabad (2 October 1930), Kusut (11 April 1935), Bandpay (2 July 1957), Babol Kenar (2 August 1971), Kojoor (28 May 2004), Marzi Kola (16 January 2012), Kiasar (21 March 2013), Surak (20 March 2017) and Juybar (23 September 2018).

Fig. 3, which was provided using GeoMap software, depicts the epicenter of the earthquakes with magnitudes greater than 5 Richter occurred around the study area within the last 50 years. Table 1 and Fig. 3 show the high seismic potential of the study area which highlights the need for site effect evaluation.

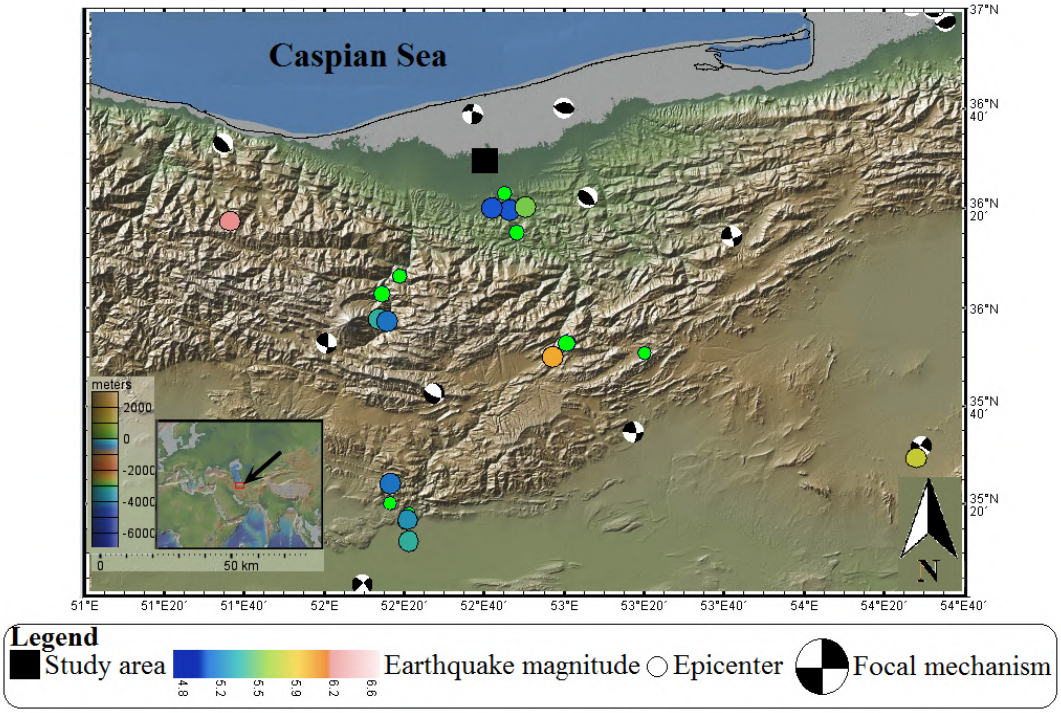


Figure 3. Earthquakes with magnitudes of more than 5 Richter occurred around the study area.

In order to analyze site effect, nonlinear method using PLAXIS software was applied in this study. Nonlinear analysis is in fact, the analysis of real nonlinear response of soil mass using direct numerical integration in the time domain. By integrating the equation of motion in short- time steps, any linear or nonlinear stress- strain model or even complex behavioral model can be solved [22]. Nonlinear dynamic analysis in PLAXIS software is divided into three general sections. The first part is modeling geometry, selecting materials and appropriate constitutive model, introducing boundary conditions, static and dynamic loading, and generating finite element mesh. The second part is introducing the first conditions of the model and finally, the third part is receiving results from the software [33]. In this study, 6-node triangular elements were used. To analyze the propagation of waves and the impact of alluvium on earthquake, some characteristics such as soil type, number and thickness of soil layers, soil density, moisture content, groundwater level and shear wave velocity should be determined. This data set is called the dynamic site profile. The shear wave velocities are obtained by down-hole tests and other data are found through borehole logs and laboratory tests. The results of down-hole tests showed that Babol soil type is generally type IV according to soil classification in standard No. 2800. Fig. 4 indicates the results of down-hole tests for one of the boreholes (BH1).

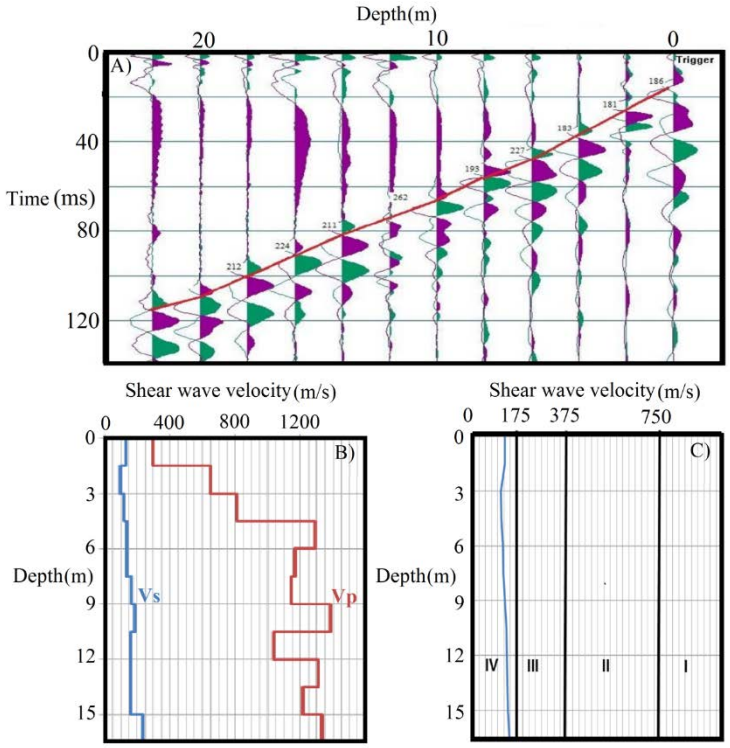


Figure 4. Down-hole test for BH1 borehole (a) Shear wave mapping (b) Shear and compressional wave velocity profiles (c) Variation of mean shear wave velocity with depth and its classification according to standard No. 2800.

The Mohr-Coulomb elasto-plastic model was selected as the appropriate behavioral model in this study. The side boundaries are restricted in the horizontal direction and the bottom boundary is restricted in both horizontal and vertical directions. Since soil is a semi-infinite space, special boundary conditions have to be defined for dynamic problems such as earthquakes. Without these boundary conditions, the waves reflect on the boundaries due to the disturbance. To avoid this wrong reflection, absorbent boundaries are applied using the damping spring at the boundary. In PLAXIS software, the conditions of absorbing reflection waves from the boundaries are provided using dampers. Moreover, the earthquake is simulated by a predefined inductive displacement at the bottom boundary. Another important issue in dynamic analysis is the numerical instability of wave propagation that can be occurred due to inappropriate modeling. To provide accurate wave propagation in a model, maximum element size (Δl) should be less than one-tenth of the longest wavelength (λ):

$$\Delta l \le \frac{\lambda}{10}. \tag{1}$$

For most of the earthquakes, frequency range of Fourier spectrum is between 0 and 10 Hz. In order to avoid numerical instability, Eq. (2) was applied in the numerical modeling:

$$\lambda \le \frac{c}{f}, \tag{2}$$

where c is wave propagation velocity and f is frequency. Since the lowest shear wave velocity in this research is 110 m/s and the highest earthquake frequency is 10 Hz, it can be expressed that:

$$\Delta l \le \frac{110}{10 \times 10} = 1.1 \text{ m}. \tag{3}$$

To improve the accuracy, Δl was considered 1 m in this study. In order to analyze site response, selection of appropriate accelerogram is very important [25, 34–35].

In order to estimate the earthquake hazard within a radius of 150 km from Babol city, first, all tectonic activities are identified and mapped using satellite imagery and aerial photographs. Then, the seismic features of faults and the seismic history of the study area are investigated. At the next step, the seismic model of the study area is proposed and important seismic sources are identified. The seismic characteristics of each region are determined using the data of earthquakes as well as the empirical

relationships. Then, seismic parameters are predicted based on probabilistic statistics method. Finally, appropriate accelerograms are introduced and scaled. In this study, accelerograms of Bam, Naghan, Tabas, Baladeh, San Fernando and Northridge earthquakes were used. It should be mentioned that at least 3 stations were evaluated for each earthquake. Several factors such as spiky behavior, near or far field and vibration duration of earthquakes were considered for selection of stations and accelerograms. In fact, considering different parameters and accelerograms causes most of the possible earthquake scenarios to be investigated. The process of scaling accelerograms should be in such a way that response spectrum of accelerograms at the end of the computation is similar to the target response spectrum for each design level. For this purpose, first, applying the main accelerogram in the frequency domain, the response spectrum of the considered accelerogram is calculated and then, by considering the values of the original accelerogram response spectrum and the target response spectrum, the scaling process is performed. This process is repeated several times until scaled accelerogram response spectrum matches target response spectrum as much as possible. Finally, using inverse Fourier transform in time domain, the scaled accelerogram is obtained.

Fig. 5 shows one of the modified earthquakes for Babol in which green and red accelerograms are related to original and modified earthquakes, respectively. After modeling and application of seismic loading, the results of site analysis for different zones (90 boreholes) are obtained.

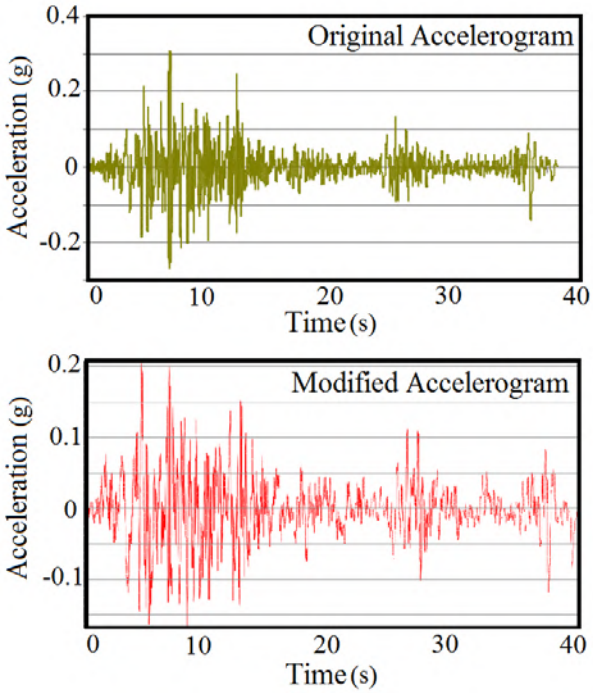


Figure 5. One of the scaled earthquakes for Babol site (Tabas earthquake-Deyhook station, horizontal component).

3. Results and Discussion

In this section, after modeling dynamic profiles at different zones, results of their nonlinear analyses are compared with each other. Utilization of response spectrum is one of the common methods for description of ground motion. Although the response spectrum cannot accurately describe the actual ground motion, it contains valuable information about the impact of ground motion on structures [22, 36–37]. The tripartite response spectra were used in this study because they contain information about displacement, pseudo-velocity and pseudo-acceleration response spectra [22]. Since it is not possible to present the results of 90 analyses individually, the similar results were collected in one group. Overall, the tripartite response spectra were classified into 5 types. Several parameters such as natural site period, acceleration time-history and velocity time- history were considered in this classification. Fig. 6 shows five different types of tripartite response spectra in Babol city which should not be mistaken with soil types in standard No. 2800. As observed, for acceleration sensitive range (period < 0.5 s), response spectra are close to each other. For velocity sensitive range (0.5 < period < 3 s), response spectra have the maximum difference with each other. For displacement sensitive range (period > 3 s), response spectra are also different from each other. The location of each response spectrum type in Babol city is presented in Table 2 which can be used for providing Babol zonation map.

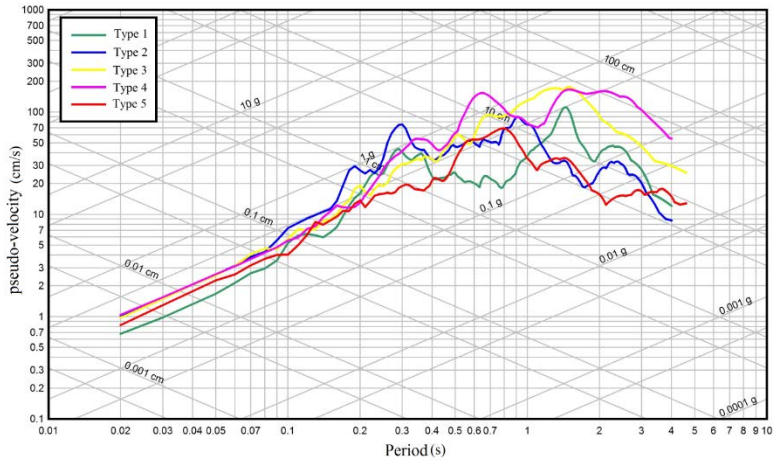


Figure 6. Five different types of tripartite response spectra.

Table 2. Location of response spectra in Babol city.

Response spectrum type No.	Location
Type 1	The central and northern parts of the city
Type 2	The west and northwest parts of the city
Type 3	The eastern and southeastern parts of the city
Type 4	The southern and southwest parts of the city
Type 5	The northeast part of the city

Fig. 7 indicates comparison of the shape factors obtained by nonlinear analyses and the design spectrum shape factor presented in standard No. 2800 for soil type IV. The obtained shape factors through nonlinear analysis shows soil amplification for different periods during seismic loading. The outputs of PLAXIS are imported into Seismosignal software and shape factors for different types are determined. The soil type IV in standard No. 2800 is a non-cohesive soil with low to medium density or soft to stiff cohesive soil. The average shear wave velocity in different soil layers up to 30 m depth from the base level, corrected standard penetration number and undrained shear strength up to 30 m depth from the base level are 175 m/s, 15 and 70 kPa, respectively [11]. Thus, the dominant soil in the study area is type IV. Several points are evident from Fig. 7:

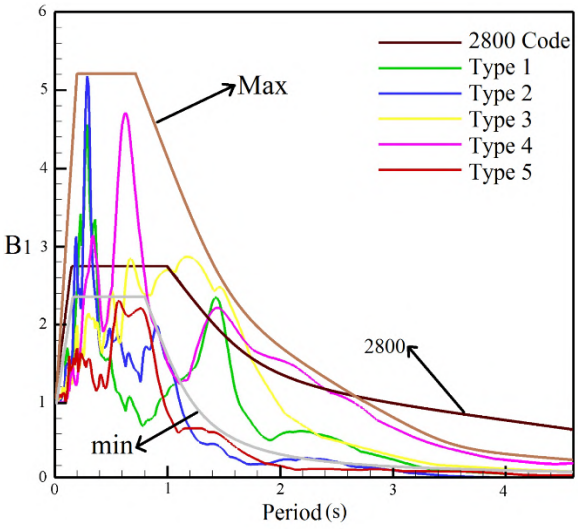


Figure 7. Shape factors obtained by nonlinear analyses and standard No. 2800 for soil type IV.

1. In various zones of Babol city, soil layers have different natural periods. When the period of site matches the structure period, resonance phenomenon occurs. This issue should be considered in urban development planning.

2. The obtained response spectra by nonlinear analyses, except for natural site periods (0 < period <
< 1 s), are in the range of the standard No. 2800 design spectrum or very close to this range. Hence, it can

be stated that unless when the natural periods of structures are within the range of 0 to 1 second, the design of the structures based on standard No. 2800 is almost safe and reliable. It should be noted that type 5 is out of this rule and the design provided by standard No. 2800 is safe in all frequency bands.

3. More than one peak is observed for some spectra (type 1 and 4) in which the first and second peaks show the period of the higher modes of site and the natural site period, respectively.

4. The design spectrum of standard No. 2800 for long periods (more than 2.5 seconds) is greater than the obtained response spectra from the nonlinear analyses.

5. For natural site periods, the shape factor presented by standard No. 2800 (except type 5) is not appropriate.

6. The difference between results of nonlinear analyses with design spectrum of standard No. 2800 becomes more obvious with increasing earthquake magnitude. This clarifies the necessity to consider the nonlinear analysis of site, particularly for the design of important structures.

7. When soil behavior is in the range of elastic or elasto-plastic, standard No. 2800 can be applied. Otherwise, nonlinear analysis method is recommended.

8. The declining part of the design spectrum presented by standard No. 2800 (period > 2.5 s) should be modified and the shape factor needs to be reduced. On the other hand, for shorter periods (period < 1s), the shape factor presented by standard No. 2800 should be increased.

In order to reveal the differences between the results found by nonlinear analysis and standard No. 2800, base shear and drift for one to six-story structures (common structures in Babol) are calculated using three different design approaches which are design spectrum of standard No. 2800 and the maximum and minimum spectra found by the site analysis. The maximum site spectrum is the spectrum that other spectra are below it (Fig. 7) and the minimum site spectrum is the spectrum that only type 5 spectrum (the lowest spectrum) is below it (Fig. 7). For modeling of the structures, ETABS software was used. In order to avoid over-resistance in the members and also to increase the accuracy of the results, the columns and beams are selected so that the stress ratio is close to 1.

Fig. 8 shows the 5-story structure model in this study. Fig. 9 shows variation of base shear values obtained using three different shape factors against the number of structure stories. The base shear values for all of the structures designed using the minimum spectrum were lower than the ones designed by standard No. 2800. In other words, in the areas of the city where the minimum spectrum is dominated, design of the structures using standard No. 2800 seems safe and uneconomic. For the areas of the city where the maximum spectrum is dominated, design of the structures using standard No. 2800 is unsafe.

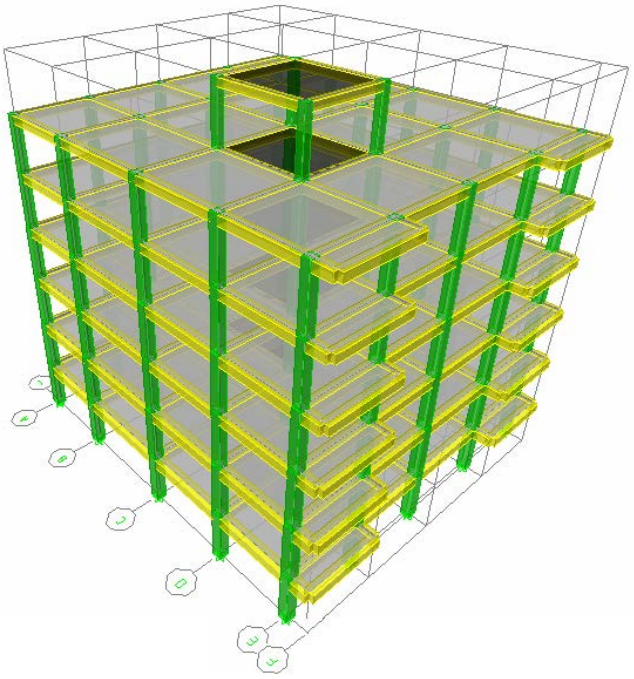


Figure 8. The 5-story structure model.

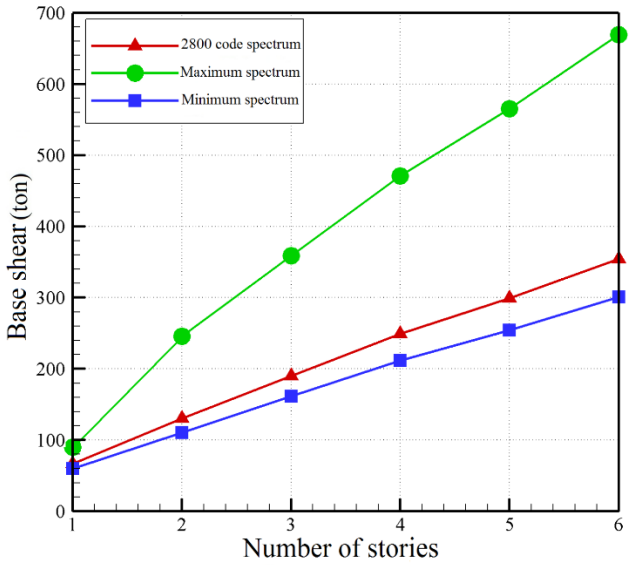


Figure 9. Variation of base shear values with the number of stories.

The results presented so far are related to the structures with the common number of stories in Babol city (one to six-story structures). At this stage, for a more detailed study of the site and structure effects, the base shear values are calculated for buildings with different frequencies. Since the tallest building in Babol city has less than 20 stories, the frequencies between 0.5 and 10 Hz were evaluated. Fig. 10 indicates variation of base shear with structure frequency. It is observed that the greatest base shear occurs at a frequency of about 1 Hz. This issue should be considered in the future design of structures in this city.

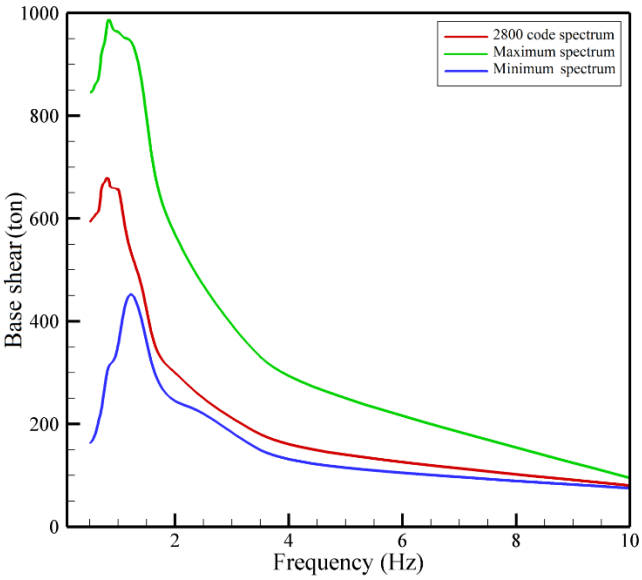


Figure 10. Variation of base shear with structure frequency.

Figs. 11 and 12 indicate variation of the number of stories with drift for a 6- and 4-story structure designed with the three mentioned spectra, respectively. For both of these Figs., the values of drifts achieved by the minimum spectrum are less than the ones presented by standard No. 2800. Therefore, in the areas of the city where this spectrum is dominated, design of the structures using standard No. 2800 is safe. Furthermore, the values of drifts obtained by the maximum spectrum are more than the ones presented by standard No. 2800. This can cause the structure to collapse during an earthquake.

The results of the modeling depict that design of structures based on standard No. 2800 is unsafe and uneconomic in some areas. Thus, consideration of site effect, particularly site-specific design spectrum, is necessary for design of structures. It should be remarked that the periods of the considered structures (common structures in Babol) were less than 1 s. Therefore, the difference between the results obtained by the minimum spectrum and standard No. 2800 is not considerable.

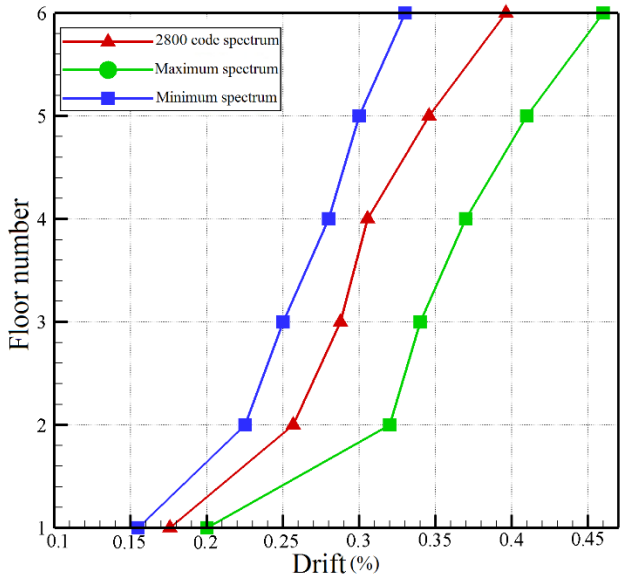


Figure 11. Variation of the floor number with drift for a 6-story structure.

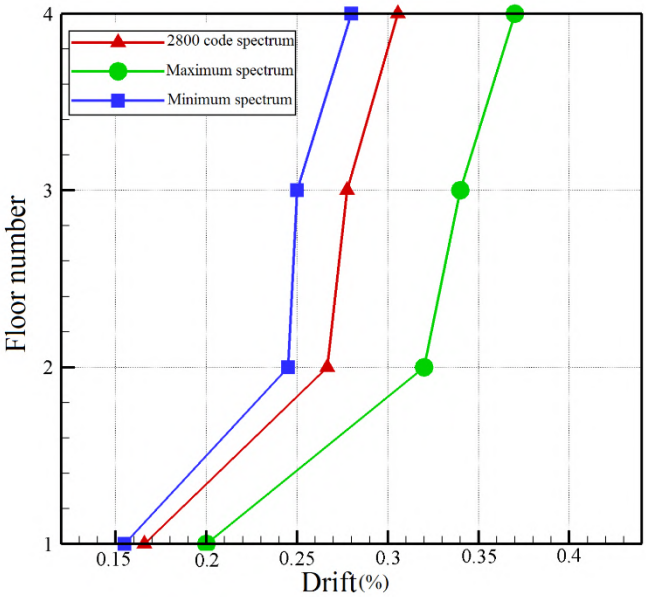


Figure 12. Variation of the floor number with drift for a 4-story structure.

4. Conclusions

In this study, nonlinear analysis method was used for evaluation of site effect and achievement of appropriate design spectrum in Babol city. Regarding to the nonlinear site response analysis, the following conclusions achieved:

1. Using seismic, geotechnical and geophysical data, dynamic profiles of 90 regions in Babol were modeled and 5 types of response spectra were introduced. Evaluation of the tripartite response spectra of these 5 types indicates that their behavior differ substantially from one another in some parts of the frequency range. This issue illustrates the importance of site effect consideration.

2. In order to compare the results obtained by nonlinear analysis with standard No. 2800, the shape factors of different types were compared with the design spectrum of soil type IV of standard No. 2800. This comparison indicated that the response spectrum obtained through analysis is different from the Iranian seismic code design spectrum.

3. The standard No. 2800 design spectrum is conservative for long periods. For natural site periods, except for type 5, the shape factor presented by the standard No. 2800 is not appropriate. It can be stated that application of standard No. 2800 is only recommended for elastic or elasto-plastic ranges. Otherwise, nonlinear analysis method should be employed.

4. To further investigate the differences in the results of site analysis with standard No. 2800, base shear and drift of 1 to 6-story structures (common structures in Babol) were calculated using the standard No. 2800 design spectrum and the maximum and minimum spectra obtained from the site analyses. The results showed that base shear and drift values for all structures designed using the minimum response spectrum were lower than the ones designed by standard No. 2800. It can be expressed that in areas of the city where this spectrum is dominant, design of the structures using standard No. 2800 is safe.

5. Base shear and drift values for structures that were designed using the maximum response spectrum were higher the ones designed by standard No. 2800. In other words, in areas of the city where this spectrum is dominated, the design using standard No. 2800 is unsafe and structures are seriously damaged during earthquakes. In addition, the greatest base shear occurs at a frequency of about 1 Hz. This issue should be considered in the future design of structures in this city. Finally, it can be concluded that consideration of site effect phenomenon in standard No. 2800 is very necessary.

References

1. Kockar, M.K., Akgun, H. Evaluation of the site effects of the Ankara basin, Turkey. Journal of Applied Geophysics. 2012. 83. Pp. 120–134. DOI: 10.1016/j.jappgeo.2012.05.007
2. Rezaei, S., Choobbasti, A.J., Kutanaei, S.S. Site effect assessment using microtremor measurement, equivalent linear method, and artificial neural network (case study: Babol, Iran). Arabian Journal of Geosciences. 2015. 8. Pp.1453–1466. DOI: 10.1007/s12517-013-1201-1
3. Rezaei, S., Choobbasti, A.J. Evaluation of local site effect from microtremor measurements in Babol City, Iran. Journal of Seismology. 2018. 22. Pp. 471–486. DOI: 10.1007/s10950-017-9718-5
4. Pamuk, E., Ozer, C. The site effect investigation with using horizontal-to-vertical spectral ratio method on earthquake data, South of Turkey. Geotectonics. 2020. 54. 4. Pp. 563–576. DOI: 10.1134/S001685212004010X
5. Asakereh, A., Tajabadipour, M. Analysis of local site effects on seismic ground response under various earthquakes. AUT Journal of Civil Engineering. 2018. 2. Pp. 227–240. DOI: 10.22060/AJCE.2018.13696.5253
6. Kohrangi, M., Bazzurro, P., Vamvatsikos, D. Seismic risk and loss estimation for the building stock in Isfahan: part II–hazard analysis and risk assessment. Bulletin of Earthquake Engineering. 2021. 1. Pp. 1–25. DOI: 10.1007/s10518-020-01036-2
7. Zafarani, H., Jafarian, Y., Eskandarinejad, A., Lashgari, A., Soghrat, M.R., Sharafi, H., Afraz-e Haji-Saraei, M. Seismic hazard analysis and local site effect of the 2017 Mw 7.3 Sarpol-e Zahab, Iran, earthquake. Natural Hazards. 2020. 103. Pp. 1783–1805. DOI: 10.1007/s11069-020-04054-0
8. Vedugo, R., Ochoa-Cornejo, F., Gonzalez, J., Valladares, G. Site effect and site classification in areas with large earthquakes. Soil Dynamics and Earthquake Engineering. 2019. 126. No. 105071. DOI: 10.1016/j.soildyn.2018.02.002
9. Bisch, P., Carvalho, E., Degee, H., Fajfar, P., Fardis, M., Franchin, P., Kreslin, M., Pecker, A., Pinto, P., Plumier, A. Somja, H. Eurocode 8: seismic design of buildings worked examples. 2011. Luxembourg.
10. New Zealand society for earthquake engineering. The seismic assessment of existing buildings. Technical Guidelines for Engineering Assessments. Part B – Initial Seismic Assessment. 2017. Wellington.
11. Permanent Committee for Revising the Iranian Code of Practice for Seismic Resistant Design of Buildings (Standard No. 2800), 4th Edition. Building and Housing Research Center. 2014 (in Persian).
12. Hoshmand, S., Fatemi Aghda, S.M., Hashemi Tabatabaei, S. Soil classification using standard No. 2800, UBC 1997, IBC 2006, Eurocode 8 2004 (case study: Piroozi Avenue, Tehran, Iran). Journal of Engineering Geology. 2011. 1. Pp. 1177–1192.
13. Nicknam, A., Yousefi Dadras, E. Modification of the design response spectra in Iranian standard 2800 (fourth version) taking into account the directivity effects. Amirkabir Journal of Science and Research. 2014. 46. Pp. 165–188.
14. Nicknam, A., Mazarei, A., Ganjvar, M. Assessment of Iran seismic design response spectra (standard No. 2800) regarding site-distance effects particularly at near fault sites. Amirkabir Journal of Civil Engineering. 2017. 49. Pp. 547–564. DOI: 10.22060/ceej.2016.862
15. Nicknam, A., Kazemi, M.T., Nicknam, A. Evaluation and comparison of near- and far-fault earthquakes using design spectrum of standard No. 2800. Journal of Civil Engineering Islamic Azad University. 2008. 1. Pp. 71–79.
16. Choobbasti, A.J., Rezaei, S., Farrokhzad, F., Heidarzadeh Azar, P. Evaluation of site response characteristics using nonlinear method (Case study: Babol, Iran). Frontiers of Structural and Civil Engineering. 2014. 8. Pp. 69–82. DOI: 10.1007/s11709-014-0231-4
17. Uniform Building Code. International conference of building officials. 1997.
18. International code council. 2018's International building code. 2018.
19. National earthquake hazards reduction program. NEHRP recommended seismic provisions for new buildings and other structures. 2009.
20. Trifunac, M.D. Site conditions and earthquake ground motion – A review. Soil Dynamics and Earthquake Engineering. 2016. 90. Pp. 88–100. DOI: 10.1016/j.soildyn.2016.08.003
21. Sánchez-Sesma, F.J., Palencia, V.J., Luzón, F. Estimation of local site effects during earthquakes: an overview. ISET Journal of Earthquake Technology. 2002. 39. Pp. 167–193.
22. Kramer, S.L. Geotechnical earthquake engineering. New Jersey, 1996. 653 p.
23. Adampira, M., Alielahi, H., Panji, M., Koohsari, H. Comparison of equivalent linear and nonlinear methods in seismic analysis of liquefiable site response due to near-fault incident waves: a case study. Arabian Journal of Geosciences. 2015. 8. Pp. 3103–3118. DOI: 10.1007/s12517-014-1399-6
24. Rezaei, S., Choobbasti, A.J. Liquefaction assessment using microtremor measurement, conventional method and artificial neural network (case study: Babol, Iran). Frontiers of Structural and Civil Engineering. 2014. 8. Pp. 292–307. DOI: 10.1007/s11709-014-0256-8

25. Shreyasvi, C., Venkataramana, K., Chopra, S. Local site effect incorporation in probabilistic seismic hazard analysis – A case study from southern peninsular India, an intraplate region. Soil Dynamics and Earthquake Engineering. 2019. 123. Pp. 381–398. DOI: 10.1016/j.soildyn.2019.04.035
26. Rezaei, S., Shooshpasha, I., Rezaei, H. Evaluation of ground dynamic characteristics using ambient noise measurements in a landslide area. Bulletin of Engineering Geology and the Environment. 2020. 79. Pp. 1749–1763. DOI: 10.1007/s10064-019-01637-5
27. Verdugo, R. Seismic site classification. Soil Dynamics and Earthquake Engineering. 2019. 124. Pp. 317–329. DOI: 10.1016/j.soildyn.2018.04.045
28. Rajabzadeh, H., Mehrnahad, H. Comparison of equivalent linear and nonlinear analyses in site response (case study: Tabas city). Journal of Engineering Geology. 2018. 1. Pp. 41–62.
29. Ehsani, N., Ghaemmaghamian, M.R., Fazlavi, M., Haghshenas, A. Investigation of site effects using numerical and experimental methods in Karaj. Journal of Engineering Geology. 2017. 1. Pp. 1–28.
30. Navarro, M., García-Jerez, A., Alcalá, F.J., Vidal, F., Enomoto, T. Local site effect microzonation of Lorca town (SE Spain). Bulletin of Earthquake Engineering. 2014. 12. Pp. 1933–1959. DOI: 10.1007/s10518-013-9491-y
31. Purnachandra Rao, N., Rabi Kumar, M., Seshunarayana, T., Shukla, A.K., Suresh, G., Pandey, Y., Dharma Raju, R., Pimprikar, S.D., Chandra, D., Kalpna, G., Mishra, P.S., Harsh G. Site amplification studies towards seismic microzonation in Jabalpur urban area, central India. Physics and Chemistry of the Earth. 2011. 36. Pp. 1247–1258. DOI: 10.1016/j.pce.2011.01.002
32. Belash, T.A., Ivanova, T.V. Earthquake resistance of buildings on thawing permafrost grounds. Magazine of Civil Engineering. 2020. 93. Pp. 50–59. DOI: 10.18720/MCE.93.5
33. Brinkgreve, R.B.J., Vermeer, P.A. Plaxis Manual (Version8). University of Stuttgart. Germany A.A. Balkema / Rotterdam / Brookfield-D. 2006.
34. Milana, G., Azzara, R.M., Bertrand, E., Bordoni, P., Cara, F., Cogliano, R.,Cultrera, G., Di Giulio, G., Duval, A.M., Fodarella, A., Marcucci, S., Puccilo, S., Regnier, J., Riccio, G. The contribution of seismic data in microzonation studies for downtown L'Aquila. Bulletin of Earthquake Engineering. 2011. 9. Pp. 741–759. DOI: 10.1007/s10518-011-9246-6
35. Sokolova, O.V. The selection of soil models parameters in Plaxis 2D. Magazine of Civil Engineering. 2014. 4. Pp. 10–15. DOI: 10.5862/MCE.48.2
36. Lu, T., Huo, J., Rong, M. Nonlinear response analysis of soil layers under severe earthquake. Procedia Environmental Sciences. 2012. 12. Pp. 940–948. DOI: 10.1016/j.proenv.2012.01.369
37. Takewaki, I. Critical excitation for elastic–plastic structures via statistical equivalent linearization. Probabilistic Engineering Mechanics. 2002. 17. Pp. 73–84. DOI: 10.1016/S0266-8920(01)00030-3

Contacts:

Sadegh Rezaei, S_Rezaei1366@yahoo.com
Hasanzadeh Ali, a_hasanzade64@yahoo.com

Received 10.09.2020. Approved after reviewing 29.03.2021. Accepted 31.03.2021.



Magazine of Civil Engineering

ISSN 2712-8172

journal homepage: http://engstroy.spbstu.ru/

DOI: 10.34910/MCE.110.9

The behaviour of thin-walled beam with restrained torsion

V.V. Galishnikova*[a], *T.H. Gebre*[b]

[a] *National Research Moscow State Civil Engineering University, Moscow, Russia*

[b] *Peoples' Friendship University of Russia, Moscow, Russia*

**E-mail: tesfaldethg@gmail.com*

Keywords: thin-walled structures, restrained torsion, section properties, angle of twist, open section, closed sections, non-uniform warping, torsional stress

Abstract. In this paper, the behaviour of thin-walled sections of a bar with restrained torsion is studied. Neglecting these warping behaviours may generate significant errors, particularly for open profile torsion or shear bending of short beams. The governing equation for non-uniform torsion is used to study the behaviour of the beam with restrained torsion. The variation of the primary torsional moment, secondary torsional moments and warping moments for different value of characteristic number for torsion are presented graphically. Finally, the behaviour and comparison of all torsional moment components with three different thin-walled sections are illustrated by presenting and discussing their results. The section properties, displacements, rotations, stresses and their distribution within the span are compared based on the required value of characteristic number for torsion. It is found that for all thin-walled sections, the characteristic number for torsion is the key criteria for the study of the behaviour of thin-walled sections of a bar with restrained torsion.

1. Introduction

The behaviour of a bar with restrained torsion differs significantly from stretching and bending moreover their mathematical formulations varies. In analyses of thin-walled structures subjected to torsion, the effect of warping must be considered as the axial stresses mainly occur at the points of action of concentrated torsion moments (except for free ends) and at sections with warping restraints. The most profitable and effective way to construction of prefabricated structures is to use the system of light steel thin-walled structures, and also thermal insulation, facing and vapor sealing [1]. Normally, thin-walled sections do not behave according to the law of the plane sections employed by Euler-Bernoulli-Navier however the general theory of thin-walled section developed by Vlasov [2]. If warping is not restrained, the applied twisting moment is entirely carried by uniform torsion as a result the shear contribution to the deformation energy can be considered small enough [3–4]. Torsion leads not only to cross-section rotation about the centre of twist but at the same time the points of the section undergo different displacements along the longitudinal axis [5]. For warping restrained, the member develops additional shearing stresses, as well as normal stresses as warping stresses are not to be ignored [6–7]. The resulting stresses are primarily shear stresses (uniform torsion) or a combination of shear and longitudinal stresses (non-uniform torsion). The distribution of these stresses through the thin-wall section depends to a large extent on the cross sectional geometry and specifically whether it is open or closed sections [8]. In order to include warping shear stresses in the global equilibrium of the bar, that is to account for the secondary torsional moment deformation effect, an additional kinematical component (along with the angle of twist) is generally required, increasing the difficulty of the problem at hand [9].

Remarkable growth has been made since the 1945s in classical theories of torsion of thin-walled beams members with the consideration of warping, but it was limited to symmetric cross sections due to its complexity. There are many studies on non-uniform torsion with or without consideration of warping effects

Galishnikova, V.V., Gebre, T.H. The behaviour of thin-walled beam with restrained torsion. Magazine of Civil Engineering. 2022. 110(2). Article No. 11009. DOI: 10.34910/MCE.110.9

© Galishnikova, V.V., Gebre, T.H., 2022. Published by Peter the Great St. Petersburg Polytechnic University.

This work is licensed under a CC BY-NC 4.0

as theories and also as analysis using commercial FEM codes [8–16]. Similarly, researchers worldwide have extensively used fibre-reinforced polymer (FRP) strengthening materials to enhance the combined load strengths of reinforced concrete (RC) beams [18–23]. It has various well-known advantages such as high strength to weight ratio, high corrosive resistance, and easy-to-apply character [24]. The effect of span length of cantilever RC beams under pure torsion had been studied using a non-linear finite element analysis [25]. The element stiffness matrix and load vectors are derived using the primary and secondary warping functions [17–18]. Warping effects occur mainly at the points of action of the concentrated torsional moments (except for free beam ends) and at sections with free-warping restrictions [19–20]. The warping effect was included through an additional degree of freedom at each nodal point in the form of the first derivative of the angle of twist of the cross-section of the beam [10, 21]. Meanwhile, the torsional analysis of thin walled sections including shear has been studied in Ref. [15, 22–26]. The analysis of uniform torsion shows that the warping of bars depends on the shape of their section. A new torsion element of thin-walled beams including shear deformation which accounts for the warping deformation and shear deformation due to restrained torsion is developed [27–28]. Prismatic bars of solid and hollow sections or thin-walled section with a single interior vertex (for example an angle, a tee or a cross) do not warp but all other sections will experience warping of the cross section, depending on the geometry of the cross section [38]. Neglecting these warping stresses may generate significant errors specially for open profile torsion or shear-bending of short beams, and the situation may be even more critical for composite beams [6–7]. Warping-based stresses and deformations in closed sections, however, are assumed to be insignificant and have been therefore neglected [39]. Reasonably strong warping is expected to have effect in open than closed cross-sections and its significance is anticipated to be restricted to open cross-sections. Restraining the warping deformation causes the twist rate to be zero at the point of restraint and this causes a local effective torsional stiffening that affects the global torsional response of the beam [40]. The difference between the displacements and stresses due to uniform and non-uniform torsion is most pronounced for thin-walled sections. Warping of a thin-walled structures due to torsion stands for all the longitudinal displacements caused by the torsional rotation of the member cross-section around its shear centre. Thin-walled beam, because of its specific properties, has a unique internal force factor – bi-moment, which in certain cases can cause large normal stresses in cross-section [41].

In this paper, the behaviour of thin-walled sections of a bar with restrained torsion using the governing equation for non-uniform torsion is considered. This study is extensively applied to bars of closed and open sections of thin-walled steel cross section subjected to concentrated torsional loading and to the most general torsional boundary conditions. The variation of primary torsional moment $\left(\mathrm{M_{TP}}\right)$, secondary torsional moments $\left(\mathrm{M_{TS}}\right)$ and warping moments $\left(\mathrm{M_{\omega}}\right)$ for different value of characteristic number for torsion $\left(\theta\right)$ are presented graphically. Finally, the behavior and comparison of all torsional moment components with three different thin-walled sections are illustrated by presenting and discussion their results.

2. Methods

2.1. Defining Governing Equations

The governing equation for non-uniform torsion is used to study the behaviour of a bar with restrained torsion and it is derived for bars with thin-walled sections with local coordinate systems $\mathrm{y_1}, \mathrm{y_2}, \mathrm{y_3}$ as shown in Fig. 1 [31].

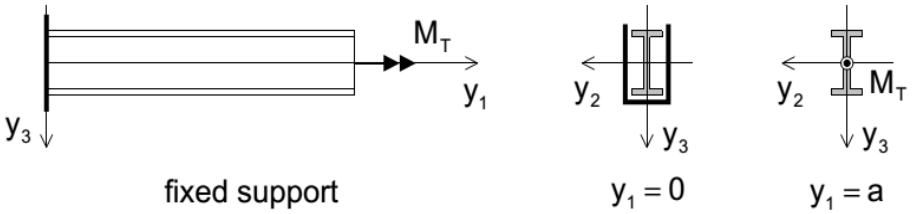


Figure 1. Torsion of prismatic bar.

When the bar is subjected to the arbitrarily distributed twisting moment $\mathrm{M_T}$ and its angle of twist is defined by the following governing equation (2.1) with boundary value problem [13, 18, 34, 42].

$$\frac{dM_T}{dy_1} + m_T = 0,$$
$$EC_\omega \frac{d^4\beta_1}{dy_1^4} - GJ\frac{d^2\beta_1}{dy_1^2} = m_T, \tag{2.1}$$

where β_1 is angle of twist, E, G are elastic constant, C_ω is warping constant, J is torsion constant, m_T is twisting load per unit length of bar.

If a bar undergoes non-uniform torsion, the total applied twisting moment $\mathrm{M_T}$ is resisted by an internal twisting moment that consists of two components as given in equation (2.2). The primary internal moment is the twisting moment $\mathrm{M_{TP}}$ due to uniform torsion (St Venant torsion). The secondary internal moment is the twisting moment $\mathrm{M_{TS}}$ is due to warping restraint and the twisting moments are expressed in terms of the angle of rotation β_1 and the properties of the shape of the section. The applied torque is resisted by a combination of the uniform and warping torques and it is given with its differential equation of non-uniform torsion.

$$\mathrm{M_T} = \mathrm{M_{TP}} + \mathrm{M_{TS}} = GJ\frac{d\beta_1}{dy_1} - EC_\omega \frac{d^3\beta_1}{dy_1^3}, \tag{2.2a}$$

where $\mathrm{M_T}$ is total twisting moment, $\mathrm{M_{TP}}$ is primary twisting moment due to uniform torsion, $\mathrm{M_{TS}}$ is secontary twisting moment due to warping restraint.

For an element with constant $\mathrm{M_T}$, the warping torsion $\mathrm{M_{TS}}$ generates a generalized force called Bimoment $\left(\mathrm{M_\omega}\right)$ as follows:

$$\mathrm{M_\omega} = -EC_\omega \frac{d^2\beta_1}{dy_1^2}. \tag{2.3b}$$

The total shear stress $\sigma_{12\mathrm{T}}$ due to torsion is the sum of the primary shear stress $\sigma_{12\mathrm{p}}$ due to the primary twisting moment for open section and the secondary shear stress $\sigma_{12\mathrm{s}}$ due to the secondary twisting moment for warping restraints.

$$\sigma_{12\mathrm{T}} = \sigma_{12\mathrm{p}} + \sigma_{12\mathrm{s}}. \tag{2.3}$$

Consider the homogeneous form of the governing equation (2) and let the characteristic number for torsion of a bar be defined as follows:

$$EC_\omega \frac{d^4\beta_1}{dy_1^4} - GJ\frac{d^2\beta_1}{dy_1^2} = 0,$$
$$\frac{d^4\beta_1}{dy_1^4} - \left(\frac{\theta}{a}\right)^2 \frac{d^2\beta_1}{dy_1^2} = 0, \tag{2.4}$$
$$\theta := a\sqrt{\frac{GJ}{EC_\omega}},$$

where θ is characteristic number for torsion, a is length of the bar.

The general solution for the homogeneous equation (2.4) is satisfied by the following assumed twisting angle function $\beta_1\left(\mathrm{y_1}\right)$ and it yields to the exact solutions of the angle of twists, its derivatives, twisting moments, and bimoments of a node. They are given by

$$\beta_1 = c_1 \sinh\frac{\theta y_1}{a} + c_2 \cosh\frac{\theta y_1}{a} + c_3\frac{y_1}{a} + c_4. \quad (2.5)$$

Based on the derivatives of equation (2.5) the following equations are obtained:

$$\frac{d\beta_1}{dy_1} = c_1\left(\frac{\theta}{a}\right)\cosh\frac{\theta y_1}{a} + c_2\left(\frac{\theta}{a}\right)\sinh\frac{\theta y_1}{a} + c_3\frac{1}{a}, \quad (2.6)$$

$$\frac{d^2\beta_1}{dy_1^2} = c_1\left(\frac{\theta}{a}\right)^2\sinh\frac{\theta y_1}{a} + c_2\left(\frac{\theta}{a}\right)^2\cosh\frac{\theta y_1}{a}, \quad (2.7)$$

$$\frac{d^3\beta_1}{dy_1^3} = c_1\left(\frac{\theta}{a}\right)^3\cosh\frac{\theta y_1}{a} + c_2\left(\frac{\theta}{a}\right)^3\sinh\frac{\theta y_1}{a}, \quad (2.8)$$

$$\frac{d^4\beta_1}{dy_1^4} = c_1\left(\frac{\theta}{a}\right)^4\sinh\frac{\theta y_1}{a} + c_2\left(\frac{\theta}{a}\right)^4\cosh\frac{\theta y_1}{a}. \quad (2.9)$$

The free coefficients c_1 to c_4 are determined so that the boundary conditions at the ends of the bar are satisfied. If the vertex $y_1 = 0$ is fixed and a twisting moment M_T is applied at vertex $y_1 = a$ which is free to warp. Solving equation (2.5) with the boundary conditions and the free coefficients are given below:

$$c_3 = \frac{M_T a}{GJ},\ c_1 = -\frac{c_3}{\theta},\ c_2 = \frac{c_3}{\theta}\tanh\theta,\ c_4 = -\frac{c_3}{\theta}\tanh\theta.$$

These coefficients are substituted into expression (2.5) and the angle of twist is given below:

$$\beta_1 = \frac{M_T a}{GJ\theta}\left(\tanh\theta\left(\cosh\frac{\theta y_1}{a} - 1\right) - \left(\sinh\frac{\theta y_1}{a} - \frac{y_1}{a}\right)\right). \quad (2.10)$$

Based on equation (2.10), the following equations of M_{TP}, M_{Ts} and M_ω for a node are obtained.

$$M_{TP} = M_T + M_T\left(\tanh\theta\sinh\frac{\theta y_1}{a} - \cosh\frac{\theta y_1}{a}\right), \quad (2.11)$$

$$M_{TS} = -M_T\left(\tanh\theta\sinh\frac{\theta y_1}{a} - \cosh\frac{\theta y_1}{a}\right), \quad (2.12)$$

$$M_\omega = -\frac{M_T\theta}{a}\left(\tanh\theta\cosh\frac{\theta y_1}{a} - \sinh\frac{\theta y_1}{a}\right). \quad (2.13)$$

2.2. Numerical case studies

In this study, the variation of M_{TP}, M_{TS} and M_ω with different value of θ is investigated. Different section types are considered as it is given in Table 5 and the section properties, displacements, rotations, stresses are to be compared for all cases in addition their distribution with in the span is compared based on their values of θ. Tables 1 to 3 show comparatively for different value of θ along the span of the beam, the initial value of θ is 1 and the maximum is 10. The variation of M_{TP}, M_{TS} and M_ω for different value of θ are presented. The results are tabulated below to bars of closed and/or open sections of thin walled steel cross section subjected to different torsional loading and to the most general torsional boundary conditions. In Table 1, the values are obtained based on equation (2.11) as it is expressed in a dimensionless form for diverse values of θ as shown below.

Table 1. Variation of M_{TP} for different value of θ.

y_1/a	M_{TP} / M_T				
	θ = 1	θ = 2.5	θ = 5	θ = 7.5	θ = 10
0	1.00	1.00	1.00	1.00	1.00
0.2	0.87	0.61	0.37	0.22	0.14
0.4	0.77	0.38	0.14	0.05	0.02
0.6	0.70	0.25	0.05	0.01	0.00
0.8	0.66	0.18	0.02	0.00	0.00
1	0.65	0.16	0.01	0.00	0.00

Similarly, In Table 2 and Tables 3–4, the values are obtained based on equations (2.12) and (2.13) respectively and they are expressed in a dimensionless form for different values of θ as shown below.

Table 2. Variation of M_{TS} for different value of θ.

y_1/a	M_{TS} / M_T				
	θ = 1	θ = 2.5	θ = 5	θ = 7.5	θ = 10
0	0.00	0.00	0.00	0.00	0.00
0.2	0.13	0.39	0.63	0.78	0.86
0.4	0.23	0.62	0.86	0.95	0.98
0.6	0.30	0.75	0.95	0.99	1.00
0.8	0.34	0.82	0.98	1.00	1.00
1	0.35	0.84	0.99	1.00	1.00

Table 3. Variation of M_ω for different value of θ with θ/α = 2.

y_1/a	M_ω / M_T				
	θ = 1	θ = 2.5	θ = 5	θ = 7.5	θ = 10
0	–0.38	–0.49	–0.50	–0.50	–0.50
0.2	–0.29	–0.30	–0.18	–0.11	–0.07
0.4	–0.21	–0.17	–0.07	–0.02	–0.01
0.6	–0.13	–0.10	–0.02	–0.01	0.00
0.8	–0.07	–0.04	–0.01	0.00	0.00
1	0.00	0.00	0.00	0.00	0.00

Table 4. Variation of M_ω for different value of θ with θ/α = 4.

y_1/a	M_ω / M_T				
	θ = 1	θ = 2.5	θ = 5	θ = 7.5	θ = 10
0	–0.19	–0.25	–0.25	–0.25	–0.25
0.2	–0.14	–0.15	–0.09	–0.06	–0.03
0.4	–0.10	–0.09	–0.03	–0.01	0.00
0.6	–0.07	–0.05	–0.01	0.00	0.00
0.8	–0.03	–0.02	0.00	0.00	0.00
1	0.00	0.00	0.00	0.00	0.00

According to equation (2.5), with the solution function for $\beta_1(y_1)$ and replacing the integration constants with the deformations, the following stuffiness relation is obtained. Considering the non-uniform torsion, the warping effect is contained within through an additional degree of freedom at each nodal point of the beam.

$$K_T = \frac{EC_\omega}{a^3} \begin{vmatrix} k_{T1} & k_{T2} & k_{T3} & k_{T4} \\ k_{T2} & k_{T6} & k_{T7} & k_{T8} \\ k_{T3} & k_{T7} & k_{T11} & k_{T12} \\ k_{T4} & k_{T8} & k_{T12} & k_{T16} \end{vmatrix}$$

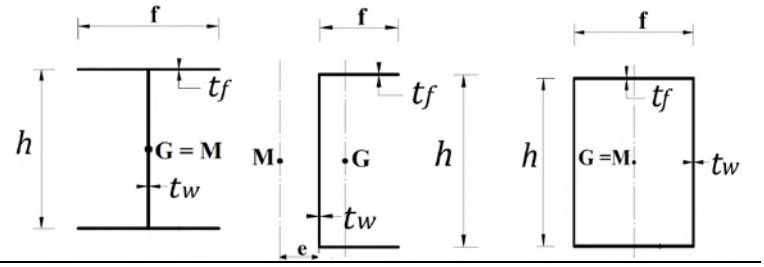
$$K_{T1} = K_{T11} = S * \theta \sinh\theta,\ K_{T6} = K_{T16} = S * (\cosh\theta - \frac{\sinh\theta}{\theta}) * a^2$$

$$K_{T2} = K_{T4} = S*(\cosh\theta - 1) * a,\ K_{T8} = S * \left(\frac{\sinh\theta}{\theta} - 1\right) * a^2$$

$$S = \left(\frac{\theta^2}{Q}\right),\ Q = 2(1-\cosh\theta) + \theta\sinh\theta,\ K_{T3} = -K_{T1},\ K_{T7} = K_{T12} = -K_{T2}$$

Different section types are given in Table 5 which are the I section, rectangular hollow section, and channel section. Considering the prismatic bar of Fig. 1 as it is fixed at vertex $y_1 = 0$ and subjected to a twisting moment of M_T without warping restraint at vertex $y_1 = a$. The section properties, displacements, rotations, stresses are to be compared for all cases and compared their distribution within the span based on the required value of θ.

Table 5. Different section types.

Section type			
h(mm)	400	400	400
f(mm)	180	180	180
t_f(mm)	11	11	11
t_w(mm)	8	8	8
$E = 200*10^6\ kN/m^2$	$M_T = 1.0\ kN\,m$	$G = 77*10^6\ kN/m^2$	

3. Results and Discussions

3.1. The variation of M_{TP}, M_{TS} and M_ω for different value of θ

The behavior and variation of M_{TP} and M_{Ts} for different value of θ which ranges from 1 to 10 are presented graphically in Fig. 2. Considering a point nearly to the support at $y_1 = 0$ for Fig. 1, the total torsional moment is largely carried by the primary twisting moment, whereas the secondary twisting moment is small. At points in the span, the torsion is carried partly as St. Venant torsion (i.e. by the St. Venant shear stresses) and partly as warping torsion (i.e. by the shear stresses caused by the restraint of warping. For θ=L both torsion mechanisms contribute to M_T throughout the beam in both cases but with the increasing of the value of θ the influence of the twisting moment role to the M_T varies as shown in the Fig. 2. In view of Fig. 2 (a) with increasing of θ value of M_{TP} reduces fast and the torsional moment is dominated by St. Venant in a major part of the beam. Similarly, in Fig. 2(b), with the increasing value of θ, the St. Venant moment is growing, and the torsional moment M_T is dominated by St. Venant in a major part of the beam in both cases.

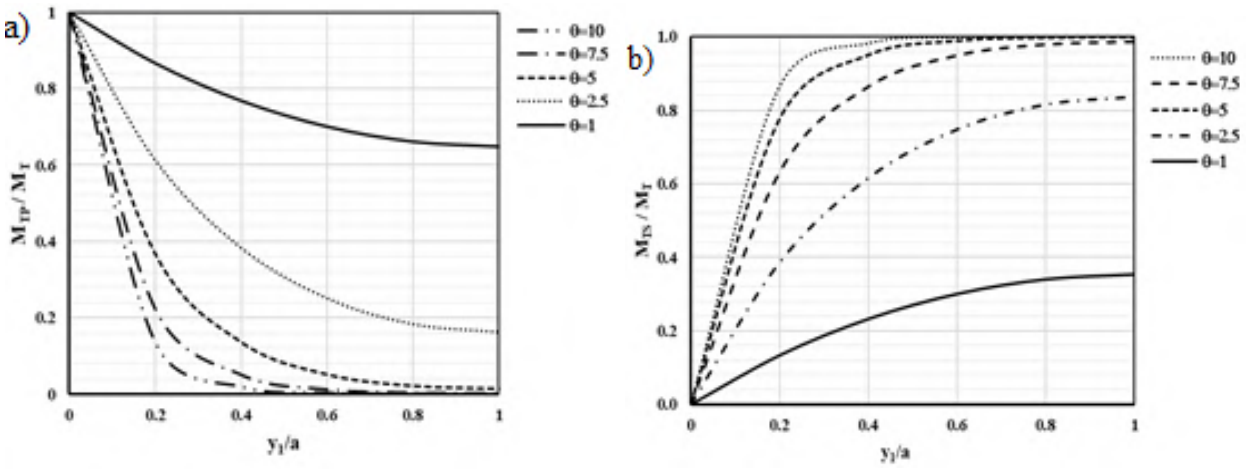


Figure 2. Variation of M_{TP} and M_{TS} for different value of θ.

Similarly, the behavior and variation of warping moment (M_ω) for different value of θ which ranges from 1 to 10 are presented graphically in Fig. 3 As the characteristics number for torsion (θ) is an indicator of how quickly the effect of warping restraint dissipates because the warping moment varies based on the restrained conditions of the beam. The variation of M_ω in the Fig. 3 displays the greater values at the fixed support where the warping is prevented and induces the largest normal stresses. At the free end the beam can warp freely as a result the normal stresses is zero, thus $M_\omega(a)=0$. The two graphs below are plotted for different value of θ/a (i.e. θ/a = 2 and 4) as it is for general case. The distribution of M_ω varies differently in both cases with varying values of θ and thus the normal warping stress differs along the beam based on the position of restrained torsion and section type.

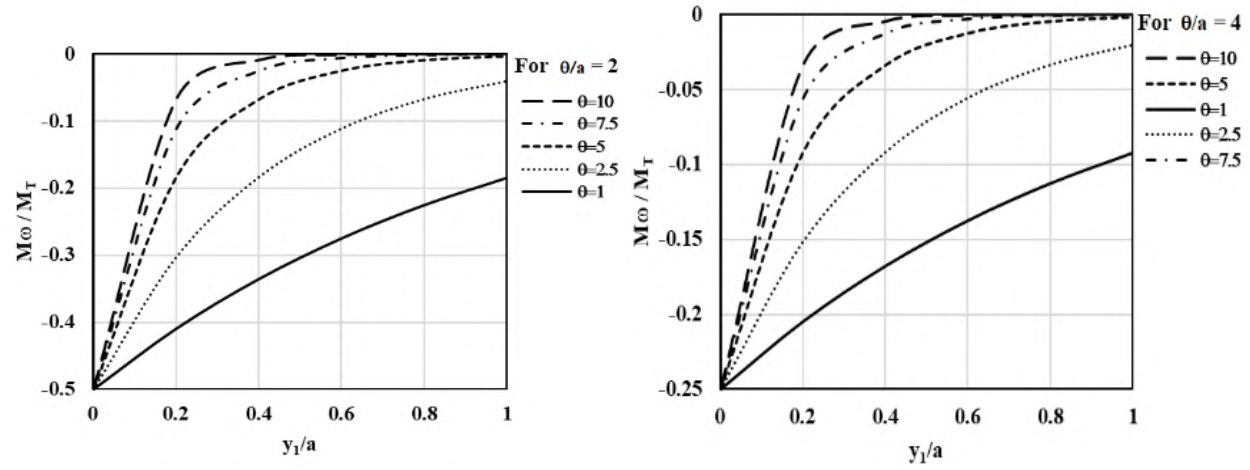


Figure 3. Variation of M_ω for different value of θ.

3.2. Comparison of M_T components with three different thin walled sections

The section properties, displacements, rotations, stresses are to be compared for all cases and compared their distribution with the span based on the required value of θ.

Case I: Refereeing Table 5, for an I- sections, the values of C_ω, J, θ and $\beta_1(a)$ are computed below:

$$C_\omega=\frac{1}{24}t_f b^3 h^2=0.4277*10^{-6}\,\mathrm{m}^6,\ J=\frac{1}{3}(2ft_f{}^3+ht_w{}^3)=0.2280*10^{-6}\,\mathrm{m}^4,$$

$$\theta_{\mathrm{Isec.}}=1.812,$$

$$\beta_1=-0.1257\sinh 1.812+0.119208\cosh 1.812+0.2278-0.119208,$$

$$\beta_1=0.109\ \text{radians}=6.25\ \text{degrees}.$$

The angle of twist for uniform torsion of an I-section of the bar is:

$$\beta_{1,\text{uniform}} = \frac{a\,M_T}{G\,J} = \frac{4.0}{77*10^6 \bullet .228*10^{-6}} = 0.228 \text{ radians} = 13.06 \text{ degrees}$$

The variation of the uniform, non-uniform angle of twist, M_{TP}, M_{Ts} and M_T on the axis of the bar are shown in Fig. 4. The rotation at vertex $y_1 = a$ due to non-uniform torsion is around 50 percent of the rotation for uniform torsion of an I-section. Both M_{TP} and M_{Ts} contribute to M_T through the span of the beam and the torsional stresses are due to St Venant shear stresses and the restraint of warping. The applied twisting moment is resisted entirely by the secondary twisting moment at support $(y_1 = 0)$ and entirely by the primary twisting moment at $y_1 = a$. According to the studies on [18, 27], our results for the variation of the uniform, non-uniform angle of twist, M_{TP}, M_{Ts} and M_ω on the axis are compared for further verifications and the results are some. The distribution of the total moment between uniform and non-uniform torsion at intermediate points is shown in Fig. 4.

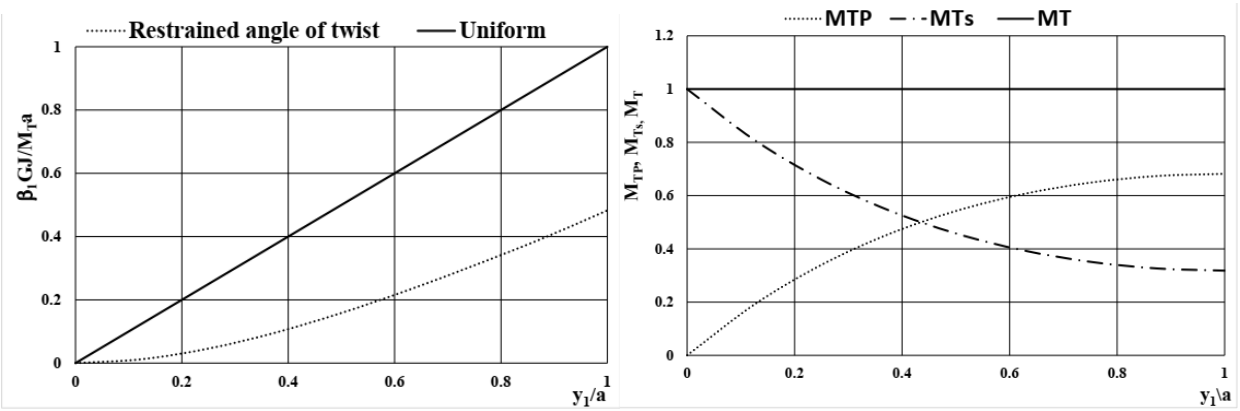


Figure 4. The normalised graphs of β_1, M_{TP}, M_{TS} and M_T of restrained I-beam section.

Furthermore, the values of β_1 of equation 2.5 and its derivatives are plotted in Fig. 5 to show their comparisons and behaviours along the length of the member. The behaviour of the flanges can be observed in the graph for β_1 and its first derivatives (β_1'). They show the variation in twist to which St. Venant shear strains and stresses are proportional to the primary torsional moments. The curvature of the flanges is also associated with the graph β_1'' and it is proportional to the warping moment in one flange. A combined graph for β_1' and β_1''' is shown in the Fig. 5(b) so β_1' is representing for the primary twisting moment and β_1''' belongs to the secondary twisting moments. The graph of β_1''' belongs to the characteristics of the rate of change of curvature and it is proportional to the warping shear force in the flange in addition to the warping torsional moment. Based on the Fig. 5(b) β_1' contributes 68 % and β_1''' contributes 32 % of the total torsional moment.

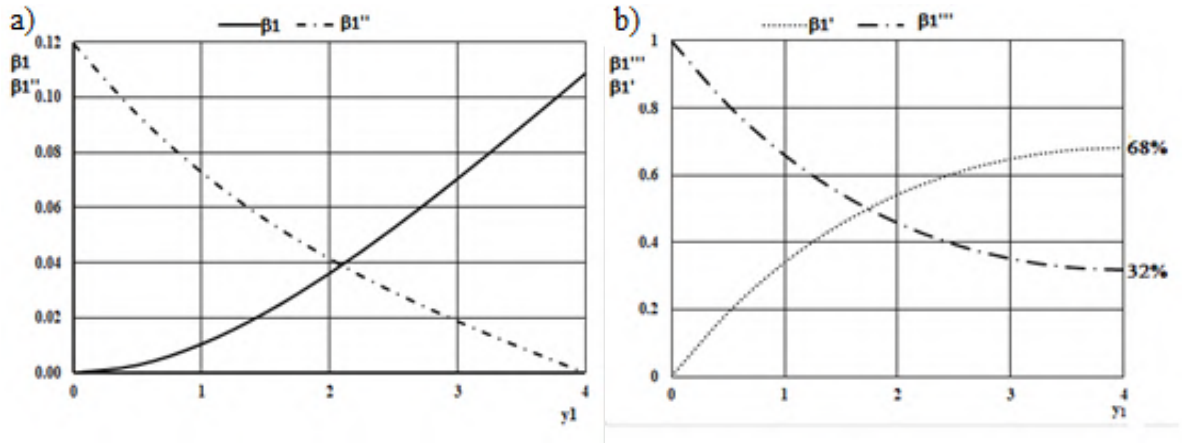


Figure 5. Decomposition of total twisting moment for an I-beam.

For an I-section, the longitudinal stress σ_{11} at $y_1 = 0$ due to non-uniform torsion and the warping function are computed as below:

$$\omega = \pm\frac{1}{4} f\, h = \pm 18.0 * 10^{-3}\ \mathrm{m}^2,$$

$$\sigma_{11} = -\omega\frac{M_T}{C_\omega}\tanh\theta\left(\frac{a}{\theta}\right) = \pm 0.0980 * 10^{6}\ \mathrm{kN/m^2}$$

The primary shear stress at the free end $(y_1 = a)$ is computed as given below and it varies linearly over the thickness of the walls of the section.

$$\text{flange:} \quad \tau_{max} = \pm\frac{M_T\, t_f}{J} = \pm 48.2\ \mathrm{N/mm^2},$$

$$\text{web:} \quad \tau_{max} = \pm\frac{M_T\, t_w}{J} = \pm 35.1\ \mathrm{N/mm^2}$$

The secondary shear stress at node $y_1 = 0$ is computed by determining the static moments of the warping function and it is constant over the thickness of the walls of the section. The contributions of the walls to the static moment of the warping function are computed based on the shear flow at the external vertices. The shear stress due to warping restraint is:

$$\sigma_{12s} = \frac{F_\omega}{t_f} = -\frac{20.83}{0.011} = -1893.6\ \mathrm{kN/m^2} = -1.9\ \mathrm{N/mm^2}$$

The distributions of the stress σ_{11}, warping function (ω) and secondary shear stresses σ_{11} over the section due to the non-uniform torsion are shown in Fig. 6.

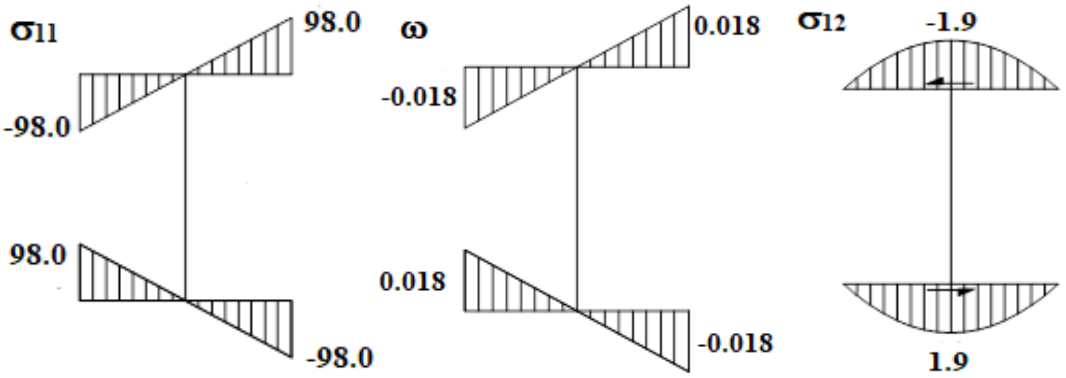


Figure 6. Distribution of σ11, ω and σ12p $(\mathrm{N/mm^2})$.

Case II: Similarly, for rectangular hollow cross-section, which is given in Table 5, the values for C_ω, J, θ and $\beta_1(a)$ are computed below:

$$C_\omega = \frac{2}{3}\omega_0^2(f\, t_f + h\, t_w) = 0.2875 * 10^{12}\ \mathrm{mm^6},$$

$$J = \frac{2 f^2 h^2 t_w t_f}{f\, t_w + h\, t_f} = 0.1562 * 10^{9}\ \mathrm{mm^4}$$

$$\theta_{Rec.sec.} = 57.85$$

$$\beta_1 = 5.749 * 10^{-6} \bullet (-\sinh 57.85 + \cosh 57.85 - 1.0) + 0.3326 * 10^{-3}$$

$$\beta_1 = 0.327 * 10^{-3}\ \text{radians} = 0.0187\ \text{degrees}$$

The angle of twist for uniform torsion of the rectangular section of the bar is:

$$\beta_{1,uniform} = \frac{a\, M_T}{G\, J} = \frac{4.0}{77 * 10^{6} \bullet 0.1562 * 10^{-3}} = 0.333 * 10^{-3}\ \text{radians}$$

The variation of the uniform and non-uniform angle of twist (restrained torsion) on the axis of rectangular hollow cross-section of the bar are shown in Fig. 7. For rectangular hollow cross-section as the value of θ is large and the angle of twist is very small in its magnitude. The angle of twist at points nearer to the support has significant magnitude as shown in the Fig. 7 and suddenly drops to a small value at the free end. The rotation at vertex $y_1 = a$ due to uniform and non-uniform torsion is almost the same and its magnitude is negligible comparing with an open section.

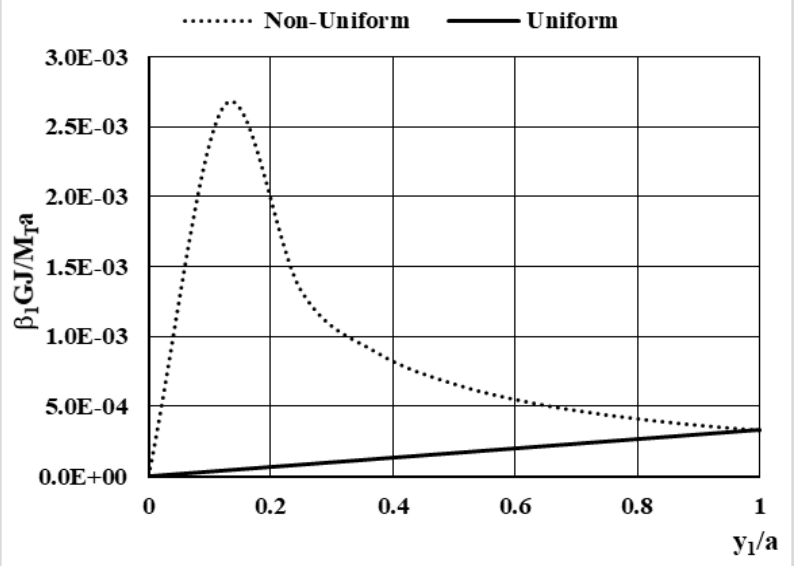


Figure 7. The normalised graphs of β_1 of restrained rectangular hollow cross-section.

The longitudinal stress σ_{11} at $y_1 = 0$ due to non-uniform torsion of rectangular hollow section is given below and the distribution of this stress over the section is shown in Fig. 8:

$$\omega_0 = \frac{1}{4} f\, h \frac{\mu - 1}{\mu + 1}$$

$$\text{with} \quad \mu := \frac{h}{t_w}\frac{t_f}{f} \quad \omega = \pm\omega_0 = \pm 9.124 * 10^{-3}\ \text{m}^2$$

$$\sigma_{11} = -\omega \frac{M_T}{C_\omega} \tanh\theta\left(\frac{a}{\theta}\right) = \mp 2.2\ \text{N/mm}^2$$

The primary shear stress is null at $y_1 = a$ and it is computed with expressions shown below. It is constant over the thickness of the walls of the section.

$$\text{flange}: \sigma_{12p} = \frac{M_T}{2 f\, h\, t_f} = \pm 0.63\ \text{N/mm}^2,$$

$$\text{web}: \sigma_{12p} = \frac{M_T}{2 f\, h\, t_w} = \pm 0.86\ \text{N/mm}^2$$

The secondary shear stresses (σ_{12}) at the support $(y_1 = 0)$ depend on the Static moments (S_ω) of the warping function. The increments of the static moment for the walls are given by the expression below:

$$\eta = \frac{180}{11} + \frac{400}{8} = 66.36$$

$$S_0 = -\frac{9.124*10^{-3}}{6 \bullet 66.36} \bullet (0.18^2 - 0.40^2) = -2.92*10^{-6}\ m^4$$

$$\text{wall AB}: S_{(1)} = S_0 - \frac{1}{4}\omega_0\, f\, t_f = -2.92*10^{-6} - 4.516*10^{-6} = -7.44*10^{-6} m^4$$

$$\text{wall BC}: S_{(2)} = S_0 + \frac{1}{4}\omega_0\, f\, t_w = -2.92*10^{-6} + 7.299*10^{-6} = 4.38*10^{-6} m^4$$

Based on the above solutions and static moment of the section, the variations of secondary shear stress over the section are shown in Fig. 8:

$$\sigma_{12s} = -\frac{M_T}{t}\frac{S_\omega}{C_\omega} = -\frac{1.0}{0.2875*10^{-6}}\frac{S_\omega}{t} = -3.4783*10^6 \frac{S_\omega}{t}\ kN/m^2$$

The distributions of the stress σ_{11}, warping function (ω) and secondary shear stresses σ_{12} over the section due to the non-uniform torsion are shown in Fig. 8.

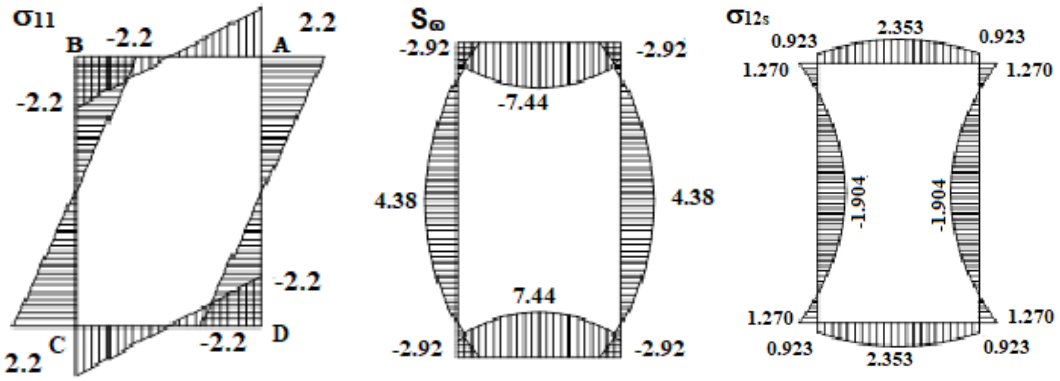


Figure 8. Stress (σ_{11}) (a), Static moments (S_ω), secondary shear stress (σ_{12s}) (N/mm^2).

Case III: Likewise, by considering the channel section of Table 5, the values for C_ω, J, θ and $\beta_1(a)$ are calculated as given below:

$$C_\omega = \frac{\left(f - \frac{t_w}{2}\right)^3 * h^2 * t_f}{12}\left[\frac{2ht_w + 3\left(f - \frac{t_w}{2}\right)t_f}{ht_w + 6\left(f - \frac{t_w}{2}\right)t_f}\right] = 0.580*10^{-6}\ m^6,$$

$$J = \frac{1}{3}(2f\, t_f^{\,3} + h\, t_w^{\,3}) = 0.218*10^{-6}\ m^4$$

$$\theta = 1.52$$

$$\beta_1 = -0.157 \sinh 1.52 + 0.142 \cosh 1.52 + 0.238 - 0.142$$

$$\beta_1 = 0.083 \text{radians} = 4.75 \text{ degrees}$$

The angle of twist for uniform torsion of the rectangular section bar is:

$$\beta_{1,\text{uniform}} = \frac{a M_T}{G J} = \frac{4.0}{77*10^6 \times 0.218*10^{-3}} = 0.24 \text{ radians} = 13.75 \text{ degrees}$$

The variation of the uniform and non-uniform angle of twist (restrained torsion) on the axis of the channel section of a bar is shown in Fig. 9. The rotation at vertex $y_1 = a$ due to non-uniform torsion is 40 percent of the rotation for uniform torsion of the channel section.

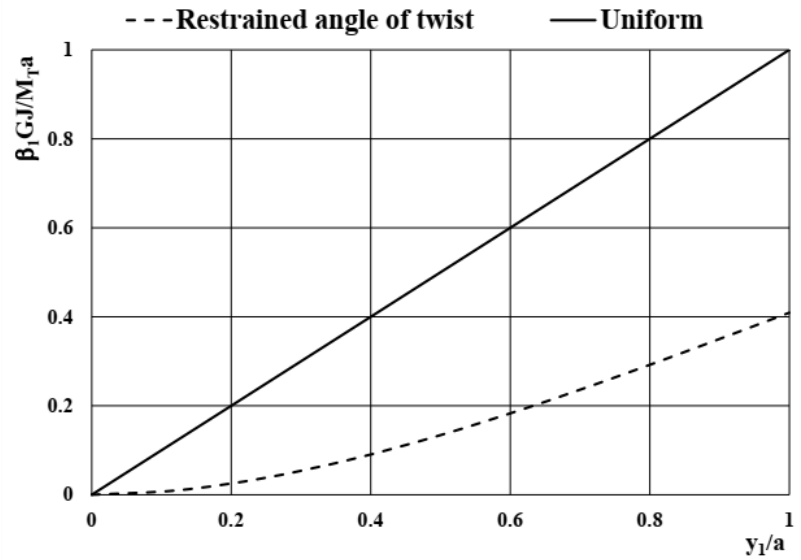


Figure 9. The normalised graphs of β_1 of restrained Chunnel section.

For channel section, the longitudinal stress (σ_{11}) at $y_1 = 0$ due to non-uniform torsion and the warping function are computed as below:

$$\omega_A = \frac{h}{2} * (f - t_w - e) = 21.4 * 10^{-3} m^2$$

$$\omega_B = -e * \frac{h - t_f}{2} = -13.8 * 10^{-3} m^2$$

$$\sigma_{11A} = \omega_A \frac{M_T}{C_\omega} \tanh\theta \left(\frac{a}{\theta}\right) = 124.6 \ N/mm^2$$

$$\sigma_{11B} = -\omega_B \frac{M_T}{C_\omega} \tanh\theta \left(\frac{a}{\theta}\right) = -80.3 \ N/mm^2$$

The values and distribution of the warping function at the external vertices and longitudinal stress are given in Fig. 8: Correspondingly the primary shear stress in the flange and web plates at support is zero and at node $y_1 = a$ is computed as follow. It varies linearly over the thickness of the walls of the section.

$$\text{flange}: \quad \tau_{max} = \pm \frac{M_T \, t_f}{J} = \pm \frac{0.011}{0.218 * 10^{-6}} \ kN/m^2 \ \hat{=} \ \pm 50.0 \ N/mm^2$$

$$\text{web}: \quad \tau_{max} = \pm \frac{M_T \, t_w}{J} = \pm \frac{0.008}{0.218 * 10^{-6}} \ kN/m^2 \ \hat{=} \ \pm 36.4 \ N/mm^2$$

The secondary shear stress is null at section and at node $y_1 = 0$ is computed by determining the static moments of the warping function.

$$S_0 = 0.5 t_f (f - 0.5 t_w) h * (0.5f - 0.25 t_w - e) = 7.36 * 10^{-6} \ m^4$$

$$\text{wall AB}: S_{(2)} = \frac{1}{4} h \, t_f [(f - 0.5 t_w) - e]^2 = 12.6 * 10^{-6} m^4$$

$$\text{wall BC}: S_{(1)} = S_0 - \frac{1}{8} t_w \, eh^2 = -3.68 * 10^{-6} m^4$$

$$\sigma_{12s0} = -\frac{M_T}{t_f}\frac{S_\omega}{C_\omega} = -1.01 N/m^2$$

$$\sigma_{12s1} = -\frac{M_T}{t_w}\frac{S_\omega}{C_\omega} = 0.07 N/m^2$$

$$\sigma_{12s2} = -\frac{M_T}{t_f}\frac{S_\omega}{C_\omega} = -1.15 N/m^2$$

The distributions of the stress σ_{11}, Static moments (S_ω) and secondary shear stresses σ_{11} over the section due to the non-uniform torsion are shown in Fig. 10.

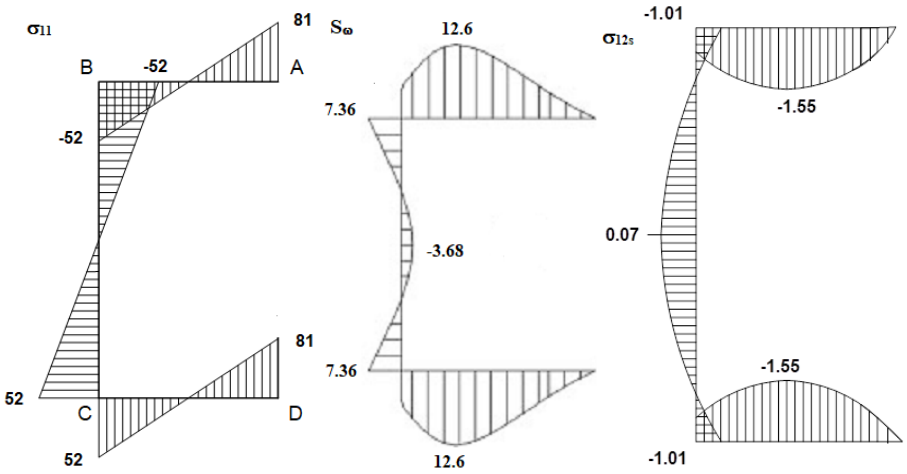


Figure 10. Stress (σ_{11}) , Static moments (S_ω), secondary shear stress (σ_{12s}) (N\mm^2).

A combined graph for angle of twist for closed and open sections is shown in Fig. 11 for both uniform and restrained torsion. The rotation at vertex $y_1 = a$ due to non-uniform torsion are 50 percent of the rotation for uniform torsion of I section and 40 percent of the rotation for uniform torsion of Chunnel section. For closed channels like rectangular hollow cross-section, the rotations in uniform and non-uniform torsions are considered negligible as their magnitudes are very small compared to the open cross sections as shown in Fig. 11.

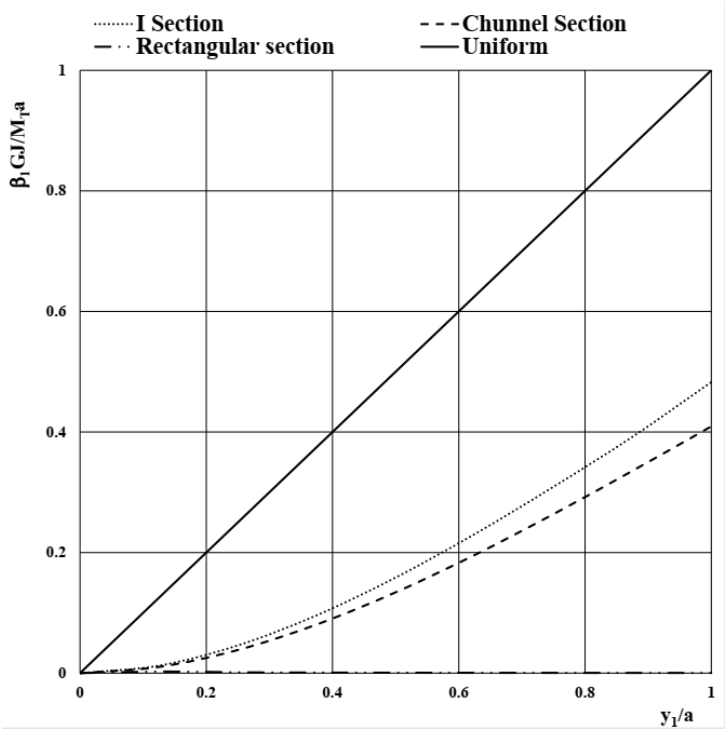


Figure 11. The combined normalised graphs of β_1 for all restrained section types.

In this study, the characteristic number for torsion is the main criteria to study the behaviour of a bar with restrained torsion and the variation of the uniform, non-uniform angle of twist, M_{TP}, M_{Ts} and M_{ω} on the axis of the bar are expressed as a function of the characteristic number for torsion and all results are compared with different studies [14, 15, 27]. From Fig. 11, the normalization graph clearly presents the combined graph for angle of twist for closed and open sections for both uniform and restrained torsion. For closed channels like rectangular hollow cross-section, the rotations are very small and are considered negligible but comparing to different studies [29, 43] it shows that the effect of warping must be considered in the case of non-uniform torsion of closed-section beams.

4. Conclusion

In this study, the characteristic number for torsion was adopted to study the behaviour of a bar with restrained torsion. The resulting responses from all cases using different value for the characteristic number for torsion were analyzed and compared. According to the previous findings, it is concluded that:

1. When considering fixed support conditions Vlasov torsion must be accounted as the behaviour for St. Venant and Vlasov torsion existing for all section types.

2. In this study, we used the hyperbolic than polynomial shape functions as it gave the exact results as the analytical solution.

3. With the increasing of θ value, M_{TP} reduces fast and the torsional moment is dominated by St. Venant in a major part of the beam but for θ = 1 both torsion mechanisms contribute to M_T. The distribution of $M\omega$ varies with the different values of θ and $\theta^* a$ consequently the normal warping stress differs along the beam based on the position of restrained torsion and section type.

4. The angle of twist of non-uniform torsion differs from uniform torsion by 50, 1.8, and 41 percents for the I-section, rectangular tube, and channel section, respectively.

5. Normal stresses dominate the stress within the bar as the cross-section is restrained and Vlasov shear stresses are very small and vanished when the normal stress reached maximum. Contradictory to this, at the free end the shear stress is dominated by St. Venant shear stresses and its maximum value is located at the mid of the flange.

6. The primary shear stress is considerably lower for the closed than open sections. The secondary shear stress is depending on the static moments of the warping function.

7. For closed channels like rectangular hollow cross-section, the rotation and warping are very small and are considered negligible but comparing to different studies it shows that the effect of warping must be considered in the case of non-uniform torsion of closed-section beams.

References

1. Pavlenko, A.D., Rybakov, V.A., Pikht, A.V., Mikhailov, E.S. Non-uniform torsion of thin-walled open-section multi-span beams. Magazine of Civil Engineering. 2016. 67 (7). Pp. 55–69. DOI: 10.5862/MCE.67.6
2. Vlasov, V.Z. Thin-walled Elastic Beams. Springfield, Va.: National Technical Information Service. Virginia,1984. 493 p.
3. Petrolo, A.S., Casciaro, R. 3D beam element based on Saint Venànt's rod theory. Computers and Structures. 2004. 82 (29–30). Pp. 2471–2481. DOI: 10.1016/j.compstruc.2004.07.004
4. Gebre, T.H., Galishnikova, V.V. The impact of section properties on thin-walled beam sections with restrained torsion. Journal of Physics: Conference Series. 2020. 1687 (1). DOI: 10.1088/1742-6596/1687/1/012020
5. Selyantsev, I.M., Tusnin, A. Cold-formed steel joints with partial warping restraint. Magazine of Civil Engineering. 2021. 101(1). 10101. DOI: 10.34910/MCE.101.1
6. El Fatmi, R. Non-uniform warping including the effects of torsion and shear forces. Part I: A general beam theory. International Journal of Solids and Structures. 2007. 44 (18–19). Pp. 5912–5929. DOI: 10.1016/j.ijsolstr.2007.02.006
7. Tsipiras, V.J., Sapountzakis, E.J. Bars under nonuniform torsion – Application to steel bars, assessment of EC3 guidelines. Engineering Structures. 2014. 60. Pp. 133–147. DOI: 10.1016/j.engstruct.2013.12.027.
8. Saadé, K., Espion, B., Warzée, G. Non-uniform torsional behaviour and stability of thin-walled elastic beams with arbitrary cross-sections. Thin-Walled Structures. 2004. 42 (6). Pp. 857–881. DOI: 10.1016/j.tws.2003.12.003
9. Tsipiras, V.J., Sapountzakis, E.J. Secondary torsional moment deformation effect in inelastic nonuniform torsion of bars of doubly symmetric cross-section by BEM. International Journal of Non-Linear Mechanics. 2012. 47 (4). Pp. 68–84. DOI: 10.1016/j.ijnonlinmec.2012.03.007. URL: http://dx.doi.org/10.1016/j.ijnonlinmec.2012.03.007
10. Lopez, F.L. A 3D Finite Beam Element for the Modelling of Composite Wind Turbine Wings. 2013.126 p.
11. Qi, H., Wang, Z., Zhang, Z. An Efficient Finite Element for Restrained Torsion of Thin-Walled Beams Including the Effect of Warping and Shear Deformation. IOP Conference Series: Earth and Environmental Science. 2019. 233 (3). DOI: 10.1088/1755-1315/233/3/032029
12. Murín, J., Aminbaghai, M., Kutiš, V., Královič, V., Sedlár, T., Goga, V., Mang, H. A new 3D Timoshenko finite beam element including non-uniform torsion of open and closed cross-sections. Engineering Structures. 2014. 59. Pp. 153–160. DOI: 10.1016/j.engstruct.2013.10.036

13. Sapountzakis, E.J. Bars under Torsional Loading: A Generalized Beam Theory Approach. ISRN Civil Engineering. 2013. 2013. Pp. 1–39. DOI: 10.1155/2013/916581
14. Pavazza, R., Matoković, A., Vukasović, M. A theory of torsion of thin-walled beams of arbitrary open sections with the influence of shear. Mechanics Based Design of Structures and Machines. 2020. 0 (0). Pp. 1–36. DOI: 10.1080/15397734.2020.1714449.
15. Kuttke, P., Kurfürst, A., Scheiner, S., Hellmich, C. Sequential 1D/2D Finite Element analyses of tramway rails under bending and restrained torsion, based on the principle of virtual power. Mechanics of Advanced Materials and Structures. 2019. 6494. DOI: 10.1080/15376494.2019.1647317
16. Mohareb, M., Nowzartash, F. Exact finite element for nonuniform torsion of open sections. Journal of Structural Engineering. 2003. 129 (2). Pp. 215–223. DOI: 10.1061/(ASCE)0733-9445(2003)129:2(215)
17. Sapountzakis, E.J., Tsipiras, V.J., Gkesos, P.G. Warping transmission in 3-D beam element including secondary torsional moment deformation effect. ECCOMAS Special Interest Conference – SEECCM 2013: 3rd South-East European Conference on Computational Mechanics, Proceedings – An IACM Special Interest Conference. 2013. Pp. 470–480.
18. Liping Wang1 and Ben Young, M.A. Restrained Torsion of Thin-Walled Beams. ASCE Journal of Structural Engineering. 2007. 1. Pp. 1–18. DOI: 10.1061/(ASCE)ST.1943-541X
19. Zojaji, A.R., Kabir, M.Z. Analytical approach for predicting full torsional behaviour of reinforced concrete beams strengthened with FRP materials. Scientia Iranica. 2012. 19 (1). Pp. 51–63. DOI: 10.1016/j.scient.2011.12.004.
20. Askandar, N.H., Mahmood, A.D., Kurda, R. Behaviour of RC beams strengthened with FRP strips under the combined action of torsion and bending. European Journal of Environmental and Civil Engineering. 2020. Pp. 1–17. DOI: 10.1080/19648189.2020.1847690.
21. Ganganagoudar, A., Mondal, T.G., Suriya Prakash, S. Analytical and finite element studies on behaviour of FRP strengthened RC beams under torsion. Composite Structures. 2016. 153. Pp. 876–885. DOI: 10.1016/j.compstruct.2016.07.014.
22. Alabdulhady, M.Y., Sneed, L.H., Carloni, C. Torsional behaviour of RC beams strengthened with PBO-FRCM composite – An experimental study. Engineering Structures. 2017. 136. Pp. 393–405. DOI: 10.1016/j.engstruct.2017.01.044.
23. Ubaydulloyev, M.N. Calculations of strengthened open profile thin-walled element enclosing structures. Magazine of Civil Engineering. 2014. 52 (8). DOI: 10.5862/MCE.52.6
24. Al-Rousan, R., Abo-Msamh, I. Impact of anchored CFRP on the torsional and bending behaviour of RC beams. Magazine of Civil Engineering. 2020. 96 (4). Pp. 79–93. DOI: 10.18720/MCE.96.7
25. Al-Rousan, R., Abo-Msamh, I. Bending and torsion behaviour of CFRP strengthened RC beams. Magazine of Civil Engineering. 2019. 92(8). Pp. 48–62. DOI: 10.18720/MCE.92.4
26. Banić, D., Turkalj, G., Brnić, J. Finite element stress analysis of elastic beams under non-uniform torsion. Transactions of Famena. 2016. 40 (2). Pp. 71–82. DOI: 10.21278/TOF.40206
27. Gunnlaugsson, G.A., Pedersen, P.T. A finite element formulation for beams with thin-walled cross-sections. Computers and Structures. 1982. 15 (6). Pp. 691–699. DOI: 10.1016/S0045-7949(82)80011-4.
28. Chen, S., Ye, Y., Guo, Q., Cheng, S., Diao, B. Nonlinear model to predict the torsional response of U-shaped thin-walled RC members. Structural Engineering and Mechanics. 2016. 60 (6). Pp. 1039–1061. DOI: 10.12989/sem.2016.60.6.1039
29. Murín, J., Kutiš, V., Královič, V., Sedlár, T. 3D beam finite element including nonuniform torsion. Procedia Engineering. 2012. 48. Pp. 436–444. DOI: 10.1016/j.proeng.2012.09.537
30. Aminbaghai, M., Murin, J., Kutiš, V., Hrabovsky, J., Kostolani, M., Mang, H.A. Torsional warping elastostatic analysis of FGM beams with longitudinally varying material properties. Engineering Structures. 2019. 200 (April). Pp. 109694. DOI: 10.1016/j.engstruct.2019.109694.
31. Murin, J., Aminbaghai, M., Hrabovsky, J., Mang, H. Second-order torsional warping modal analysis of thin-walled beams. COMPDYN 2017 – Proceedings of the 6th International Conference on Computational Methods in Structural Dynamics and Earthquake Engineering. 2017. 1. Pp. 1–19. DOI: 10.7712/120117.5406.16926
32. Emre Erkmen, R., Mohareb, M. Torsion analysis of thin-walled beams including shear deformation effects. Thin-Walled Structures. 2006. 44 (10). Pp. 1096–1108. DOI: 10.1016/j.tws.2006.10.012
33. El Fatmi, R. Non-uniform warping including the effects of torsion and shear forces. Part II: Analytical and numerical applications. International Journal of Solids and Structures. 2007. 44 (18–19). Pp. 5930–5952. DOI: 10.1016/j.ijsolstr.2007.02.005.
34. Pavazza, R., Matoković, A. Bending of thin-walled beams of the open section with the influence of shear, part I: Theory. Thin-Walled Structures. 2017. 116. Pp. 357–368. DOI: 10.1016/j.tws.2016.08.027
35. Ritchie, S.J.K., Leevers, P.S. Non-uniform and dynamic torsion of elastic beams. Part 1: Governing equations and particular solutions. Journal of Strain Analysis for Engineering Design. 1999. 34 (5). Pp. 303–311. DOI: 10.1243/03093249991513641
36. Wang, Z.Q., Zhao, J.C., Gong, J.H. A new torsion element of thin-walled beams including shear deformation. Applied Mechanics and Materials. 2011. 94–96. Pp. 1642–1645. DOI: 10.4028/www.scientific.net/AMM.94-96.1642
37. Wang, Z.Q., Zhao, J.C., Zhang, D.X., Gong, J.H. Restrained torsion of open thin-walled beams including shear deformation effects. Journal of Zhejiang University: Science A. 2012. 13 (4). Pp. 260–273. DOI: 10.1631/jzus.A1100149
38. Prokić, A., Mandić, R., Vojnić-Purčar, M., Folić, R. Torsional buckling of thin-walled beams in presence of bi-moment induced by axial loads. Computers & Smctures.1993. Vol. 47. No. 6. pp. 1065–1070.
39. Murin, J., Sedlar, T., Kralovic, V., Goga, V., Kalas, A., Aminbaghai, M. Numerical analysis and measurement of non-uniform torsion. Civil-Comp Proceedings. 2012. 99. Pp. 1–18. DOI: 10.4203/ccp.99.11
40. Floros, M.W., Smith, E.C. Finite element modelling of open-section composite beams with warping restraint effects. AIAA Journal. 1997. 35 (8). Pp. 1341–1347. DOI: 10.2514/2.242
41. Lalin, V.V., Rybakov, V.A., Ivanov, S.S., Azarov, A.A. Mixed finite-element method in V.I. Slivker's semi-shear thin-walled bar theory. Magazine of Civil Engineering. 2019. 89 (5). Pp. 79–93. DOI: 10.18720/MCE.89.7
42. Sapountzakis, E.J. Solution of non-uniform torsion of bars by an integral equation method. Computers and Structures. 2000. 77 (6). Pp. 659–667. DOI: 10.1016/S0045-7949(00)00020-1
43. Rubin, H. Torsions-Querschnittswerte für rechteckige Hohlprofile nach en 10210-2:2006 und en 10219-2:2006. Stahlbau. 2007. 76 (1). Pp. 21–33. DOI: 10.1002/stab.200710004

Contacts:

Vera Galishnikova, GalishnikovaVV@mgsu.ru

Tesfaldet Hadgembes Gebre, tesfaldethg@gmail.com

Received 27.09.2020. Approved after reviewing 08.04.2021. Accepted 04.06.2021.



Magazine of Civil Engineering

ISSN 2712-8172

journal homepage: http://engstroy.spbstu.ru/

DOI: 10.34910/MCE.110.10

Belite-containing clinkers from phosphoric slags for refractory materials

A. Shaikezhan ***, A.D. Anuarova**** 

Karaganda State Technical University, Karaganda, Republic of Kazakhstan

**E-mail: anuarova_ayaulym@mail.ru*

Keywords: phosphoric slag, carbide lime, belite clinker, refractory material

Abstract. The article studies the possibility of using phosphoric slag (PS) to obtain stabilized belite clinkers. It is shown that granulated PS as a silica-containing component of a cement raw mixture meets the demand of wide and effective use of production wastes. The complexity of using raw materials is increased with the use of carbide residue in the mixture that is a by-product of the synthetic rubber plant. The experimental data were obtained by chemical, optical, X-ray and thermal analysis methods. Chemical and mineralogical composition and materials properties have been studied before and after heat-treating. The optimal composition of belite clinkers has been selected. The physical and technical parameters of clinkers have been determined. A method for producing refractory products from belite-containing materials has been developed. Mathematical models to determine technological parameters for the refractory products manufacturing based on belite-containing clinkers have been composed.

1. Introduction

The research direction of the granulated phosphoric slags (PS) use as a basis for binding composites is considered in [1–2], where it is also emphasized that the entertainment volume of these slags for obtaining construction products does not exceed 30 % of those generated in production. It must be assumed that not all types of granulated PS can be used as active agents to cements, and for such slags any other areas of disposal should be found. The use of granulated PS as a silica-containing component, which completely replaces a clay one in the traditional Portland cement raw mixture, is proposed by different authors (A.N. Toropov, M.A. Bredig and etc.). It meets the requirements of a widespread use of production waste and by-products, complex production of cement with other industrial products. It is known that PS contain phosphoric anhydride and calcium fluoride's impurities. The first is a stabilizer of β-C_2S, and the second is an effective silication mineralizer. High-temperature phase equilibria in the 2CaO, SiO_2 – 3CaO, P_2O_5 system were studied in [3]. Taking into account the above circumstances and the great practical importance of refractory materials, it is of interest to obtain cement of belite composition.

Calcium orthosilicate – $2CaO{\cdot}SiO_2$ and its polymorphic forms have been studied by many scientists (Y.M. Butt, V.V. Timashev, H. Midgley, R. Nares, A.N. Toropov, M.A. Bredig and etc.). Belite synthesized in vitro is based on phosphogypsum [4–11]. Utilization of other wastes to obtain cements of belite composition [12–15] does not include phosphoric slags. The high melting point of C_2S has been known for a long time and, according to the latest data, it is 2130 °C [16]. The possibility of using a belite clinker as a refractory material was proved in [17]. The invention has not found any practical application. It does not contain any data on the optimal technological parameters of production. The results of systematic studies of orthosilicates as refractory materials show a high burning temperature of products and complexity of clinker charge. It seemed to us that these disadvantages could be eliminated, if we use the phosphoric slags as a silica-containing component in the C_2S synthesis. The PS advantages over other silica-containing materials are obvious: slags begin to come into the liquid phase at relatively low temperatures; they contain phosphorus, manganese and fluorine impurities, which stabilize high temperature modifications of C_2S and accelerate silicate formation processes.

Shaikezhan, A., Anuarova, A.D. Belite-containing clinkers from phosphoric slags for refractory materials. Magazine of Civil Engineering. 2022. 110(2). Article No. 11010. DOI: 10.34910/MCE.110.10

© Shaikezhan, A., Anuarova, A.D., 2022. Published by Peter the Great St. Petersburg Polytechnic University.

 This work is licensed under a CC BY-NC 4.0

This is also confirmed by the studies from [18] in relation to the effects of the P_2O_5 and CaF_2 concentration on clinker with a high alite content.

The aim of the work is to find out the possibility of obtaining a stabilized belite refractory by replacing phosphoric slags known natural silica-containing materials in a cement raw mixture. For this it was necessary:

- to study the characteristics of phosphoric slag as a clay-replacing component of a cement raw mixture;
- to study new raw material mixtures for obtaining stabilized belite clinker;
- to determine the technological parameters for the manufacture of belite refractory.

2. Methods

Mixtures for producing belite-containing clinkers are composed of phosphoric slags and carbonates. In this research, we have used granulated phosphoric slags from the "Kazphosphat" LLP, which operates on the basis of phosphate raw materials from Karatau (the Republic of Kazakhstan). Limestone and carbide air-slaked lime were used as a lime component. The chemical composition of raw materials is shown in the Table 1.

Table 1. Chemical composition of raw materials, mass. %.

Material	SiO_2	CaO	Al_2O_3	Fe_2O_3	MgO	SO_3	P_2O_5	CaF_2	MnO	Loss of ignition	Amount
lime	3.51	53.30	1.09	0.62	0.13	–	–	–	–	42.10	100.75
carbide lime	2.74	62.03	1.94	0.40	0.19	0.23	–	–	–	31.59	99.12
phosphoric slag (I)	38.46	42.15	3.50	1.54	3.97	0.31	1.91	5.33	–	2.33	99.74
phosphoric slag (II)	40.20	42.16	2.27	1.91	4.56	0.03	2.02	5.03	0.28	1.02	99.48

The main slag components are calcium and silicon oxides. Its acidity index is 1.00. Under the microscope, the slag particles have a plane-limited fragmental shape with sharp corners and winding edges. The grain configuration is mostly wrong. The slag structure is X-ray amorphous. The IR spectrum is characterized by broad absorption bands in the range of 400–1500 cm^{-1}; two of them are intense with maxima at 500 and 1000 cm^{-1}, three of them are weak in the form of shoulders at 715, 1220, and 1430 cm^{-1} (Fig. 1, a). According to spectroscopic data, slag is a mixture of silicates of various structures, including both ortho (a rather wide frequency interval in the range of 850-1000 and 500 cm^{-1}) and more condensed forms (absorption with maxima at 715 and 1220 cm^{-1}) according N.I. Plyusnina**.** Absorption at 860 and 1430 cm^{-1} in the form of shoulders is due to vibrations of carbonate ion and indicates the presence of calcite impurity in the slag composition. After dissolution of the glass phase with 2 % citric acid in the fixed residue, there identified crystalline phases in the form of wollastonite (d = 4.04; 2.98; 2.70 and 2.54 Å) and quartz (d = 4.23; 3.34; 2.46 Å) (Fig. 2, a) using X-Ray. As for the IR spectrum of this precipitate (Fig. 2, b), in contrast to the slag spectrum, there appear bands in the form of shoulders at 565.600 cm^{-1} and a band of medium intensity at 805 cm^{-1}. The first ones are due to symmetric stretching vibrations γ_S Si – O – Si, the second indicates the presence of precipitated quartz according A.N. Lazarev.

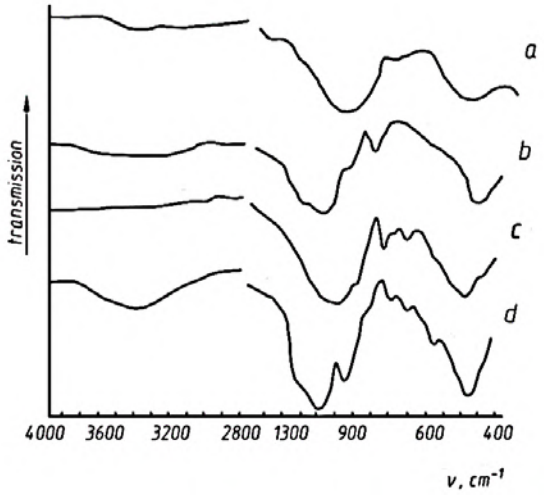


Figure 1. IR spectra of phosphoric slag: a – run-of-mine; b – after washing using citric acid; c – heat-treated at 850 °C – 0.5 h; d – heat-treated and washed with citric acid.

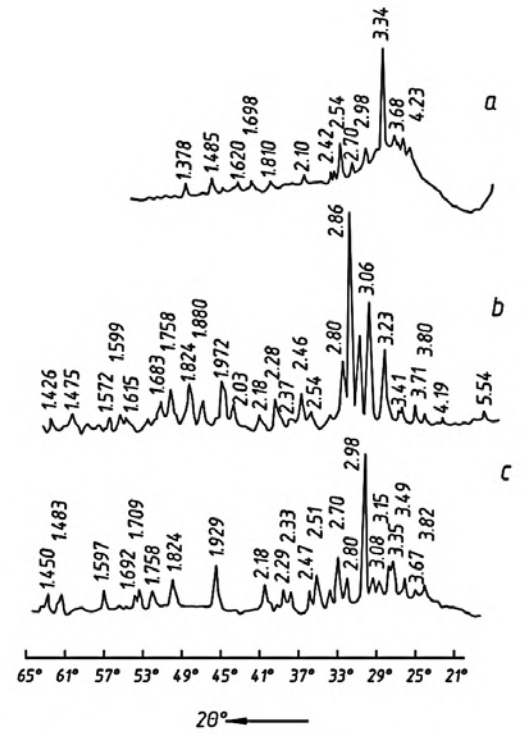


Figure 2. Slag X-ray photographs: a – washed with citric acid; b – heat-treated at 850 °C – 0.5 h; c – heat-treated and washed with citric acid.

Slag DTA curves (Fig. 3) are characterized with endoenergic effect at 680 °C which is due to pre-crystallization softening of the glass phase and the exothermic effect of crystallization of main phases at 850 °C. The crystallizing phases at this temperature are pseudo-wollastonite (d = 3.23; 2.80; 2.46; 1.972 and 1.824 Å), wollastonite (d = 2.96; 2.28 and 1.880 Å) and melilite (d = 3.06; 2.86; and 1.758 Å) (Fig. 2, b). The IR spectrum of the heat-treated slag (Fig. 1, c) is characterized by absorption bands in the range of 450 – 1200 cm^{-1}. In the range of 900 – 1100 cm^{-1}, there are stretching vibrations γ(Si – O) β- wollastonite. Its metasilicate chains [(SiO_3)] are characterized by absorption in the range of 560 – 680 cm^{-1}, caused by stretching vibrations of Si – O – Si (γS Si – O – Si) bridges. These vibrations include the bands at 560.650.680 cm^{-1}.

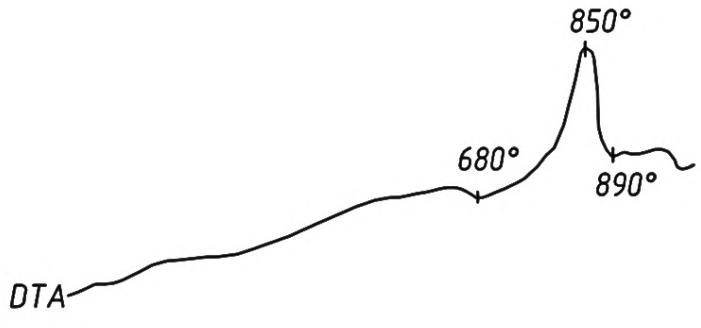


Figure 3. Slag DTA curves.

A characteristic feature of the α-wollastonite spectrum, which contains ring anions $[Si_3O_9]^{6-}$ in its structure, is a band at 725 cm^{-1}, which is due to the symmetric stretching vibration γS Si – O – Si. The absorption bands at 480 and 560 cm^{-1} refer to bending vibrations of the ring anion. The melilite identification using the IR spectrum is rather difficult, since the latter belongs to pyrosilicates containing aluminum as a cation capable to form a covalent links with oxygen. It leads to an increase in the vibration frequencies of Me – O, and makes it difficult to identify the γS Si – O – Si band, which is in the range 640 – 650 cm^{-1}. However, it can be assumed that the spectrum complexity in the region of 500 – 800 cm^{-1} does not exclude melilite presence in the heat-treated slag. But in the spectrum of heat-treated slag washed with citric acid (Fig. 1, d), the bands assigned to α-wollastonite disappear, and the absorption minimum at 1000 cm^{-1} observed in the spectrum of β-wollastonite is clearly revealed. X-ray data of this sediment (Fig. 1, c) also indicate the presence of hematite (d = 2.70; 2.51; and 1.824 Å) and fluorite (d = 3.15 and 1.929 Å). The phosphatic slag taken for these studies consists mainly of glass with a microheterogeneous structure. It contains pseudo-wollastonite, wollastonite, melilite, hematite and fluorine, which crystallizes as fluorite after

being heat-treated. Phosphorus is also a part of glass, since no independent phosphorus-containing phase was found. The slag crystalline phases are represented by wollastonite and quartz. Calcite is present as an impurity.

Limestone particles consist of irregular isometric tabular colorless grains. Well-formed rhombohedrons peculiar to calcite are rarely found. There can be twins too.

Carbide air-slaked lime is a waste product of the Karaganda Synthetic Rubber Plant. A real powder density is 2260 kg.m^3, specific surface is 677.0 m^2.kg. The powder is a mixture of hydroxide N_g = 1.560 ± 0.003; N_p = 1.550 ± 0.003. Calcite crystals have N_g = 1.658 ± 0.003 and N_p = 1.486 ± 0.003; intergrown pieces with a black or dark-brown opaque matter are often observed. The X-Ray shows reflexes at d = 4.85; 2.61; and 1.917 Å is related to portlandite, at d = 3.87; 3.01; and 2.28 Å – to calcite.

The chemical analysis of starting materials was carried out according to was carried out in accordance with the requirements of regulatory documents: Russian State Standard GOST 5382-91 (CIS interstate standard) 'Cements and materials for cement production. Chemical analysis methods'. Raw mixtures and phase composition of clinkers were calculated as described in the common method [19] according to a given value of the saturation coefficient (SC). Raw mixtures burning was carried out in a chamber electric resistance furnace CHO-3.2×6×2.5/15M1 with the U-shaped heaters made of molybdenum silicide with the CM 400/400 type operating in an oxidizing atmosphere. The accuracy of temperature maintenance in the working space is ± 0.5 % of the nominal temperature. Isothermal burning was carried out in a tubular furnace of the /SUOL-0.25.2.5/14k type. The amount of unreacted calcium oxide was determined by the alcohol-glycerate method according to Russian State Standard GOST 5382-91 (CIS interstate standard). The phase composition of clinkers was studied by X-ray, rational-chemical, microscopic, and spectroscopic analyzes.

Presence of wollastonite, cuspidin, fluorite, fluoro- and hydroxylapatites in the cakes was monitored by the X-ray phase analysis of precipitate after citric acid extraction. In this case, the solution passes through alite, belite, phosphates, silicophosphates and intermediate substances. The sintered materials in 2 % citric acid were processed according as per the method described in [20]. To establish the clinkers intermediate phases, we used the method according S.M. Royak and other authors, based on the complete solubility of di- and tricalcium silicates in a 5 % solution of boric acid.

In order to select the optimal compositions for determining physical and technical properties of refractory materials based on belite-containing materials, there were prepared raw materials with SC = 0.60 – 0.85 with an interval of 0.05. To determine refractory some samples were molded from the mixture in the form of cylinders with the following dimensions: ø 5 cm and h = 0.5 cm, for apparent density and porosity – ø 5 cm and h = 5 cm. The burning temperature of materials for determining refractory was 1350 °C with a dwell time of 2 hours, for apparent strength and porosity – 1350 – 1500 °C with an interval of 50 °C without dwell. Cooling was abrupt. Clinkers refractory was determined according to Russian State Standard GOST R 53788-2010 (CIS interstate standard) 'Refractories and refractory raw materials. Methods of refractoriness determination', density and porosity – according to Russian State Standard GOST 2409-2014 (CIS interstate standard) 'Refractories. Method for determination of bulk density, apparent and true porosity, water absorption'. The SC for optimal clinkers was 0.70 and 0.75. A belite clinker is burnt at 1350 – 1400 °C. The rate of temperature rise was 12 – 26 deg.h. Cooling was slow as the oven cools down. The resulting clinkers were crushed using jaw crushers and divided into fractions with the following sizes: coarse 1 – 3 mm, average 0.5 – 1 mm, average 0.5 – 1 mm, fine < 0.5 mm.

When selecting the optimal parameters of the refractories technology from belite-containing materials, the method of mathematical planning of a four-factor experiment at five levels was used. Accordingly, cylinders ø 5 cm and h = 5 cm were molded. The average rate of temperature rise during burning was 8 – 21 deg.h. Sample cooling was abrupt. For certain values of apparent porosity and density using generalized equations, the technological parameters for obtaining refractories were selected.

3. Results and Discussion

There were investigated mixtures of $CaCO_3$ ("h") and granulated PS with the contents (wt. %) 42.53 and 57.47, respectively. Limestone decarbonization at 1000 °C is completed in 15 minutes, and at 1100 and 1200 °C – in 5 minutes. At the last two temperatures, calcium oxide reacts completely in 15 and 10 minutes. The reaction rate is high at the beginning of heating. After 15 minutes it significantly slows down at 1000 °C.

The final product consists almost 90 % of C_2S, which is represented by the β-modification. At 1200 °C, starting from 5 min, the C_2S part is stabilized in the α′ – form. In the X-ray radiograph 4 d = 2.66; 2.22; 1.920 Å belongs to α′ – C_2S; d = 2.93; 1.60; 1.41 Å – C_5A_3. The rest are β – C_2S reflections.

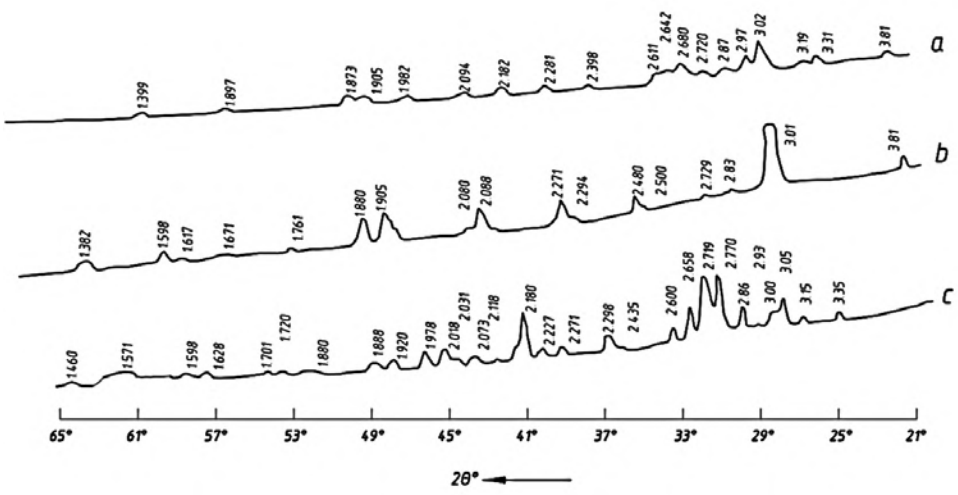


Figure 4. X-ray radiograph of spectra: a – 1000, 5 min; b – 1100, 1 min; c – 25 min.

The mixture was burnt at 1000 – 1200 °C in order to clarify the effect of burning duration on the crystallization of phases. Belite crystals grow from 2 – 4 (1000 °C, 30 min) and 10 min (1200 °C, 30 min) to 5 – 6 and 15 μm after 60 minutes. They form intergrown pieces. After burning at 1200 °C, polysynthetic twins are often found. There were observed rounded isotropic grains from the impurities with a relatively low index of refringence (obviously, $C_{11}A_7 \cdot CaF_2$). When treating the cake with 2 % citric acid, P_2O_5 completely goes into solution in the same way as $C_{11}A_7 \cdot CaF_2$ and C_4AF. Only half of the total amount of fluorite remains in the insoluble part with a trace impurity of periclase. Thus, a mixture of slags with $CaCO_3$ to obtain a belite clinker should be burnt at 1100 °C.

To study the features of high-temperature interaction of phosphoric slags with calcium oxide in carbide air-slaked lime. The mixture is composed of 38.40 % lime and 61.60 % granulated slag. The chemical and phase composition of clinker is shown in the Tables 2 and 3.

Table 2. Chemical composition of clinkers with SC = 0.67, % by weight.

Material	SiO_2	CaO	Al_2O_3	Fe_2O_3	MgO	Mn_2O_3	P_2O_5	CaF_2	SO_3	Amount
clinker	29.49	58.00	2.43	1.62	3.29	0.19	1.42	3.54	0.12	100

Table 3. Phase composition of clinkers.

$2CaO \cdot SiO_2$	$3CaO \cdot 2SiO_2 \cdot CaF_2$	$4CaO \cdot Al_2O_3 \cdot Fe_2O_3$	$12CaO \cdot 7Al_2O_3$	$3CaO \cdot P_2O_5$	MgO
68.9	16.6:	4.6	2.8	3.1	3.3

In order to select the optimal composition and establish the burning temperature of belite clinkers for obtaining refractory materials, 6 mixtures were made with SC from 0.60 to 0.85. The data on the mixtures composition are shown in the Tables 4 and 5.

The mixtures were burnt under isothermal conditions at 1100, 1200, and 1300 °C with a dwell time of 30 min. The silicate-forming reaction completion was controlled by the degree of absorption of calcium oxide (Table 6).

As shown in the Table 6, in samples with SC = 0.60 – 0.70 (clinker 1 – 3), a complete absorption of lime occurs at 1100 °C with a dwell time of 30 minutes. The completion of silicate-forming reaction was controlled by the degree of recovery of calcium oxide (Table 6).

As shown in the Table 6, in samples with SC = 0.60 – 0.70 (clinker 1 – 3) a complete absorption of lime occurs at 1100 °C. With increasing SC starting from 0.75, the calcium oxide is not completely absorbed as a result of tricalcium silicate formation from excess calcium oxide and dicalcium silicate.

As it can be seen from the data in Table 6, in samples with SE (saturation efficiency) = 0.67 – 0.70 (clinker 1 – 3), complete assimilation of lime occurs at 1100 °C. With an increase in SE, starting from 0.75, calcium oxide is insufficiently absorbed because of the formation of tricalcium silicate from excess calcium oxide and dicalcium silicate.

Table 6. Composition of free calcium oxide in burnt samples, weight %.

Temperature, C	Clinker					
	1	2	3	4	5	6
1100	no	no	0.86	4.35	9.36	12.29
1200			no	2.21	3.86	4.75
1300				2.17	2.41	3.13

On the DTA curve of the belite mixture, the effect (Fig. 5) at 515 °C is caused by the dehydration of $Ca(OH)_2$. Effects observed in the temperature range 805 – 898 °C, due to decarbonization of $CaCO_3$. The first stage of the process characterizes the kinetic stage of decomposition, the rate of which is determined by the energy of formation and crystallization of CaO [21]. The second and third stages (878 and 898 °C) are diffusion stages, the rate of which depends on the thickness of the CaO shell and neoplasms. The exothermic effect at 1042 °C corresponds to the formation of C_2S. With further heating of the mixture, liquid phases appear (endo-effects at 1120 and 1142 °C), which is confirmed by the appearance of exothermic effects at 1135 and 1042 °C during cooling.

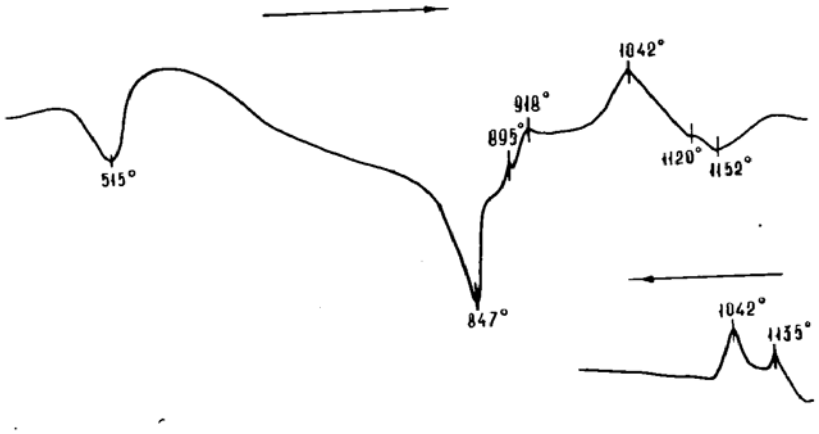


Figure 5. Thermogram of the belite mixture.

Consequently, in the mixture under study, the formation of a liquid phase occurs at a temperature that is much lower than the minimum temperature of the appearance of a clinker melt from a traditional raw mixture, which corresponds to 1280 °C [22–23]. The high reactivity of cement raw mixtures is due to the low softening temperature of phosphoric slags (1050 – 1100 °C) and CaF_2 impurities in them (3 – 6 %). CaF_2 catalyzes belite formation according to the mechanisms previously established by Gatt [24].

The burnt products phase composition was defined by X-ray. The main component of all samples is dicalcium silicate (Fig. 6). Presence of tricalcium silicate in the clinker 3 is confirmed by a reflex at 3.05 Å. With increasing the C_3S content in the samples, another line appears at 1.74 Å (clinker 5).

The X-ray picture analysis of borate extract residues (Fig. 7) shows that impurities are represented by magnesium oxide (d = 2.10; 1.480 Å), fluorite (d = 3.15; 1.937; 1.647 Å) and tetracalcium aluminoferrite (d = 7.23; 2.76; 2.64; 1.910 Å). In clinkers with the SC = 0.60 and 0.65 due to the lack of calcium oxide melilite (d = 2.86; 1.761 Å) and wollastonite (d = 2.97 Å) are found.

The calculated phase compositions of clinkers at 1300 °C are presented in the Table 7. The amount of dicalcium silicate at the maximum absorption of calcium oxide is 49 – 82 %. With increasing the SC, the dicalcium silicate content decreases due to the formation of tricalcium silicate, which number in the 5 clinker reaches 31 %. Silicates amount is about 80 %.

To determine the physical and technical parameters of clinkers 1 – 5, the tablets were molded and burnt at 1350 °C. In the clinkers 1 – 3, calcium oxide is completely absorbed, in the clinkers 4 and 5, the amount of unreacted calcium oxide is 0.40 and 0.82 %.

According to definitions of the “St. Petersburg Institute of Refractories” JSC, the clinkers 1 and 2 have a refractory below 1580 °C, the clinkers 3 – 5 – above 1770 °C. The Table 8 shows that with increasing clinkers’ SC, their burning shrinkage and apparent porosity decrease, but water absorption increases. The apparent porosity of the clinker 4 is 26 – 23 %, the clinker 5 is 40 – 35 %. Water absorption of the clinker 4 and 5, respectively, is 7-10 and 20 – 16 %. The clinkers apparent density at 1300 – 1350 °C is in the range of 200 – 250 $kg.m^3$.

Thus, it has been identified that the clinkers 1 and 2 have low refractory, and the clinker 5 has a relatively high apparent porosity and water absorption. Taking into account these data, clinkers with saturation coefficients 0.70 and 0.75 were selected to determine the possibility of obtaining a refractory material.

Table 4. Component and chemical composition of raw mixtures.

Mixture	Component composition, wt.%		100 % oxides composition									
	lime	slag	SiO_2	CaO	Al_2O_3	Fe_2O_3	MgO	CaF_2	P_2O_5	MnO	SO_3	LOI
1	38.84	61.16	24.94	46.39	2.57	1.18	2.48	3.27	1.17	0.15	0.19	17.66
2	42.23	56.77	23.39	46.86	2.46	1.14	2.31	3.03	1.09	0.14	0.18	19.40
3	47.12	52.88	22.03	47.27	2.36	1.11	2.17	2.82	1.02	0.13	0.16	20.93
4	50.58	49.42	20.82	47.64	2.28	1.07	2.03	2.64	0.95	0.12	0.15	22.30
5	53.68	46.32	19.73	47.94	2.21	1.05	1.91	2.47	0.89	0.11	0.14	23.52
6	56.47	43.53	18.75	48.27	2.14	1.02	1.81	2.32	0.84	0.10	0.13	24.62

Table 5. Excepted phase composition and clinkers characteristic.

Clinker	C_3S	C_2S	CS	C_4AF	$C_{12}A_7$	CaF_2	MgO	SC	n	p
1	-	73.53	9.13	4.37	4.26	3.97	3.02	0.60	6.65	2.17
2	-	82.89	0.38	4.31	4.16	3.76	2.87	0.65	6.49	2.15
3	15.58	68.13	-	4.25	4.07	3.57	2.74	0.70	6.35	2.14
4	30.21	54.03	-	4.21	3.98	3.40	2.62	0.75	6.20	2.12
5	43.75	40.97	-	4.16	3.90	3.23	2.50	0.80	6.06	2.16
6	56.30	28.86	-	4.11	3.82	3.08	2.40	0.85	5.94	2.10

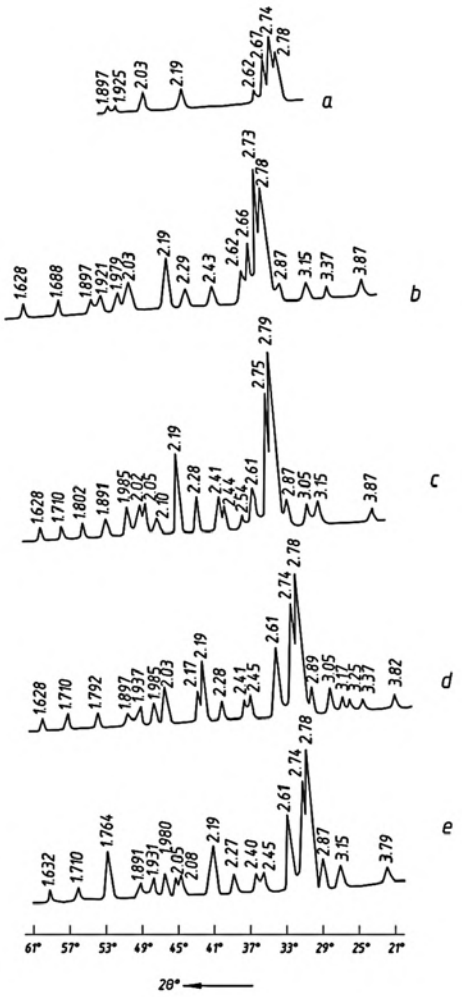


Figure 6. Clinkers X-ray photographs burnt at 1300 °C with a dwell time of 30 min a, b, c, d, e, respectively, clinkers 1, 2, 3, 4 and 5.

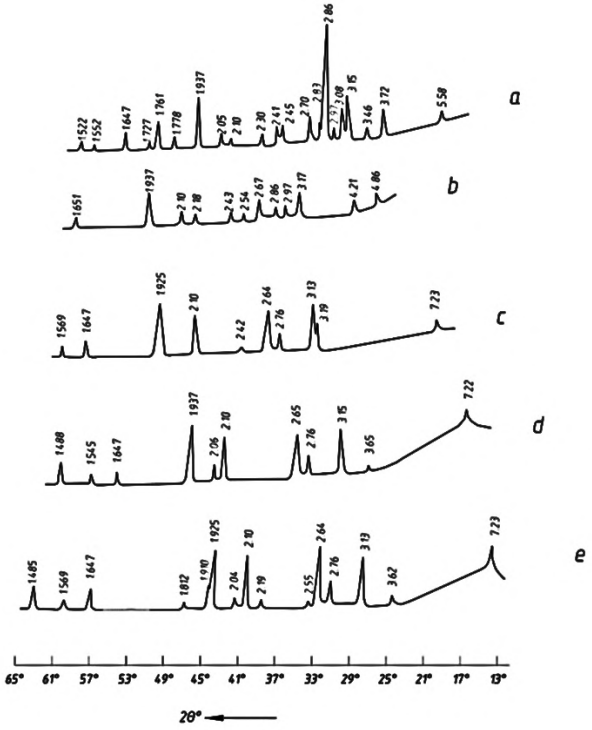


Figure 7. X-ray photographs of clinkers' borate extract residues a, b, c, d, e, respectively, clinkers 1, 2, 3, 4 and 5.

Table 7. Phase composition of clinkers.

Clinker	Phases content, wt.%							
	$CaO_{fr.}$	CS	C_2S	C_3S	C_4AF	$C_{12}A_7$	CaF_2	MgO
1	no	3.98	81.25	no	5.50	2.70	3.30	3.20
2	no	1.37	82.52	no	5.87	2.65	4.15	4.15
3	no	no	65.88	15.66	4.89	2.97	4.34	4.34
4	2.17	no	69.57	10.31	8.21	1.64	2.74	4.67
5	2.41	no	49.18	30.79	5.93	2.33	3.03	4.61

As our research shows, granulated phosphoric slag is an exceptional material that provides synthesis of a belite clinker (C2S ≈ 90 %) at 1100 °C in 15 minutes. Kinetics of the C_2S formation at 1000 and 1100 °C is satisfactorily described (Fig. 8) by the Tamman-Fishbeck equation. The apparent activation energy is 88 kJ.mol.

Table 8. Physical and technical indicators of clinkers.

Clinker	Clinker SC	Burning temperature, °C						
		1350				1400		
		volume burning shrinkage, %	apparent density, kg.m^3	apparent porosity, %	water absorption, %	volume burning shrinkage, %	apparent density, kg.m^3	apparent porosity, %
1	2	3	4	5	6	7	8	9
3	0.70	32.7	1480	2.49	5.93	35.2	1220	2.45
4	0.75	31.5	2370	2.44	9.66	35.1	1810	2.45
5	0.80	25.8	3710	2.04	18.02	20.3	3960	1.97

Continuation Table 8.

Burning temperature, °C								
1400		1450				1500		
water absorption, %	volume burning shrinkage, %	apparent density, kg.m^3	apparent porosity, %	water absorption, %	volume burning shrinkage, %	apparent density, kg.m^3	apparent porosity, %	water absorption, %
10	11	12	13	14	15	16	17	18
4.93	33.4	1940	2.56	7.53	34.9	1480	2.37	6.22
7.79	37.6	2620	2.42	10.71	38.2	2370	2.37	9.95
19.96	26.7	3680	2.16	16.86	30.7	3520	2.11	16.59

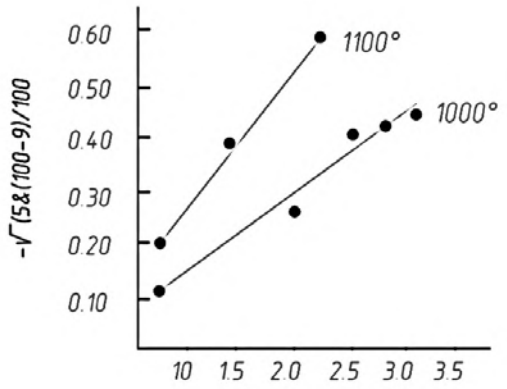


Figure 8. Kinetic data of the C_2S formation reaction.

The high reacting capacity of granulated phosphoric slags is explained by their low softening point (1050 – 1100 °C) and the presence of calcium fluoride which is evenly distributed up to 6 %. The latter has a strong catalytic effect on the C_2S formation.

Carbide lime, mainly consisting of $Ca(OH)_2$ and having a developed specific surface area reduces the burning temperature up to 950 – 1000 °C. In this case, the value of the apparent activation energy decreases up to 44 kJ.mol. A belite clinker is represented by a dicalcium silicate. Secondary phases: C_4AF, $C_{12}A_7$, MgO, and CaF_2. These phases are formed from the CS, melilite and cuspidin at the moment of their initiation or after crystallization according to the reactions:

$$CaO \cdot SiO_2 + CaO = 2CaO \cdot SiO_2 \quad (1)$$

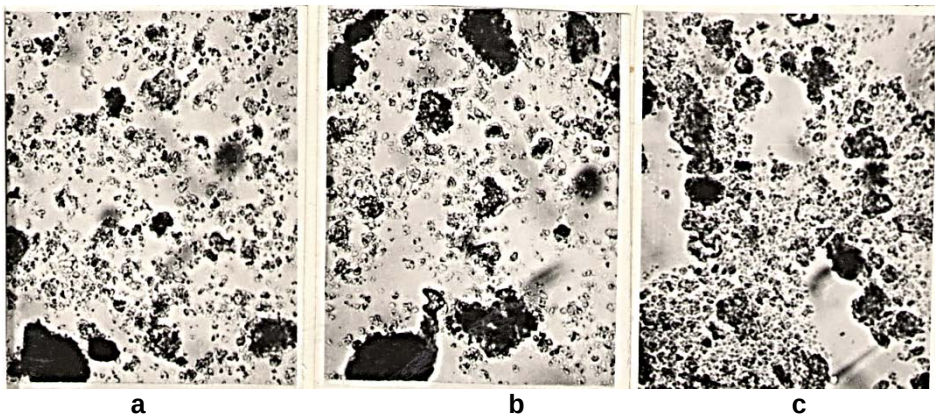
$$3CaO \cdot 2SiO_2 \cdot CaF_2 + CaO = 2(2CaO \cdot SiO_2) + CaF_2 \quad (2)$$

$$7(2CaO \cdot Al_2O_3\ SiO_2 + 12CaO = 7(2CaO \cdot SiO_2) + 12CaO\ 7Al_2O_3 \quad (3)$$

$$2CaO \cdot MgO\ 2SiO_2 + 2CaO = 2(2CaO \cdot SiO_2) + MgO \quad (4)$$

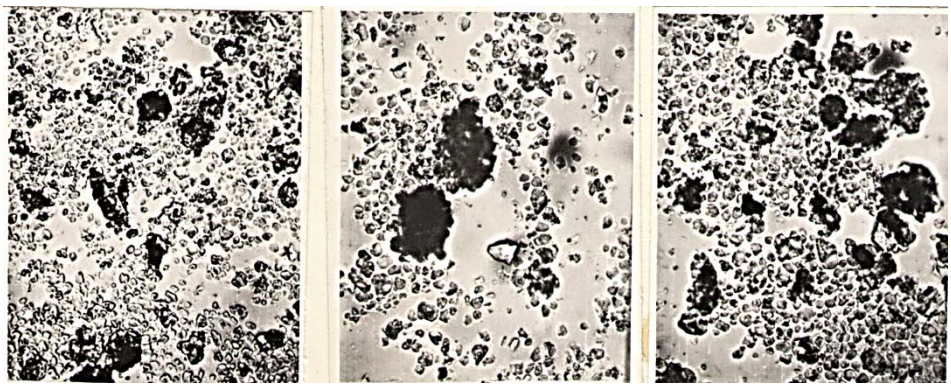
With a lack of CaO or incomplete burning processes, wollastonite, melilite and cuspidin are observed in the reaction mixture along with the reaction products. Fluorine does not evaporate. From a stoichiometric mixture with a single burning, the Nares solid solution characterized by the composition: CaO – 66.5 %, SiO_2.- 26.5 % b P_2O_5 – 7 % according to R.W. Nurse is formed at 1500 °C after 60 minutes. At 1200 °C, the degree of calcium oxide absorption in 30 minutes is 49 % in a mixture of pure reagents and 85 % when SiO_2 is replaced by granulated PS. In the belite clinker, C_2S is in the β-form. After burning at 1200 °C, α′ – C_2S also appears.

Microscopic immersion studies show that belite crystals grow with increasing temperature and firing duration (Fig. 9 and 10). After 1200 and 1000 °C, 30 minutes they have dimensions, accordingly, 10 and 2 – 4 microns, and after 60 minutes – 15 and 5 – 6 microns. Crystals form intergrowths. In cakes fired at 1200℃, polysynthetic twins of belite are often found. C_5A_3 is represented by isotropic grains of a rounded shape and relatively low refractive index.



a **b** **c**

Figure 9. Micrograph of the mixture for dicalcium silicate at 100 °C x 240, N II: a – 30 minutes; b – 60 minutes; c – 120 minutes.



a b c

Figure 10. Micrograph of the mixture for dicalcium silicate at 1200 °C x 240, N II: a – 30 minutes; b – 60 minutes; c – 120 minutes.

For two years, the samples did not show any signs of silicate decomposition. The resistance to silicate degradation does not deteriorate with an increased CaF_2 content, but the reaction rate of the C_2S formation is increased.

When developing a method for refractories producing from belite-containing materials, the effect of grain size composition of clinkers, the samples pressing pressure, the burning temperature and the dwell time were studied. By means of the mathematical planning method of experiment the dependences of apparent porosity and density on these factors were found. The maximum density is achieved with the following ratio of the fraction, wt.%: fine – 70 %, coarse – 25 %, average – 5 %, which is consistent with the literature data. With an increase in the pressing pressure and burning temperature, the refractories density increases proportionally. Sintering occurs due to the formation of a binder from low-melting compounds. The partial dependences of density from dwell time are exponential: when the dwell time increases up to 120 min, the density increases insignificantly, and then practically is not changed.

Compared to density, the porosity dependence on the studied factors is inverse. In the same fraction ratios, the samples have the minimum porosity due to the maximum packing density of grains. As the pressing pressure and burning temperature increase, the porosity decreases. It corresponds to the statement that during heat-treating the grains size and shape increase, and the pores decrease as a result of filling them with a low-melting binder. The samples dwell time in the oven for more than 120 min does not lead to a noticeable change in density and porosity.

Generalized equations of the response function are obtained on the basis of partial functions:

for belite clinker with SC = 0.75, a) density

$$\rho = \frac{\left(-0.000028X_1^2 + 0.003826X_1 + 2.24946\right)\left(2.237 + 0.009\lg X_2\right)}{12.81\left(1.964 + 0.89\lg X_3\right)^{-1}\left(1 - e^{-0.022652X_4{}^{0.010654}}\right)^{-1}},$$

$$R = 0.87,\ t_R = 16.4 > 2.$$

b) apparent porosity

$$P_0 = \frac{\left(0.000563X_1^2 - 0.08306X_1 + 30.1919\left(31.495 - 0.3\lg X_2\right)\right)}{21787.77\left(43.208 - 36.18\lg X_3\right)^{-1}\left(1 - e^{-0.423128X_4{}^{-0.058842}}\right)^{-1}},$$

$$R = 0.87,\ t_R = 16.4 > 2.$$

for belite clinker with SC = 0.70, a) density

$$\rho = \frac{\left(-0.0000354X_1^2 + 0.005096X_1 + 2.21972\right)\left(2.251 + 0.05\lg X_2\right)}{12.747\left(1.794 + 1.28\lg X_3\right)^{-1}\left(1 - e^{-0.02312026X_4{}^{0.005171}}\right)^{-1}},$$

$$R = 0.97,\ t_R = 85.41 > 2.$$

b) apparent porosity

$$P_0 = \frac{\left(0.001288X_1^2 - 0.1633X_1 + 31.6574\left(30.138 - 0.20\lg X_2\right)\right)}{21313.83\left(53.916 - 62.01\lg X_3\right)^{-1}\left(1 - e^{-0.377133X_4{}^{-0.034356}}\right)^{-1}},$$

$$R = 0.81,\ t_R = 10.57 > 2.$$

To obtain refractories with high performance indicators such as mechanical strength, slag resistance, and etc., it is necessary to achieve a low apparent porosity of products with their high apparent density.

In the considered interval, the following levels of factors may be most appropriate:

1. Size composition. The maximum packing density is achieved with 70 % fine, 25 % coarse and 5 % average fractions. But in view of high energy costs required for fine grinding of a large amount of material the following fractions ratio is recommended: fine – 25 %, coarse – 70 % and average – 5 %. With a given grain composition, the porosity value is 2–4 % higher than in the first size composition.

2. Molding pressure. The highest raw material density is provided by the pressure of 80 – 100 MPa.

3. Burning temperature. To ensure the best sintering, it is recommended burning at a maximum temperature of 1450 °C out of the studied ones.

4. Extract. Since the process reaches saturation in 120 minutes, from the point of view of saving energy resources and achieving the maximum density of refractories the burning time can be limited to two hours.

The selected values of technological process were substituted into the response function equations. The results are shown in the Table 9.

Table 9. Rating values of optimization settings.

Belite clinker	Optimization settings	
	ρ, g.cm^3	P_0, %
SC = 0.75	2.49	23.05
SC = 0.70	2.47	22.82

As the table shows, the obtained porosity values are in the range of 7 – 23 %, which meets the regulatory requirements for refractories. The obtained density values are far from the maximum possible. The bulk density by the phase composition is 3.23 g.cm^3.

The melting temperatures range of the main crystalline phases is above the studied region, where only solid-phase reactions and sintering occur due to melting of low-melting phases. Achieving the values of apparent density of refractories close to the maximum is impossible in this area.

Belite clinkers were tested to obtain refractory products, which were characterized by the following indicators: apparent porosity 23–25 %; volume burning shrinkage – up to 10 %; strength in compression – 50 MPa; refractory – above 1770 °C; after shrinkage at 1550 °C – 1.3 ÷ 1.4 %; temperature of the deformation beginning under of load of 2 kp.cm^2 – circa 1400℃; thermal stability – 3–4 water thermal cycling. These data refer to the products obtained by semi-dry molding under a pressure of 80-100 MPa of a size composition burden:

fraction	5-1 mm	80-70 %
	1-0.08 mm	10-15 %
	no greater than 0.08 mm	10-15 %

Mixing moisture content is 10 %. Burning temperature is 1350–1400 °C.

In compliance with the physical and technical indicators of the specified clause 7, belite clinkers were tested to obtain refractory products, which were characterized by the following indicators: apparent porosity 23–25 %; volumetric fire shrinkage – up to 10 %; compressive strength – 50 MPa; fire resistance – above 1770 °C; additional shrinkage at 1550 °C – 1.3 ÷ 1.4 %; the temperature of the onset of deformation under a load of 2 kgf.cm^2 is about 1400 °C; heat resistance – 3–4 water heat cycles.

4. Conclusions

1. The experiments setting up to study the possibility for obtaining a stabilized belite refractory by replacing with phosphoric slags the known natural silica-containing materials in a cement raw mixture has been proved. Both limestone and air-slaked lime were used as the second ingredient of burden.

2. It is shown that granulated phosphoric slag is mainly represented by a pseudo-wollastonite glass. The slag crystalline phases are represented by wollastonite and quartz.

3. Thermal transformations in phosphoric slags and clinker formation processes in the phosphoric slags mixtures with lime-containing components have been studied. The processes of chemical property and kinetics have been described. The parameters for refractory materials obtaining have been determined.

4. Belite clinkers with SC = 0.60–0.85 have been investigated. Clinkers with SC = 0.70 and 0.75 with a burning temperature of 1350–1400 °C are optimal for obtaining refractories.

5. To determine the technological parameters for refractories production based on belite-containing clinkers, a mathematical model has been drawn up. Apparent density and apparent porosity have been selected as optimization parameters, and the factors have been selected as size composition, molding pressure, burning temperature and holding.

6. To obtain refractories with the best physical and technical characteristics, it is necessary to use a raw mixture with 25 % of fine fraction (less than 0.5 mm), 5 % of average – (1–0.5 mm) and 70 % of coarse – (3–1 mm), to apply a molding pressure of 100 MPa, and to burn at a temperature of 1450 °C.

7. Based on experimental data and a mathematical model, a refractory made of belite-containing clinkers with the following calculated physical and technical parameters is proposed: with SC = 0.70 – P_0 = 22.82 %, ρ = 2.47 g.cm^3; with SC = 0.75 – P_0 = 23.05 %, ρ = 2.49 g.cm^3. Belite clinkers were tested to produce refractory products, which confirmed the research results.

References

1. Gryzlov, V.S. Electrothermophosphoric slags as a basis of binding composites. Building materials. 2014. 10. Pp. 66–69. (rus)
2. Shaikezhan, A, Anuarova, A.D., Antonovic, V. Cement slurry from electro-phosphoric slag. Magazine of Civil Engineering. 2020. 98(6). Pp. 9806–9806. DOI:10.18720/MCE.98.6.
3. Nurse, R.W., Welch, J.H., Gutt, W. High-temperature phase equilibria in the system dicalcium silicate - Tricalcium phosphate. Journal of the Chemical Society (Resumed). 1959. Pp. 1077–1083. DOI:10.1039/JR9590001077.
4. Shen, Y., Qian, J.S., Huang, Y.B., Yang, D.Y. Synthesis of belite sulfoaluminate-ternesite cements with phosphogypsum. Cement & Concrete Composites. 2015. 63. Pp. 67–75. DOI:10.1016/j.cemconcomp.2015.09.003.
5. Bullerjahn, F., Schmitt, D., Ben Haha, M. Effect of raw mix design and of clinkering process on the formation and mineralogical composition of (ternesite) belite calcium sulphoaluminate ferrite clinker. Cement and Concrete Research. 2014. 59. Pp. 87–95. DOI:10.1016/j.cemconres.2014.02.004.
6. Chen, I.A., Hargis, C.W., Juenger, M.C.G. Understanding expansion in calcium sulfoaluminate-belite cements. Cement and Concrete Research. 2012. 42(1). Pp. 51–60. DOI:10.1016/j.cemconres.2011.07.010.
7. Chen, I.A., Juenger, M.C.G. Synthesis and hydration of calcium sulfoaluminate-belite cements with varied phase compositions. Journal of Materials Science. 2011. 46(8). Pp. 2568–2577. DOI:10.1007/s10853-010-5109-9.
8. Ioannou, S., Reig, L., Paine, K., Quillin, K. Properties of a ternary calcium sulfoaluminate-calcium sulfate-fly ash cement. Cement and Concrete Research. 2014. 56. Pp. 75–83. DOI:10.1016/j.cemconres.2013.09.015.
9. Elhoweris, A., Glasser, F.P., Galan, I. Stabilisation of alpha ' dicalcium silicate in calcium sulfoaluminate clinker. Advances in Cement Research. 2020. 32(3). Pp. 112–124. DOI:10.1680/jadcr.18.00050.
10. Galan, I., Elhoweris, A., Hanein, T., Bannerman, M.N., Glasser, F.P. Advances in clinkering technology of calcium sulfoaluminate cement. Advances in Cement Research. 2017. 29(10). Pp. 405–417. DOI:10.1680/jadcr.17.00028.
11. Ren, C.Z., Wang, W.L., Li, G.L. Preparation of high-performance cementitious materials from industrial solid waste. Construction and Building Materials. 2017. 152. Pp. 39–47. DOI:10.1016/j.conbuildmat.2017.06.124.
12. de Carvalho, J.M.F., Campos, P.A.M., Defaveri, K., Brigolini, G.J., Pedroti, L.G., Peixoto, R.A.F. Low Environmental Impact Cement Produced Entirely from Industrial and Mining Waste. Journal of Materials in Civil Engineering. 2019. 31(2). Pp. 9. DOI:10.1061/(asce)mt.1943-5533.0002617.
13. Julphunthong, P. Synthesizing of calcium sulfoaluminate-belite (CSAB) cements from industrial waste materials. Materials Today-Proceedings. 2018. 5(7). Pp. 14933–14938. DOI:10.1016/j.matpr.2018.04.033. URL: %3CGo.
14. Liu, Y., Zheng, Y. Active belite cement clinker produced with mineral waste. Advanced Materials Research. 2012. 610–613. Pp. 2378–2385
15. Boughanmi, S., Labidi, I., Megriche, A., El Maaoui, M., Nonat, A. Natural fluorapatite as a raw material for Portland clinker. Cement and Concrete Research. 2018. 105. Pp. 72–80. DOI:10.1016/j.cemconres.2018.01.006.
16. Lidin, R.A., Andreyeva, L.L., Molochko, V.A. Konstanty neorganicheskikh veshchestv [Constants of inorganic substances]. Drofa. Moscow, 2006. (rus)
17. Kukolev, G.V., Dudavskiy, I.Y. Sposob polucheniya ogneupornykh izdeliy [Method of refractory products obtaining]. 77222A1. 1949. (rus)
18. Guan, Z. Vliyaniye fosfora na obrazovaniye portlandtsementnogo klinkera s vysokim soderzhaniyem alita [Phosphorus impact on the Portland cement clinker formation with a high alite content]. Cement and its application. 2011. 1. Pp. 144–149. (rus)
19. Kholin, I.I. Spravochnik po proizvodstvu tsementa [Handbook for cement production]. Gosstroyizdat. Moscow, 1963. (rus)
20. Kelman, F.I. Methods of analysis in the control of production of sulfuric acid and phosphorus fertilizers [Analysis methods during control of the sulfuric acid and phosphoric fertilizers production]. Goskhimizdat. Moscow, 1963. (rus)
21. Kravchenko, I.I., Vlasova, M.T., Yudovich, B.E. High strength and extra fast hardening Portland cements [Vysokoprochnyye i bystrotverdeyushchiye portlandtsementy]. Stroyizdat. Moscow, 1971. (rus)
22. Hewlett, P.C., Liska, M. Lea's chemistry of cement and concrete. 2019.

23. Swayze, M.A. A report on studies of; 1. The ternary system of CaO-C5A3 -C2F, 2. The quaternary system CaO-C5A3 -C2F-C2S, 3. The quaternary system as modified by 5% magnesia, Part 1. American Journal of Science. 1946. 244(2). DOI:10.2475/ajs.244.2.65.
24. Gatt, V. Proizvodstvo portlandtsementa iz fosfatsoderzhashchego syr'ya [Production of Portland cement from phosphate-containing raw materials]. Fifth International Congress on Cement Chemistry. Stroyizdat. Moscow, 1973. Pp. 46–47. (rus)

Contacts:

Amankeldi Shaikezhan, shikg_a@mail.ru
Ayaulym Anuarova, anuarova_ayaulym@mail.ru

Received 22.10.2020. Approved after reviewing 26.04.2021. Accepted 30.04.2021.



Magazine of Civil Engineering

ISSN 2712-8172

journal homepage: http://engstroy.spbstu.ru/

DOI: 10.34910/MCE.110.11

Estimation of soil properties by an artificial neural network

***I.V. Ofrikhter*[a]*, *A.B. Ponomaryov*[b], *A.V. Zakharov*[a], *R.I. Shenkman*[a]**

[a] *Perm National Research Polytechnic University, Perm, Russia*

[b] *Peter the Great St. Petersburg Polytechnic University, St. Petersburg, Russia*

**E-mail: ian.ofrikhter@gmail.com*

Keywords: soils, soil mechanics, shear strength, geotechnical engineering, neural networks

Abstract. Empirical dependencies are often used in various fields of geotechnics and civil engineering. The existing empirical formulas are mainly developed with the use of regression and multiple regression. Recently, another predictor is gaining more and more popularity - artificial neural networks. Artificial neural networks (ANNs) are one of the artificial intelligence methods relatively new to geotechnical science. This paper discusses the use of artificial neural networks to estimate the mechanical parameters of soils based on known physical characteristics. This problem has been of interest to geotechnical scientists for a long time, and some new correlations between mechanical and physical characteristics still appear. To develop this correlation a fully connected artificial neural network of direct propagation was used in the research. The neural network was trained on the data of laboratory tests of soil samples in the city of Novosibirsk, Russia. The article contains a description of the main features of correlations developing with artificial neural networks. As a result of this study, an artificial neural network was obtained that allows predicting the angle of friction and specific cohesion of clay soil with reasonable accuracy. The topology of the neural network is proposed, and the comparison of the estimation accuracy with the existing equations is carried out. According to the comparison of the results, it turned out that the ANN allows increasing the estimation accuracy of both parameters.

1. Introduction

Friction angle and cohesion are among the essential geotechnical parameters of soils. Determining these parameters requires sampling and rigorous laboratory testing. It is both time-consuming and needs careful supervision. They are used in the design of structures, both by analytical methods and by the finite element method. The accuracy of determining the soil base's mechanical characteristics most strongly affects the proposed structural solutions for foundations.

However, it is onerous to conduct many laboratory soil tests to determine the soil base's cohesion and friction angle in some cases. The very primary soil data to be determined in any geological survey is the soil's physical characteristics. Simultaneously, it is well known that having the data about the soil's physical properties can approximate some of the mechanical properties. Previously, many researchers develop their correlations, trying to improve the accuracy of such predictions.

Several studies have reported the correlation between the effective angle of shearing resistance and plasticity index [1, 2]. Jain [3], in his research, states that the angle of internal friction depends on dry density, particle size distribution, the shape of particles, surface texture, and water content. Cohesion depends on particle size, clay minerals type, water content, and some other parameters. Roy et al. [4] conducted another similar study in 2014. In this work, the authors suggest correlating cohesion and angle of shearing resistance with specific gravity angle and soil bulk density, respectively. Using multiple regression and neural network approach, Goktepe et al. [5] analyzed relations between index properties

Ofrikhter, I.V., Ponomaryov, A.B., Zakharov, A.V., Shenkman, R.I. Estimation of soil properties by an artificial neural network. Magazine of Civil Engineering. 2022. 110(2). Article No. 11011. DOI: 10.34910/MCE.110.11

© Ofrikhter, I.V., Ponomaryov, A.B., Zakharov, A.V., Shenkman, R.I., 2022. Published by Peter the Great St. Petersburg Polytechnic University.

This work is licensed under a CC BY-NC 4.0

and shear strength parameters of plastic clays. Mousavi et al. [6] used genetic programming to develop a correlation between the internal friction angle and the physical properties of soils, such as the fine and coarse content, density, and liquid limit.

To develop correlations between soil variables, most geotechnical researchers use well-known mathematical approaches such as regression and multiple regression. Recently, however, neural networks for developing empirical correlations have become more and more promising. The very concept of artificial neural networks was proposed in the 1950s [7]. In 1994, there were proposals to use ANN in civil engineering [8]. Researchers believe that neural networks are the most promising method for the mathematical description of geotechnical characteristics [9]. Several researchers are currently developing databases that will facilitate artificial intelligence to analyze geotechnical data [10].

Although artificial neural networks (ANN) have not yet become a daily practice, they have already been used many times in different geotechnical problems. In some cases, it is possible to successfully replace the finite difference method with deep neural networks [11]. Resilient modulus of fine-grained materials was modeled with the use of ANN [12]. In addition, ANNs were used to prediction of the swelling potential of clay soils [13]. Many studies are devoted to the use of ANN for calculating the bearing capacity of the pile [14–16], piled raft [17], and shallow foundations [18]. ANNs were also used to analyze slope stability [19], reinforced sand strength [20], and many other geotechnical engineering issues. Some scientists previously carried out the development of correlation dependences of soil's mechanical properties on physical parameters [21–24].

It is important to note that the use of ANN changes the methodological order of conducting research. It is necessary to hypothetically assume a specific model of the system's operation in the usual order. Then you have to develop a mathematical description and, at last, carry out approbation in experiments. When researching using an ANN, the development of a mathematical description is actually automated by learning algorithms for a neural network. In the current state, it is a method of backpropagation of an error [25]. Simultaneously, the role of experimental data, their completeness, and the quality of their storage in digital form increase significantly.

2. Methods

In this study, an artificial neural network (ANN) was used to predict soils' mechanical characteristics. The artificial neural network is a mathematical model that in a simplified form emulates the work of the human brain. In particular, neural networks allow, to some extent, to imitate a person's ability to cognize and learn.

The most common ANN form that performs complex regression tasks and predicts various characteristics is a fully connected feedforward neural network. In general, such a model consists of an input layer, a hidden layer, and an output layer (Fig. 1). Because each neuron of the previous layer is connected with each neuron of the next one, the neural network is called fully connected.

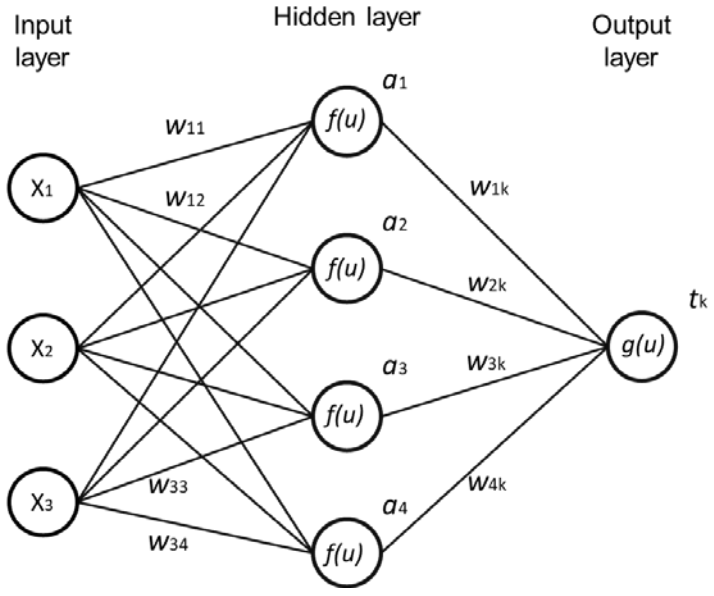


Figure 1. Fully connected direct propagation artificial neural network (ANN).

Fig. 1 X_i values in the input layer are the initial data of the predicted process. w_{ij} is link weights. The link weight w_{ij} is the number by which the output of the previous layer is multiplied. The neurons of the hidden and output layers are $f(u)$ and $g(u)$, where u is the sum of the input values multiplied by the corresponding connection weights w_{ij}. The functions $f(u)$ and $g(u)$ are called activation functions. In some papers, this functions are called perceptron, and the neural network is called multilayer perceptron. This historical name is not entirely correct. A perceptron can only give output values of 1 or 0, while a neuron's output can be anything between 1 and 0. This is a simplified explanation of the difference, but it should give a general idea. The parameters a_i and t_k are the outputs of the activation functions $f(u)$ and $g(u)$. Because of the above, a_i and t_k can be written as follows:

$$a_j = f\left(\sum_{i=1}^{N} w_{ij} x_i + b\right), \quad (1)$$

$$t_k = g\left(\sum_{j=1}^{N} w_{jk} a_j + b_k\right). \quad (2)$$

As can be seen from formulas (1) and (2), in this example, the activation functions $f(u)$ and $g(u)$ are linear. However, in real cases, the form of the function is selected individually. The artificial neural network in Fig. 1 has three neurons in the input layer, four neurons in the hidden layer, and one neuron in the output layer. In general, the output layer can include any number of neurons. Depending on the task, the hidden layer could consist of several neuron layers. The number of neurons and layers in the hidden layer is limited only by computational capabilities and expediency. In general, the more complex the process being modeled, the more neurons and layers are needed.

Before the ANN can make predictions, it is necessary to assign the correct bond weights and activation function coefficients. For this, the neural network needs to be trained. Neural network training is the process of finding weights of connections and coefficients of activation functions by means of successive iterations. The most common method for training neural networks is the backpropagation algorithm [25].

A training dataset is needed to train a neural network. A training dataset is a set of input and output data, by the example of which the network will be trained to make predictions of the output parameter based on the initial data. The key meaning of the ongoing process remains in the form of a set of numbers – weights of connections and activation function coefficients. As a rule, it is not available for interpretation. Simultaneously, a neural network can find and reproduce connections between phenomena, even if engineers do not know this connection. This is a massive advantage over traditional statistical methods.

The soil properties dataset for this research was collected from laboratory test data. A total of 420 shear test data of 102 cohesive soil layers were used. Sampling was carried out in the area of the city of Novosibirsk, Russia. All data were entered into a table, a small fragment of which is presented in Table 1.

Table 1. Fragment of the laboratory shear test data.

Sampling depth, m	Natural moisture content	Liquid limit	Plastic limit	Plasticity index	Bulk density, g/cm^3	Dry density, g/cm^3	Void ratio	Friction angle at natural humidity, degrees	Cohesion at natural Moisture Content, kPa
1.5	0.20	0.30	0.18	0.12	2.05	1.71	0.591	21	34
3.0	0.21	0.29	0.18	0.11	2.03	1.68	0.619	22	28
3.0	0.23	0.27	0.17	0.10	1.96	1.59	0.711	19	21
2.0	0.15	0.27	0.18	0.09	1.67	1.45	0.876	25	39
3.0	0.11	0.30	0.19	0.11	1.49	1.34	1.030	25	71
4.5	0.12	0.29	0.20	0.09	1.42	1.27	1.142	24	63

The soil's initial characteristics were sampling depth, natural moisture content, liquid limit, plastic limit, plasticity index, bulk density, dry density, and void ratio. Particle density was not used as an initial parameter, as all clay samples in the dataset had a particle density of 2.71 g/cm^3 to 2.72 g/cm^3. Accordingly, the neural network has seven neurons on the input layer. In this study, two ANNs were trained

to predict the friction angle at natural humidity and specific cohesion at natural humidity. As a result, we got two ANNs with eight input parameters and one output parameter in each.

ANNs are believed to provide more accurate results when they do not extrapolate the range of data used for training [8, 26]. Although this is not the significant difference between ANN and other models, this feature is still a limitation. Therefore, it should be noted that the model, which is proposed in this article, is applicable and tested only in a limited range of data. The content of input and output characteristics used for training and testing is presented in Table 2.

Table 2. Fragment of the laboratory shear test data.

Input parameter	Range of values presented in the database
Sampling depth, m	1–27
Liquid limit	0.13–0.48
Plastic limit	0.11–0.30
Bulk density, g/cm^3	1.42–2.12
Dry density, g/cm^3	1.27–1.91
Output parameters	
Friction angle at natural humidity	14–31
Cohesion at natural humidity, kPa	10–69

When a neural network is trained, the simultaneous development of the generalization and memorization effects is observed. Generalization is the ability of a neural network to capture and reproduce some parameters' dependence on others. Memorization is the ability of a neural network to memorize a specific combination of inputs and outputs. In general, when developing an NN, generalization is a positive effect, and memorization is negative. When the neural network does not look for dependencies but remembers the data offered to it, it is overfitting. Memorizing data requires a more significant model size than generalization. Therefore, with the same number of training examples, a more extensive neural network is more likely to start memorizing data rather than looking for dependencies. The ANN's size should be sufficient to generalize the available sample but should not be too large to develop the overfitting effect.

The training dataset is used to fit the link weights using the backpropagation algorithm directly. A neural network has several hyperparameters that a person selects. These are such parameters as network topology, type of activation functions, loss function, number of learning epochs, learning step, etc. The validation dataset is not involved in finding the weights but is used to select these parameters. Therefore, it cannot be said that the validation dataset has no effect on the learning process. Finally, the test dataset is used to validate the finished model.

The entire dataset must be split into several parts to detect overfitting. This separation is called the cross-validation technique. According to the generally accepted rule [27], the dataset can be divided into training, validation, and test datasets. Several researchers have conducted a series of tests to determine the optimal ratios for different datasets [28]. For geotechnical issues, there are recommendations [28] based on which 20 % of the dataset should be used for validation. The rest data should be distributed by 70 % and 30 % for the training and test samples, respectively. Since the studies of the correlation of physical and mechanical properties of soils were carried out earlier [22, 29], there were no particular difficulties with the choice of hyperparameters in this study. Therefore, the entire dataset was divided into 80 % for training and 20 % for testing.

3. Results and Discussion

The artificial neural network has been trained with different types of architecture. Linear and ReLU activation functions gave the best results. Each training was tested at least ten times. ANN for friction angle prediction contained three layers of 150 neurons in the hidden layer. The hidden layer for cohesion prediction consisted of 4 layers of 200 neurons each. The input layers are the same for both ANNs.

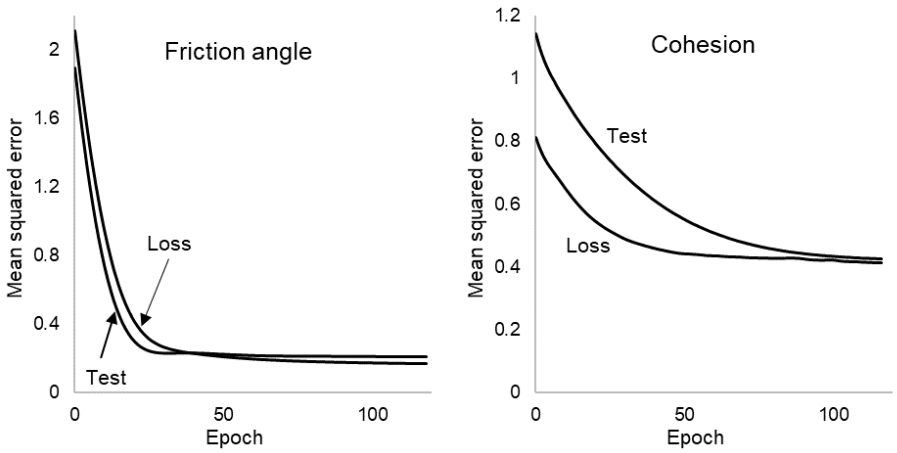


Figure 2. MSE plot of test and training (loss) datasets.

The error fall during training was plotted for both ANNs (Fig. 2) to track the effect of overfitting. Mean squared error (MSE) was used as a loss function for ANN training. Fig. 1 shows that the error decreased evenly throughout the ANNs fitting. In recent epochs, the loss function and the test dataset error have approximately the same values. This means that the network is not overfitted.

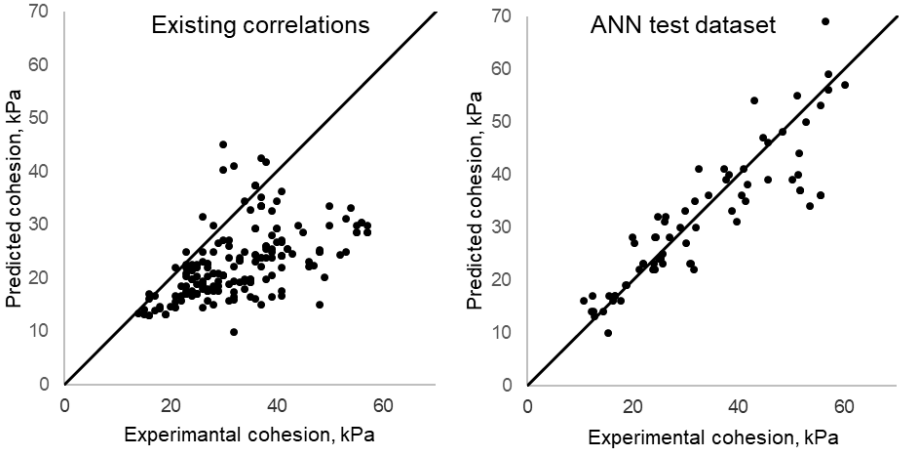


Figure 3. Comparison of experimental and predicted values of cohesion according to existing correlation and proposed ANN.

A comparison was made with the empirical dependencies presented in table A.2 of the national standard SP 22.13330.2016. Comparing the obtained data with the existing correlations included in national standards are presented in Fig. 3 and 4. As shown in Fig. 3, the proposed ANN-based method makes it possible to estimate the cohesion much more accurately than the existing correlations. The mean absolute percentage error (MAPE) of the ANN is 15.33 %. MAPE of existing correlations – 50.43 %.

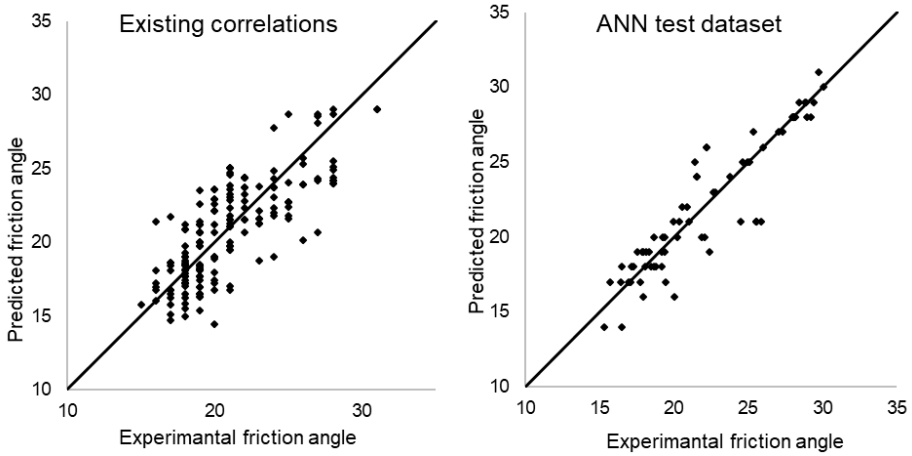


Figure 4. Comparison of experimental and predicted values of friction angle according to existing correlation and proposed ANN.

Comparison of experimental and predicted values of friction angle according to existing correlation and proposed ANN is shown in Fig. 4. In this case, the existing correlation dependences predict well the angle of internal friction. The estimation error using existing methods was 9.1 %. The ANN predicts the angle of internal friction with an accuracy of 6.5 %. An artificial neural network made it possible to build a more accurate correlation, but in general, both methods give good results.

Another identified advantage of an artificial neural network is the range of predicted values. Existing correlations are often applicable for clayey soils with $0 \leq IL \leq 1$. However, in the available dataset, about 47 % of the data had IL values, which were outside these limits. The artificial neural network was trained on a dataset that included negative IL, and this allowed the ANN to predict the angle of internal friction angle and cohesion over a broader range.

4. Conclusion

1. This article discusses the problems of using artificial neural networks to build correlation dependences for many variables. Based on the comparison results, it can be concluded that ANN is a promising method of analysis in geotechnics.

2. The article proposes a neural network topology that allows predicting soils' mechanical characteristics by their physical parameters. The accuracy of the determination is higher than that of the well-known statistical methods.

3. Since both the training dataset and the test dataset were collected in the same region, the proposed dependency may give an increased error in other regions. This may be due to regional soil conditions that are not considered in the original soil parameters. This problem can be avoided by using data from different regions.

5. Acknowledgements

This research was carried out with the financial support of the Ministry of Science and Higher Education of the Russian Federation in the framework of the program of activities of the Perm Scientific and Educational Center "Rational Subsoil Use"

References

1. Brooker, E.W., Ireland, H.O. Earth Pressures at Rest Related to Stress History. Canadian Geotechnical Journal. 1965. 2(1). Pp. 1–15. DOI: 10.1139/t65-001
2. Stark, T.D., Eid, H.T. Slope Stability Analyses in Stiff Fissured Clays. Journal of Geotechnical and Geoenvironmental Engineering. 1997. 123(4). Pp. 335–343. DOI: 10.1061/(asce)1090-0241(1997)123:4(335)
3. Rajeev Jain, Pradeep Kumar Jain, S.S.B. Computational Approach to predict Soil Shear Strength, International Journal of Engineering Science and Technology. International Journal of Engineering Science and Technology. 2010. 2(8). Pp. 3874–3885.
4. Roy, S., Dass, G. Statistical models for the prediction of shear strength parameters at Sirsa, India. International Journal of Civil and Structural Engineering. 2014. 4(4). Pp. 483–498.
5. Goktepe, A.B., Altun, S., Altintas, G., Tan, O. Shear strength estimation of plastic clays with statistical and neural approaches. Building and Environment. 2008. 43(5). Pp. 849–860. DOI: 10.1016/j.buildenv.2007.01.022
6. Mousavi, S.M., Alavi, A.H., Gandomi, A.H., Mollahasani, A. Nonlinear genetic-based simulation of soil shear strength parameters. Journal of Earth System Science. 2011. 120(6). Pp. 1001–1022. DOI: 10.1007/s12040-011-0119-9
7. Bishop, J.M. History and philosophy of neural networks. Computational Intelligence – Vol. 1. 2015. 1(February). Pp. 400.
8. Flood, I., Kartam, N. Neural networks in civil engineering. I: Principles and understanding. Journal of Computing in Civil Engineering. 1994. 8(2). Pp. 131–148. DOI: 10.1061/(ASCE)0887-3801(1994)8:2(131)
9. Moayedi, H., Mosallanezhad, M., Rashid, A.S.A., Jusoh, W.A.W., Muazu, M.A. A systematic review and meta-analysis of artificial neural network application in geotechnical engineering: theory and applications. 32(2) 2020.
10. Hui Wang, Xiangrong Wang, Robert Liang. Study AI based methods characterization geotechnical site2020. 51 p.
11. Gao, W., Lu, X., Peng, Y., Wu, L. A Deep Learning Approach Replacing the Finite Difference Method for in Situ Stress Prediction. IEEE Access. 2020. 8. Pp. 44063–44074. DOI: 10.1109/ACCESS.2020.2977880
12. Khasawneh, M.A., Al-jamal, N.F. Modeling resilient modulus of fine-grained materials using different statistical techniques. Transportation Geotechnics. 2019. 21. DOI: 10.1016/j.trgeo.2019.100263
13. Ermias, B., Vishal, V. Application of Artificial Intelligence for Prediction of Swelling Potential of Clay-Rich Soils. Geotechnical and Geological Engineering. 2020. 38(6). Pp. 6189–6205. DOI: 10.1007/s10706-020-01427-x
14. Suman, S., Das, S.K., Mohanty, R. Prediction of friction capacity of driven piles in clay using artificial intelligence techniques. International Journal of Geotechnical Engineering. 2016. 10(5). Pp. 469–475. DOI: 10.1080/19386362.2016.1169009
15. Harandizadeh, H. Developing a new hybrid soft computing technique in predicting ultimate pile bearing capacity using cone penetration test data. Artificial Intelligence for Engineering Design, Analysis and Manufacturing: AIEDAM. 2020. 34(1). Pp. 114–126. DOI: 10.1017/S0890060420000025
16. Alzo'ubi, A.K., Ibrahim, F. Predicting Loading–Unloading Pile Static Load Test Curves by Using Artificial Neural Networks. Geotechnical and Geological Engineering. 2019. 37(3). Pp. 1311–1330. DOI: 10.1007/s10706-018-0687-4
17. Rabiei, M., Choobbasti, A.J. Innovative piled raft foundations design using artificial neural network. Frontiers of Structural and Civil Engineering. 2020. 14(1). Pp. 138–146. DOI: 10.1007/s11709-019-0585-8

18. Ray, R., Kumar, D., Samui, P., Roy, L.B., Goh, A.T.C., Zhang, W. Application of soft computing techniques for shallow foundation reliability in geotechnical engineering. Geoscience Frontiers. 2020. DOI: 10.1016/j.gsf.2020.05.003
19. Das, S.K., Biswal, R.K., Sivakugan, N., Das, B. Classification of slopes and prediction of factor of safety using differential evolution neural networks. Environmental Earth Sciences. 2011. 64(1). Pp. 201–210. DOI: 10.1007/s12665-010-0839-1
20. Harikumar, M., Sankar, N., Chandrakaran, S. Prediction of strength parameters of sand combined with three dimensional components using Artificial Neural Networks. Australian Geomechanics Journal. 2016. 51(1). Pp. 97–108.
21. Kim, E., Stine, M.A., de Oliveira, D.B.M., Changani, H. Correlations between the physical and mechanical properties of sandstones with changes of water content and loading rates. International Journal of Rock Mechanics and Mining Sciences. 2017. 100. Pp. 255–262. DOI: 10.1016/j.ijrmms.2017.11.005
22. Pham, B.T., Son, L.H., Hoang, T.A., Nguyen, D.M., Tien Bui, D. Prediction of shear strength of soft soil using machine learning methods. 1662018.
23. Minns, A.W., Hall, M.J. Modélisation pluie-débit par des réseaux neuroneaux artificiels. Hydrological Sciences Journal. 1996. 41(3). Pp. 399–417. DOI: 10.1080/02626669609491511
24. Wrzesiński, G., Lechowicz, Z., Sulewska, M.J. Application of Artificial Neural Networks for the prediction of undrained shear modulus in cohesive soils. Ce/Papers. 2018. 2(2–3). Pp. 833–838. DOI: 10.1002/cepa.774
25. Goh, A.T.C. Back-propagation neural networks for modeling complex systems. Artificial Intelligence in Engineering. 1995. DOI: 10.1016/0954-1810(94)00011-S
26. Tokar, A.S., Johnson, P.A. Rainfall-runoff modeling using Artificial Neural Networks. Journal of Hydrologic Engineering. 1999. 4(3). Pp. 232–239. DOI: 10.1061/(ASCE)1084-0699(1999)4:3(232)
27. Stone, M. Cross-Validatory Choice and Assessment of Statistical Predictions (With Discussion). Journal of the Royal Statistical Society: Series B (Methodological). 1976. 38(1). Pp. 102–102. DOI: 10.1111/j.2517-6161.1976.tb01573.x
28. Shahin, M.A., Maier, H.R., Jaksa, M.B. Data division for developing neural networks applied to geotechnical engineering. Journal of Computing in Civil Engineering. 2004. 18(2). Pp. 105–114. DOI: 10.1061/(ASCE)0887-3801(2004)18:2(105)
29. Jasim, M.M., Al-Khaddar, R.M., Al-Rumaithi, A. Prediction of bearing capacity, angle of internal friction, cohesion, and plasticity index using ANN (case study of Baghdad, Iraq). International Journal of Civil Engineering and Technology. 2019. 10(1). Pp. 2670–2679.

Contacts:

Ian Ofrikhter, ian.ofrikhter@gmail.com
Andrey Ponomaryov, andreypab@mail.ru
Alexander Zakharov, zaharav@mail.ru
Roman Shenkman, Rshen@list.ru

Received 10.11.2020. Approved after reviewing 27.04.2021. Accepted 11.05.2021.



Magazine of Civil Engineering

ISSN 2712-8172

journal homepage: http://engstroy.spbstu.ru/

DOI: 10.34910/MCE.110.12

Bearing capacity of skirted footing subjected to inclined loading

R.P. Shukla

National Institute of Technology Srinagar, Hazratbal, Srinagar, Jammu and Kashmir, India

E-mail: rpshukla.2013@iitkalumni.org

Keywords: bearing capacity, improvement factor, skirt, inclined loading, cohesive soil

Abstract. Skirted foundations are popular nowadays due to relatively higher bearing capacity and greater stability than strip footing. Foundations are generally subjected to inclined loading in the field. This study aimed to determine the effect of load inclination on bearing capacity, failure mechanism, and efficiency of skirted footing resting on cohesive soil using the finite element method. The footing has been assumed to be rigid, while the skirt has been assumed to be rigid as well flexible in nature. The bearing capacity of footing increases with the increase in skirt length, undrained strength, and footing depth. The provision of the skirt increases the bearing capacity by 1.4–5 times the capacity of strip footing. The bearing capacity decreases with an increase in load inclination, but the effectiveness of the skirt is found to increase. However, efficiency decreases significantly with an increase in the footing depth. The failure mechanism, as well as skirt effectiveness, is independent of soil strength. The failure zone always remains in the bulb shape, irrespective of any other factors. The skirt efficiency enhances by the provision of the rigid skirt in place of a flexible skirt.

1. Introduction

A large number of techniques and methods have been developed over the last three decades to improve the bearing capacity [1]. Provision of the skirt is one of the techniques to enhance the bearing capacity. Various experimental and numerical studies observed that the provision of the skirt enhances the bearing capacity significantly under different loading conditions [2]. The skirted footing constrains the soil mass between skirts, increasing footing depth and bearing capacity [3]. Numerous studies have been carried out to understand the application and advantages of skirted footing under different soil conditions, especially where shallow foundations are not recommended, such as soils with low bearing capacity, sites with scouring problems, and marine environment [4–7]. Randolph and Watson [8] suggested that the failure planes do not extend to the ground level in skirted footings, unlike the conventional strip footings. In another study, Al-Aghbari and Mohamedzein [7] concluded that the provision of skirts increases the bearing capacity of the foundation by 1.5 to 8.1 times the capacity of conventional circular footings in cohesive soils. However, Yun and Bransby [9] noted that the contribution of end bearing resistance of skirts is insignificant and can be ignored while designing the foundation.

The provision of structural skirts has decreased the overall settlement and increased strip footings bearing capacity [10–12]. It has also been reported that under inclined loading, the optimum length of the skirt is equal to half the width (B) of the footing. Nazir and Azzam [13] reported that small-scale circular footing bearing capacity increased substantially when sand piles were used along with the skirts. Some studies highlighted the effectiveness of skirted footings on loose soils [6, 14–16]. In another study on the behaviour of skirted circular footings on soils with significant strength heterogeneity, Mana et al. [17] observed that a higher number of internal skirts are required; however, the required number of internal skirts reduces with an increase in embedment depth. In a similar study, Mana et al. [18] reported that under the combined effect of seepage and swelling, the displacement of the skirt varies between 0.1 and 1 times

Shukla, R.P. Bearing capacity of skirted footing subjected to inclined loading. Magazine of Civil Engineering. 2022. 110(2). Article No. 11012. DOI: 10.34910/MCE.110.12

© Shukla, R.P., 2022. Published by Peter the Great St. Petersburg Polytechnic University.

This work is licensed under a CC BY-NC 4.0

the foundation diameter. Stergiou et al. [19] noted that the critical spacing between skirts is approximately four times of footing diameter under vertical loading. Azzam [20] reported the increment in skirted footing displacement resting on slopes subjected to seismic action. Some studies found that increasing the skirt length is relatively less effective than increasing the depth of conventional strip footings [3,9, 17, 21–22]. However, some other studies concluded that the provision of the skirts is more effective compared to increasing the depth of conventional strip footings [23–25].

From the literature, it can be established that the provision of the skirt increases bearing capacity and reduces the settlement, owing to an increase in the foundation depth. Most of the studies on the skirted foundations are confined to circular and other isolated footings subjected to vertical loading. Strip footing is a frequently used foundation in rural areas, especially in developing countries. Also, footing may be subjected to inclined load as well. Only a very few studies considered the skirted strip footing subjected to inclined loading. However, earlier studies have not discussed the failure mechanism and skirt efficiency in a detailed manner. Therefore, it is essential to assess the influence of skirts on the improvement of the bearing capacity of strip footing subjected to inclined loading.

2. Methods

2.1. Numerical Modelling

A finite element plane strain model has been used to simulate the problem. The domain area has been assumed to be large enough to avoid any boundary effect. The footing width (B) has been assumed constant throughout the study. The minimum length and width of the domain have been maintained to 30B and 15B, respectively. All displacements have been restrained along the bottom horizontal boundary. Only vertical displacements have been allowed along the vertical boundaries. The numerical model used in the study is shown in Fig. 1.

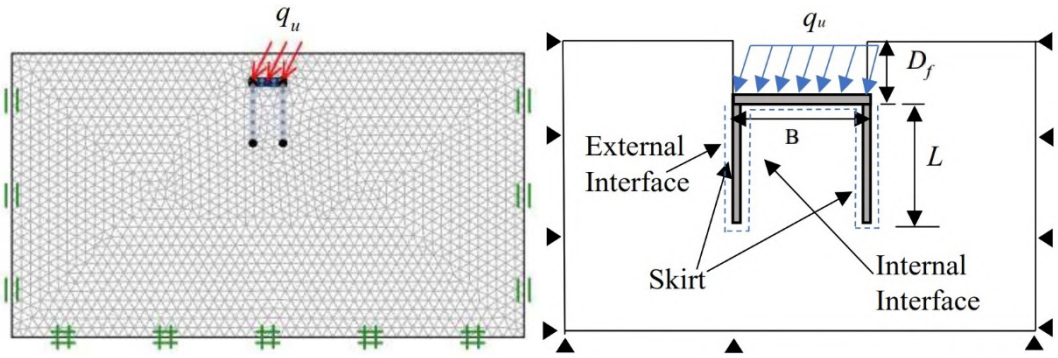


Figure 1. Details of Models: (a) the numerical model; (b) details of the modelling.

Previous studies on skirted footing revealed that the separation is insignificant in the inner interface between soil and skirt [26–27]. Therefore, the adhesion factor was assumed to be 1, which indicates no slipping condition. While for the external interface, the value varied from 0.5 to 1.0, which demonstrates the partial mobilisation. Three to four adoptive iterations were used in the earlier studies to get stable results [28–29]. It allows the refinement of mesh in particular areas where shear is dissipating. More than 9000 elements do not improve the result significantly. Therefore, 9000 elements were used in the first adoptive iterations. The number of elements was increased to 12000 in the third adaptive iteration.

The soil has been modelled as a 15 node Gauss element, and the foundation has modelled as a rigid material (undeformable) plate element. The skirt has also been modelled as a plate element made of infinite stiffness. A standard rigid connection (zero degrees of freedom) was made between the skirts and the bottom foundation plate, allowing efficient transfer of loading from bottom foundation plates to skirts. Mohr-Coulomb model is used to model the soil. The load was applied in terms of load multiplier. The resultant pressure, q_u has two components, one horizontal component (H), and other vertical components (V). The loading inclination (θ) with the ground surface and resultant loading (q_u) can be expressed as:

$$\cos(\theta) = q_u / H,$$

$$\sin(\theta) = q_u / V,$$

$$(q_u)^2 = H^2 + V^2.$$

A number of factors affecting the performance of skirted strip footings, such as length of skirts, type of soil, strength parameters of soil, load inclination, and depth ratio of footing, are considered in the analysis. The skirt length (L) to footing width (B) ratio is varied from 0 to 2 with an interval of 0.5. Similarly, the footing depth (D_f) is varied from 0 to 1.5B, with an interval of 0.5B. A number of studies used undrained strength to characterise the consistency of cohesive soils [30]. In the present study, the broad range of undrained strength has varied from 20 kPa to 320 kPa. This range is sufficient to replicate the probable range of soil consistency. Based on the literature review, the unit weights of soil have varied from 14 kN/m^3 to 17 kN/m^3. The parameters considered in the study are presented in Table 1.

Table 1. Details of considered parameters.

c_u (kPa)	Consistency	$c_u/(\gamma B)$	L/B	(D_f/B)	Loading inclination (H/V)	No. of analysis
20	Soft	0.7	0, 0.5, 1, 1.5, 2.0	0, 0.5,1.0	0, 0.5, 1, 1.5, 2	150
20	Medium	1.4	0, 0.5, 1, 1.5, 2.0	0, 0.5,1.0	0, 0.5, 1, 1.5, 2	150
80	Stiff	2.8	0, 0.5, 1, 1.5, 2.0	0, 0.5,1.0	0, 0.5, 1, 1.5, 2	150
160	Very stiff	5.7	0, 0.5, 1, 1.5, 2.0	0, 0.5,1.0	0, 0.5, 1, 1.5, 2	150
320	Hard	10.6	0, 0.5, 1, 1.5, 2.0	0, 0.5,1.0	0, 0.5, 1, 1.5, 2	150

2.2. Verification of the Numerical Model

Before analysing the skirted footing under inclined loading, the model used in the present study has been verified using earlier studies [31–33]. The bearing capacity factor ($N_{q)}$, which considers the effect of soil weight, has been compared with earlier studies in Table 1. The average values are close to those presented by Yin et al. [31] using FLAC. However, N_q is much higher than those determined by traditional limit equilibrium theories [32–33]. The difference in the bearing capacity factors indicates the limitation of earlier traditional theories. These theories replaced the surcharge loading to equivalent uniformly distributed loading. This assumption neglects the shearing resistance of soil above the base of the footing. Therefore, Terzaghi [32] and Meyerhof [33] provide more conservative N_q.

The normalized bearing capacity ($q_u/\gamma B$) is also compared with the results of Kusakabe et al. [34] for purely cohesive soil and shown in Fig. 2(a). Kusakabe et al. [34] presented both lower and upper-bound solutions. The present study results are lower than the upper bound solution and more than the lower bound bearing capacity. The results of skirted footings are also compared with the results of an experimental study carried out by Al-Aghbari and Mohamedzein [16] and the numerical study results of Laymin et al. [35], and shown in Figs. 2 (b) and 2(c), respectively. The improvement factor (I_f), which is defined as the ratio of bearing capacity of the skirted footing to the strip footing, has also been compared with earlier studies. The improvement factor (I_f), indicates the effectiveness of the skirt. Fig. 2 shows that the results are shows comparable to those determined by Al-Aghbari and Mohamedzein [16] and Laymin et al. [35]. The comparison shown in Tables 1, 2, and Fig. 2 depicts that the present model can be used to predict the behaviour of skirted footing in the clay.

Table 2. Comparison of numerical results (N_q) determined by the present study with earlier studies.

Studies	ϕ = 25^0	ϕ = 30^0	ϕ = 35^0	ϕ = 40^0	ϕ= 45^0
Present study	15.50	24.70	45.20	89.70	195.56
Yin et al. (2001)	12.00	22.00	44.00	70.00	180.00
Meyerhof (1965)	10.70	18.40	34.78	64.10	134.70
Terzaghi (1943)	12.65	22.50	41.40	81.30	173.30

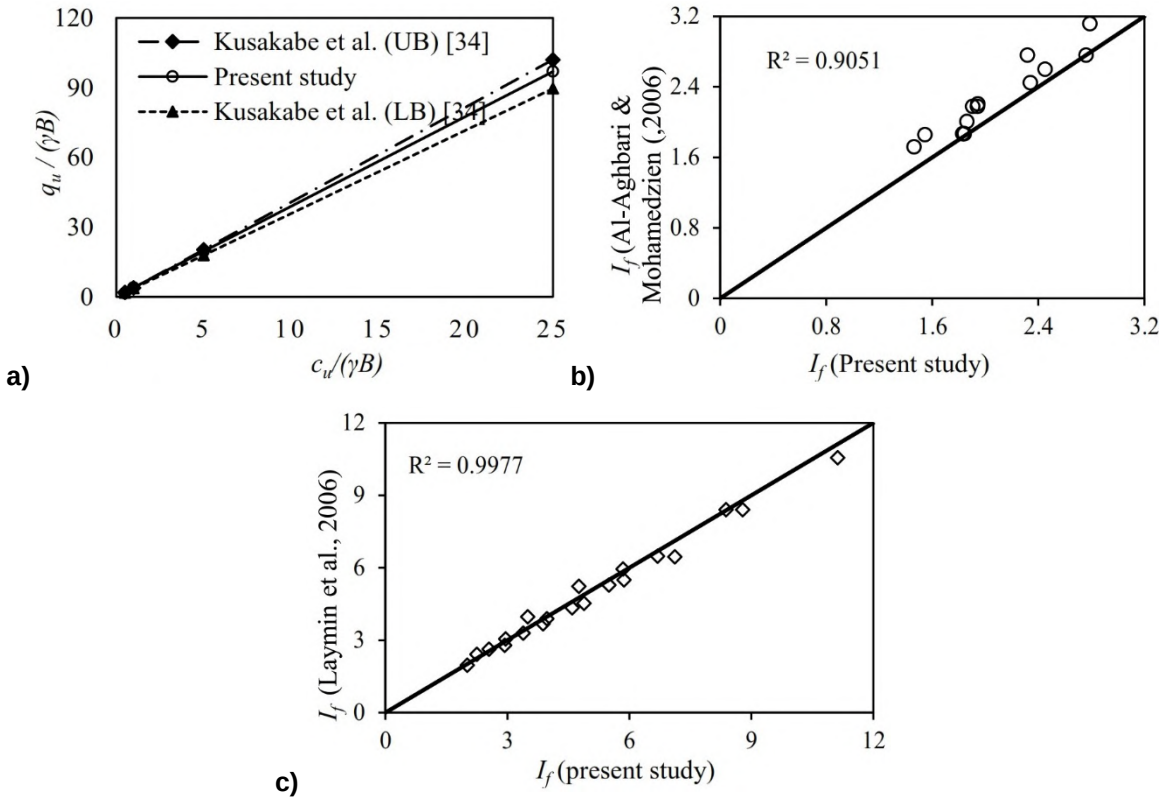
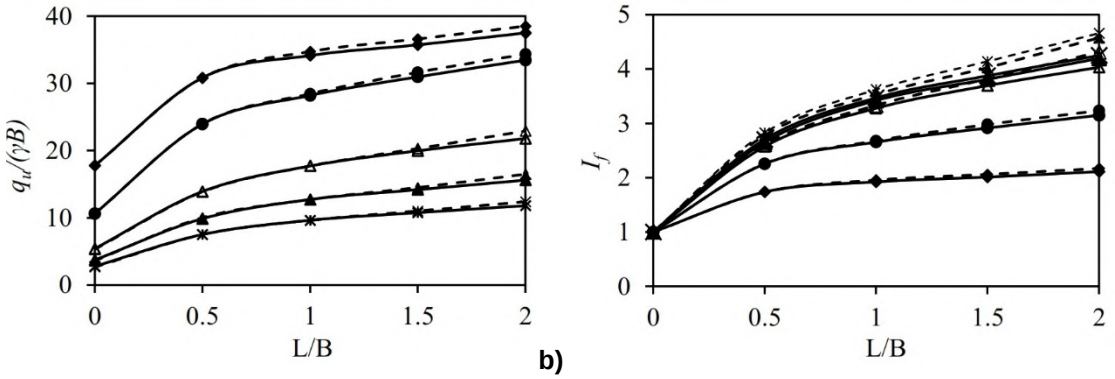


Figure 2. Verification of the model through comparison with published studies: (a) with Kusakabe et al. [34], (b) with Al-Aghbari and Mohamedzein [16], (c) with Laymin et al. [35]

3. Results and Discussions

The results of rigid and flexible skirted footings are presented together for comparing the behaviour. The flexible skirted footing results are shown in the solid lines and rigid skirted footing results by the dashed line in each plot. The bearing capacity decreases with the adhesion factor decreasing due to reduced adhesion between the skirt and soil. However, the improvement factor shows the only marginal change.

The effect of the length of the skirt on bearing capacity ($c_u/\gamma B$) and improvement factor (I_f) is shown in Fig. 3. The bearing capacity improves continuously with an increase in the length of flexible and rigid skirts, but the increment rate becomes less observable at higher skirt lengths (L/B > 1.5). The increase in bearing capacity is due to increased footing depth [3]. The increase in bearing capacity is maximum for purely vertical loading, and the footing is resting on the ground surface. The influence of skirt length on bearing capacity reduces with footing depth. Similar to the bearing capacity factor, the bearing capacity improvement (I_f) increases with skirt length. The bearing capacity improvement augments with an increase in load inclination (Fig. 3 b, d, e), and the maximum is observed at maximum load inclination. The strip footing does not support large lateral loads, and footing may even slide at a small horizontal load, especially when embedment depth is small. However, the bearing capacity increases significantly with footing depth for inclined and horizontal loading.



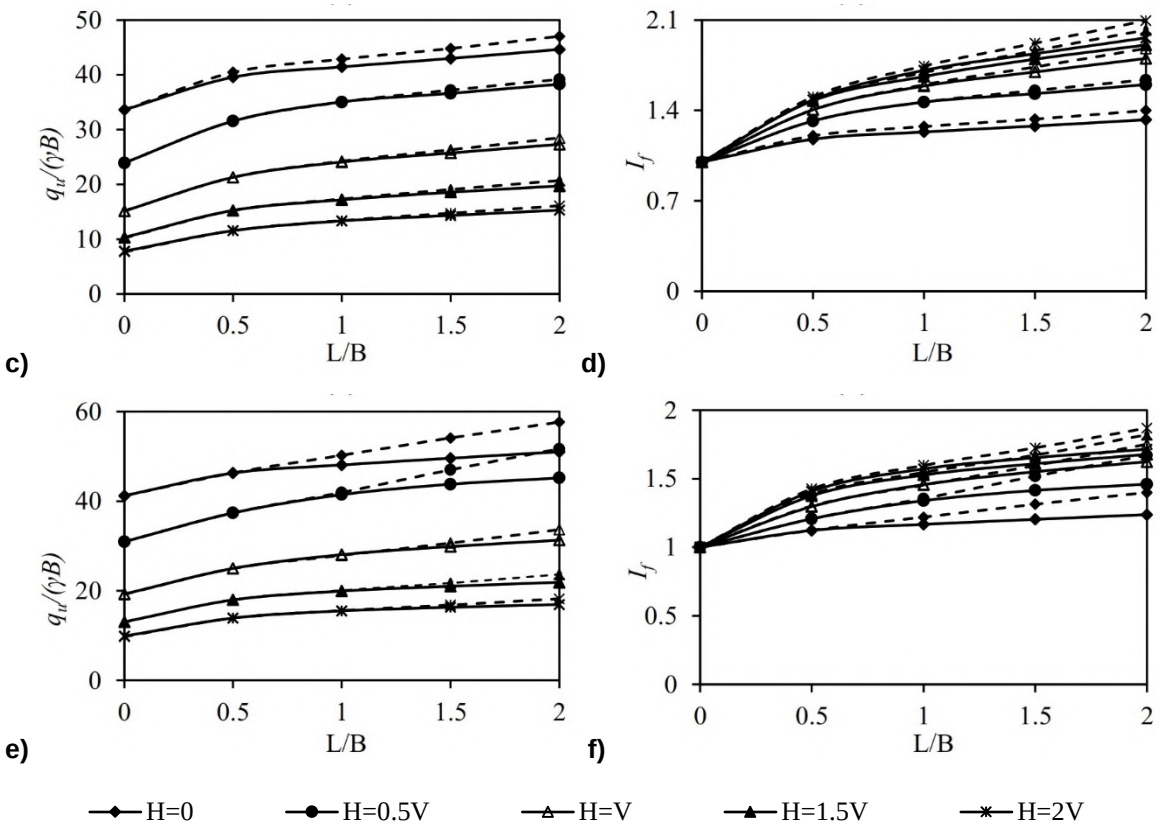


Figure 3. Variation of bearing capacity and I_f with skirt length (a) $q_u/\gamma B$, D_f/B = 0; (b) I_f, D_f/B = 0; (c) $q_u/\gamma B$, D_f/B = 0.5; (d) I_f, D_f/B = 0.5; (e) $q_u/\gamma B$, D_f/B = 1.0; (f) I_f, D_f/B = 1.

The effect of skirt length on the failure mechanism is shown in Fig. 4. It shows that the failure mechanism changes with skirt length. The failure surface is not developing clearly in strip footing, but it becomes more evident with an increase in the skirt length. The failure zone area also increases with an increase in the skirt length, which increases the bearing capacity. The change in the failure mechanism is more noticeable with the provision of the small skirt (from L/B = 0 to L/B = 0.5). The failure mechanism and shape of the shear zone do not change with skirt length. The failure zone always remains in bub shape irrespective of skirt length. However, the strip footing subjected to purely vertical loading resting on clayey soils generally shows the circular shear zone [28, 36]. The area of the failure zone progressively increases with an increase in the skirt length. It can also be seen that the failure zone moves gradually toward the right side of the skirt axis, which is also the opposite of the direction of horizontal force. It is due to the rotation of the skirt tip.

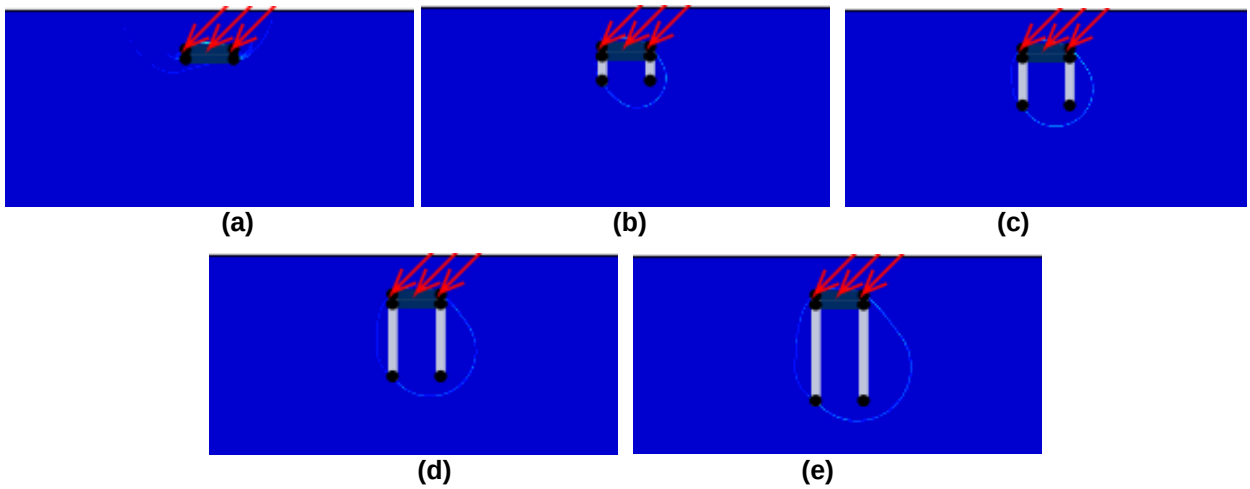


Figure 4. Effect of skirt length on failure mechanism: (a) L/B = 0, (b) L/B = 0.5, (c) L/B = 1.0, (d) L/B = 1.5, (e) L/B = 2.0.

The effect of footing depth (D_f/B) on bearing capacity and improvement for skirted footing is shown in Fig. 5. Interestingly, the bearing capacity increases and skirt efficiency reduces linearly with footing depth.

The reduction in efficiency is noticeably up to the depth of 0.5B and remains almost constant with a further increase in the depth (Fig. 5, b, d, f). The bearing capacity factor increases due to an increase in surcharge and confinement, but the effectiveness of the skirt (I_f) is reduced. The influence of embedment depth on bearing capacity and efficiency of the skirt decreases with an increase in the skirt length. The bearing capacity improvement with footing depth is substantial under purely vertical loading but diminishes with horizontal loading. The efficiency reduction is due to a decrease in the confining effect and due to the rotation of the skirt.

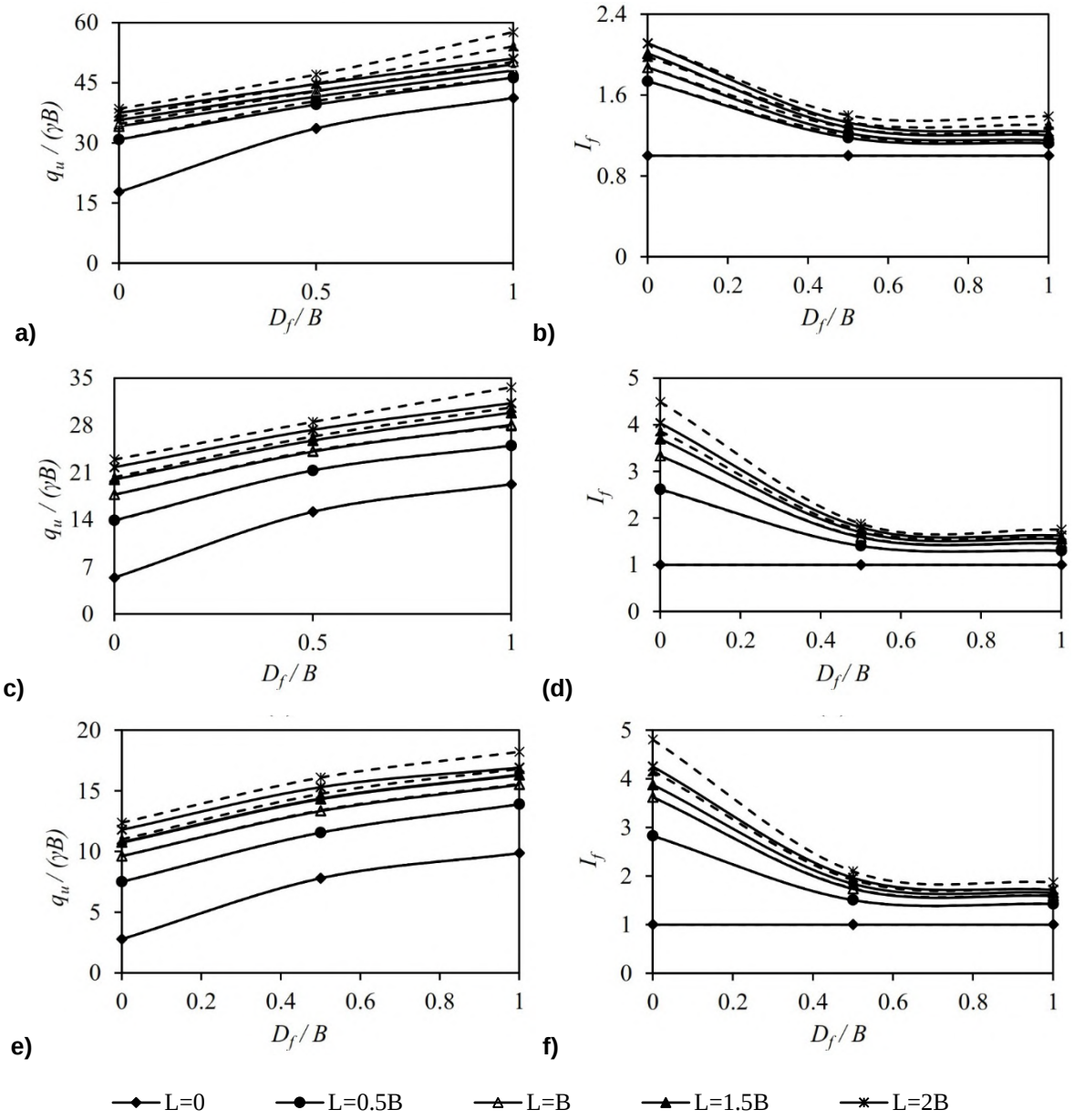
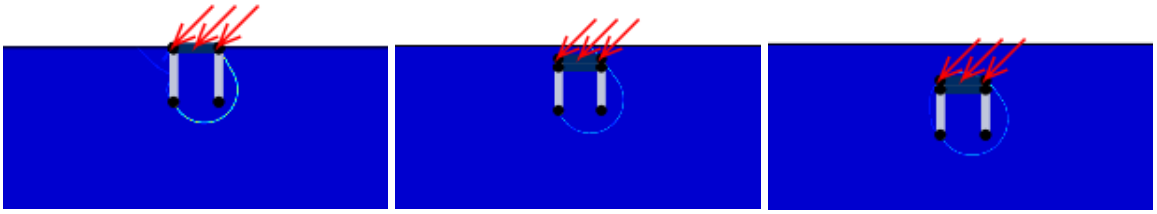


Figure 5. Variation of bearing and I_f with depth ratio: (a) $q_u/\gamma B$, H/V = 0; (b) I_f, H/V = 0; (c) $q_u/\gamma B$, H/V = 1; (d) I_f, H/V = 1; (e) $q_u/\gamma B$, H/V = 2; (f) I_f, H/V = 2.

The effect of change in footing depth on the failure surface is shown in Fig. 6. The failure mechanism remains almost unchanged with a change in the footing depth. The area of the failure zone remains almost constant, with an increase in the skirt length. With an increase in the footing depth, the surcharge on footing increases, which increases the bearing capacity (Fig. 5 a, c, e). However, the change in the failure zone area is relatively significant in strip footing, which causes a sharp increase in the bearing capacity factor compared to the skirted footing. As I_f represent the efficiency of skirt relative to strip footing, the I_f reduces with footing depth. A similar reduction in skirted footing efficiency has been observed in the skirted footing under purely vertical loading. As bearing capacity increases with increases in the footing depth, the moment acting on the skirt tips also increases, which increases the rotation of the failure surface toward the right side of the footing axis. It causes a decrease in the efficiency of the skirt.



(a) (b) (c)

Fig. 6. Effect of footing embedment depth on bearing capacity: (a) D_f/B = 0, (b) D_f/B = 0.5, (c) D_f/B = 1.0.

Fig. 7 shows that bearing capacity reduces, and the improvement factor increases with an increase in load inclination (H: V). The adverse effect of load inclination on bearing capacity is maximum for strip footing but diminishes with an increase in skirt length. The improvement factor increases linearly up to load inclination of 1; further, the increase in load inclination has only marginal influence. The bearing capacity and skirt efficiency are relatively higher for a rigid skirt than for a flexible skirt. The difference between rigid and flexible skirts becomes more noticeable with the increase in skirt length.

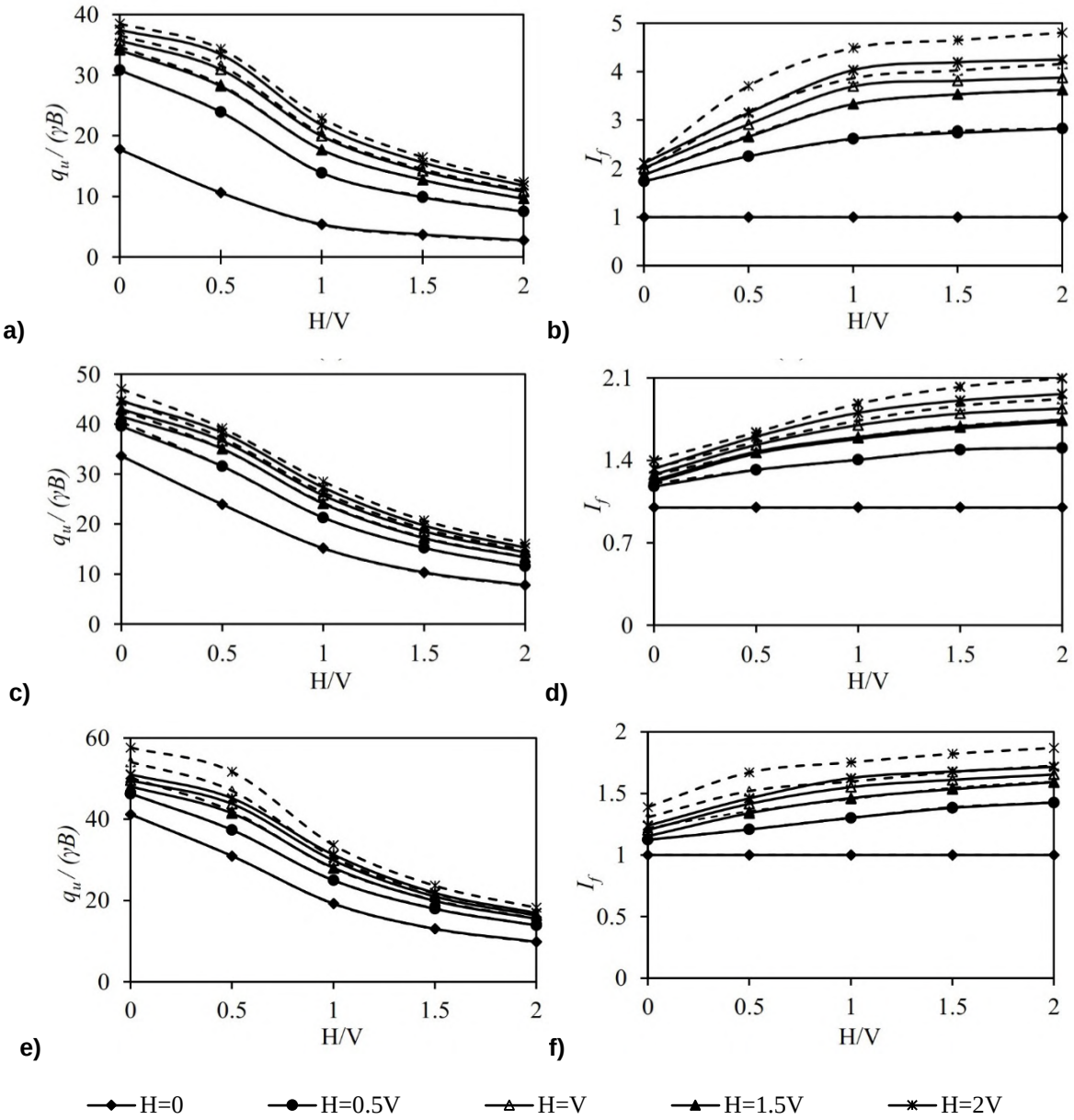


Figure 7. Variation of bearing capacity and I_f with load inclination: (a) $q_u/\gamma B$, D_f/B = 0; (b) I_f, D_f/B = 0; (c) $q_u/\gamma B$, D_f/B = 0.5; (d) I_f, D_f/B = 0.5; (e) $q_u/\gamma B$, D_f/B = 1; (f) $q_u/\gamma B$, D_f/B = 1.

The effect of load inclination on the failure mechanism is shown in Fig. 8. It shows that the failure mechanism changes abruptly from confined failure to general shear failure with a change in load inclination. The failure zone remains bulb shape, irrespective of load inclination. Increasing the load inclination reduces the failure zone gradually only. As shown in Fig. 7 (a, c, e), it leads to an almost linear decrease in the bearing capacity. However, in strip footing, the effect of load inclination on bearing capacity is more severe, and bearing capacity decreases significantly as compared to the skirted footing. As I_f represent the efficiency or normalized bearing capacity relative to strip footing, skirted footing efficiency increased with an increase in the load inclination.

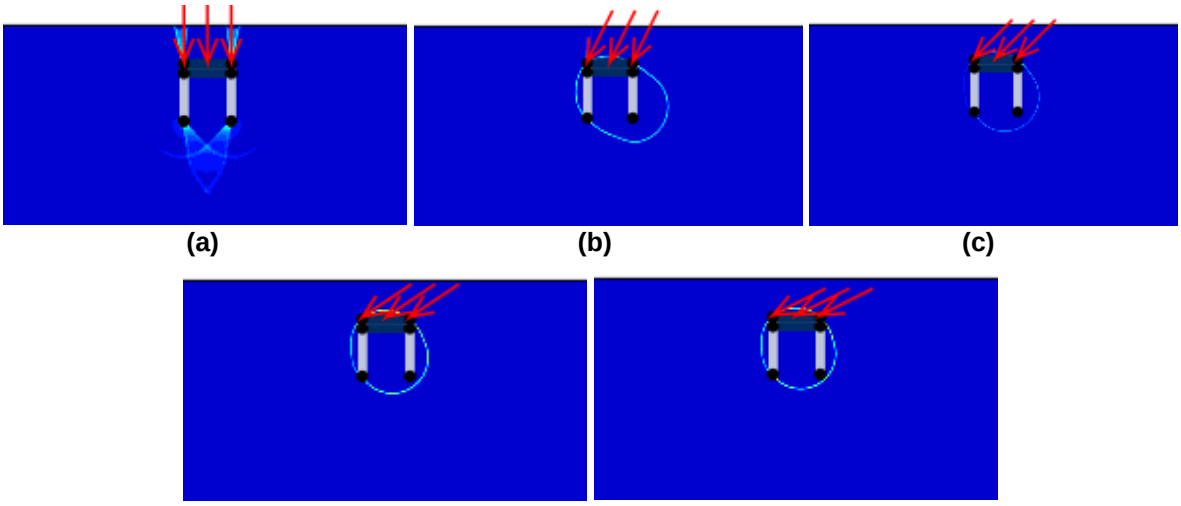
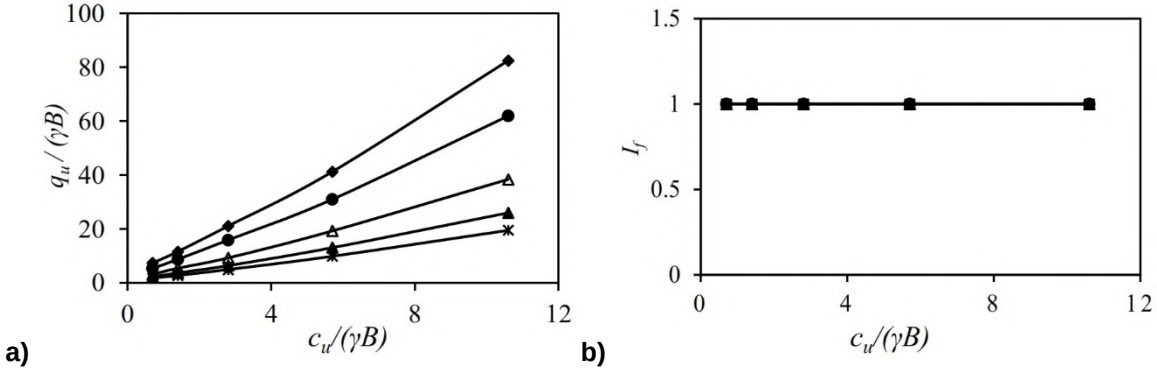


Fig. 8. Effect of load inclination on failure mechanism: (a) H/V = 0; (b) H/V = 0.5; (c) H/V = 1.0; (d) H/V = 1.5; (e) H/V = 2.

The effect of undrained strength ($c_u/\gamma B$) for a skirted footing with D/B of 1 is shown in Fig. 9. The bearing capacity increases linearly with an increase in the undrained strength of the soil. Interestingly, the improvement factor is independent of soil strength (Fig. 9, c, d, f). The rate of increase in the bearing capacity is almost linear in strip and skirted footings. Therefore, the depth factor remains independent. Earlier studies highlighted that the efficiency of the skirt is a function of soil confinement or soil density in cohesionless soils [10–14]. However, the confinement does not increase with the soil strength in cohesive soil. Therefore, the failure mechanism of skirted footing does not change with the change in soil undrained strength. The area of the failure zone also remains almost the same irrespective of soil shear strength. Consequently, skirted footing efficiency is also almost constant, increasing the undrained strength considering the other parameters constant.



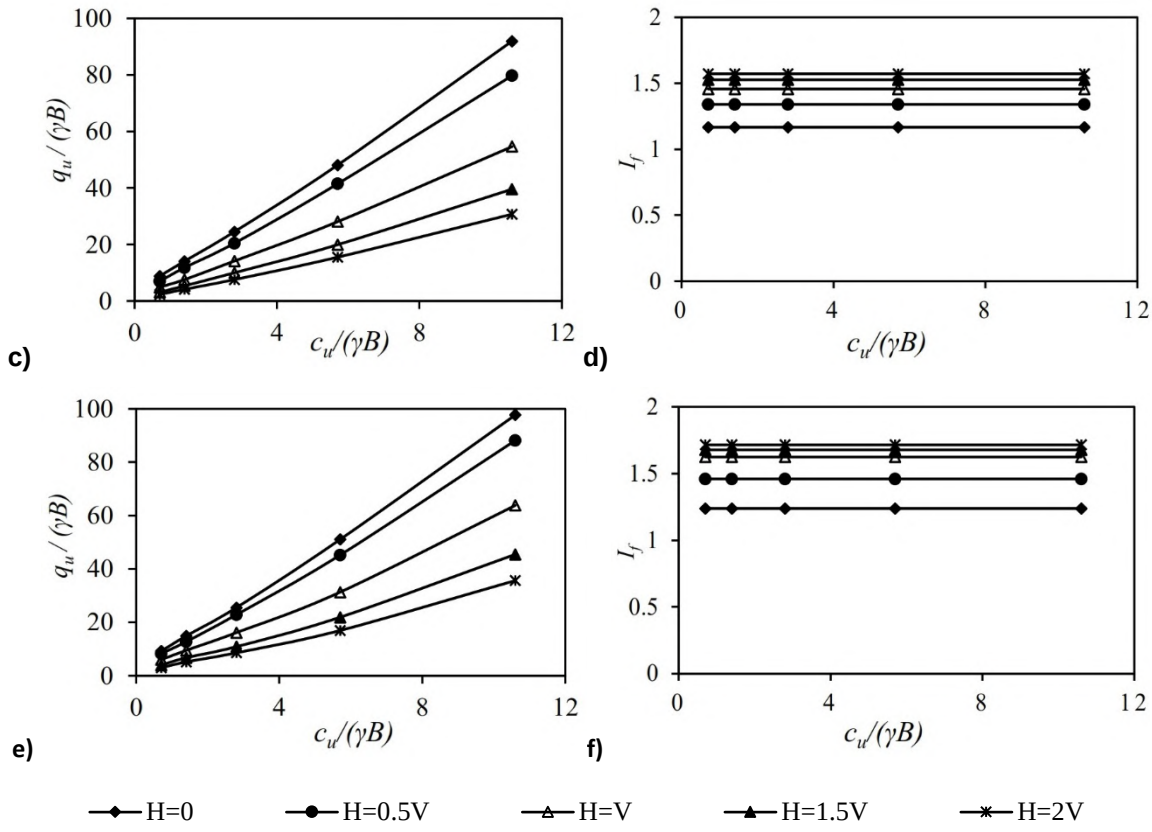


Figure 9. Variation of bearing capacity and I_f with undrained strenth: (a) $q_u/\gamma B$, L/B = 0; (b) I_f, L/B = 0; (c) $q_u/\gamma B$, L/B = 1; (d) I_f, L/B = 1; (e) $q_u/\gamma B$, L/B = 2; (f) I_f, L/B = 2.

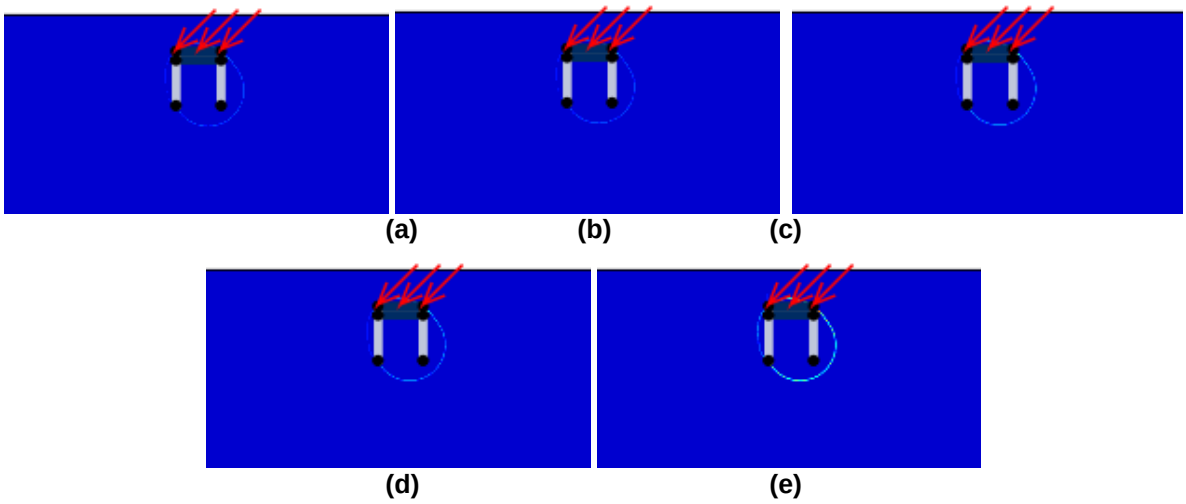


Figure 10. The effect of soil undrained strength on failure mechanism: (a) $c_u/(\gamma B)$ = 0.7, (b) $c_u/(\gamma B)$ = 0.1.4, (c) $c_u/(\gamma B)$ = 2.8, (d) $c_u/(\gamma B)$ = 5.7, (e) $c_u/(\gamma B)$ = 10.6.

4. Conclusions

The bearing capacity increases with the provision of the skirt. However, the efficiency of the skirt under inclined load is the function of many factors. The bearing capacity enhancement and the skirt's effectiveness are more visible in a rigid skirt than in a flexible skirt.

The bearing capacity and skirt effectiveness increase with skirt length. The provision of a small length skirt (L/B > 1) changes in failure mechanism and failure zone area significantly, but a further increase in the skirt length changes the failure zone progressively. The failure zone area reduces and moves opposite to the load direction with an increase in the load inclination.

The bearing capacity of skirted footing capacity reduces with increasing the load inclination. However, the effectiveness of the skirt (i.e., I_f) initially increases with an increase in the load inclination but becomes saturated for $\mathrm{H/V}$ of greater than 1.0.

The failure mechanism changes from confined failure to shear failure with increased load inclination. The bulb shape shear zone is the most prominent under inclined loading in cohesive soil.

The bearing capacity increases, and the effectiveness of the skirt reduce with footing depth. The adverse effect of footing depth on skirt efficiency intensified with skirt length. But the failure mechanism remains almost unchanged.

The bearing capacity of skirted footing increases with soil strength. However, the failure mechanism and efficacy of the skirt remain unaffected with an increase in the soil undrained strength.

References

1. Azzam, W.R. Finite element analysis of skirted foundation adjacent to sand slope under earthquake loading. HBRC Journal. 2015. 11(2). Pp. 231–239. DOI: 10.1016/j.hbrcj.2014.04.001
2. Shukla, R.P. Bearing capacity of a skirted footing on slopes. PhD thesis. Indian Institute of Technology, Roorkee, India. 2019
3. Tani, K., Craig, W.H. Bearing capacity of circular foundations on soft clay of strength increasing with depth. Soils and Found. 1995. 35 (4). Pp. 21–35. . DOI: 10.3208/sandf.35.4_21
4. Bransby, M.F., Randolph, M.F. The effect of skirted foundation shape on response to combined V-M-H Loadings. Int. J. Offshore Polar Eng. 1999. 9(3). Pp. 214–218.
5. Hu, Y., Randolph, M.F., Watson, P.G. Bearing response of skirted foundation on nonhomogeneous soil. J. Geotech. Geoenviron. Engineering. 1999. 125(11). Pp. 924–935. DOI: 10.1061/(ASCE)1090-0241(1999)125:11(924)
6. Al-Aghbari, M.Y., Mohamedzein, Y.A. Model testing of strip footings with structural skirts. Pro. of the Institution of Civil Eng.-Ground Improvement. 2004. 8(4). Pp. 171–177. DOI: 10.1680/grim.8.4.171.41844
7. Al-Aghbari, M.Y., Mohamedzein, Y.A. Improving the performance of circular foundations using structural skirts. Proceedings of the Institution of Civil Engineers-Ground Improvement. 2006. 10(3). Pp. 125–132. DOI: 10.1680/grim.2006.10.3.125
8. Randolph, M.F., Watson, P.G. Bearing response of skirted foundation on nonhomogeneous soil. J. Geotech. Geoenviron. Eng., ASCE. 1999. 125(11). Pp. 924–934. DOI: 10.1061/(ASCE)1090-0241(1999)125:11(924)
9. Yun, G., Bransby, M.F. The undrained vertical bearing capacity of skirted foundations. Soils and Foundations. 2007b. 47(3). Pp. 493–506. DOI: 10.3208/sandf.47.493
10. Al-Aghbari, M.Y., Mohamedzein, Y.A. The use of skirts to improve the performance of a footing in sand. International Journal of Geotechnical Engineering. 2018. Pp. 1–8. DOI: 10.1080/19386362.2018.1429702
11. Al-Aghbari, M.Y., Dutta, R.K. Performance of square footing with structural skirt resting on sand Geomech. Geoeng., An International Journal. 2008. 3(4). Pp. 271—277. DOI: 10.1080/17486020802509393
12. Saleh, N.M., Alsaied, A.E., Elleboudy, A.M. Behavior of skirted strip footing under eccentric load. 17th Int. Conf. on Soil Mechanics and Geotechnical Engineering, 2008. Pp. 586–589.
13. Nazir, A.K., Azzam, W.R. Improving the bearing capacity of footing on soft clay with sand pile with/without skirt. Alexandria Engineering Journal. 2010. 49. Pp. 371–377. DOI: 10.1016/j.aej.2010.06.002
14. Eid, H.T. Bearing capacity and settlement of skirted shallow foundations on sand. International Journal of Geomechanics. 2013. 13(5). Pp. 645–652. DOI: 10.1061/(ASCE)GM.1943-5622.0000237
15. EL Wakil A. Z. Bearing capacity of skirt circular footing on sand. Alexandria Engineering Journal. 2013. 52. Pp. 359–364. DOI: 10.10-16/j.aej.2013.01.007
16. Al-Aghbari, M.Y., Mohamedzein, Y.A. Bearing capacity of strip foundations with structural skirt. Geotech. Geotechnical and Geological Engineering. 2004. 22(1). Pp. 43–57. DOI: 10.1023/B:GEGE.0000013997.79473.e0
17. Mana, D.S., Gourvenec, S., Martin, C.M. Critical skirt spacing for shallow foundations under general loading. J. Geotech. Geoenviron. Engineering. 2013. 139(9). Pp. 1554–1566. DOI: 10.1061/(ASCE)GT.1943-5606.0000882
18. Mana, D.S., Gourvenec, S., Randolph, M.F. Numerical modelling of seepage beneath skirted foundations subjected to vertical uplift. Computers and Geotechnics. 2014. 55. Pp. 150–157. DOI: 10.1016/j.compgeo.2013.08.007
19. Stergiou, T., Terzis, D., Georgiadis, K. Undrained bearing capacity of tripod skirted foundations under eccentric loading. Geotechnik. 2015. 38(1). Pp. 17–27. DOI: 10.1002/gete.201400029
20. Azzam, W.R. Finite element analysis of skirted foundation adjacent to sand slope under earthquake loading. HBRC Journal. 2015. 11(2). Pp. 231–239. DOI: 10.1016/j.hbrcj.2014.04.001
21. Bransby, M.F., Yun, G. J. The undrained capacity of skirted strip foundations under combined loading. Geotechnique. 2009. 59(2). Pp. 115–125. DOI: 10.1680/geot.2007.00098
22. Vulpe, C. Design method for the undrained capacity of skirted circular foundations under combined loading: effect of deformable soil plug. Géotechnique. 2015. 65(8). Pp. 669–683. . DOI: 10.1680/geot.14. P.200
23. Chetia, N., Saikia, B.D. Improvement of bearing capacity of model footing with structural skirts on soft ground. 50th IGC, 17-19 DECEMBER 2015, Pune, Maharashtra, India. 2015.
24. Park, J.S., Park, D., Yoo, J.K. Vertical bearing capacity of bucket foundations in sand. Ocean Engineering. 2016. 121. Pp. 453–461. DOI: 10.1016/j.oceaneng.2016.05.056
25. Zhang, P., Ding, H. Bearing capacity of the bucket spudcan foundation for offshore jack-up drilling platforms. Petroleum Exploration and Development. 2011. 38(2). Pp. 237–242. DOI: 10.1016/S1876-3804(11)60029-3
26. Mana, D.S., Gourvenec, S.M., Randolph, M.F., Hossain, M.S. Failure mechanisms of skirted foundations in uplift and compression. International Journal of Physical Modelling in Geotechnics. 2012. 12(2). Pp. 47–62. DOI: 10.1680/ijpmg.11.00007
27. Chen, W., Randolph, M.F. External radial stress changes and axial capacity for suction caissons in soft clay. Géotechnique. 2007. 57(6). Pp. 499–511. DOI: 10.1680/geot.2007.57.6.499

28. Shukla, R.P., Jakka, R.S. Determination and prediction of bearing capacity on clayey slopes. Acta Geotechnica Slovanica. 2019. 16(2). Pp. 50–65. DOI: 10.18690/actageotechslov.16.2.50-65.2019
29. Shukla, R.P., Jakka, R.S. Failure mechanism and slope factors for a footing resting on slopes. Magazine of Civil Engineering. 2021. 104 (04). Pp. 1-15. DOI: 10.34910/MCE.104.1
30. Terzaghi, K., R.B. Peck (1948). Soil Mechanics in Engineering Practice. John Wiley & Sons. Inc., New York.
31. Yin, J.H., Wang, Y.J., Selvadurai, A.P.S. Influence of nonassociativity on the bearing capacity of a strip footing. Journal of geotechnical and geoenvironmental engineering. 2001. 127(11). Pp. 985–989. DOI: 10.1061/(ASCE)1090-0241(2001)127:11(985)
32. Terzaghi, K. Theoretical Soil Mechanics, Wiley, New York. 1943.
33. Meyerhof, G.G. (1965). Shallow Foundations. J. Soil Mech. Found. Eng., ASCE, 91(SM2). Pp. 21–31.
34. Kusakabe, O., Kimura, T., Yamaguchi, H. Bearing capacity of slopes under strip loads on the top surfaces. Soils and foundations. 1981. 21(4). 29–40. DOI: 10.3208/sandf1972.21.4_29
35. Lyamin, A.V., Salgado, R., Sloan, S.W., Prezzi, M.Two-and three-dimensional bearing capacity of footings in sand. Géotechnique. 2007. 57(8). 647–662. DOI: 10.1680/geot.2007.57.8.647
36. Griffiths, D.V., Fenton, G.A., Manoharan, N. Bearing capacity of rough rigid strip footing on cohesive soil: probabilistic study. Journal of Geotechnical and Geoenvironmental Engineering. 2002. 128(9). Pp. 743–755. DOI: 10.1061/(ASCE)1090-0241(20-02)128:9(743)

Contacts:

Rajesh Prasad Shukla, rpshukla.2013@iitkalumni.org

Received 17.11.2020. Approved after reviewing 20.04.2021. Accepted 22.04.2021.



Magazine of Civil Engineering

ISSN 2712-8172

journal homepage: http://engstroy.spbstu.ru/

DOI: 10.34910/MCE.110.13

Pile group effect at vertical vibrations

A.O. Kolesnikov*[a] ✉, ***V.N. Popov*[b]**, ***T.N. Kostiuk*[a]**

[a] *Novosibirsk State University of Architecture and Civil Engineering (Sibstrin), Novosibirsk, Russia*

[b] *Khristianovich Institute of Theoretical and Applied Mechanics SB RAS, Novosibirsk, Russia*

**E-mail: ao_kolesnikov@mail.ru*

Keywords: piles, pile groups, soil-pile interaction, soil analysis, soil modulus, wave model, half space

Abstract. Analysis of the applicability of wave model solution to evaluate the variation of the dynamic stiffness in the pile foundation versus the distance between piles at the vertical vibrations; both experimental data from references and our own measurements in field are involved. To justify the reliability of the solutions of the wave models used to determine the dynamic stiffness values of the pile foundations at the vertical vibrations, we use the data obtained experimentally for the determination of natural frequencies in the cap-bound groups. The data obtained for the natural frequencies of 3×3 floating piles with different distances between them are considered. In addition, the data found at the forced vertical vibrations of the cap-bound groups of 2×2 piles under different loads and at different distances between the piles are involved. Processing of available amplitude-frequency curves involves the solution of the inverse problem with the theory of nonlinear vibrations to determine the parameters of the "pile group – soil" system, namely the effective mass, stiffness, and damping. The correlation between the measured and predicted data is evaluated by using the data obtained at the description of the pile groups in soil behavior. It has been found that the relations obtained at the solution of wave models and used to calculate the dynamic stiffness at the vertical vibrations of pile foundations consider the mutual effect of the piles in the group and permit satisfactory accuracy of the results. The maximum discrepancy between the results and experimental data is 15 %.

1. Introduction

High accuracy of the evaluated characteristics of the vibrations in the pile foundations installed under the machines with dynamic loadings is always a topical task [1–25]. The dynamic interaction between the pile and pile foundation and soil is among the least understood issues, and the combined effect of grouped piles makes it even more complex. In the cases when the distance between piles is large, the group stiffness can be evaluated via simple summing up the stiffnesses of individual piles. However, the piles located close to each other demonstrate the essential mutual effect and finally their efficiency may change considerably. To evaluate the dynamic interaction of the piles, both between each other and with the soil, the theories describing the processes and experiments, and experimental researches are necessary to verify their applicability.

Note that the activities to determine the amplitude-frequency characteristics of the pile foundations have been performed for a long time but still are far from over. The accurate theoretical solution of the problem of the dynamic interaction between the pile and soil is complicated by the non-linear character of the process, thus approximate approaches are applied. Particularly, the approaches proposed in [9–12] are among them. Many researches are devoted to the interaction of one pile with the soil under the dynamic loading, but at the same time, the behavior of pile groups is studied, too. Numerical simulation methods involving finite or boundary elements are commonly used to evaluate the dynamic condition of pile structures in complex application environment [16–19].

Kolesnikov, A.O., Popov, V.N., Kostiuk, T.N. Pile group effect at vertical vibrations. Magazine of Civil Engineering. 2022. 110(2). Article No. 11013. DOI: 10.34910/MCE.110.13

© Kolesnikov, A.O., Popov, V.N., Kostiuk, T.N., 2022. Published by Peter the Great St. Petersburg Polytechnic University.

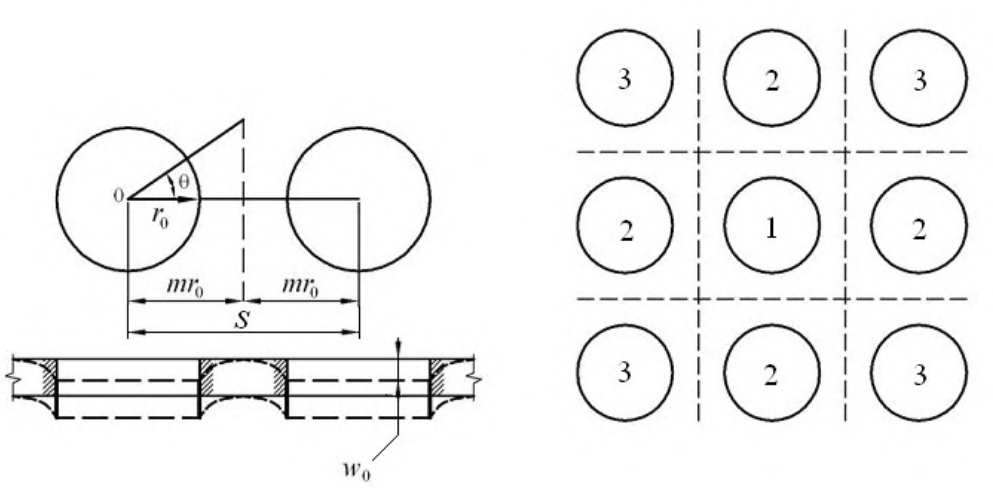
This work is licensed under a CC BY-NC 4.0

For most engineering tasks, the interaction between the pile and soil is usually successfully explained by the elasticity theory and, as is shown by many theoretical and experimental works, wave models simulate quite accurately the vibration process of the pile foundations in soil [1–5, 14, 25]. The Lamb analysis of the reactions of the semi-infinite elastic medium excited by a periodical vertical force acting along the vertical axis is the first investigation in this field (1904) [26]. Today, the solutions found for the tasks of the vibrating infinite plate with a round cut are used successfully to determine the amplitude-frequency characteristics of the pile foundations under the dynamic loadings [14]. However, generalization of this result for the cases when there is more than one cut is of practical interest. To find the link between motions and reactions on the side surface of embedded solid bodies, either in-lined or grouped, the authors of [16, 27, 28] proposed the solution for the task with the vertical vibrations of the plate with several round cuts; they also derived the formulas to find the stiffness and damping characteristics of the system (see schematic in Fig. 1). But the issue of reliability and accuracy of these results still remains open.

In view of this, the present work analizes the wave model solution applied to the evaluation of the dynamic stiffnesses varying of the pile foundations at the vertical vibrations, with due regard to the distance between piles; we use the theoretical evaluations from [27, 28] and compare them with the experimental data from references [7–9, 29, 30]. The results of series of field experiments performed by the authors are considered; the experiments aim to determine the natural frequencies of the pile foundations with floating cap-bound pile groups 3×3 ($s/d = m =$ 2, 3, 5, d is the pile diameter, s is the distance between central axes of neighboring piles) [29, 30]. The results obtained experimentally are compared with theoretical solutions. Along with it, the measurement results obtained in field for the forced vertical vibration of the cap-bound pile groups 2×2 at $s/d = m = 2, 3, 4$ and under different loadings are considered [7–9]. The effective mass, stiffness, and damping of the pile system in soil are determined by the measured non-linear amplitude-frequency characteristics at the inverse task solution. Then, the theory of non-linear vibrations is used to calculate the amplitude-frequency curves which are then compared with experimental results.

2. Methods

Agreement between the measured and predicted data was evaluated for the description of the non-linear behavior of the pile and soil system regarding the distances between piles.



a **b**

Figure 1. Arrangement of cuts in a wavering thin plate: a) two neighboring ones, b) according to the 3×3 scheme.

In [14], considering warping axisymmetric vibrations of the infinitely thin layer with one round cut (radius r_0) described by the equation of motion of the elastic medium at zero volume forces in the cylindrical system of coordinates (r,t) as

$$\frac{\mu}{r}\frac{\partial}{\partial r}r\frac{\partial w}{\partial r}=\rho\frac{\partial^2 w}{\partial t^2},$$

with the boundary condition on the contour

$$w(r_0,\theta,t)=w_0e^{i\omega t},$$

the authors determine that the reaction of the single-thickness soil layer applied to the pile side surface is described as

$$S_{w0}(kr_0)w_0e^{i\omega t}=\mu w_0e^{i\omega t}(S_{w1,0}+iS_{w2,0}),$$

where the real $S_{w1,0}$ and imaginary $S_{w2,0}$ dimensionless parts of S_{w0} can be presented as

$$\begin{aligned}S_{w1,0}(kr_0)&=2\pi kr_0\frac{J_0(kr_0)J_1(kr_0)+Y_0(kr_0)Y_1(kr_0)}{J_0^2(kr_0)+Y_0^2(kr_0)},\\ S_{w2,0}(kr_0)&=\frac{4}{J_0^2(kr_0)+Y_0^2(kr_0)}.\end{aligned}\quad(1)$$

Here, J_n,Y_n are the Bessel 1st and 2nd kind functions, $w=w(r,t)$ is the motion along the axis z, ρ is the density; $\mu=V_s^2\rho$ is the Lame coefficient, $k=\omega/\sqrt{\mu/\rho}$.

The warping vibrations of the layer with several round cuts in line are described in [16]; the cuts radii are r_0, the centers are located within the distance of $s=2r_0m$ or m diameters from each other, $m>1$ (see schematic in Figure 1a), as well as for the inner cut in line as is shown in Figure 1b, for which the reaction of the single-thickness soil layer attached to the pile side surface is, according to [27],

$$S_{w1}(kr_0,kr_g)w_0e^{i\omega t}=\mu w_0e^{i\omega t}(S_{w1,1}+iS_{w2,1}),$$

where, $r_g=mr_0$, and $S_{w1,1},S_{w2,1}$ are the real and imaginary dimensionless components, so S_{w1} can be presented as

$$S_{w1,1}(kr_0,kr_g)=S_{w1,0}-\frac{3}{2}S_{w1cor}(kr_0,kr_g),$$

$$S_{w2,1}(kr_0,kr_g)=S_{w2,0}-\frac{3}{2}S_{w2cor}(kr_0,kr_g),$$

$$S_{w1cor}(kr_0,kr_g)=\pi kr_0\frac{J_0(kr_0)J_1(kr_g)+Y_0(kr_0)Y_1(kr_g)}{J_0^2(kr_0)+Y_0^2(kr_0)}C,$$

$$S_{w2cor}(kr_0,kr_g)=\pi kr_0\frac{Y_0(kr_0)J_1(kr_g)+J_0(kr_0)Y_1(kr_g)}{J_0^2(kr_0)+Y_0^2(kr_0)}C,$$

$$C=\frac{\sum_{n=1}^{2}J_{2n-1}(kr_0)\left[Y_{2n-2}(kr_0)-Y_{2n}(kr_0)\right]-Y_{2n-1}(kr_0)\left[Y_{2n-2}(kr_0)-Y_{2n}(kr_0)\right]}{\sum_{n=1}^{2}J_{2n-1}(kr_0)\left[Y_{2n-2}(kr_g)-Y_{2n}(kr_g)\right]-Y_{2n-1}(kr_0)\left[Y_{2n-2}(kr_g)-Y_{2n}(kr_g)\right]},$$

here, opposite to (1), there are additive terms regarding the effect of neighboring cuts.

The expressions describing the reaction of the boundary (not corner) cut (schematic in Fig. 1b) were found in [28]

$$S_{w2}(kr_0,kr_g)w_0e^{i\omega t}=\mu w_0e^{i\omega t}(S_{w1,2}+iS_{w2,2}),$$

$$S_{w1,2}(kr_0, kr_g) = S_{w1,0}(kr_0) - \frac{5}{4} S_{w1cor}(kr_0, kr_g),$$

$$S_{w2,2}(kr_0, kr_g) = S_{w2,0}(kr_0) - \frac{5}{4} S_{w2cor}(kr_0, kr_g),$$

and for the corner cut

$$S_{w3}(kr_0, kr_g) w_0 e^{i\omega t} = \mu w_0 e^{i\omega t} (S_{w1,3} + iS_{w2,3}),$$

$$S_{w1,3}(kr_0, kr_g) = S_{w1,0}(kr_0) - \frac{7}{8} S_{w1cor}(kr_0, kr_g),$$

$$S_{w2,3}(kr_0, kr_g) = S_{w2,0}(kr_0) - \frac{7}{8} S_{w2cor}(kr_0, kr_g).$$

Thus, the dynamic stiffnesses S_{wj} are described by the complex functions which depend on the vibration frequency ω, cut size r_0. The reactions go ahead the respective motions by time intervals Δ_j which are found in accordance with $\Delta_j = \arctan(S_{w2j} / S_{w1j})$. The parameters characterizing the motion amplitude can be estimated from the relation $A_j = (S_{w1j}^2 + S_{w2j}^2)^{0.5}$.

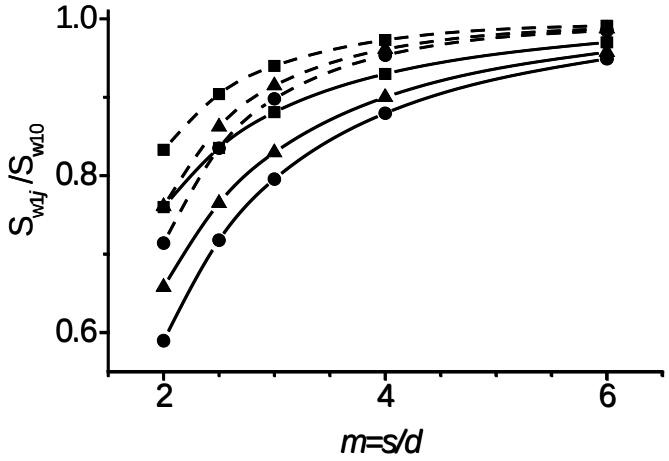


Figure 2. Variation of the relative stiffness at $kr_0 =$ 0.05 (dashed curves) and $kr_0 =$0.35 (solid curves) from the distance between the piles and their position in a group • (*j*=1), ▲ (*j*=2), ■ (*j* = 3)

Fig. 2 illustrates the variation of the relative dynamic stiffness S_{w1j} / S_{w10}, $j = 1$, 2, 3 at $kr_0 =$0.05, 0.35 versus the distance between the piles and their position in the group in accordance with the schematic in Fig. 1b. The presented results lead to the conclusion that the reducing distance between the piles may cause the stiffness reduction up to 40 %.

To verify the presented theoretical evaluations of the dynamic interaction for the “pile-soil” system, the results of a series of field measurements are used; the experiments were carried out with the cap-bound groups of hanging piles 3×3 (schematics in Fig. 3 and Fig. 1b) and were purposed to determine the natural frequencies of the pile foundations. All three test pile foundations were made as a monolithic reinforced cap with the sizes 1.0×1.0×0.2 m supported by 9 rigidly fastened piles with the diameter $d =$ 76 mm $(r_0 = d/2)$, the working length $h =$1.4 m; the piles are made from metal tubes, with the wall thickness of 3.5 mm. The distance between pile axes was 2*d*, 3*d* and 5*d*. Mass of the whole structure was $M =$ 690 kg. The cap has no contact with the soil. The impulse loading was carried out by a steel ballast – a 6 kg parallelepiped freely falling on the surface of each tested pile foundation from the height of 0.5 m.

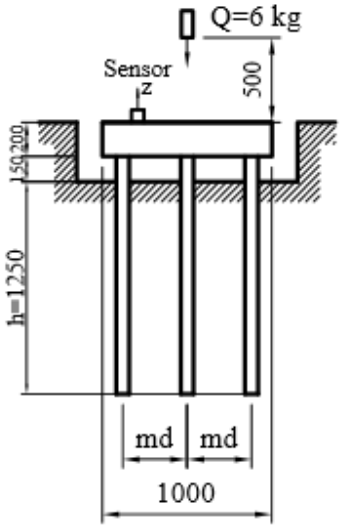


Figure 3. Schematics of experimental researches of tested foundations.

The soil is the test field contained down to 9.3 m from slightly wet loessial sand clay, the density $\rho = 17.0$ kN/m^3 and deformation modulus $E =$ 14 MPa, medium-hard loam is the sub-soil. No ground water in the field. The value of the cross waves rate for the test field soil was found experimentally as $V_s =$ 146 m/s.

Investigation results obtained in the experimental field [29, 30] to determine the natural frequencies of foundations are presented in Fig. 4 and in Table 1.

Table 1. Measured natural frequencies.

Distance between piles	Measured frequency f_z, Hz (the average value) [29, 30]
2*d*	82.90
3*d*	91.36
5*d*	101.05

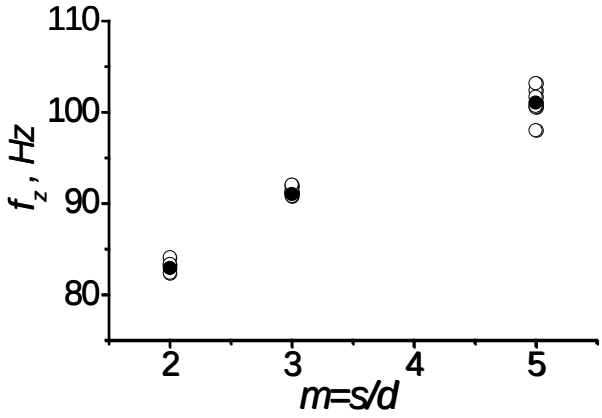


Figure 4. Measured natural frequencies of the pile foundations 3×3 at different s/d o – experiment, • – average value [29, 30].

The natural frequencies λ_z at the vertical vibrations of the pile foundations and stiffness K_z, in the presence of damping, are related as

$$\lambda_z = 2\pi f_z \approx \sqrt{K_z / M}, \quad K_z \approx \lambda_z^2 M,$$

where, M is the mass of the whole structure.

The stiffnesses of the pile groups were found for various s involving the measurement results from Table 1 and formula

$$K_z^g(m) = [2\pi f_z(m)]^2 M \quad (2)$$

Theoretical evaluations of the stiffness for the pile groups were found with the relations

$$K_z^g(m) = GhS_{w1}^g(kr_0, mkr_0) \quad (3)$$

hence it follows that the value of the grouped pile stiffness factor S_{w1}^g is related to the dimensionless frequency of vibrations kr_0 and pile position in the cap. For the considered pile foundations from 3×3 piles, S_{w1}^g is determined in accordance with the schematic in Fig. 1b by the formula

$$S_{w1}^g(kr_0, mkr_0) = S_{w1,1}(kr_0, mkr_0) + 4S_{w1,2}(kr_0, mkr_0) + 4S_{w1,3}(kr_0, mkr_0),$$

where $m = s/d$, $k = \omega/V_s$, ω is the angular frequency of vibrations, V_s is the rate of transversal waves in soil, $G = V_s^2\rho = \mu$ is the shear modulus. In the cases under consideration, the dimensionless vibration frequency $kr_0 = 0.15$ is the average value within the range from 0.13 to 0.17.

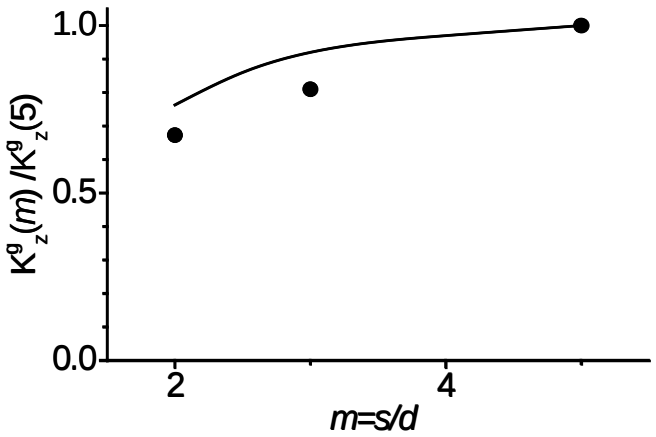


Figure 5. Changes in system stiffness versus the distance between piles (solid line – result of calculation, • –experiment [29, 30]).

The results obtained by the engineering calculations involving formulas (2), (3) are shown in Fig. 5. The calculated curve and dots illustrate the varying stiffnesses in respect to the value at $s/d = 5$. The values of the natural frequencies of the foundations with different distances between piles found by the formula (3) show the maximal difference with the test data, which is below 14 %. This result proves that the calculations in the framework of the used approximations permit obtaining the satisfactory agreement with experimental findings [29, 30].

In order to determine the dynamic stiffness and damping at the vertical vibrations of the pile-soil system, the inverse task [31] was solved involving the theory of non-linear vibrations at the processing of the amplitude-frequency curves available in [7, 8]. First, the effective mass, stiffness and damping are determined by the measured values of the vibration amplitudes and frequencies. Then, these parameters are used to verify the obtained formulas by means of comparison of the calculation and dynamic test results in the field for the frequencies and amplitudes of the vibrations of the cap-bound 2×2 floating piles [7–9].

Let us consider the action of the harmonically changing force with the amplitude proportional to the frequency square ω on the pile foundation

$$P_z = r_e m_e \omega^2,$$

then the motion equation can be written for the system under consideration as follows

$$M\ddot{z} + \Phi K_z \dot{z} + K_z z = m_e r_e \omega^2 \sin \omega t.$$

Here, M is the effective mass which includes M_0 and the mass of the attached soil vibrating together with the pile foundation. The solution of this equation is written as

$$z = \frac{m_e r_e \omega^2}{\sqrt{(K_z - M\omega^2)^2 + (K_z \Phi \omega)^2}} \sin \omega t$$

whereas the variation of the maximal amplitude A is described by the formula

$$A = \frac{m_e r_e}{M} \frac{\omega^2}{\sqrt{(K_z / M - \omega^2)^2 + (\Phi \omega K_z / M)^2}}. \quad (4)$$

It follows from (4) that the amplitude depends on the impact force frequency in a complex manner. In the onset regime, the vibration amplitude is $A_\infty = m_e r_e / M$ Before the system comes into the onset regime, the resonance is possible

$$A_{res} = \frac{A_\infty}{\Phi \sqrt{(K_z / M)(1 - \Phi^2 K_z / 4M)}}, \quad (5)$$

at the frequency

$$\omega_{res} = \sqrt{\frac{K_z / M}{1 - \Phi^2 K_z / 2M}}, \quad \Phi^2 K_z / M < 2. \quad (6)$$

The relations (5), (6) permit evaluating Φ and K_z / M , if the values A_{res} and f_{res} ($\omega_{res} = 2\pi f_{res}$) are found during the measurements on site

$$K_z / M = \omega_{res}^2 \sqrt{1 - \left(A_\infty / A_{res}\right)^2}, \quad \Phi = \omega_{res}^{-1} \sqrt{\frac{2 - 2\sqrt{1 - \left(A_\infty / A_{res}\right)^2}}{\sqrt{1 - \left(A_\infty / A_{res}\right)^2}}}.$$

The performed experimental investigations focused on determination of the vibration frequencies and amplitudes of the groups of cap-bound floating 2×2 piles at different values of the vertical harmonic action [7–9]. All experimental foundations were made as a monolithic reinforced cap with overall sizes 0.57×0.57×0.25 m supported by 4 rigidly fixed concrete piles with the diameter $d =$ 100 mm, the working length $h =$ 1.5 m. The distance between the pile axes s was 2d, 3d and 4d. The caps do not touch the soil. The tests were carried out at different eccentric momenta $m_e r_e =$ 0.0187; 0.0278; 0.0366 and 0.0450 where m_e is the mass of the eccentric rotary element in the vibrator, and r_e are the mass eccentricities. The methodology of the vibration tests is described in [8]. The mass of each foundation is $M =$ 1200 kg including the rotary element mass. The shear modulus value G of the experimental field soil is from $14 \cdot 10^6$ N/m^2 to $26 \cdot 10^6$ N/m^2, the transverse wave V_s velocities lie in the range of 95–150 m/s, they depend on the depth [9]. Table 2 presents the determined resonance frequencies f_{res} and amplitudes A_{res}.

Table 2. Resonant frequencies f_{res} and amplitudes A_{res}.

$m_e r_e$, kg·m	s/d = 2		s/d = 3		s/d = 4	
	A_{res}, (μm)	f_{res}, (Hz)	A_{res}, (μm)	f_{res}, (Hz)	A_{res}, (μm)	f_{res}, (Hz)
0.0187	0.0358	29.61	0.0317	35.45	0.0262	38.21
0.0278	0.0510	29.22	0.0422	34.41	0.0381	36.71
0.0366	0.0633	28.95	0.0589	33.35	0.0501	35.18
0.0450	0.0832	28.46	0.0707	32.73	0.0619	33.50

The data from Table 2 with the resonance frequencies f_{res} and amplitudes A_{res} $(s = 4d)$ are used to determine the values of K_z^g / M and Φ for the pile group at different s. The results of calculation are given in Table 3.

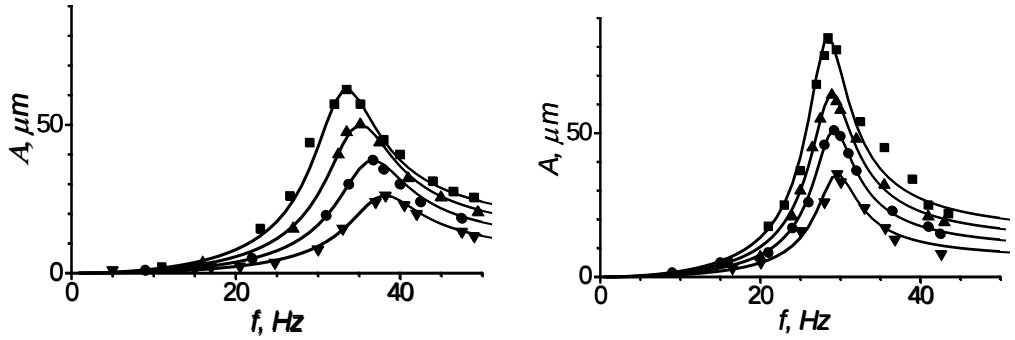
Table 3. Calculated K_z^g / M ***and*** Φ***.***

$m_e r_e$,	$s/d = 2$		$s/d = 3$		$s/d = 4$	
(kg·m)	K_z^g / M, (1/s²)	Φ, (s)	K_z^g / M, (1/s²)	Φ, (s)	K_z^g / M, (1/s²)	Φ, (s)
0.0187	$3.41 \cdot 10^4$	$0.89 \cdot 10^{-3}$	$4.88 \cdot 10^4$	$0.84 \cdot 10^{-3}$	$5.62 \cdot 10^4$	$0.95 \cdot 10^{-3}$
0.0278	$3.32 \cdot 10^4$	$0.94 \cdot 10^{-3}$	$4.57 \cdot 10^4$	$0.97 \cdot 10^{-3}$	$5.18 \cdot 10^4$	$1.00 \cdot 10^{-3}$
0.0366	$3.25 \cdot 10^4$	$1.01 \cdot 10^{-3}$	$4.31 \cdot 10^4$	$0.94 \cdot 10^{-3}$	$4.71 \cdot 10^4$	$1.05 \cdot 10^{-3}$
0.0450	$3.15 \cdot 10^4$	$0.96 \cdot 10^{-3}$	$4.14 \cdot 10^4$	$0.98 \cdot 10^{-3}$	$5.31 \cdot 10^4$	$1.10 \cdot 10^{-3}$

As we know $m_e r_e$, according to [28], the effective mass M can be evaluated involving the experimental values for A_∞ – $M = m_e r_e / A_\infty$, and then it should be specified for further calculations. The resulting M is 3200 kg that is much bigger than the mass of the structure $M_0 =$ 1200 kg. This result is in good agreement with the estimations of the effective mass presented in [7, 8] which were obtained by another method [32].

3. Results and Discussion

Figure 6a presents the non-linear amplitude-frequency curves calculated with the found K_z^g / M and Φ at different $m_e r_e$ [7, 8] for the pile group at $s = 4d$. Extra calculations were made for $s = 2d$ at $M = 3200$ kg and respective values of K_z^g / M and Φ as an extra verification (Fig. 6b).



a **b**

Figure 6. Experimental and calculated frequency curves of the pile group 2×2 at *s* = 4*d* (a), at *s* = 2*d* (b), for different values $m_e r_e =$ 0.0187 (▼), 0.0278 (●), 0.0366 (▲), 0.0450 (■) (kg·m) [7, 8] (curves – results of calculations)

The data presented in Fig. 6 show that the theoretical results satisfactory agree with the measurement data from the references [7, 8].

The values of K_z^g / M for the pile group permit evaluating the natural frequencies λ_z at the vertical vibrations pile foundations and damping – $\lambda_z \approx \sqrt{K_z / M}$ The results given in Table 4 lead to the conclusion that the natural frequencies drop as the excitation intensity rises, which agrees with the conclusions of [31] about the non-linear behavior of the considered "piles-soil" system. The decay modulus varies weakly, its average value is evaluated as $\Phi \approx 0.97 \cdot 10^{-3}$ s. Comparison with the experiment proves that the analytical methods permit describing the major peculiarities of the amplitude-frequency behavior of the pile groups at low vertical vibrational actions. In the considered cases, the effective mass and damping

preserve their values as the excitation intensity rises. Fig. 7 presents the variation of the dynamic stiffness determined by the experimental results in respect to the maximal value at $s/d = 4$.

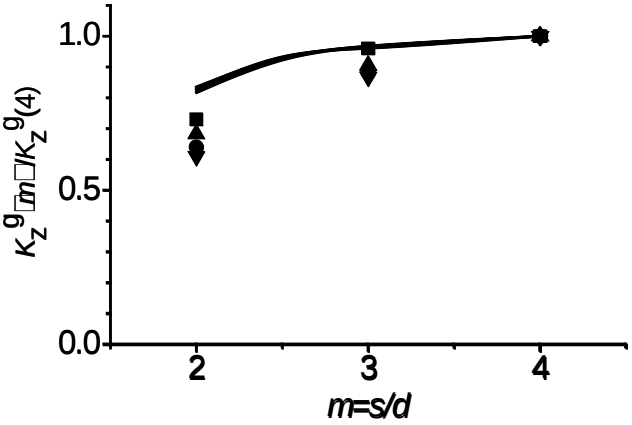


Figure 7. Variation of the relative stiffness of the pile group 2×2 versus the distance between the piles in the group: experiment at different values $m_e r_e$ = 0.0187 (▼), 0.0278 (•), 0.0366 (▲), 0.0450 (■) (kg·m) [8], (curves – computation results)

Theoretical evaluation of the stiffness for the pile group is found with the relations

$$K_z^g(m) = 4GhS_{1,3}(kr_0, mkr_0),$$

at the dimensionless vibration frequency $kr_0 =$ 0.08, the average value within the range 0.06–0.1. The closely spaced curves in Fig. 7 illustrate the variation of the computed stiffnesses in respect to the maximal value at $s/d = m = 4$ for different $m_e r_e$.

It follows from the comparison of the theoretical evaluation and experimental findings that the considered analytical method permits predicting the peculiarities of the dynamic interaction between the piles in the group. The maximal difference between the experimental results and theoretical evaluations which involves the interaction effect between the piles under the action of the vertical vibration loadings is about 15 % at $s/d = 2$, whereas at $s/d = 3$, the difference in results is maximum 5 %. Note at the same time that we ignore the interaction with soil under the pile end, which may be essential. However, the final conclusion of the satisfactory agreement of the calculation and experiment [7, 8] is valid; it is evident though that the development of theoretical evaluations of the interaction of pile groups between each other and soil needs further improvement. Experimental data obtained after the tests with full-scale pile foundations in the field conditions should be involved.

4. Conclusions

1. The results obtained from engineering calculations involving analytical expressions to determine the natural frequencies of the foundations with different distances between piles have the maximal disagreement with the experimental findings of 14 %, which proves the adequacy of the used approximations.

2. The analytical methods under consideration permit predicting the major peculiarities of the interaction between piles in a group under the action of vertical vibration loadings on the foundation. The maximal difference between the experimental data and theoretical evaluations which consider the effect of pile interaction is about 15 % at $s/d = 2$ and is maximum 5 % at $s/d = 3$.

3. At the solution of the inverse task, use of the measured values of the foundation vibration amplitudes and frequencies permit determining the parameters of the system “cap-bound pile group – soil”, i.e. the effective mass, stiffness and damping with the satisfactory agreement of the calculation results and experimental data. It was found that the stiffness reduces as the intensity of vertical actions rises. The calculated amplitude-frequency curves involving the calculated mass of the soil-pile system, stiffness and damping agree with the values measured for the vertical vibrations.

4. The performed investigations lead to a conclusion that the relations obtained in the framework of the wave models and used to calculate the dynamic stiffnesses at the vertical vibrations of pile foundations, allow considering the mutual effect of piles in the group and satisfactory accuracy of the results, which is confirmed by the comparison with the experimental findings.

5. Acknowledgements

The research has been carried out within the Program of Fundamental Research of the State Academies of Sciences (project No. 121030500137-5).

References

1. Prakash, S., Puri, V.K. Foundations for machines: analysis and design [Online]. New York: J. Wiley & Sons, 1988. 656 p.
2. Prakash, S., Sharma, H.D. Pile foundations in engineering practice [Online]. New York: John Wiley & Sons, 1990. 768 p
3. Pyatetzkij, V.M., Aleksandrov, B.K., Savinov, O.A. Sovremennye fundamenty mashin i ih avtomatizirovannoe proektirovanie [Modern machine foundations and their automated design]. Moscow: Strojizdat, 1993. 415 p. (rus)
4. Savinov, O.A. Sovremennye konstrukcii fundamentov pod mashiny i ih raschet [Modern construction foundations of machines and their calculation] [Online]. Leningrad: Strojizdat. 1979. 200 p. (rus)
5. Guo, W.D. Theory and practice of pile foundations [Online]. CRC Press, 2013. 576 p.
6. Novak, M., El Sharnouby, B. Evaluation of dynamic experiments on pile group [Online]. Journal of Geotechnical Engineer-ing. 1984. 110(6). Pp. 738–756.
7. Rashidifar, M.A., Rashidifar, A.A., Abertavi, A. Nonlinear characteristics of the pile soil system under vertical vibration. Universal Journal of Engineering Science. 2016. 4(4). Pp. 59–65. DOI: 10.13189/ujes.2016.040401
8. Manna, B., Baidya, D.K. Dynamic nonlinear response of pile foundations under vertical vibration – Theory versus experiment. Soil Dynamics and Earthquake Engineering. 2010. 30(6). Pp. 456–469. DOI: 10.1016/j.soildyn.2010.01.002
9. Das, S.K., Manna, B., Baidya, D.K. Prediction of pile-separation length under vertical vibration using ANN [Online]. 14th Asian Regional Conference on Soil Mechanics and Geotechnical Engineering 2011. Hong Kong, China. Pp. 887–892.
10. El Naggar, M., Novak, M. Nonlinear axial interaction in pile dynamics. Journal of Geotechnical Engineering. 1994. 120(4). Pp. 678–696. DOI: 10.1061/(ASCE)0733-9410(1994)120:4(678)
11. Matlock, H., Foo, S.H.C., Bryant, L.M. Simulation of lateral pile behavior under earthquake motion [Online]. Proceedings of the ASCE Geotechnical Engineering Division Specialty Conference, XI. 1978. Pp. 600–619.
12. Novak, M., Sheta, M. Approximate approach to contact problems of piles. Proceedings: Dynamic Response of Pile Foundation: Analytical Aspects. NY: ASCE. 1980. Pp. 53–79.
13. Veletsos, A.S., Dotson, K.W. Vertical and torsional vibration of foundations in inhomogeneous media. Journal of Geotechnical Engineering. 1988. 114(9). Pp. 1002–1021. DOI: 10.1061/(ASCE)0733-9410(1988)114:9(1002)
14. Baranov, V.A. O raschete vynuzhdennyh kolebanij zaglublennogo fundamenta [About the computation of the forced vibrations of the embedded pile foundation]. In Issues of dynamics and strength questions. Proceedings of the Riga Polytechnical Institute. Riga 1967. No. 14. Pp. 195-209.
15. Nuzhdin, L.V., Zabylin, M.I. Zhestkost' i dempfirovanie vertikal'nyh kolebanij svajnogo fundamenta v sloistyh osnovaniyah [Stiffness and damping of vertical vibrations of the pile foundation in the layered lower stratum]. Izvestiya vuzov. Building and Architecture. 1990. No. 12. Pp. 36–41. (rus)
16. Kolesnikov, A., Popov, V. Estimation of dynamic responses on contours of several round cuts at thin plate vibrations. Proceedings of ISEC – 9th International Structural Engineering and Construction Conference: Resilient Structures and Sustainable Construction. Valencia, Spain. 2017. DOI: 10.14455/ISEC.res.2017.69
17. Wu, W., Wang, K., Zhang, Z., Leo, C. Soil-pile interaction in the pile vertical vibration considering true three-dimensional wave effect of soil. International Journal for Numerical and Analytical Methods in Geomechanics. 2013. 37(17). Pp. 2860–2876. DOI: 10.1002 /nag.2164
18. Medina, C., Aznárez, J., Padrón, L., Maeso, O. Effects of soil-structure interaction on the dynamic properties and seismic response of piled structures. Soil Dynamics and Earthquake Engineering. 2013. 53. Pp. 160–175. DOI: 10.1016/j.soildyn.20-13.07.004
19. Allani, M., Holeyman, A. Numerical evaluation of effects of nonlinear lateral pile vibrations on nonlinear axial response of pile shaft. Soils and Foundations. 2013. 53(3). Pp. 395–407. DOI: 10.1016/j.sandf.2013.04.002
20. Khalil, M.M., Hassan, A.M., Elmamlouk, H.H. Dynamic behavior of pile foundations under vertical and lateral vibrations. HBRC Journal. 2019. 15(1). P. 55–71. DOI: 10.1080/16874048.2019.1676022
21. Amiri, A.M., Ghanbari, A.A., Derakhshandi, M. An analytical model for estimating the vibration frequency of structures located on the pile group in the case of floating piles and end-bearing pile march. Civil Engineering Journal. 2018. 4(2). Pp. 450–468. DOI: 10.28991/cej-0309105
22. Biswas, S., Manna, B. Experimental and theoretical studies on the nonlinear characteristics of soil-pile systems under coupled vibrations. Journal of Geotechnical and Geoenvironmental Engineering. 2018. 144(3). P. 04018007. DOI: 10.1061/(ASCE)-GT.1943-5606.0001850
23. Biswas, S., Manna, B., Baidya, D.K. Experimental and theoretical study on the nonlinear response of full-scale single pile under coupled vibrations. Soil Dynamics and Earthquake Engineering. 2017. 94. Pp. 109–115. DOI: 10.1016/j.soildyn.2017.01.012
24. Gazetas, G., Markis, N. Dynamic pile-soil-pile interaction. Part I: Analysis of axial vibration. Earthquake Engineering and Structural Dynamics. 1991. 20(2). Pp. 115–132. DOI: 10.1002/eqe.4290200203
25. Novak, M. Dynamic Stiffness and Damping of Piles [Online]. Canadian Geotechnical Journal. 1974. 11(4). Pp. 574–598.
26. Lamb, H. On the propagation of tremors over the surface of an elastic solid [Online]. Philosophical Transactions. London, Ser. A. 1904. 203. Pp. 1–42.

27. Kolesnikov, A.O., Popov, V.N. Ocenka dinamicheskih reakcij na konturah neskol'kih kruglyh vyrezov pri kolebaniyah plastiny [Evaluation of the dynamic reactions on the contours of several round cuts at the plate vibrations] [Online]. Structural Mechanics of Engineering Constructions and Buildings. 2014. No 3. Pp. 37–43.
28. Kolesnikov, A.O., Popov, V.N. Dinamicheskie reakcii na konturah krugovyh vyrezov s uchyotom ih vzaimnogo raspolozheniya pri kolebaniyah plastiny [Dynamic reactions on round cut contours regarding their mutual location at the plate vibrations] [Online]. Izvestiya VNIIG B.E. Vedeneeva. 2017. 283. Pp. 3–10. (rus)
29. Kolesnikov, A.O., Popov, V.N., Kostyuk, T.N. Issledovanie vliyaniya zaglubleniya i raspolozheniya svaj na sobstvennye chastoty pri kolebaniyah fundamentov [Analysis of the effect of embedment and position of piles on the natural frequencies at pile foundation vibrations]. Izvestiya vuzov. Building. 2019. No. 5. Pp. 39–52. DOI 10.32683/0536-1052-2019-725-5-39-52 (rus)
30. Kolesnikov, A.O., Kostiuk, T.N., Popov, V.N. Calculation of foundation vertical stiffness with the piles mutual influence effect. Structural Mechanics of Engineering Constructions and Buildings. 2019. 15(3). Pp. 229–236. DOI: 10.22363/1815-5235-2019-15-3-229-236 (rus)
31. Manna, B., Baidya, D.K. Nonlinear vertical dynamic response of pile groups. Proceedings of the 17th International Conference on Soil Mechanics and Geotechnical Engineering. IOS Press, 2009. Pp. 1128–1131. DOI: 10.3233/978-1-60750-031-5-1128
32. Novak, M. Data reduction from nonlinear response curves. Journal of Engineering Mechanics. 1971. 97(EM4). Pp. 1187–1204.
33. Lorenz, H. Elasticity and damping effects of oscillating bodies on soil. Symposium on Dynamic Testing on Soils. ASTM STP, 1953. No. 156. Pp. 113–122. DOI: 10.1520/STP49606S
34. Gan, S., Zheng, C., Kouretzis, G., Ding, X. Vertical vibration of piles in viscoelastic non-uniform soil overlying a rigid base. Acta Geotechnica. 2020. 15. Pp. 1321–1330. DOI: 10.1007/s11440-019-00833-7
35. Kolesnikov, A.O., Kostyuk, T.N., Popov, V.N. Attenuation of the soil vibration amplitude at pile driving. Magazine of civil engineering. 2020. 3(95). Pp. 49–56. DOI: 10.18720/MCE.95.5
36. Amiri, A. M., Ghanbari, A., Derakhshandi, M. Analytical model for natural frequency of SDOF system considering soil–pile–structure interaction. International Journal of Civil Engineering. 2018. 16(4). Pp. 1–13. DOI: 10.1007/s40999-018-0284-1
37. Li, Q., Shu, W., Cao, L., Duan, W., Zhou, B. Vertical vibration of a single pile embedded in a frozen saturated soil layer. Soil Dynamics and Earthquake Engineering. 2019. No. 122. Pp. 185–195. DOI: 10.1016/j.soildyn.2019.03.032
38. Luan, L., Ding, X., Cao, G., Deng, X. Development of a coupled pile-to-pile interaction model for the dynamic analysis of pile groups subjected to vertical loads. Acta Geotechnica. 2020. 15. Pp. 3261–3269. DOI: 10.1007/s11440-020-00972-2
39. Cui, C., Meng, K., Wu, Y., Chapman, D. Dynamic response of pipe pile embedded in layered visco-elastic media with radial inhomogeneity under vertical excitation. Geomechanics and Engineering. 2018. 16(6). Pp. 609–618. DOI: 10.12989/gae.2018.16.6.609

Contacts:

Aleksei Kolesnikov, ao_kolesnikov@mail.ru
Vladimir Popov, popov@itam.nsc.ru
Tatiana Kostiuk, tanyakostuk26@gmail.com

Received 19.11.2020. Approved after reviewing 02.09.2021. Accepted 03.11.2021.



Magazine of Civil Engineering

ISSN 2712-8172

journal homepage: http://engstroy.spbstu.ru/

DOI: 10.34910/MCE.110.14

Performance of elastomeric seismic isolators under long-period earthquakes

O. Abrar *** **, *S. Tuhta

Department of Civil Engineering, Ondokuz Mayis University, Samsun, Turkey

**E-mail: obaidullah.abrar@gmail.com*

Keywords: earthquake engineering, seismic isolation, elastomeric isolator, finite element method, long-period earthquake, nonlinear analysis

Abstract. This research investigates the performance of elastomeric (laminated rubber) seismic isolators for the protection of medium-rise structures under the effect of long-period earthquakes. A finite element model of a midrise structure with elastomeric seismic isolators has been modeled and the dynamic performance of the structure has been examined under the effect of the 1985 Michoacán (Mexico City), 2003 Tokachi-Oki, 2010 El Mayor, and the 2016 Kaikoura earthquakes. The performance of the structure is studied in three cases, all equipped with elastomeric isolators with different natural periods. The natural-period of isolators in the first, second, and third cases is 2.5, 4, and 5 seconds, respectively. The comparison of the three cases in terms of mitigating earthquake energy shows that the effectiveness of elastomeric seismic isolators with lower periods (2–3 seconds) is significantly limited under the effect of long-period earthquakes. In common practice, elastomeric seismic isolators are produced and used with a natural period of 2–3 seconds, a seismic isolator having a period within the mentioned range will have serious shortcomings for dissipating earthquake energy when subjected to a long-period earthquake. The results of this study indicate that elastomeric seismic isolators with 5-seconds exhibited considerably better performance compared to that of 2.5 and 4-second seismic isolators.

1. Introduction

Seismic base isolation is considered a reliable technique for the protection of structures under effect strong ground motions, general idea of seismic isolation is to increase the natural period of structure to a point that enables the structures to safely overcome the harmful effect of an earthquake. Elastomeric seismic isolators (e.g. laminated rubber bearing, lead rubber bearing, high damping rubber bearing, etc.) are among the most commonly used seismic isolation devices which are produced with a 2 to 3 seconds natural period [1, 2]. However, based on earthquake event reports the effectiveness of elastomeric seismic isolators considerably diminishes when subjected to a long-period earthquake (a ground motion with a longer period which does not fall within the range of the mentioned elastomeric isolator period), for instance, there have been serious damages in the seismic isolation devices of buildings under the long-period effect of the 2011 Tohoku earthquake [3]. The relatively short natural period of these seismic isolation devices is dominated by the longer period of the long-period earthquake and as a result of it, the story acceleration of the structure will not be dissipated as much as expected for a seismic isolated structure, eventually, the seismic isolator will fail in severe cases due to large displacements (exceeding the displacement limit of the elastomeric isolators) [4].

The harmful effect of long-period earthquakes has long been observed in seismically active regions several times, long-period earthquakes are generated due to rupture propagation and wave radiation in near-field ground motions. It is also generated due to seismic wave amplification in a distant sedimentary soft-soil basin and it imposes a serious threat to structures located far from the epicenter of the earthquake [5]. 1985 Michoacán, 1999 Chi-chi, 2003 Tokachi-Oki, 2010 El Mayor, 2011 Tohoku, 2016 Kaikoura

Abrar, O., Tuhta, S. Performance of elastomeric seismic isolators under long-period earthquakes. Magazine of Civil Engineering. 2022. 110(2). Article No. 11014. DOI: 10.34910/MCE.110.14

© Abrar, O., Tuhta, S., 2022. Published by Peter the Great St. Petersburg Polytechnic University.

 This work is licensed under a CC BY-NC 4.0

earthquakes are noted as the worst examples of the long-period ground motions [5–9]. The 2011 Tohoku earthquake generated a long-period earthquake affecting much of the east coast of Japan, tall buildings have been subjected to large displacement due to the long-period effect of the earthquake. For instance, a 52-floor building in Osaka located 770 km from the epicenter of the earthquake had a 1.32 m displacement, Osaka region has a dominant period of 6 seconds which correlates with the dominant period of the long-period earthquake that happened in the sedimentary soil layers of Osaka region [3].

In the literature, there are several studies regarding the enhancement of seismic base isolation systems, different methods are used to improve the performance of seismic isolation. Ismail et al. proposed a novel seismic isolation device equipped with a mechanism to effectively dissipate the near-fault pulse-like earthquakes [10]. Kasimzade et al. developed a seismic isolation system that intends to provide a longer period for the structures for improving the overall performance of important structures against near-fault and long-period earthquakes [11, 12]. Herbut suggests the usage of a wave generator in the soil-foundation boundary of the structure to reduce the amplitude of ground motion [13]. Tavakoli et al. examined the performance of fixed-base and seismically isolated buildings under the effect of far-field and near-fault ground motions [14]. Plenty of studies on seismic base isolation are focused on short-period and short-duration ground motions [15–18]. On the other hand, few studies are dedicated to the effect of the long-period earthquakes on seismic isolated structures and are focused on special structures such as oil tanks and bridges [19, 20].

This paper investigates the performance of low-period (2.5 seconds) elastomeric seismic isolation (laminated rubber bearing) devices in comparison with a figurative seismic isolator with a longer period (4 and 5 seconds) for protection of a 4-story building against the effect of long-period earthquakes. The finite element model of a 4-story seismically isolated structure has been prepared in a manner that the superstructure and the seismic isolators exhibit linear and nonlinear behaviors respectively. The dynamic finite element model has been solved using LS-DYNA explicit solver under the effect of the 1985 Mexico City, 2003 Tokachi-Oki, 2010 El Mayor, and the 2016 Kaikoura earthquakes.

2. Method

2.1. Model Description

A finite element model of a 4-story building (Fig. 1) with a system of laminated rubber seismic isolators has been prepared. The model consists of 36 columns each laying on a seismic isolator, the isolators are positioned on a raft foundation. One-dimensional beam elements (Hughes Liu) are used to model the columns and beams of the superstructure, for modeling the foundation and the bases of the columns 8-node constant stress solid element is used. All parts of the structure are modeled using elastic material (C30 concrete), except for the seismic isolators which are modeled using a special material, the nonlinear seismic isolator which exhibits hysteresis behavior.

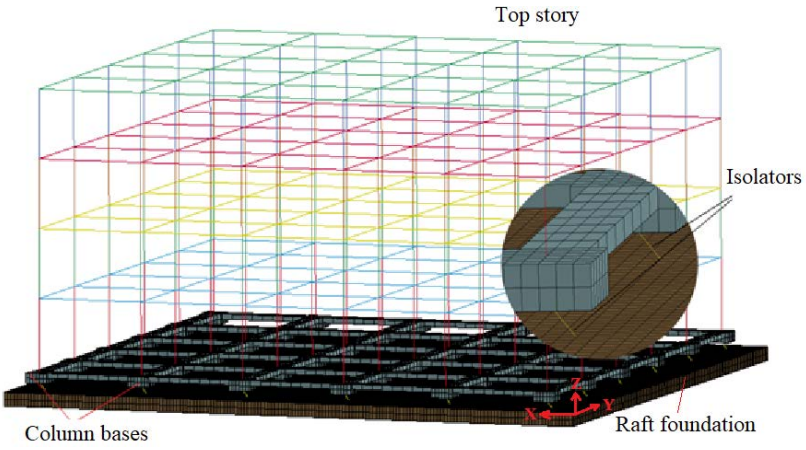


Figure 1. Finite element model of the 4-story seismic isolated structure.

Seismic isolators are modeled using a single discrete beam element which has the capability of representing an elastomeric isolator. The general properties of the seismic isolators are calculated based on the building and its soil characteristics and the calculated seismic isolator parameters are assigned to the respective beam element. The properties of the seismic isolator are modeled by considering the bidirectionally coupled plasticity theory which satisfies the nonlinear hysteresis behavior proposed by Wen [21]. The algorithm for solving the nonlinear seismic isolator was developed by Nagarajaiah et al [22]. The general representation of the equation of motion (equation 1) and the nonlinear formulation (equation 2) of the seismic isolation system are presented as follows.

$$[m]\{\ddot{u}\}+[c]\{\dot{u}\}+[k]\{u\}+[L]\{f_r\}=-[m]\{e\}\{\ddot{u}_g\}, \tag{1}$$

$$f_r = c_b\dot{u}_b + \alpha k_b u_b + (1-\alpha)\, f_y Z, \tag{2}$$

$$\dot{Z} = \left[Au_b - \beta |\dot{u}_b| Z |Z|^{n-1} - \tau\dot{u}_b |Z|^n \right] u_y^{-1}. \tag{3}$$

Here, m, c, k, $\ddot{u}$, $\dot{u}$, and u are the mass, damping, stiffness matrices, acceleration, velocity, and displacement vectors of the model respectively. The matrix L refers to the location of isolators and f_r represents the nonlinear hysteresis restoring force of the isolator which satisfies Wen's nonlinear model. $\ddot{u}_g$ is the acceleration vector of ground motion and the vector e refers to the influence coefficient of displacement transformation respective to each degree of freedom. k_b, c_b, u_b, $\dot{u}_b$, f_y, and u_y are the stiffness, damping, displacement, velocity, yield force, and yield displacement components of the seismic isolator respectively. α refers to the ratio of the post-yield to pre-yield stiffness of the seismic isolator. Z is the non-dimensional hysteresis displacement component of Wen's nonlinear model and can be presented via equation (3). A, β, and τ are dimensionless parameters of the isolator that are determined based on experimental tests. n is a constant which controls the smoothness of transition from elastic to the plastic response.

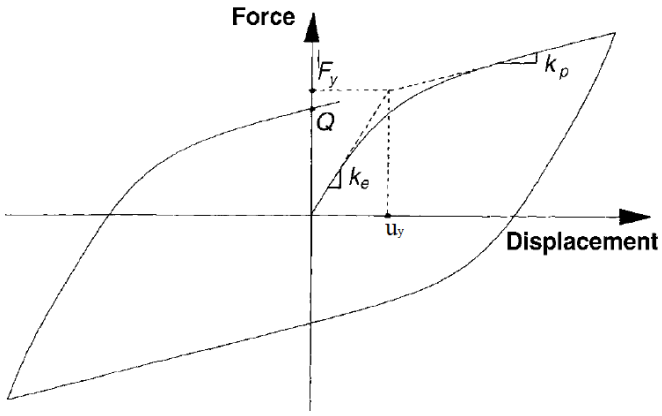


Figure 2. Hysteresis restoring force-displacement curve of seismic isolator.

2.2. Properties of Isolators

The properties of the laminated rubber seismic isolators are calculated based on the characteristics of the structure and the properties of the soil on which the structure is going to be built. There are various codes and regulations for the calculation of the properties of the seismic isolators. In this study, the standard published by the American Society of Civil Engineers (ASCE 7-10 and ASCE 41-13) has been used [23], [24]. Vertical stiffness (k_v), yield force (f_y), and yield displacement (u_y) of the isolator is calculated as three cases depending on the selected period of the isolator (T_D) using the following equations.

$$K_{D\min} = \frac{4\pi^2 W}{T_D^2 g}, \tag{4}$$

$$D_D = \frac{gS_{D1}T_D}{4\pi^2 B_D}. \tag{5}$$

Here, W is the weight of structure imposed on a single seismic isolator, K_b, B_D, and D_D are the horizontal stiffness, damping coefficient, and design displacement of the isolator respectively. S_{D1} is the spectral response acceleration parameter of the ground motion and g is the gravitational acceleration. The sectional area (A_r) and the post-yield stiffness (K_p) of the rubber bearing are calculated based on equations (6) and (7) respectively.

$$A_r = \frac{K_D t_r}{R_T}, \tag{6}$$

$$K_p = \frac{GA_r f_L}{R_T}, \tag{7}$$

where t_r is the thickness of a single rubber layer separated by steel sheet, G is the shear modulus of the rubber, and R_T is the total rubber thickness and f_L is a factor commonly taken as 1.5. Experimentally, yield displacement (u_y) is calculated as 0.05 – 0.1 times of R_T. The characteristic-strength of the isolator is calculated using equation (8), using the described parameters the yield force of the isolator is calculated by equation (9).

$$u_y = \frac{Q}{5.5K_p}, \tag{8}$$

$$F_y = Q + K_p u_y. \tag{9}$$

Having the above parameters, the vertical stiffness (K_v) of the isolator is calculated using equation (10).

$$K_V = \frac{\left(E_c A_r\right)}{R_T}, \tag{10}$$

$$E_c = \frac{6GS^2K}{6GS^2 + K}. \tag{11}$$

Equation (11) is used to calculate the elasticity modulus of the rubber-steel composite which is bonded under specific heat and pressure. K is the bulk modulus of the rubber, the value of the K and G varies for different rubber compounds, it varies 1000 – 2500 MPa and 0.45 – 1 MPa respectively [1]. S is a factor that refers to the shape of the hysteresis loop of the elastomeric isolator, ideally, it ranges between 12 – 20. In accordance with the presented equations, the properties of the laminated rubber seismic isolators are calculated and presented in Table 1.

Table 1. Properties of computed laminated rubber seismic isolators.

Parameters	T_D: 2.5 s	T_D: 4 s	T_D: 5 s
K_v (N/m)	2.674E+09	8.884E+08	6.249E+08
K_b (N/m)	1.793E+06	7.002E+05	4.481E+05
F_y (N)	1.165E+05	9.103E+04	7.282E+04
u_y (m)	0.01	0.02	0.025
R_T (m)	0.2	0.4	0.5

2.3. Numerical Analysis

The performance of presented seismic isolators for mitigation of ground motion accelerations in the 4-story building is investigated under the effect of five earthquake ground motions as provided in Table 2 and Fig. 3. The ground motion accelerations records are obtained from the Virtual Data Center (VDC) [25] and Pacific Earthquake Engineering Research Center (PEER) ground motion record databases [26].

Table 2. List of earthquakes used in numerical analysis.

Earthquake	Year	M_w	Station	PGA (m/s^2)	PGD (cm)	Hypo-central Distance (km)
Michoacán, Mexico	1985	8.1	La Union	1.6	7.10	83.9
El Mayor, USA/Mexico	2010	7.2	El Centro Array 11	5.7	39.7	61.8
El Mayor, USA/Mexico	2010	7.2	Chihuahua	2.4	44.7	25.7
Tokachi Oki, Japan	2003	8.3	Kushiro Gov. Building	2.6	15.7	136.1
Kaikoura, New Zealand	2016	7.8	Seddon Fire Station	7.1	20.7	145.3

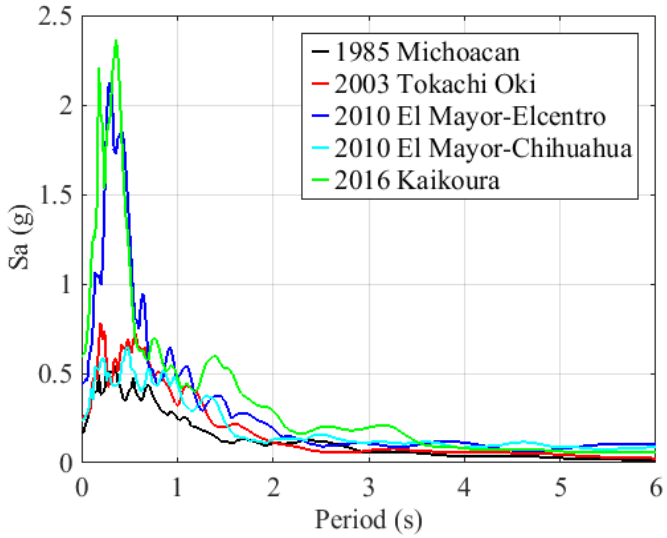


Figure 3. The spectral acceleration of earthquake excitations used in numerical analysis.

For conducting finite element nonlinear dynamic analysis, LS-DYNA explicit solver code has been used, each analysis required 5-10 hours varying based on the duration of ground motion excitation. A computer with a capacity of 16 CPU cores and 32 GB of RAM has been used to conduct the respective dynamic analyses.

3. *Results and Discussion*

The top story acceleration, top story displacement of the building, and the nonlinear hysteresis force-displacement responses of seismic isolators with different periods (2.5s, 4.0s, and 5s) have been obtained and presented comparatively via Fig. 4-8.

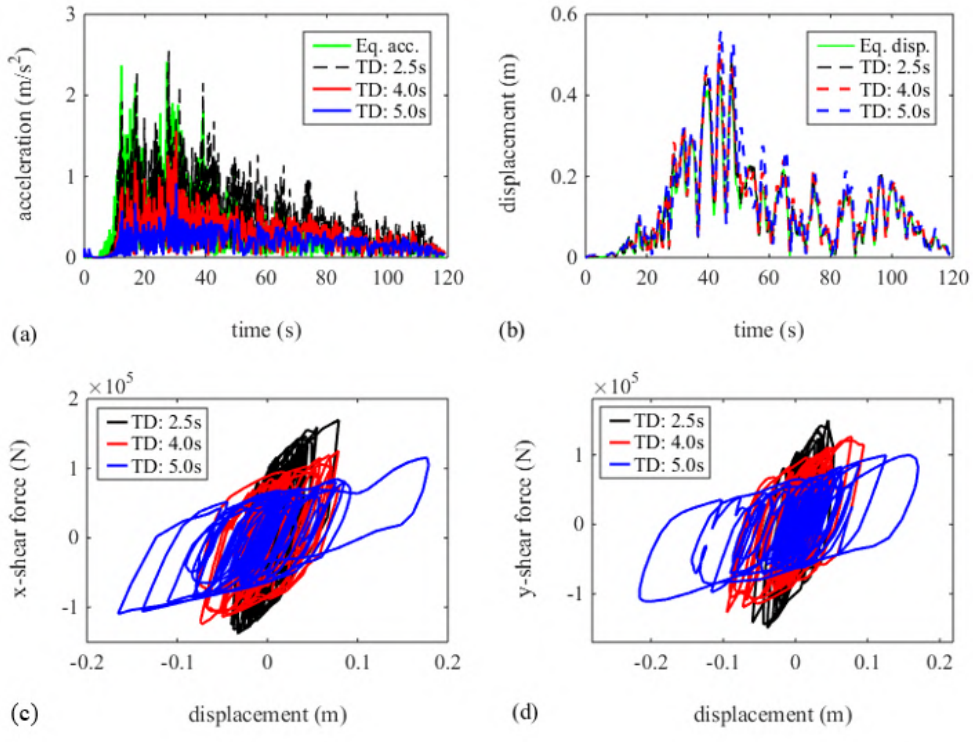


Figure 4. El Mayor-Chihuahua (2010) response: (a) top story acceleration, (b) top story displacement, (c) and (d) hysteresis force-displacement curve in x and y directions respectively.

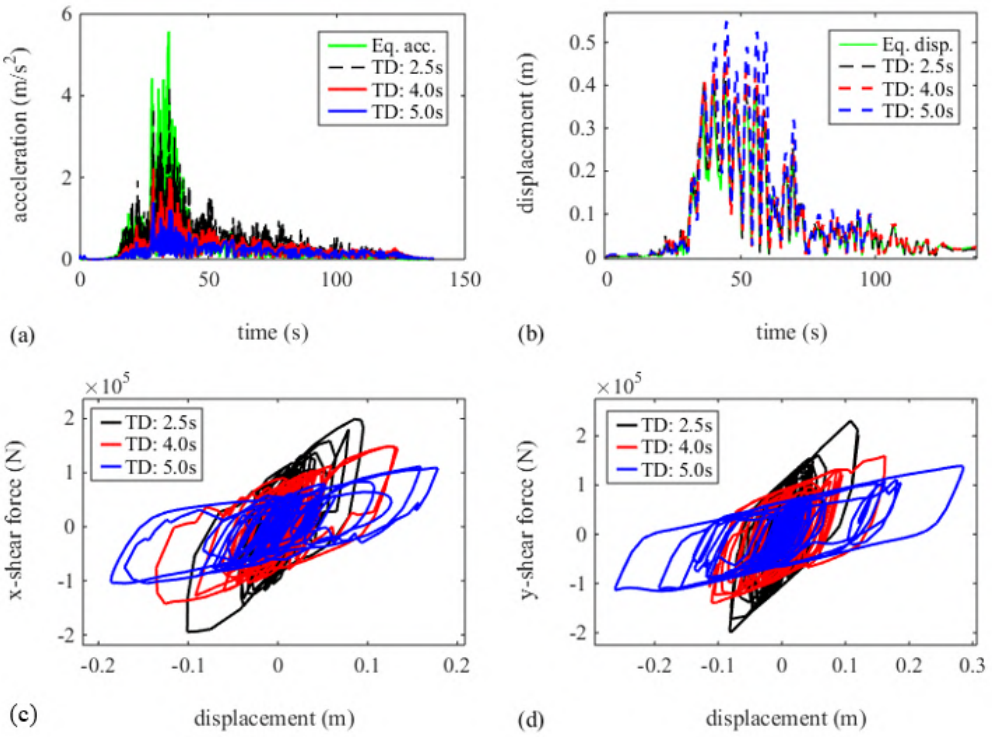


Figure 5. El Mayor-El Centro (2010) response: (a) top story acceleration, (b) top story displacement, (c) and (d) hysteresis force-displacement curve in x and y directions respectively.

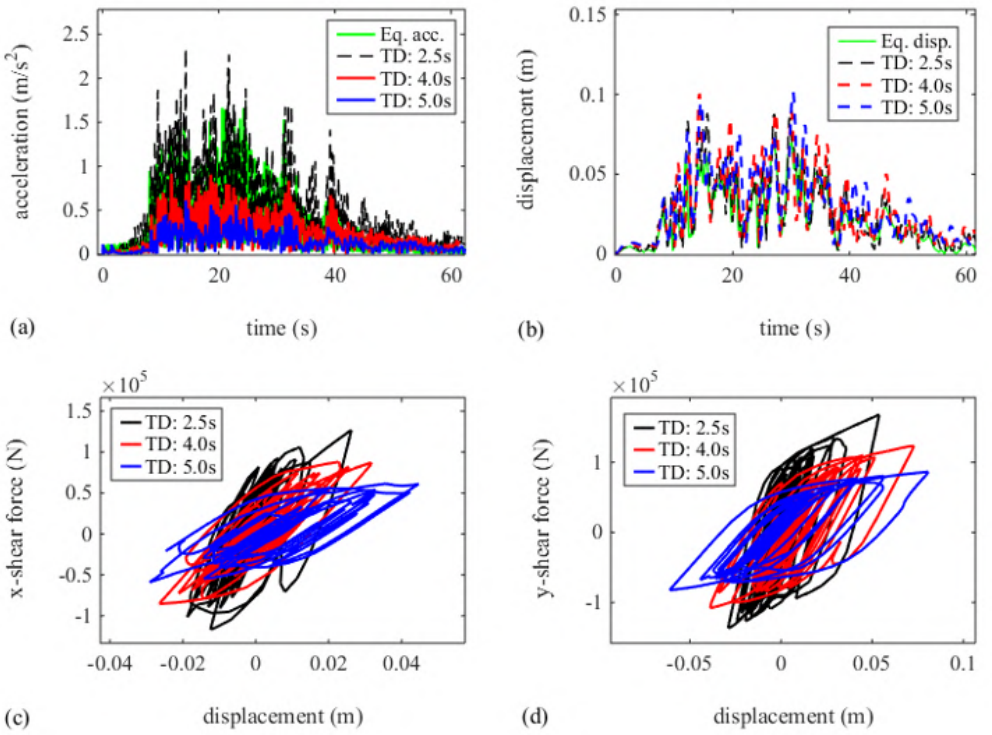


Figure 6. Michoacán (1985) response: (a) top story acceleration, (b) top story displacement, (c) and (d) hysteresis force-displacement curve in x and y directions respectively.

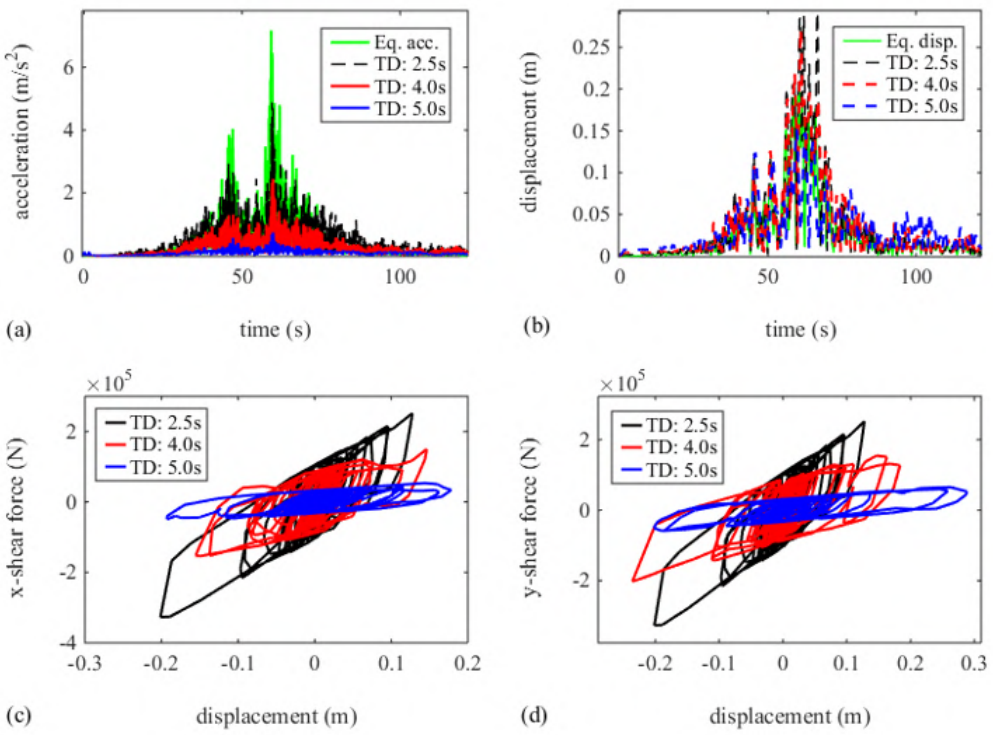


Figure 7. Kaikoura (2016) response: (a) top story acceleration, (b) top story displacement, (c) and (d) hysteresis force-displacement curve in x and y directions respectively.

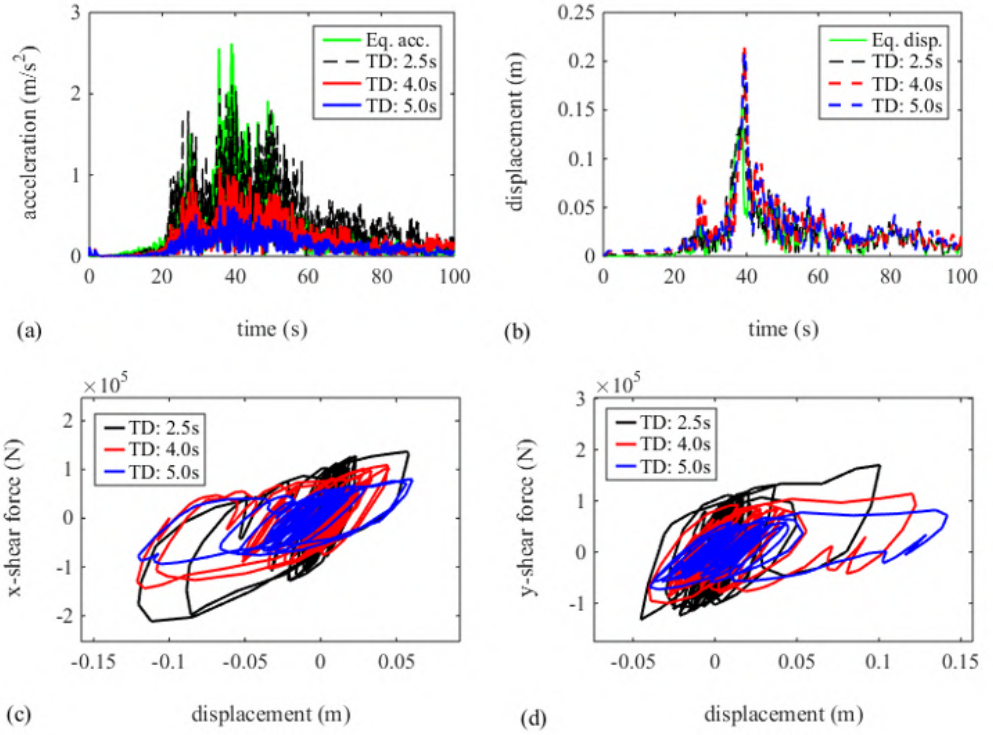


Figure 8. Tokachi-Oki (2003) response: (a) top story acceleration, (b) top story displacement, (c) and (d) hysteresis force-displacement curve in x and y directions respectively.

Top story acceleration results indicate that the response of seismic isolators with 4s and 5s-period is significantly lower than the 2.5s-period isolator, the top story acceleration response has relatively decreased by increasing the period of the isolator as presented in Fig. 4a, 5a, 6a, 7a, and 8a. The reduction in acceleration response of the superstructure is due to the reason that longer period of the 5s and 4s-period isolator, in this case, the isolator has more elasticity and has the capability of larger displacement compared to that of the 2.5s-period isolator. The hysteresis force-displacement behavior of the isolator implies that 5s and 4s-period isolator had larger displacement compared to that of the 2.5s-period isolator, meanwhile, the shear force on the isolators have dropped significantly as shown in Fig. 4c, 4d, 5c, 5d, 6c, 6d, 7c, 7d, 8c, and 8d.

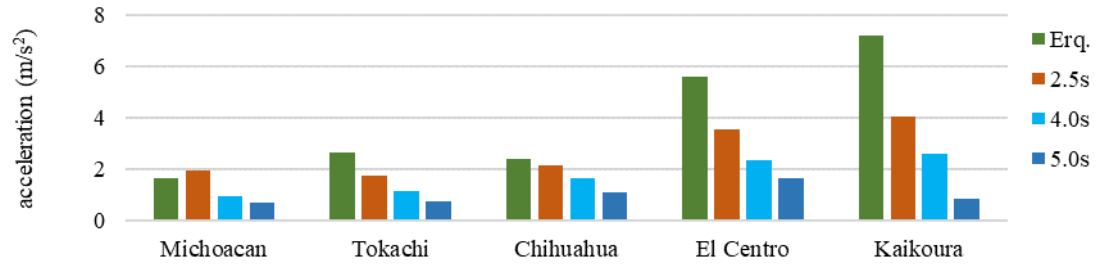


Figure 9. Comparison of top story acceleration response of the model under respective earthquakes.

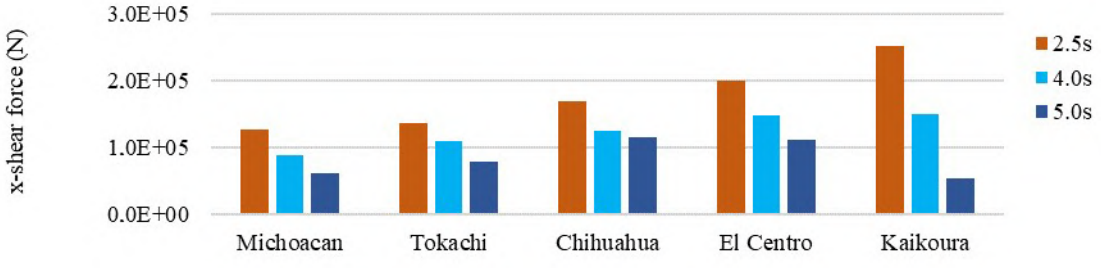


Figure 10. Comparison of shear force response of isolators under respective earthquakes in the x-direction.

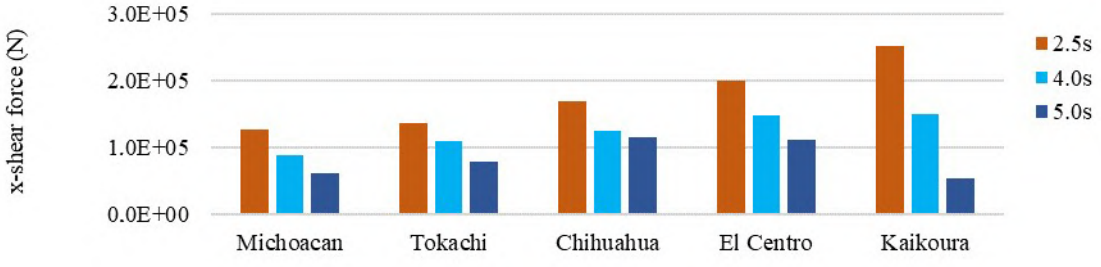


Figure 11. Comparison of shear force response of isolators under respective earthquakes in the x-direction

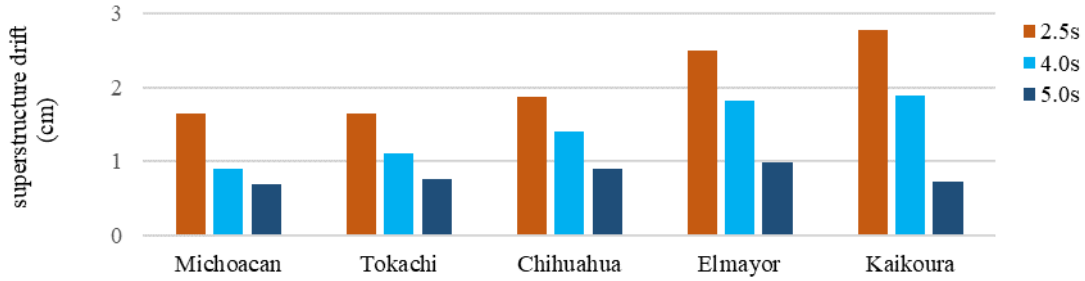


Figure 12. Comparison of superstructure drift under the effect of respective earthquakes.

Overall, the acceleration response of the top story of the structure has decreased by 35.65 % and 60.54 % for 4s and 5s-period isolator respectively in comparison with the 2.5s-period seismic isolator as shown in Fig. 9. Similarly, the base shear in the seismic isolator with 4s and 5s-period have decreased by 28.80 % and 49.50 % respectively in comparison with the 2.5s-period seismic isolator as presented in Fig. 10 and 11. The story drift of the model under the effect of respective earthquakes is shown in Fig. 12, similar to the acceleration and base shear response, the story drift has decreased in 4 and 5s-period seismic isolators in comparison with the 2.5s-period isolator.

The design of an elastomeric seismic isolator with a 5s-period and above requires a deep study on the materials that are used in the production of elastomeric isolators. Usage of highly resilient rubber compounds with highly durable materials (e.g. carbon fiber) as shims is an option for the design of such isolators, and it is a topic for future studies.

4. Conclusion

In this study, the seismic performance of three different elastomeric (laminated rubber) seismic isolators with different natural periods has been studied comparatively. Dynamic analysis of the seismic isolated structure has been conducted under the effect of five long-period earthquakes. The outcome of the study can be concluded as follows:

1. The earthquake mitigation performance of commonly produced elastomeric seismic isolators (with 2-3s-period) is significantly low under the effect of long-period earthquakes; it could lead to failure of the seismic isolators due to the concentration of shear force on seismic isolators.

2. For inhibition of long-period earthquakes a seismic isolator with a longer natural period is required that could allow larger displacement capabilities.

3. Increasing the period of elastomeric isolators to 4-5 s has considerably increased the effectiveness of the elastomeric isolators in terms of dissipating the energy of earthquakes in the top stories of the superstructure.

4. The shear-force on seismic isolators has been decreased relatively with increasing the period of the seismic isolators, 5-second period isolator has the lowest shear force response.

5. The isolator model with 4 and 5s- period can be used as a reference to be implemented in the protection of buildings in regions with the high possibility of occurring long-period ground motions which can impose serious threats to buildings equipped with conventionally implemented elastomeric seismic isolators with a 2-3s period.

References

1. Naeim, F. The Seismic Design Handbook. 1. New York, Springer, 2001. ISBN: 978-1-4613-5681-3
2. Ozden, B. LOW-COST SEISMIC BASE ISOLATION USING SCRAP TIRE PADS (STP). MSc. Ankara - Turkey, Middle East Technical University, 2006.
3. Saito, T. Behavior of response controlled and seismically isolated buildings during severe earthquakes in Japan. Energy, Environment and Innovation Magazine. 2015. Pp. 31–37.
4. Jangid, R.S. Optimum friction pendulum system for near-fault motions. Engineering Structures. 2005. 27(349–359). DOI: https://doi.org/10.1016/j.engstruct.2004.09.013
5. Kazuki, K., Hiroe, M.A. A seismological overview of long-period ground motion. Journal of Seismology. 2008. 12(2). Pp. 133–143. DOI: https://doi.org/10.1007/s10950-007-9080-0
6. Bozorgnia, Y., Bertero, V.V. Earthquake Engineering: From Engineering Seismmology to Performance-Based Engineering. Washington D.C., CRC Press LLC, 2004. ISBN: 0-203-48624-2.
7. Duputel, Z., Rivera, L. Long-period analysis of the 2016 Kaikoura earthquake. Physics of the Earth and Planetary Interiors. 2017. 265(April). Pp. 62–66. DOI: 10.1016/j.pepi.2017.02.004
8. Hall, J.F., Heaton, T.H., Halling, M.W., Wald, D.J. Near-source ground motion and its effects on flexible buildings. Earthquake Spectra. 1995. 11(4). Pp. 569–605. DOI: https://doi.org/10.1193/1.1585828
9. Loh, C.H., Wu, T.C., Huwang, N.E. Application of the empirical mode decomposition – Hilbert spectrum method to identify near-fault ground-motion characteristics. Bulletin of the Seismological Society of America. 2001. 9(5). Pp. 1339–1357. URL: https://pdfs.semanticscholar.org/7d25/84484237712d714539f34324048bd3611cdf.pdf
10. Ismail, M., Rodellar, J., Ikhouane, F. Performance of structure–equipment systems with a novel roll-n-cage isolation bearing. Computers & Structures. 2009. 87(23–24). Pp. 1146–1631. DOI: https://doi.org/10.1016/j.compstruc.2009.09.006
11. Kasimzade, A.A., Abrar, O., Atmaca, G., Kuruoglu, M. New structural seismic protection for high-rise building structures. Journal of Vibroengineering. 2020. 22(4). Pp. 831–848. DOI: doi.org/10.21595/jve.2019.20741
12. Kasimzade, A.A., Abrar, O., Kuruoglu, M., Atmaca, G. New Structural Seismic Isolation for Nuclear Containment Structures. Science and Technology of Nuclear Installations. 2020. 2020(9573653). Pp. 1–15. DOI: doi.org/10.1155/2020/9573653
13. Herbut, A. A proposal for vibration isolation of structures by using a wave generator. Soil Dynamics and Earthquake Engineering. 2017. 100. Pp. 573–585. DOI: https://doi.org/10.1016/j.soildyn.2017.07.005
14. Tavakoli, H.R., Naghavi, F., Goltabar, A.R. Dynamic Reponse of the Base-Fixed and Isolated Building Frames Under Far and Near-Fauld Earthquakes. Arabian Journal of Science and Engineering. 2014. 39. Pp. 2573–2585. DOI: 10.1007/s13369-013-0891-8
15. Han, J., Kyu, M., Choi, I. Experimental study on seismic behavior of lead-rubber bearing considering bi-directional horizontal input motions. Engineering Structures. 2019. 198(August). Pp. 2019.
16. Jian, F., Xiaohong, L., Yanping, Z. Optimum design of lead-rubber bearing system with uncertainty parameters. Structural Engineering and Mechanics. 2015. 56(6). Pp. 959–982.
17. Pradip, D.J., Sunila, G., Dume, S.M. Earthquake performance of RC Buildings using Elastomeric Base Isolation Controls. International Journal of Engineering Research and Applications. 2013. 3(6). Pp. 1518–1524.
18. Shoaei, P., Tahmasebi, H., Mehdi, S. Seismic reliability-based design of inelastic base-isolated structures with lead-rubber bearing systems. Soil Dynamics and Earthquake Engineering. 2018. 115(June). Pp. 589–605.
19. Anajafi, H., Poursadr, K., Roohi, M., Santini-Bell, E. Effectiveness of Seismic Isolation for Long-Period Structures Subject to Far-Field and Near-Field Excitations. 2020. 6(24). DOI: 10.3389/fbuil.2020.00024.
20. Cheng, X., Jing, W., Li, D. Dynamic response of concrete tanks under far-field, long-period earthquakes. Proceedings of the Institution of Civil Engineers – Structures and Buildings. 2019. Pp. 1–14. DOI: 10.1680/jstbu.18.00024.

21. Wen, Y.K. Method for Random Vibration of Hysteretic Systems. Journal of Engineering Mechanics. 1976. 102(2). Pp. 249–264.
22. Nagarajaiah, S., Reinhorn, A.M., Constantinou, M.C. Nonlinear Dynamic Analysis of 3-D-Base-Isolated Structures. Journal of Structural Engineering. 1991. 117(7). Pp. 2035–2054. DOI:doi.org/10.1061/(ASCE)0733-9445(1991)117:7(2035).
23. ASCE 7-16. Minimum Design Loads for Buildings and Other Structures. Reston, American Society of Civil Engineers, 2016.
24. ASCE 41-13. Seismic Evaluation and Retrofit of Existing Buildings. Reston, American Society of Civil Engineers, 2013.
25. VDC. Storng-Motion Virtual Data Center. USGS, 2020. URL: https://www.strongmotioncenter.org/vdc/scripts/earthquakes.plx
26. PEER. PEER Strong Ground Motion Database. Berkeley University, 2018. URL: https://ngawest2.berkeley.edu/

Contacts:

Obaidullah Abrar, obaidullah.abrar@gmail.com
Sertac Tuhta, stuhta@omu.edu.tr

Received 08.02.2021. Approved after reviewing 06.04.2021. Accepted 07.04.2021.



Magazine of Civil Engineering

ISSN 2712-8172

journal homepage: http://engstroy.spbstu.ru/

DOI: 10.34910/MCE.110.15

Nanostructured high-performance concretes based on low-strength aggregates

***A.S. Rassokhin*[a,c]*, *A.N. Ponomarev*[b], *A.I. Karlina*[c]**

[a] *Peter the Great St. Petersburg Polytechnic University, St. Petersburg, Russia*

[b] *Peoples' Friendship University of Russia, Moscow, Russia*

[c] *Moscow State University of Civil Engineering, Moscow, Russia*

**E-mail: rassokhinaleksandr@gmail.com*

Keywords: high-performance concrete, nanostructured concrete, hydrotechnical concrete, strength enhancement

Abstract. In the modern world, construction is often located in remote and hard-to-reach regions, where there are no acceptable quality aggregates for concrete. The transportation of high-quality aggregates leads to a significant increase in the cost of concrete. This paper considers the possibility of developing high-performance concretes using aggregates available in the construction region. This is possible with the use of modern achievements in the field of construction science and construction chemistry, as well as nanotechnology. The strength and mineralogical properties of gneissic granite from the Kem river bed, as well as gabbro-diabase, were investigated. During the experimental work, a high-performance nanostructured concrete based on low-strength gneissic granite was developed. The strength and operational properties of the concrete were determined. The dynamic of gain in strength of concrete at the ages of 7, 28, and 180 days was also studied. The developed binder combination can also be used to produce high-performance concretes with other low-strength aggregates.

1. Introduction

In the modern world, construction is often located in remote and hard-to-reach regions with adverse climatic conditions. However, there is also a need for high-quality building materials in such regions. This can be considered on the example of the northern regions of Russia. Moreover, this particular case can be scaled, since the proposed solutions are universal and applicable in other similar situations since other low-strength aggregates can be used in the developed binders for the manufacturing of high-performance concrete.

Regions of the North of Russia have huge economic and energy potentials [1]. But considering the absence of large settlements and the underpopulation far away from the coastal strip, the transport infrastructure is developed very limitedly [2], which always leads to additional huge logistic expenses for the construction of large construction projects. That concerns such objects as, for example, small hydropower plants. Their energy potential for the northern regions is proved and there are already constructions of several of them conducted [3]. Moreover, there is a long-term global movement to abandon nuclear power in its current form for the benefit of other methods of obtaining energy, especially after the Fukushima accident [4].

Small hydropower plants and other infrastructure facilities can be built on such northern rivers as Pechora, Northern Dvina, Kem, Mezen.

Rassokhin, A.S., Ponomarev, A.N., Karlina, A.I. Nanostructured high-performance concretes based on low-strength aggregates. Magazine of Civil Engineering. 2022. 110(2). Article No. 11015. DOI: 10.34910/MCE.110.15

© Rassokhin, A.S., Ponomarev, A.N., Karlina, A.I., 2022. Published by Peter the Great St. Petersburg Polytechnic University.

This work is licensed under a CC BY-NC 4.0

In particular, this problem also occurred during the construction of small hydroelectric power plants in the Karelia on the Kem river.

The bed of the Kem river consists of gneissic granite. Moreover, it should be noted that it is one of the most widespread rocks of the Karelia region.

Due to the fact that gneissic granite has a layered structure and inclusions of low-strength minerals, it quite often has a low mechanical performance [5]. For that reason, it is not suitable for use in responsible construction, as like small hydropower plants in a traditional way, because a high-strength hydrotechnical concrete is necessary for this task. It is regulated by the Russian national standard GOST 26633-2015 “Heavy-weight and sand concrete. Specifications“ as well as DaCS (SP) 40.13330.2012 “Concrete and reinforced concrete dams. Updated version of Building code (SNiP) 2.06.06-85”.

The construction of such objects means remoteness from large settlements and, as a further consequence, developed transportation infrastructure is absent. Therefore, the transportation of high-quality fillers for concrete to the site often increases the cost of concrete significantly.

This problem also occurred during the construction of small hydroelectric power stations in Karelia on the Kem River. The nearest sandpits and stone pit with suitable loose materials for this construction were at a distance of about 200 km from the construction site.

In view of this, developers try to use those materials, which are in the location of the construction site, whenever it is possible. For the production of concrete of low classes, it is possible to use low-quality aggregates, such as broken brick, crushed concrete, crushed stone from stones mined on the location of the construction site, etc [6–8]. However, for the high-quality hydrotechnical concrete developing other technical solutions are necessary.

Hydrotechnical concretes are subject to special requirements because of their special operating conditions, especially if they are in northern regions. The most stringent requirements are imposed in the zone of variable water level since operating conditions imply unequal climatic effects, as well as unequal water saturation of concrete. For that reason, strict requirements for freeze-thaw resistance and waterproofing are imposed on the concrete of the variable water level. Moreover, due to the movement of water, concrete should have increased resistance to abrasion. Additionally, a characteristic feature of hydrotechnical concrete is the determination of grade strength at the age of 180 days. This is due to the operating conditions of hydrotechnical concrete in a water-saturated state, which contributes to the gain of strength after 28 days [9, 10].

Fortunately, the science in the 21st century (in particular the concrete science) has moved far ahead and rather large amounts of additives to concrete have appeared. For example, the water-cement ratio can be significantly reduced with plasticizing agents [11]. This allows to increase the strength of concrete or reduce the amount of cement in concrete. Silica fumes lead to more homogeneity of concrete mixture, as well as to mechanical characteristics enhancement [12]. Cement accelerators [13], cement hardening retarders [14] allow you to regulate the hardening time of concrete, then it is especially relevant if the concrete needs to be transported or concrete work is carried out in adverse weather conditions. The use of non-metallic fibers leads to a flexural strength enhancement of concrete, as well as an increase in its ductility [15]. When properly used, they allow obtaining high characteristics of concrete, even when using low-quality raw materials.

An overview of scientific publications also shows that using modern methods, it is possible to develop high-strength concretes using low-strength aggregates [16–18].

Moreover, the use of additional binders, such as silica fume and shale ash, reduces the environmental impact from the region, since they are industrial waste and need to be disposed of [19, 20].

Also, nanomodifiers are the most prospective ones [21]. For the moment, a large number of studies are already available, where the effectiveness of using catalytic amounts of various nanoparticles to significantly improve the characteristics of concrete has been proved [22–24]. Due to the rapid development of various methods of nanomaterials producing new types of nanoparticles are regularly synthesized in recent years. Based on a review of the literary data, as well as the authors' studies, it can be concluded that at the present point in time carbon nanomaterials show the highest efficiency. In particular, there are carbon nanotubes and carbon toroidal nanoparticles [25–27]. The authors of this paper had several studies on the influence of carbon toroidal nanoparticles on the properties of cement matrices, as well as polymer matrices [28]. In these papers, it was found that the introduction of catalytic amounts of carbon toroidal nanoparticles into concrete led to a significant increase in the strength of concrete since carbon toroidal nanoparticles became centres of crystallization of cement stone.

Furthermore, numerous almost significant results on their use have been obtained. High-disperse silica fumes and fine-ground cement can also be considered as inorganic nanomaterials [29, 30]. Fine

crushing increases the specific surface area of the substance, which increases its chemical activity. Moreover, it is worth noting that with fine crushing/milling, even many materials that are not binders in the macrostate in any kind can have binding properties after fine crushing/milling [31, 32].

Also, there are a sufficient number of studies on the positive effect of carbon nanomodifiers on the frost resistance of concrete, as well as other fine-milled additives [33, 34].

Based on the above, the task of this research is to develop a high-strength nanostructured concrete with high mechanical and operational characteristics. The feature of this concrete is the use of local raw materials as aggregate. It allows to lower the logistic expenses and, as a result, the construction cost, and also to lower the environmental pressure on the region. This is especially relevant if the construction is conducted in highly protected regions, and additional actions (such as the investigation of deposits of high-quality rocks for the construction) negatively influence the ecological situation of the region. Moreover, the increased traffic flows would influence the quality of the roads of the region and the ecological situation of the region.

2. Methods

2.1. Concrete aggregates

Inert aggregate from the boulders of gneissic granite has been used for the development of empirical research. Boulders have been mined in the Kem river bed and have been crushed down in several steps.

Gneissic granite has a multilayer structure. The characteristics of each of the layers are quite different. The goal of crushing it in several stages was to consist in that on each of the stages to sift soft rocks that disintegrate the first.

At the first stage, the boulders were crushed into small fragments, into fractions of 150–200 mm, and further on, into fractions of crushed stone of 3–10, of 10–20 mm. Fractions were obtained by sieving on laboratory sieves. Gneissic granite sand of fraction of 0–2.5 mm was pulverized from the fraction of 0–3 mm.

The crushing of samples of a stone from local explosive rocks was made in a laboratory jar mill 80JM-1a.

For comparison, gabbro-diabase crushed stone of three different manufactures was also investigated: Berezovsk Ltd., Goloday-gora Ltd., Ramrucheyskoe Ltd. Two of the gabbro-diabase mines (Goloday-gora Ltd., Ramrucheyskoe Ltd.) were located in the same region where gneissic granite was mined. The mineralogical composition of gabbro-diabase from the Urals (Berezovsk Ltd.) was also investigated to expand the geography of the comparison.

2.2. Determination of gneissic granite crushed stone characteristics

The freeze-thaw resistance of gneissic granite crushed stone was determined according to Russian national standard GOST 8269.0-97. The freeze-thaw resistance of crushed stone was determined by loss of sample weight when immersed in saturated sodium sulphate solution and the following drying according to the method described in Russian national standard GOST 8269.0-97.

The sodium sulphate solution was prepared in the following way. 185 grams of anhydrous sodium sulphate according to Russian national standard GOST 4166 were weighed and dissolved in one litre of distilled water heated to 40 °C by gradually adding anhydrous sodium sulphate to it with careful stirring until the solution was saturated. After that, the solution was cooled to room temperature, was drained into a bottle and was stored for 2 days.

An analytical sample of gneissic granite crushed stone was poured into a vessel in one layer, poured with a solution of sodium sulphate so that the gneissic granite crushed stone was completely immersed in the solution. This was maintained therein for 20 hours at room temperature.

Next, the solution was drained (for reuse), and a vessel with gneissic granite crushed stone was placed for 4 hours in a drying cabinet “Snol”, in which the temperature was maintained (105 ± 5) °C. After that, the gneissic granite crushed stone was cooled to room temperature and again poured with the solution.

Subsequent test cycles consisted of maintaining the gneissic granite crushed stone for 4 hours in a sodium sulphate solution, drying for 4 hours, and cooling to room temperature.

After 3, 5, 10, and 15 cycles, the crushed stone sample was washed with hot water to remove sodium sulphate, dried in a laboratory oven «Snol» to a constant mass, and sieved through with a sieve mesh of 5 mm.

The residue on the sieve was weighed on laboratory weights VTB-12, and weight loss of gneissic granite crushed stone (Δm, %) was determined by the formula:

$$\Delta m = \frac{m - m_1}{m} 100, \quad (1)$$

where m is the mass of the crushed stone sample before testing, g; m_1 is the mass of residue on the control sieve of 5 mm, g.

The crushability (ΔC) of gneissic granite crushed stone was determined by the grain destructiveness during compression (crushing) in the cylinder. For this purpose, a steel cylinder with a diameter and height of 150 mm according to GOST 8269.0-97 was used. Crushed stone samples are filled into the cylinder and a load of 200 kN was made using the hydraulic laboratory testing machine WK-18 ZARZAD SPRZETU (Poland). The loading speed was 1 kN/s. Laboratory scales "VTB-12" were used to determine the mass.

$$\Delta C = \frac{m - m_1}{m} 100, \quad (2)$$

where m is the mass of crushed stone test sample, g; m_1 is the mass of residue on the control sieve after sieving of crushed stone sample crushed in the cylinder, g.

Radiographic studies were conducted for the determination of the mineral composition of the crushed stone. Radiographic studies were conducted by using the automatic powder diffractometer D2Phaser (Bruker) (radiation of an x-ray tube is CoKα 1 + 2, wavelengths CoKα 1 = 1.78900 Å и CoKα 2 = 1.79283 Å, tube operating mode 30 kW/10 mA, position-sensitive detector, geometry on reflection, scheme of focusing Bregg-Brentano, speed of rotation of a sample of 20 revolutions per minute, the interval of angles of diffraction 2theta = 5-80 °, scanning step 0.02o, exposition in a point is 1.0 seconds, T = 25 °C, the atmosphere is air).

The sample was made by dry pressing of the studied substance in low-background to a ditch of single-crystal silicon (depth is 0.5 mm, the diameter of the studied area is 20 mm). The identification of the phases was contacted by using the base of powder diffraction data of the Powder Diffraction File. The results of the quantitative X-ray phase analysis are given in Table 7.

Flakiness index, water absorption, specific gravity, packed density were determined according to the method described in Russian national standard GOST 8269.0-97.

2.3. Preparation of concrete samples and determination of their characteristics

Laboratory mixing of concrete according to Russian national standard GOST 10180-2012 was carried out according to the following recipes:

Table 1. Concrete recipes.

Components	% of masses		
	Recipe №1	Recipe №2	Recipe№3
Portland Cement CEM I 42.5 N manufactured by JSC Mordovcement	18.14	18.14	18.14
Gneissic granite crushed stone (fraction of 10–20)	52.44	56.51	–
Gneissic granite sand (fraction of 0–2.5)	18.14	14.07	–
Gabbro-diabase crushed stone (fraction of 10–20)	–	–	52.44
Gabbro-diabase sand (fraction of 0–2.5)	–	–	18.14
Dry mix of:			
1. Silica fume manufactured by pilot production of INRTU			
2. Shale ash Zolest-bet manufactured by PCV LLC			
3. Modified basalt microfiber manufactured by NTC of Applied Nanotechnologies	4.03	4.03	4.03
4. Plasticizing agent REOMAX PC 3901P manufactured by KUBAN-POLYMER LLC			
5. Carbon nanoparticles Astralene manufactured by NTC of Applied Nanotechnologies			
Water of mixing according to Russian national standard GOST 23732-2011	7.25	7.25	7.25

The concrete was mixed as follows. Initially, water, binding materials and plasticizing agent were first mixed in the concrete gravity batch mixer Eco CM-71 for one minute. After that, fine aggregate and crushed stone were introduced and mixing lasted another minute. Fiber and Astralene were introduced last into the concrete mixture. The final mixing also lasted for one minute.

Nanomodifiers (Astralene) were introduced into concrete by the serial dilution method [35]. Astralene were deposited on the surface of the basalt microfiber (TC 5761-014-13800624-2004), and microfiber was introduced directly into the concrete. This resulted in a more uniform distribution of nanomaterials throughout the concrete volume.

The volume of concrete mixing was 40 litres.

Concrete density was determined according to Russian national standard GOST 10181-2014.

Concrete cubes with dimensions of 100×100×100 mm in the quantity of 30 pieces were made according to Russian national standard GOST 10180-2012.

The concrete samples were prepared in moulds and removed from the moulds after 1-day curing at room temperature. All the samples (and also the control samples) have been hardened in thermo-humidity conditions for 28 days according to Russian national standard GOST 10180-2012.

The compressive strength test of concrete cubes with dimensions of 100×100×100 mm was carried out on the hydraulic laboratory testing machine MP-1000 «Nutcracker» according to Russian national standard GOST 10180-2012.

The freeze-thaw resistance was determined on the climatic chamber SM 55/50-120 SB according to Russian national standard GOST 10060-2012. The freeze-thaw resistance was determined in a water-saturated state (F1). The dispersion of the density values of individual samples in the series before their saturation did not exceed 30 kg/m³.

Waterproofing of concrete control samples by air permeability was determined by the device AGAMA-2 according to Russian national standard GOST 12730.5-2018.

3. Results and Discussion

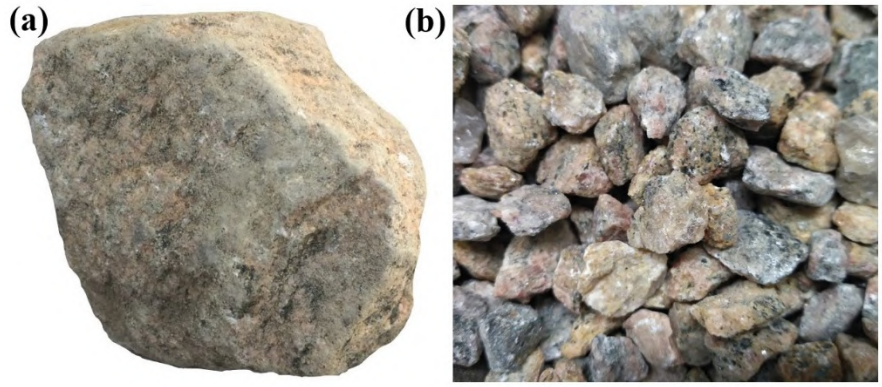


Figure 1. Large fragments of gneissic granite – (a), gneissic granite crushed stone of fraction of 10–20 mm – (b).

Table 2. Determination of crushability of gneissic granite crushed stone.

Test number	The mass before crushing, g.	Mass passed through sieve 5 mm, g.	Crushability, %	Medium value of crushability
1	3259	984	30.2	
2	3237	959	29.6	30.3
3	3281	1018	31.1	

The value of crushability corresponds to the grade of 200 according to Russian national standard GOST 8267-93, which is the lowest grade declared in Russian national standard GOST. This means that the average person will be able to easily break crushed stone with fingers of an oblong (flatness) shape or spread about a hard surface.

Table 3. Main properties of gneissic granite crushed stone.

Parameter	Unit of measure	Fraction of crushed stone	Obtained value	Regulation value	According to GOST
Flakiness index	%	10–20	34	35	Yes
		3–10	25		Yes
Freeze – thaw resistance	cycle	10–20	200	200–600	Yes
		3–10	200		Yes
Crushability	%	10–20	30.3	28–35%	Yes
		3–10			Yes
Water absorption	%	10–20	2,1	not applicable	not applicable
		3–10	2,3		
Specific gravity	–	10–20	2785	not applicable	not applicable
		3–10			
Packed density	kg/m³	10–20	1492	not applicable	not applicable
		3–10	1559		

Table 4. Main properties of gabbro-diabase crushed stone declared by manufacturer.

Parameter	Freeze – thaw resistance	Flakiness index	Crushability	Specific gravity	Packed density	Water absorption
Value	300 cycles	14 %	3.6 %	2986	1.53 kg/m³	0.1 %

The value of crushability corresponds to the grade of 1400 according to Russian national standard GOST 8267-93, which is the lowest grade declared in Russian national standard GOST.

By comparison of the properties of the gneissic granite and gabbro-diabase, a significant qualitative superiority in favour of the latter is obvious. The most significant difference is crushability (strength). The crushability of gabbro-diabase is almost 10 times the crushability of gneissic granite. The significant difference in the flakiness index is not critical, since the flakiness index can be controlled when appropriate in the industrial production of gneissic granite crushed stone. This can be done by optimizing the crushers to suit the characteristics of the gneissic granite, as well as by sieving out an excessive amount of flatness grains. [36].

Table 5. Quantitative phase analysis of gneissic granite sample (weight. %) according to the full-height analysis by Rietveld method.

Minerals	Chemical formula	% of masses
Quartz	SiO_2	41.2
Microcline	$K(AlSi_3O_8)$	17.6
Albite	$Na\ (AlSi_3O_8)$	24.3
Biotite	$K\ (Mg, Fe)_3[AlSi_3O_{10}]\ (OH, F)$	5.3
Amphibole	$(Na, Ca)_2\ (Mg, Fe^{3+}, Fe^{2+}, Al, Ti)_5\ Si_8O_{22}(OH, F)_2$	4.1
Magnetite	$Fe^{2+}Fe^{3+}{}_2O_4$	2.0
Chlorite	$(Mg, Fe)_6Si_4O_{10}(OH)_8$	3.9
Talc	$Mg_3Si_4O_{10}(OH)_2$	1.2
Calcite	$CaCO_3$	trace levels
Zirconium silicate	$ZrSiO_4$	trace levels

From these experiments it was concluded that the majority of the minerals, which are a part of crushed stone, received from sedimentary rocks of a bed of the Kem river (88.8 % of masses) is not specified on the "blacklist" of harmful components and impurity under the table A of the Russian national state standard GOST 8267-93 „Crushed stone and gravel of solid rocks for construction works. Specifications". Chlorite (3.9 % of masses), magnetite (2 % of masses) and biotite (rock-forming mica) make the exception. The amount of these rocks doesn't exceed 5.3 % of the mass according to the results of the mineralogical research.

However, for the specified harmful components of crushed stone, red lines are proceeding from the same table A of the Russian national state standard GOST 8267-93, including for magnetite, hematite, apatite, nepheline and phosphorite. Their content up to 10 % on crushed stone volume is allowed, or the

sum of the quantity of all specified minerals together should not exceed 15 % of the mass. The amount of these minerals is allowed to be up to 10 % on crushed stone volume, or the sum of the quantity of all of the specified minerals should not exceed 15 % of the mass.

At gneissic granite crushed stone from the Kem river bed, there is the only magnetite from the listed minerals. Its quantity is bearable at the rate of 10 % of the mass. The results of the mineralogical analysis of gneissic granite crushed stone from the Kem river bed showed the availability of magnetite only in the amount of 2 % of the mass. That is admissible.

The same situation occurred also for chlorite as a part of crushed stone (3.9 % of the mass) and biotite (rock-forming mica, 5.3 % of masses). According to Table A of the Russian national standard GOST 8267-93 is allowed when the total amount of layered silicates (micas, hydromicas, chlorites) will not exceed 15 % of the mass. The sum for gneissic granite crushed stone from the bed of the Kem river is not more than 9.2 % of the mass as both biotite and chlorite are minerals, which density is much more than 1 g/cm³. Consequently, the detailed analysis of the components of the structure of gneissic granite crushed stone from the Kem river bed led to a conclusion about a possibility to use the crushed stone as an aggregate for hydrotechnical concrete, because in this case, the quantities of harmful components are admissible for the recipes of hydrotechnical concrete.

Based on this, it can be concluded that there are no mineralogical and physicochemical restrictions for the use of gneissic granite crushed stone in concrete. This allows to study the mechanical characteristics of gneissic granite crushed stone, as well as the characteristics of concrete based on gneissic granite crushed stone and their compliance with actual Russian national construction standards GOST 8267-93 and GOST 26633-2015.

Table 6. Quantitative phase analysis of gabbro-diabase samples (weight. %) according to the full-height analysis by Rietveld method.

Minerals	Permissible amount, %	Amount received, %		
		Berezovsk	Goloday-gora	Ramrucheyskoe
Actinolite (Amphibole)	100	31	4	45
Feldspar (Anorthite, Albite, Microcline)	100	29	48	18
Chlorite	10	11	7	18
Biotite (mica)	10	–	–	13
Diopside - hedenbergite	100	4	17	4
Crystalline silica	100	–	10	2
Mica (Phlogopite-annite)	10	–	6	–
Dolomite	100	–	1	–
Clinozoisite	100	25	–	–

It follows from the table that even high-strength material does not always satisfy the requirements of regulatory documents. Only one of the three crushed stone satisfies the requirements for hydrotechnical concrete for the content of chlorides. Based on this analysis, crushed stone manufactured by Goloday-gora Ltd. was selected for comparative testing in concrete.

Table 7. Main properties of concretes.

Properties	Recipe № 1	Recipe № 2	Recipe № 3
Compressive strength (7 days), MPa	64.6	56.4	71.2
Compressive strength (28 days), MPa	98.2	77.5	116.6
Compressive strength (180 days), MPa	115.4	90.1	133.1
Fresch concrete density, kg/m³	2481	2487	2496
Concrete density (28 days), kg/m³	2405	2398	2416
Concrete density (180 days), kg/m³	2392	2387	2396
Freeze-thaw resistance, cycles	400	400	400
Water absorption, %	3.5	3.7	3.4
Waterproofing, Class	W20	W20	W20
Flowability, Class	F4	F4	F5
Fresh concrete density, kg/m³	2481	2487	2496

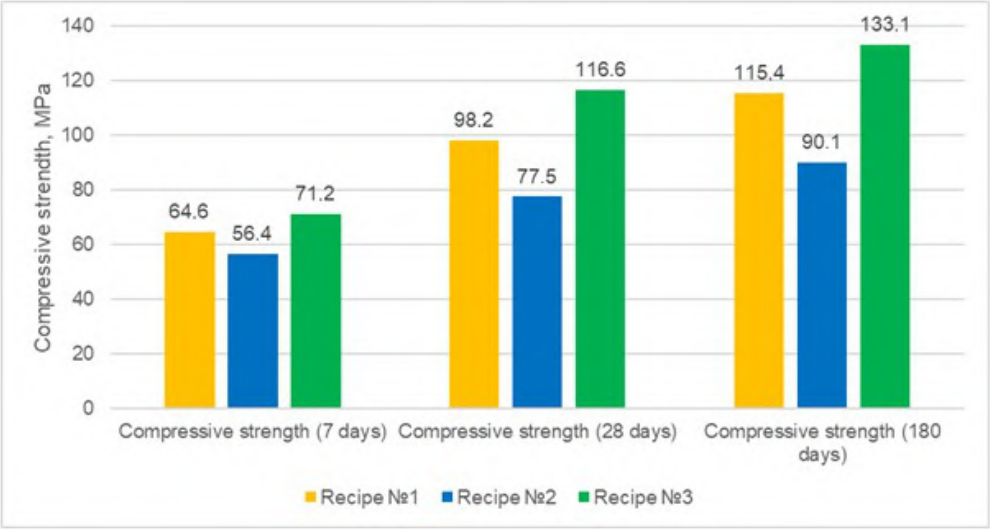


Figure 2. Compressive strength of concrete, MPa.

Table 7 and Fig. 2 show that the compressive strength of concrete with gneissic granite crushed stone of fraction of 10–20 mm differs from the compressive strength with gabbro-diabase crushed stone of fraction of 10–20 mm only by 18.7 % at the age of 28 days and 15.3 % at the age of 180 days. This is a rather nonsignificant difference considering the strength (crushability) of the crushed stone. The grade of gneissic granite in strength (crushability) was only 200 according to Russian national standard GOST 8269.0-97, while the grade of gabbro-diabase was 1400, which is the maximum strength (crushability) grade of crushed stone according to Russian national standard GOST 8269.0-97. By comparison of absolute values, the compressive strength of concrete with gneissic granite crushed stone of fraction of 10–20 mm differs from the strength of concrete with gabbro-diabase crushed stone of fraction 10–20 mm by 18.4 MPa at the age of 28 days and 17.7 at the age of 180 days.

Compressive strength values at the age of 7 days were determined as additional to characterize the concrete hardening process. At the age of 7 days, concrete with gneissic granite crushed stone of fraction of 10–20 mm had 66 % of compressive strength compared to concrete compressive strength at the age of 28 days, on the concrete with gneissic granite crushed stone of fraction of 3–10 mm had 73 % of compressive strength compared to concrete compressive strength at the age of 28 days, on the concrete of gabbro-diabase crushed stone of fraction of 10–20 mm had 61 % of compressive strength compared to concrete compressive strength at the age of 28 days.

However, following the regulatory documents for hydrotechnical concrete, it is possible to determine the grade strength at the age of 180 days. Due to the operation of hydrotechnical concrete in a water-saturated state, the strength gain does not stop at the age of 28 days but continues to gain strength further.

The difference in compressive strength in 28 and 180 days corresponds to regulatory documents, which provide for the introduction of increasing factors for analysing the strength gain of concrete after 28 days of maturing. This is also supported by numerous experimental data from other researchers, [9, 37, 38].

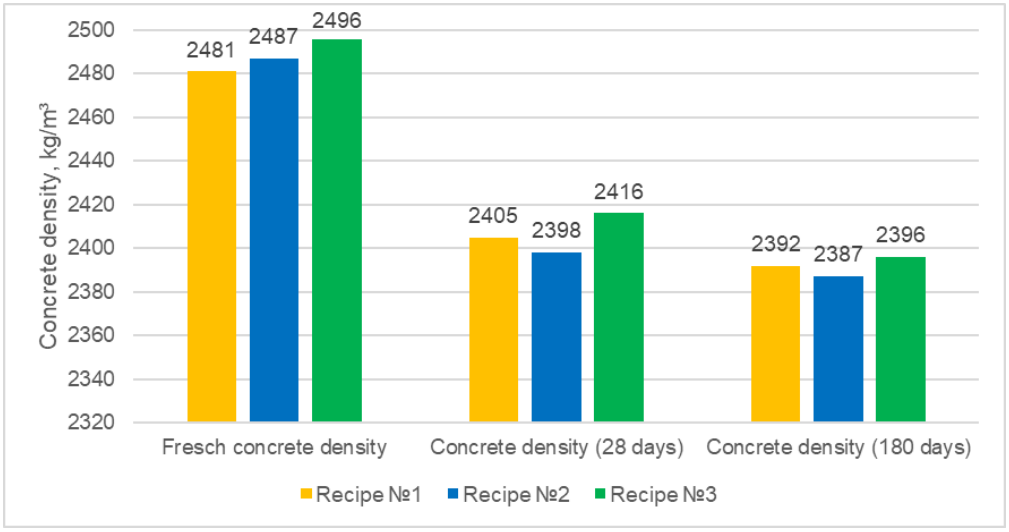


Figure 3. Fresh concrete density, kg/m³.

Table 7 and Fig. 3 show that the concrete density of all recipes is practically equal at the same age. The concrete density value is quite typical for concrete with coarse aggregate. This demonstrates that the structure of concrete is not disturbed when replacing one crushed stone with another. The lowering of concrete density does not occur even when the crushed stone of the fraction of 3–10 mm was used, although this effect is quite often observed when the aggregate size is lowered.

The difference in the flowability of concrete with aggregate from gabbro-diabase (recipe 3) in comparison with concrete based on aggregate from gneissic granite (recipes 1 and 2) is primarily associated with different water absorption of aggregates since the value of water absorption of gneissic granite (~2.2 % of masses) is significantly higher than that value of water absorption of gabbro-diabase (0.1 % of masses). Gneissic granite is saturated with water from the composition, which leads to a decrease in water amount in the matrix. The introduction of toroidal nanoparticles (Astralene) leads to a better penetration of suspension from water and binding materials deep into the crushed stone, as well as directed crystallization of cement stone [40].

This moment also has a huge positive effect. Gneissic granite crushed stone has rather large pores, which leads to saturation with a suspension of water and the binder materials. This leads to the strengthening of the crushed stone itself, as well as stronger adhesion between the crushed stone and the matrix.

Table 8. Determination of freeze-thaw resistance of concrete with gneissic granite crushed stone of fraction of 10–20 mm.

Reference sample					Control sample (12 freezing/thawing cycles)							
No	Sample dimension, cm		Ultimate load, kN	Comp. strength, MPa	No	Sample dimension, cm		Ultimate load, kN	Comp. strength, MPa	Weight, g		Weight loss, %
	length a	length b				length a	length b			before testing	after testing	
1	10	10	941.4	94.1	1	10.1	10.0	900.9	89.2	2475	2475	
2	10.1	10	960.5	95.1	2	10	10.1	910	90.1	2479	2479	
3	10	10	956.7	95.7	3	10	10	892.44	92.4	2464	2465	
4	10	10	1061.2	96.1	4	10	10	935.8	93.6	2484	2484	
5	10	10	9971.9	97.2	5	10	10	947.6	94.8	2466	2467	
6	10.1	10	1008	99.8	6	10	10	957.3	95.7	2477	2477	
Strength average value				96.3	Strength average value				92.6	Total:	Total:	
Mean root square deviation				1.8	Mean root square deviation				2.36	14845	14847	-0.02
Coefficient of variation				1.88	Coefficient of variation				2.54			
Lower range value of confidence interval, $X\kappa$ min				91.1	Lower range value of confidence interval, Xo min				86.1	No weigth loss		
The freeze-thaw resistance condition Xo>0.9 $X\kappa$ min is positive (86.1>0.9*91.1 or 86.1>82)												
These concrete samples correspond to the frost resistance grade F1400 according to Russian national standard GOST 10060-2012												

The freeze-thaw resistance of concretes with gabbro-diabase of the fraction of 10–20 mm and gneissic granite of fraction of 3–10 mm was also F1400. Calculation tables are not specified, since they do not carry a semantic charge. Tests were carried out according to the same standard method as the freeze-thaw resistance test of concrete with gneissic granite of the fraction of 10–20 mm (Table 8).

The freeze-thaw resistance value F400 is a very high class of freeze-thaw resistance even for concrete with high-quality aggregates. The freeze-thaw resistance class of concrete the most frequently used in civil engineering is class F50-150. It is safe to notice in this case that the combination of basalt microfiber (which is distributed evenly throughout the entire volume of concrete) and carbon toroidal nanoparticles (Astralene) contributes to achieving such a high freeze-thaw frost resistance class. The effect of fibers on the freeze-thaw resistance of concrete has been studied in [41, 42], and the effect of nanoparticles has been studied here [34, 43].

Concrete with freeze-thaw resistance class F400 belongs to the group of high freeze-thaw resistance. Concretes with this frost resistance class belong to the group of special concretes. They are intended for use in special cases. For example, such concretes are used when there is a variable level of water contacting the concrete structure in addition to low temperatures.

The high waterproofing class (maximum according to Russian national standard GOST 12730.5-2018) indicates that this concrete does not need additional water isolation. And even more, the concrete itself becomes a water isolation material. This is a very significant factor, as it seriously simplifies the tasks of water isolation during construction when temporary and financial resources are spent on additional water isolation.

A high class of freeze-thaw resistance in sum with a high class of waterproofing makes this one also more durable since when concrete is used in the north of Russia, the durability of concrete directly depends on its freeze-thaw resistance and waterproofing.

It should be noted that this study was originally aimed at demonstrating the fundamental possibility of developing high-strength concretes using low-quality (low-strength) aggregate. The matrix used provides extensive further opportunities for concrete development already directly for practical applications using solid industrial and construction waste, which meets the global challenges facing construction in the 21st century [39, 44]. Moreover, for the production of civil and even special-purpose concretes of low classes, it is possible to achieve a significant decrease in the amount of cement (up to 150–200 kg/m^3) using analogues of the developed matrix. Modern high performances concretes are not associated with an increased cement amount, but, above all, the use of current achievements in construction chemistry and pozzolan additives and fibers [45]. For example, when using pozzolan admixes and nanomodification, concrete strength values of more than 80 MPa were obtained in the paper [46]. Strength values of more than 100 MPa at the age of 90 days using nanomaterials were obtained in the paper [47].

It also stands to mention that this paper was not aimed at studying the effect of nanomodifiers on the properties of concrete. The influence of nanomodifiers has already been studied in previous works by the authors of this paper, as well as other researchers. Nanomodifiers were used as additives to concrete, such as silica fume, shale ash, etc., the effectiveness of which has already been proven in concrete.

4. Conclusions

1. Mineralogical, strength and climatic properties of gneissic granite crushed stone produced from gneissic granite rock by crushing were investigated. During the study, it was found that gneissic granite crushed stone has a rather high freeze-thaw resistance, but low strength and high value of water absorption. However, gneissic granite crushed stone does not have any restrictions for use in concrete in its mineralogical composition.

2. High-strength concretes with a strength of 98.2 MPa (fraction of 10 – 20 mm) and 77.5 MPa (fraction of 3 – 10 mm) at the age of 28 days based on two fractions of gneissic granite crushed stone was developed. Concrete strength increased up to 115.4 MPa (fraction of 10 – 20 mm) and up to 90.1 (fraction of 3 – 10 mm) after 180 days of maturation.

3. Obtained values of compressive strength of concrete based on low-quality gneissic granite crushed stone differed not too significantly from compressive strength of concrete made according to the same recipe using high-strength gabbro-diabase crushed stone. Compressive strength values were 98.2 MPa and 116.6 MPa (28 days) and 115.4 MPa and 131.1 MPa (180 days) for gneissic granite and gabbro-diabase crushed stone, respectively.

4. This nonsignificant difference in compressive strength of concrete compared to the huge difference in strength (crushability) of the crushed stone is due to the fact that in the case of using a low-strength aggregate, the main load was taken by the concrete matrix, not the aggregate. Due to the high value of water absorption of the crushed stone, crushed stone was saturated with a suspension of water and binder materials, which led to the strengthening of the crushed stone, as well as stronger adhesion to the concrete matrix, which made it possible to distribute the load more evenly.

5. The developed matrix makes it possible to produce high-strength concrete in hard-to-reach and remote regions with difficult access to high-strength concrete aggregates. It also makes it possible to obtain high-strength concretes when using aggregates from industrial and construction waste, which meets the global challenges facing construction in the 21st century.

6. The freeze-thaw resistance value F400 is a very high class of freeze-thaw resistance even for concrete with high-quality aggregates. The freeze-thaw resistance class of concrete the most frequently used in civil engineering is class F50-150. Concrete with freeze-thaw resistance class F400 belongs to the group of high freeze-thaw resistance. Concretes with this class of frost resistance belong to the group of special concretes. They are intended for use in special cases. For example, such concretes are used when there is a variable level of water contacting the concrete structure in addition to low temperatures.

7. It is safe to notice in this case that the combination of basalt microfiber (which is distributed evenly throughout the entire volume of concrete) and carbon toroidal nanoparticles (Astralene) makes contributes to achieving such a high freeze-thaw frost resistance class.

8. The combination of high compressive strength, the low value of water absorption, high water waterproofing class, and high freeze-thaw resistance makes the developed concrete unique since a low-strength aggregate was used.

References

1. Lazhentsev, V.N. Theoretical results of research on spatial and territorial development (on examples of the north of European Russia). Economy of Region. 2015. DOI: 10.17059/2015-4-2
2. Frolov, I.E. Development of the Russian Arctic zone: Challenges facing the renovation of transport and military infrastructure. Studies on Russian Economic Development. 2015. DOI: 10.1134/S1075700715060040
3. Ardizzon, G., Cavazzini, G., Pavesi, G. A new generation of small hydro and pumped-hydro power plants: Advances and future challenges 2014.
4. Hayashi, M., Hughes, L. The Fukushima nuclear accident and its effect on global energy security. Energy Policy. 2013. DOI: 10.1016/j.enpol.2012.11.046
5. Vishalakshi, K.P., Revathi, V., Sivamurthy Reddy, S. Effect of type of coarse aggregate on the strength properties and fracture energy of normal and high strength concrete. Engineering Fracture Mechanics. 2018. DOI: 10.1016/j.engfracmech.20-18.02.029
6. Rao, A., Jha, K.N., Misra, S. Use of aggregates from recycled construction and demolition waste in concrete. Resources, Conservation and Recycling. 2007. DOI: 10.1016/j.resconrec.2006.05.010
7. Pacheco-Torgal, F., Tam, V.W.Y., Labrincha, J.A., Ding, Y., De brito, J. Handbook of Recycled Concrete and Demolition Waste 2013.
8. De Brito, J., Agrela, F., Silva, R.V. Construction and demolition waste. New Trends in Eco-efficient and Recycled Concrete 2018.
9. Singh, M., Srivastava, A., Bhunia, D. Long term strength and durability parameters of hardened concrete on partially replacing cement by dried waste marble powder slurry. Construction and Building Materials. 2019. DOI: 10.1016/j.conbuildmat.20-18.12.005
10. Wild, S., Khatib, J.M., Jones, A. Relative strength, pozzolanic activity and cement hydration in superplasticised metakaolin concrete. Cement and Concrete Research. 1996. DOI: 10.1016/0008-8846(96)00148-2
11. Barabanshchikov, Y.G., Belyaeva, S.V., Arkhipov, I.E., Antonova, M.V., Shkolnikova, A.A., Lebedeva, K.S. Influence of superplasticizers on the concrete mix properties. Magazine of Civil Engineering. 2017. DOI: 10.18720/MCE.74.11
12. Rassokhin, A.S., Ponomarev, A.N., Figovsky, O.L. Silica fumes of different types for high-performance fine-grained concrete. Magazine of Civil Engineering. 2018. 78(2). Pp. 151–160. DOI: 10.18720/MCE.78.12
13. Aïtcin, P.C. Accelerators. Science and Technology of Concrete Admixtures 2016.
14. Zhang, L., Ji, Y., Li, J., Gao, F., Huang, G. Effect of retarders on the early hydration and mechanical properties of reactivated cementitious material. Construction and Building Materials. 2019. DOI: 10.1016/j.conbuildmat.2019.03.323
15. Wang, H., Belarbi, A. Ductility characteristics of fiber-reinforced-concrete beams reinforced with FRP rebars. Construction and Building Materials. 2011. DOI: 10.1016/j.conbuildmat.2010.11.040
16. Papayianni, I., Anastasiou, E. Production of high-strength concrete using high volume of industrial by-products. Construction and Building Materials. 2010. DOI: 10.1016/j.conbuildmat.2010.01.016
17. Lotfi, S., Eggimann, M., Wagner, E., Mróz, R., Deja, J. Performance of recycled aggregate concrete based on a new concrete recycling technology. Construction and Building Materials. 2015. DOI: 10.1016/j.conbuildmat.2015.07.021
18. Zegardło, B., Szeląg, M., Ogrodnik, P. Ultra-high strength concrete made with recycled aggregate from sanitary ceramic wastes – The method of production and the interfacial transition zone. Construction and Building Materials. 2016. DOI: 10.1016/j.conbuildmat.2016.06.112
19. Meyer, C. The greening of the concrete industry. Cement and Concrete Composites. 2009. DOI: 10.1016/j.cemconcomp.2008.12.010
20. Mahdikhani, M., Khanban, M.R. Utilization of industrial waste residue containing heavy metals as a substitute for fine aggregates. Construction and Building Materials. 2019. DOI: 10.1016/j.conbuildmat.2019.06.061
21. Frolov, A., Chumadova, L., Cherkashin, A., Akimov, L. Prospects of use and impact of nanoparticles on the properties of high-strength concrete. Applied Mechanics and Materials. 2014. DOI: 10.4028/www.scientific.net/AMM.584-586.1416
22. Nazari, A., Riahi, S., Riahi, S., Shamekhi, S.F., Khademno, A. Improvement the mechanical properties of the cementitious composite by using TiO2 nanoparticles. 2010.
23. Ponomarev, A., Knezević, M., Vatin, N., Kiski, S., Ageev, I. Nanosize scale additives mix influence on the properties of the high performance concretes. Journal of Applied Engineering Science. 2014. DOI: 10.5937/jaes12-6161
24. Douba, A.E., Emiroglu, M., Kandil, U.F., Reda Taha, M.M. Very ductile polymer concrete using carbon nanotubes. Construction and Building Materials. 2019. DOI: 10.1016/j.conbuildmat.2018.11.021
25. Raki, L., Beaudoin, J., Alizadeh, R., Makar, J., Sato, T. Cement and concrete nanoscience and nanotechnology. 2010.
26. Konsta-Gdoutos, M.S., Metaxa, Z.S., Shah, S.P. Highly dispersed carbon nanotube reinforced cement based materials. Cement and Concrete Research. 2010. DOI: 10.1016/j.cemconres.2010.02.015
27. Carriço, A., Bogas, J.A., Hawreen, A., Guedes, M. Durability of multi-walled carbon nanotube reinforced concrete. Construction and Building Materials. 2018. DOI: 10.1016/j.conbuildmat.2017.12.221
28. Ponomarev, A.N., Rassokhin, A.S. Hybrid wood-polymer composites in civil engineering. Magazine of Civil Engineering. 2016. DOI: 10.5862/MCE.68.5
29. Palla, R., Karade, S.R., Mishra, G., Sharma, U., Singh, L.P. High strength sustainable concrete using silica nanoparticles. Construction and Building Materials. 2017. DOI: 10.1016/j.conbuildmat.2017.01.129
30. Cherkashin, A.V., Pykhtin, K.A., Begich, Y.E., Sherstobitova, P.A., Koltsova, T.S. Mechanical properties of nanocarbon modified cement. Magazine of Civil Engineering. 2017. DOI: 10.18720/MCE.72.7

31. Kim, J.K., Lee, C.S., Park, C.K., Eo, S.H. The fracture characteristics of crushed limestone sand concrete. Cement and Concrete Research. 1997. DOI: 10.1016/S0008-8846(97)00156-7
32. Ramdani, S., Guettala, A., Benmalek, M.L., Aguiar, J.B. Physical and mechanical performance of concrete made with waste rubber aggregate, glass powder and silica sand powder. Journal of Building Engineering. 2019. DOI: 10.1016/j.jobe.2018.11.003
33. Ebrahimi, K., Daiezadeh, M.J., Zakertabrizi, M., Zahmatkesh, F., Habibnejad Korayem, A. A review of the impact of micro- and nanoparticles on freeze-thaw durability of hardened concrete: Mechanism perspective 2018.
34. Khushnood, R.A., Nawaz, A. Effect of adding graphite nano/micro platelets on salt freeze-thaw resistance of nano-modificent concrete. Materials Research Express. 2019. DOI: 10.1088/2053-1591/ab2d86
35. Ben-David, A., Davidson, C.E. Estimation method for serial dilution experiments. Journal of Microbiological Methods. 2014. DOI: 10.1016/j.mimet.2014.08.023
36. Ramsay, D.M., Dhir, R.K., Spence, I.M. The role of rock and clast fabric in the physical performance of crushed-rock aggregate1974
37. Menéndez, G., Bonavetti, V., Irassar, E.F. Strength development of ternary blended cement with limestone filler and blast-furnace slag. Cement and Concrete Composites. 2003. DOI: 10.1016/S0958-9465(01)00056-7
38. Uthaman, S., Vishwakarma, V., George, R.P., Ramachandran, D., Kumari, K., Preetha, R., Premila, M., Rajaraman, R., Mudali, U.K. Enhancement of strength and durability of fly ash concrete in seawater environments: Synergistic effect of nanoparticles. Construction and Building Materials. 2018. DOI: 10.1016/j.conbuildmat.2018.07.214
39. Raut, S.P., Ralegaonkar, R.V., Mandavgane, S.A. Development of sustainable construction material using industrial and agricultural solid waste: A review of waste-create bricks. Construction and Building Materials. 2011. DOI: 10.1016/j.conbuildmat.2011.04.038
40. Nisina, T.A., Ponomarev, N.A., Balykov, S.A., Pankin, N.A. Fine-grained fibre concretes modified by complexed nanoadditives. International Journal of Nanotechnology. 2017. 14 (7-8). Pp. 665–769. DOI: 10.1504/IJNT.2017.083441
41. Berkowski, P., Kosior-Kazberuk, M. Effect of Fiber on the Concrete Resistance to Surface Scaling Due to Cyclic Freezing and Thawing. Procedia Engineering. 2015. 111. Pp. 121–127. DOI.org/10.1016/j.proeng.2015.07.065
42. Nili, M., Azarioon, A., Danesh, A. et al. Experimental study and modeling of fiber volume effects on frost resistance of fiber reinforced concrete. International Journal of Civil Engineering. 2018. 16. Pp. 263–272. DOI.org/10.1007/s40999-016-0122-2
43. Khushnood, R.A., Nawaz, A. Effect of adding graphite nano/micro platelets on salt freeze-thaw resistance of nano-modificent concrete. Materials Research Express. 2019. 186. Pp. 1105–1113. DOI: 10.1088/2053-1591/ab2d86
44. Safiuddin, M., Jumaat, M.Z., Salam, M.A., Islam, M.S., Hashim, R. Utilization of solid wastes in construction materials. Academic Journals. 2010. 5(13). Pp. 1952–1963.
45. Rassokhin, A.S., Ponomarev, A.N., Shambina, S.L., Karlina, A.I. Different types of basalt fibers for disperse reinforcing of fine-grained concrete. Magazine of Civil Engineering. 2022. 109(1). Article No. 10913. DOI: 10.34910/MCE.109.13
46. Bastami, M., Baghbadrani, M., Aslani, F. Performance of nano-Silica modified high strength concrete at elevated temperatures. Construction and Building Materials. 2014. 68. Pp. 402–408. DOI: 10.1016/j.conbuildmat.2014.06.026.
47. Amin, M., Abu El-Hassan, K. Effect of using different types of nano materials on mechanical properties of high strength concrete. Construction and Building Materials. 2015. 80. Pp. 116–124. DOI: 10.1016/j.conbuildmat.2014.12.075.

Contacts:

Aleksandr Rassokhin, rassokhinaleksandr@gmail.com

Andrey Ponomarev, 9293522@gmail.com

Antonina Karlina, karlinat@mail.ru

Received 26.12.2020. Approved after reviewing 27.04.2021. Accepted 27.04.2021.

Федеральное государственное автономное образовательное учреждение высшего образования
Санкт-Петербургский политехнический университет Петра Великого

ПОЛИТЕХ
Санкт-Петербургский политехнический университет Петра Великого

Инженерно-строительный институт
Центр дополнительных профессиональных программ

195251, г. Санкт-Петербург, Политехническая ул., 29,
тел/факс: 552-94-60, www.stroikursi.spbstu.ru,
stroikursi@mail.ru

Приглашает специалистов проектных и строительных организаций,
не имеющих базового профильного высшего образования
на курсы профессиональной переподготовки (от 500 часов)
по направлению «Строительство» по программам:

П-01 «Промышленное и гражданское строительство»

Программа включает учебные разделы:

- ***Основы строительного дела***
- ***Инженерное оборудование зданий и сооружений***
- ***Технология и контроль качества строительства***
- ***Основы проектирования зданий и сооружений***
- ***Автоматизация проектных работ с использованием AutoCAD***
- ***Автоматизация сметного дела в строительстве***
- ***Управление строительной организацией***
- ***Управление инвестиционно-строительными проектами. Выполнение функций технического заказчика***

П-02 «Экономика и управление в строительстве»

Программа включает учебные разделы:

- ***Основы строительного дела***
- ***Инженерное оборудование зданий и сооружений***
- ***Технология и контроль качества строительства***
- ***Управление инвестиционно-строительными проектами. Выполнение функций технического заказчика и генерального подрядчика***
- ***Управление строительной организацией***
- ***Экономика и ценообразование в строительстве***
- ***Управление строительной организацией***
- ***Организация, управление и планирование в строительстве***
- ***Автоматизация сметного дела в строительстве***

П-03 «Инженерные системы зданий и сооружений»

Программа включает учебные разделы:

- ***Основы механики жидкости и газа***
- ***Инженерное оборудование зданий и сооружений***
- ***Проектирование, монтаж и эксплуатация систем вентиляции и кондиционирования***
- ***Проектирование, монтаж и эксплуатация систем отопления и теплоснабжения***
- ***Проектирование, монтаж и эксплуатация систем водоснабжения и водоотведения***
- ***Автоматизация проектных работ с использованием AutoCAD***
- ***Электроснабжение и электрооборудование объектов***

П-04 «Проектирование и конструирование зданий и сооружений»

Программа включает учебные разделы:

- ***Основы сопротивления материалов и механики стержневых систем***
- ***Проектирование и расчет оснований и фундаментов зданий и сооружений***
- ***Проектирование и расчет железобетонных конструкций***
- ***Проектирование и расчет металлических конструкций***
- ***Проектирование зданий и сооружений с использованием AutoCAD***
- ***Расчет строительных конструкций с использованием SCAD Office***

П-05 «Контроль качества строительства»

Программа включает учебные разделы:

- ***Основы строительного дела***
- ***Инженерное оборудование зданий и сооружений***
- ***Технология и контроль качества строительства***
- ***Проектирование и расчет железобетонных конструкций***
- ***Проектирование и расчет металлических конструкций***
- ***Обследование строительных конструкций зданий и сооружений***
- ***Выполнение функций технического заказчика и генерального подрядчика***

По окончании курса слушателю выдается диплом о профессиональной переподготовке установленного образца, дающий право на ведение профессиональной деятельности

